1. Report No.	2. Government Accession No.	3. Recipient's Catalog No.
4. Title and Subtitle **LONG-TERM POST-TENSIONED BEAM AND COLUMN EXPOSURE TEST SPECIMENS: EXPERIMENTAL PROGRAM**		5. Report Date **October 1999**
		6. Performing Organization Code
7. Author(s) **J. S. West, A. J. Schokker, C. J. Larosche, J. E. Breen, and M. E. Kreger**		8. Performing Organization Report No. Research Report 1405-3
9. Performing Organization Name and Address Center for Transportation Research The University of Texas at Austin 3208 Red River, Suite 200 Austin, TX 78705-2650		10. Work Unit No. (TRAIS)
		11. Contract or Grant No. Research Study 0-1405
12. Sponsoring Agency Name and Address Texas Department of Transportation Research and Technology Transfer Section, Construction Division P.O. Box 5080 Austin, TX 78763-5080		13. Type of Report and Period Covered Research Report (9/93-8/99)
		14. Sponsoring Agency Code

15. Supplementary Notes
Project conducted in cooperation with the U.S. Department of Transportation

16. Abstract

The use of post-tensioning in bridges can provide durability and structural benefits to the system while expediting the construction process. When post-tensioning is combined with precast elements, traffic interference can be greatly reduced through rapid construction. Post-tensioned concrete substructure elements such as bridge piers, hammerhead bents, and straddle bents have become more prevalent in recent years. Chloride-induced corrosion of steel in concrete is one of the most costly forms of corrosion each year. Coastal substructure elements are exposed to seawater by immersion or spray, and inland bridges may also be at risk due to the application of deicing salts. Corrosion protection of the post-tensioning system is vital to the integrity of the structure because loss of post-tensioning can result in catastrophic failure.

Documentation for durability design of the grout, ducts, and anchorage systems is very limited. The objective of this research is to evaluate the effectiveness of corrosion protection measures for post-tensioned concrete substructures by designing and testing specimens representative of typical substructure elements using state-of-the-art practices in aggressive chloride exposure environments. This evaluation was accomplished through long-term exposure testing of twenty-seven large-scale beam specimens and ten large-scale column specimens.

Long-term exposure testing of the beam and column specimens is ongoing, but preliminary findings indicate increased corrosion protection with increasing levels of post-tensioning, although traditional fully prestressed sections may not give as high a benefit to cost ratio as partially prestressed sections with high percentages of prestressing steel. Specimens with low permeable concrete are showing better corrosion protection than specimens with the standard concrete for bridge substructures used by the Texas Department of Transportation. Recommendations and guidelines for durable design of post-tensioned bridge substructures were developed from the findings to date, and supplementary information will be provided after final autopsy of all specimens.

17. Key Words		18. Distribution Statement	
Post-tensioned, substructure, durability, bridge, concrete, corrosion protection, tendons, coatings		No restrictions. This document is available to the public through the National Technical Information Service, Springfield, Virginia 22161.	
19. Security Classif. (of report) Unclassified	20. Security Classif. (of this page) Unclassified	21. No. of pages 282	22. Price

Form DOT F 1700.7 (8-72)   Reproduction of completed page authorized

LONG-TERM POST-TENSIONED BEAM AND COLUMN EXPOSURE TEST SPECIMENS: EXPERIMENTAL PROGRAM

by

J. S. West, A. J. Schokker, C. J. Larosche, J. E. Breen, and M. E. Kreger

Research Report 1405-3

Research Project 0-1405

*DURABILITY DESIGN OF POST-TENSIONED
BRIDGE SUBSTRUCTURE ELEMENTS*

conducted for the

Texas Department of Transportation

in cooperation with the

**U.S. Department of Transportation
Federal Highway Administration**

by the

**CENTER FOR TRANSPORTATION RESEARCH
BUREAU OF ENGINEERING RESEARCH
THE UNIVERSITY OF TEXAS AT AUSTIN**

October 1999

ACKNOWLEDGEMENTS

DISCLAIMER

NOT INTENDED FOR CONSTRUCTION,
PERMIT, OR BIDDING PURPOSES

J.E. Breen, P.E., TX #18479

M.E. Kreger, P.E., TX #65541

Research Supervisors

TABLE OF CONTENTS

LIST OF FIGURES

LIST OF TABLES

SUMMARY

The use of post-tensioning in bridges can provide durability and structural benefits to the system while expediting the construction process. When post-tensioning is combined with precast elements, traffic interference can be greatly reduced through rapid construction. Post-tensioned concrete substructure elements such as bridge piers, hammerhead bents, and straddle bents have become more prevalent in recent years. Chloride-induced corrosion of steel in concrete is one of the most costly forms of corrosion each year. Coastal substructure elements are exposed to seawater by immersion or spray, and inland bridges may also be at risk due to the application of deicing salts. Corrosion protection of the post-tensioning system is vital to the integrity of the structure because loss of post-tensioning can result in catastrophic failure.

Documentation for durability design of the grout, ducts, and anchorage systems is very limited. The objective of this research is to evaluate the effectiveness of corrosion protection measures for post-tensioned concrete substructures by designing and testing specimens representative of typical substructure elements using state-of-the-art practices in aggressive chloride exposure environments. This evaluation was accomplished through long-term exposure testing of twenty-seven large-scale beam specimens and ten large-scale column specimens.

Long-term exposure testing of the beam and column specimens is ongoing, but preliminary findings indicate increased corrosion protection with increasing levels of post-tensioning, although traditional fully prestressed sections may not give as high a benefit to cost ratio as partially prestressed sections with high percentages of prestressing steel. Specimens with low permeable concrete are showing better corrosion protection than specimens with the standard concrete for bridge substructures used by the Texas Department of Transportation. Recommendations and guidelines for durable design of post-tensioned bridge substructures were developed from the findings to date, and supplementary information will be provided after final autopsy of all specimens.

CHAPTER 1
INTRODUCTION

1.1   BRIDGE SUBSTRUCTURE DURABILITY

Durability is the ability of a structure to withstand various forms of attack from the environment. For bridge substructures, the most common concerns are corrosion of steel reinforcement, sulfate attack, freeze-thaw damage, and alkali-aggregate reactions. The last three are forms of attack on the concrete itself. Much research has been devoted to these subjects, and for the most part these problems have been solved for new structures. The aspect of most concern for post-tensioned substructures is reinforcement corrosion. The potential for corrosion of steel reinforcement in bridges is high in some areas of Texas. In the northern regions, bridges may be subjected to deicing chemicals leading to the severe corrosion damage shown in Figure 1(a). Along the Gulf Coast, the hot, humid saltwater environment can also produce severe corrosion damage, as shown in Figure 1(b).

(a) Deicing Chemical Exposure	(b) Coastal Saltwater Exposure
"Attack from Above"	"Attack from Below"

Figure 1.1 - Typical Corrosion Damage in Texas Bridge Substructures

The American Society of Civil Engineers (ASCE) produced a "report card" for America's infrastructure, as shown in Figure 1.2. Bridges faired better than most other areas of the infrastructure, receiving a grade of C-minus. However, a grade of C-minus is on the verge of being poor, and the ASCE comments that accompanied the grade indicated that nearly one third of all bridges are structurally deficient or functionally obsolete. What these statistics mean is that there are many bridges that need to be either repaired or replaced. This finding also means that more attention should be given to durability in the design process, since a lack of durability is one of the biggest contributors to the poor condition of the infrastructure.

1998 Report Card for America's Infrastructure

Subject	Grade
Roads	D-
Bridges	C-
Mass Transit	C
Aviation	C-
Schools	F
Drinking Water	D
Wastewater	D+
Solid Waste	C-

"Nearly 1 of every 3 (31.4%) bridges is rated structurally deficient or functionally obsolete.

It will require $80 billion to eliminate the current backlog of deficiencies and maintain repair levels."

Figure 1.2 - ASCE Evaluation of Infrastruture Condition

1.2   POST-TENSIONING IN BRIDGE SUBSTRUCTURES

1.2.1   Benefits of Post-Tensioning

Post-tensioning has been widely used in bridge superstructures, but has seen only limited applications in bridge substructures. There are many possible situations where post-tensioning can be used in bridge substructures to provide structural and economical benefits. Some possible benefits of post-tensioning are listed in Table 1.1.

Table 1.1 - Possible Benefits of Post-Tensioning

Benefit	Structural Behavior	Construction	Durability
Control of Deflections	✓		
Increased Stiffness	✓		
Improved Crack Control (higher cracking moment, fewer cracks, smaller crack widths)	✓		✓
Reduced Reinforcement Congestion	✓	✓	✓
Continuity of Reinforcement	✓		✓
Efficient utilization of high strength steel and concrete	✓		✓
Quick, efficient joining of precast elements	✓	✓	✓
Continuity between existing components and additions	✓	✓	✓

Although prestressing or post-tensioning is normally chosen for structural or construction reasons, many of the same factors can improve durability. For example, reduced cracking and crack widths offers the potential for improving the corrosion protection provided by the concrete. Reduced reinforcement congestion and continuity of reinforcement means that it is easier to place and compact the concrete with less opportunity for voids in the concrete. Post-tensioning is often used in conjunction with precasting. Precast concrete offers improved quality control, concrete quality, and curing conditions, all leading to improved corrosion protection. Bonded post-tensioning also provides the opportunity for multiple levels of corrosion protection for the prestressing tendon, as shown in Figure 1.3. Protection measures include surface treatments on the concrete, the concrete itself, the duct, the grout and strand or bar coatings such as epoxy or galvanizing. Post-tensioning also provides the opportunity to electrically isolate the prestressing system from the rest of the structure.
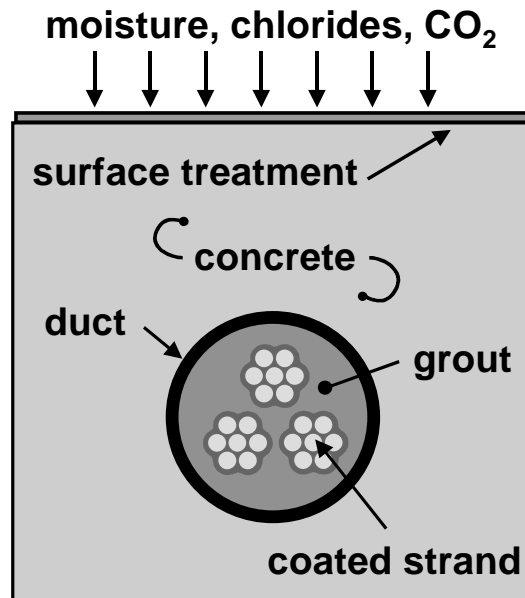
Figure 1.3 - Multilevel Corrosion Protection for Bonded Post-Tensioning Tendons

Although the concept of post-tensioning is not new, post-tensioning as it stands today is a relatively new form of construction, having been used in bridge structures in the United States for a little over forty-five years. At this stage in development, construction practices and materials are continuously improving. It is important that durability of the structure be considered during this development process. In particular, chloride-induced corrosion is a very real concern for all types of bridges. Research in this area for post-tensioned bridges is limited in part due to the long-term nature of durability studies.

The development of new post-tensioning materials and systems in recent years has made some of the durability research in this area obsolete. The current research focuses on durability testing of many different state-of-the-art variables for post-tensioning, focusing on substructure elements. A combination of electrically accelerated corrosion tests and exposure tests with varying degrees of severity are used to provide results in a timely manner.

Post-tensioned bridge substructures are becoming a more prevalent form of construction. The utilization of precast, post-tensioned substructure elements can significantly reduce traffic inference and can be particularly beneficial in large urban areas. The substructure elements also have the potential to be aesthetically pleasing alternatives as shown in Figure 1.4. This figure shows a post-tensioned precast segmental bridge pier from U.S. Highway 183 in Austin, Texas prior to addition of the superstructure. The precast components that make up this pier are shown in Figure 1.5 and 1.6. The post-tensioning ducts are evident in the close-up in Figure 1.5. A post-tensioned straddle bent from this project is shown in Figure 1.7.

Figure 1.4 - Post-Tensioned Precast Segmental Bridge Pier

Figure 1.5 - Precast Bridge Pier Segment Close Up

Figure 1.6 - Precast Bridge Pier Segments

Figure 1.7 - Post-Tensioned Straddle Bent

1.3   MIXED REINFORCEMENT IN STRUCTURAL CONCRETE

The recent development of the AASHTO LRFD (Load and Resistance Factor Design) Bridge Design Specifications explicitly recognized the use of mixed reinforcement for the first time in American bridge and building codes. Mixed reinforcement, sometimes referred to as partial prestressing, describes structural concrete members with a combination of high strength prestressing steel and nonprestressed mild steel reinforcement. The relative amounts of prestressing steel and reinforcing bars may vary, and the level of prestress in the prestressing steel may be altered to suit specific design requirements. In most cases, members with mixed reinforcement are expected to crack under service load conditions (flexural cracks due to applied loading).

In the past, prestressed concrete elements have always been required to meet the classic definition of full prestressing where concrete stresses are kept within allowable limits and members are generally assumed to be uncracked at service load levels (no flexural cracks due to applied loading). The design requirements for prestressed concrete were distinctly separate from those for reinforced concrete (nonprestressed) members and are located in different chapters or sections of the codes. The fully prestressed condition may not always lead to an optimum design. The limitation of concrete tensile stresses to below cracking can lead to large prestress requirements, resulting in very conservative designs, excessive creep deflections (camber) and the requirement for staged prestressing as construction progresses.

The use of varied amounts of prestressing in mixed reinforcement designs can offer several advantages over the traditional definitions of reinforced concrete and fully prestressed concrete:

- Mixed reinforcement designs can be based on the strength limit state or nominal capacity of the member, leading to more efficient designs than allowable stress methods.

- The amount of prestressed reinforcement can be tailored for each design situation. Examples include determining the necessary amount of prestress to:
  - balance any desired load combination to zero deflections
  - increase the cracking moment to a desired value
  - control the number and width of cracks

- The reduced level of prestress (in comparison to full prestressing) leads to fewer creep and excessive camber problems.

- Reduced volume of steel in comparison to reinforced concrete designs.

- Reduced reinforcement congestion, better detailing, fewer reinforcement splices in comparison to reinforced concrete designs.

- Increased ductility in comparison to fully prestressed designs.

Mixed reinforcement can provide a desirable design alternative to reinforced concrete and fully prestressed designs in many types of structures, including bridge substructures. Recent research at The University of Texas at Austin has illustrated the structural benefits of mixed reinforcement in large cantilever bridge substructures.

The opposition to mixed reinforcement designs and the reluctance to recognize mixed reinforcement in design codes has primarily been related to concerns for increased cracking and its effect on corrosion. Mixed reinforcement design will generally have more cracks than comparable fully prestressed designs. It has been proposed that the increased presence of cracking will lead to more severe corrosion related deterioration in a shorter period of time. Due to the widely accepted notion that prestressing steel is more susceptible to corrosion and that the consequences of corrosion in prestressed elements are more severe than in reinforced concrete (see Section 2.3.2), many engineers have felt that the benefits of mixed reinforcement are outweighed by the increased corrosion risk. Little or no research has been performed to assess the effect of mixed reinforcement designs on corrosion in comparison to conventional reinforced concrete and fully prestressed designs.

1.4   PROBLEM STATEMENT

This report represents a portion of the Texas Department of Transportation Research Project 0-1405: "Durability Design of Post-Tensioned Bridge Substructure Elements." The project title implies two main components to the research:

1. Durability of Bridge Substructures, and

2. Post-Tensioned Bridge Substructures.

The durability aspect is in response to the deteriorating condition of bridge substructures in some areas of Texas. Considerable research and design effort has been given to bridge deck design to prevent corrosion damage, while substructures have been largely overlooked. In some districts of the state, more than ten percent of the substructures are deficient, and the substructure condition is limiting the service life of the bridges.

The second aspect of the research is post-tensioned substructures. As described above, there are many possible applications in bridge substructures where post-tensioning can provide structural and economical benefits and can possibly improve durability. Post-tensioning is now being used in Texas bridge substructures, and it is reasonable to expect the use of post-tensioning to increase in the future as precasting of substructure components becomes more prevalent and as foundation sizes increase.

Problem:

The problem that bridge engineers are faced with is that there are no durability design guidelines for post-tensioned concrete structures. Durability design guidelines should provide information on how to identify possible durability problems, how to improve durability using post-tensioning, and how to ensure that the post-tensioning system does not introduce new durability problems.

1.5   RESEARCH OBJECTIVES AND PROJECT SCOPE

1.5.1   Project Objectives

The research objectives for TxDOT Project 0-1405 are as follows:

1. To examine the use of post-tensioning in bridge substructures,

2. To identify durability concerns for bridge substructures in Texas,

3. To identify existing technology to ensure durability or improve durability,

4. To develop experimental testing programs to evaluate protection measures for improving the durability of post-tensioned bridge substructures, and

5. To develop durability design guidelines and recommendations for post-tensioned bridge substructures.

A review of literature early in the project indicated that post-tensioning was being successfully used in past and present bridge substructure designs and that suitable post-tensioning hardware was readily available. It was decided not to develop possible post-tensioned bridge substructure designs as part of the first objective for two reasons. First, other research on post-tensioned substructures was already underway, and second, the durability issues warranted the full attention of Project 0-1405. The third objective was added after the project had begun. The initial literature review identified a substantial amount of relevant information that could be applied to the durability of post-tensioned bridge substructures. This search allowed the scope of the experimental portion of the project to be narrowed. The final objective represents the culmination of the project. All of the research findings are to be compiled into the practical format of durability design guidelines.

1.5.2   Project Scope

The research presented in this report represents part of a large project funded by the Texas Department of Transportation, entitled, "Durability Design of Post-Tensioned Bridge Substructures" (Project 0-1405). Nine reports are scheduled to be developed from this project as listed in Table 1.2.

Number	Title	Estimated Completion
1405-1	State of the Art Durability of Post-Tensioned Bridge Substructures	1999
1405-2	Development of High Performance Grouts for Bonded Post-Tensioned Structures	1999
1405-3	Long-Term Post-Tensioned Beam and Column Exposure Test Specimens: Experimental Program	1999
1405-4	Corrosion Protection for Bonded Internal Tendons in Precast Segmental Construction	1999
1405-5	Interim Conclusions, Recommendations and Design Guidelines for Durability of Post-Tensioned Bridge Substructures	1999
1405-6	Final Evaluation of Corrosion Protection for Bonded Internal Tendons in Precast Segmental Construction	2002
1405-7	Design Guidelines for Corrosion Protection for Bonded Internal Tendons in Precast Segmental Construction	2002
1405-8	Long-Term Post-Tensioned Beam and Column Exposure Test Specimens: Final Evaluation	2003
1405-9	Conclusions, Recommendations and Design Guidelines for Durability of Post-Tensioned Bridge Substructures	2003

Several dissertations and theses at The University of Texas at Austin were developed from the research from Project 0-1405. These documents may be valuable supplements to specific areas in the research and are listed in Table 1.3 for reference.

Table 1.3 - Project 0-1405 Theses and Dissertations, The University of Texas at Austin

Title	Author
Masters Theses	
"Evaluation of Cement Grouts for Strand Protection Using Accelerated Corrosion Tests"	Bradley D. Koester
"Test Method for Evaluating Corrosion Mechanisms in Standard Bridge Columns"	Chuck Larosche
Ph.D. Dissertations	
"Improving Corrosion Resistance of Post-Tensioned Substructures Emphasizing High Performance Grouts"	Andrea J. Schokker
"Durability Design of Post-Tensioned Bridge Substructures"	Jeffrey S. West

CHAPTER 2
LONG-TERM BEAM CORROSION TESTS

2.1   TEST CONCEPT AND OBJECTIVES

Post-tensioning may have two general effects on the durability or corrosion protection in flexural members. First, post-tensioning may improve the corrosion protection provided by the concrete by controlling the number and width of cracks in the concrete. In post-tensioned members where the concrete remains precompressed under service loading, it has been suggested that moisture and chloride penetration will be reduced as precompression limits microcracking within the structure of the concrete. The second effect is that additional components, the post-tensioning system, are introduced in the structure. Most of these components are steel and thus introduce potential sources of corrosion damage if not given proper attention in the durability design process. Thus, the durability design process for post-tensioned elements must address how to best use post-tensioning to improve corrosion protection, while ensuring that the post-tensioning hardware is protected from corrosion damage.

The term prestressed concrete has traditionally been used to describe structural concrete that is prestressed such that elastic stresses in the gross concrete section do not exceed specified limits at service load levels. The extreme fiber stress in the precompressed tensile zone is normally limited to below the modulus of rupture of the concrete. This is the classic definition of full prestressing and is equally applicable to pre-tensioned and post-tensioned concrete. Other situations may exist where it is desirable to reduce the amount of prestressing below that required by code elastic stress limits. In this situation, mild steel reinforcement may or may not be required to satisfy strength requirements, and the concrete will likely crack under service load levels. Because this reduction in the amount of prestressing is often desirable from structural and economical perspectives, it is important to evaluate its effect on the durability of the structure.

This portion of the research project consists of long-term exposure testing of large structural concrete flexural members or beams. The specific objectives are to investigate:

1) The effect of post-tensioning on durability (corrosion protection) through crack control, and

2) The relative performance of a broad scope of corrosion protection variables for multistrand post-tensioning systems.

The experimental program uses large-scale linear elements, designed as beams. The beams are subjected to combined structural loading and aggressive exposure. The specimens are tested outside the Ferguson Structural Engineering Laboratory and are exposed to cyclic wetting and drying with a 3.5% NaCl solution to promote accelerated corrosion. The majority of the specimens are continually subjected to service load conditions. The effect of post-tensioning is investigated for a range of prestressing from nonprestressed (reinforced concrete) to partially prestressed to fully prestressed. Variables investigated are the influence of crack width, high performance concrete, prestressing strand coatings, duct splices, high performance grout, and encapsulated post-tensioning systems.

The experimental program was implemented in two phases. The first phase was developed to investigate the influence of prestress level, cracking, high performance grout and post-tensioning duct splices. The second phase investigates high performance concrete, high performance grout, prestressing strand coatings and an encapsulated post-tensioning system. The beam specimen design and loading is identical for the two phases of testing.

2.2   TEST SPECIMEN

The test specimens in this experimental program are linear elements, designed as beams with a rectangular cross section. The test specimens were developed for research purposes and are not necessarily representative of any particular bridge substructure element. Linear rectangular elements were chosen for the following reasons:

- results can be applied to bent cap and column elements directly and some results may be qualitatively applied to other elements such as pile caps

- all desired variables can be readily incorporated into design

- ease of construction, handling and placement

- simplicity of controlling and maintaining loading

The element dimensions and details were selected such that covers, reinforcement sizes, post-tensioning hardware and crack widths were on a similar order of magnitude as in practical applications, with consideration for handling and loading of the specimens. A minimum of two (2) tendons (multistrand) were used in all prestressed specimens to represent practical applications of post-tensioning in bridge substructures. Using commercially available multistrand post-tensioning hardware, the maximum number of strands as governed by several possible section dimensions is shown below.

Section:	Max. No. of Strands:	Hardware:
300 mm x 450 mm (12" x 18")	2	VSL Type E5-1
400 mm x 600 mm (16" x 24")	6	VSL Type E5-3
450 mm x 600 mm (18" x 24")	8	VSL Type E5-4

The Type E multistrand anchorage hardware manufactured by VSL Corporation was selected because it is available in tendon configurations with as few as three strands. Most multistrand post-tensioning systems are not available in sizes smaller than five to seven strands per tendon. The 450 mm x 600 mm (18" x 24") section, accommodating up to eight strands in two tendons, was chosen to provide the most flexibility in the design of mixed reinforcement sections. For practical handling and loading, a nominal beam length of 15 feet was chosen.

2.2.1 Levels of Prestress

The effect of prestressing on corrosion protection is one of the main investigation areas for this testing program. In order to examine a broad range of prestressing, section reinforcement was proportioned for the following levels of prestress:

- nonprestressed

- 100% prestress based on service load/allowable stress design (100%S PS)

- 100% prestress based on ultimate (nominal) strength (100%U PS)

- intermediate level of mixed reinforcement with a nominal prestress amount between 50% and 75%

The amount of prestress, in percent, is defined as the tensile force component provided by prestressing steel at the nominal flexural capacity of the section. Prestress amounts of 100%U prestressed and the intermediate range of 50% to 75% would be traditionally classified as partial prestressing and would be expected to crack at service load levels. These sections and the nonprestressed section were designed using a strength design approach. The selected section dimensions and requirement for two tendons dictated the use of 8 strands for the 100%S PS section, 6 strands for the 100%U PS section, and 4 strands for the intermediate level of prestress (50% to 75%).

2.2.2 Section Design

The specimens used in this experimental program are not patterned after a prototype bridge element, and thus no specified design loading is available. Reinforcement was proportioned based on the total allowable service load moment (dead plus live) computed for the 100%S PS section (fully prestressed, service load design). Assuming a ratio of dead load to live load of 1.5, the calculated permissible total service load moment was used

to compute the dead and live load moments. The factored moment was then computed and used to proportion the reinforcement for the remaining sections.

2.2.2.1   Calculation of Design Loading Based on 100%S PS Section

Determination of the design loading is shown schematically in Figure 2.1. The 100%S PS section is fully prestressed to meet the stress limits specified by Clause 5.9.4 of AASHTO LRFD (Clause 18.4 of ACI 318). The section has eight prestressing strands in two tendons and was analyzed assuming the following:

- Gross section properties, elastic stresses
- $f'_c = 35$ MPa (5 ksi)
- A_{ps} = eight 12.7 mm (0.5 in.) 7-wire prestressing strands, $f_{pu} = 1860$ MPa (270 ksi)
- $f_{pi} = 0.65f_{pu}$
- Long-term losses = 15% ($f_{pe} = 0.55f_{pu}$)
- Maximum tendon eccentricity, e = 200 mm (8 in.) based on clear cover to duct of 65 mm (2.5 in.)
- Compute the total allowable moment assuming that the governing stress in the concrete (tensile or compressive) is at least 75% of the corresponding allowable value. (i.e., either $0.75f_{callow} \leq f_{cmax} \leq f_{callow}$ or $0.75f_{tallow} \leq f_{tmax} \leq f_{tallow}$)
- Neglect self weight of the beam (self weight is very small in comparison to applied forces)
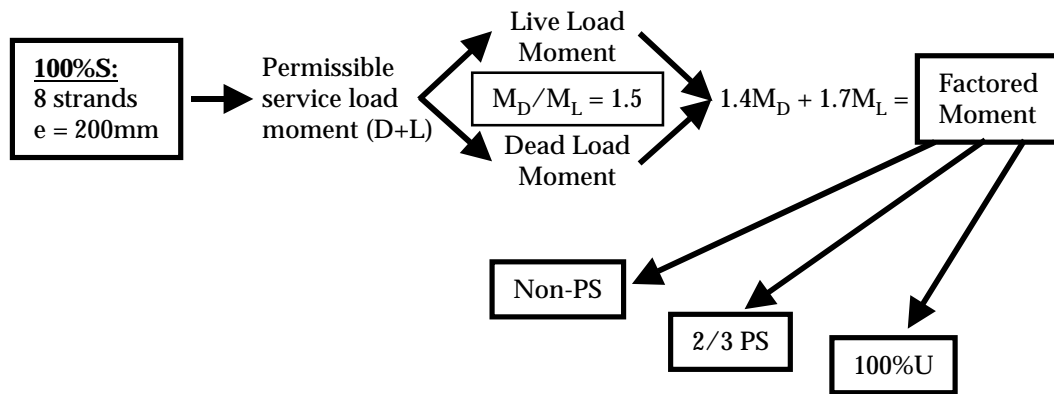
Figure 2.1 - Calculation of Design Moments

The 100%S PS section was analyzed for stresses in the concrete immediately after prestress transfer and under maximum applied loading. Calculated stresses and moments are shown in Appendix A. Based on these assumptions, a service load moment of 310 kN-m (2750 k-in.) was obtained with $f_t = 0.75f_{tallow}$ governing. The tendon profile was draped to meet stress limits at the member ends. The tendon profile and allowable limits for the steel center of gravity (cgs) are shown in Figure 2.2.

The design moment for the remaining section types was calculated based on the maximum permissible service load moment as follows:

$M_{service}$ = 310 kN-m (2750 k-in.) (based on 100%S PS section)

M_D/M_L = 1.5 (assumed)

Therefore,

M_D = 186 kN-m (1650 k-in.)

M_L = 125 kN-m (1100 k-in.)

$M_{factored}$ = 472 kN-m (4180 k-in.)

$M_{nominal}$ = 525 kN-m (4650 k-in.) (for $\phi = 0.9$)
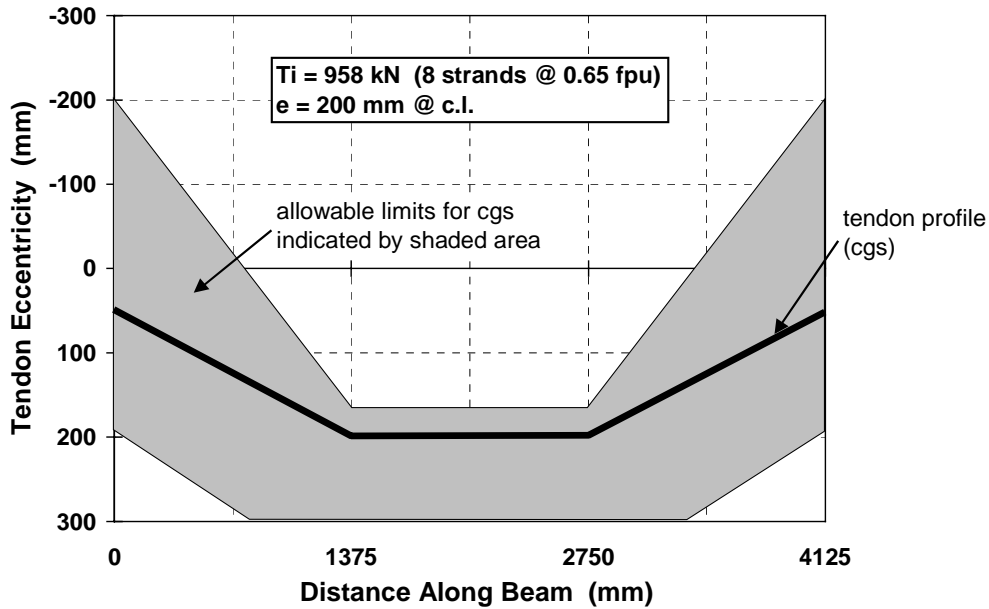
Figure 2.2 - 100%S PS Section Tendon Profile and Allowable Limits

2.2.2.2   Section Reinforcement

The required nominal flexural capacity, M_n, was used for the strength design of the remaining sections: Non-PS, 100%U prestressed and intermediate prestress (50% to 75%). The cross section size and desire for two tendons in each specimen dictated 6 strands in the 100%U PS section and 4 strands in the intermediate section (50% to 75% prestress). All sections were provided with two #5 bars (15.9 mm dia.) as compression steel.

Tension Reinforcement

The 100%S PS section was provided with two #3 bars (9.5 mm dia.) in the tension zone to aid construction of the reinforcement cages. This steel was not required as tension reinforcement to meet the reinforcement limits of AASHTO LRFD Clause 5.7.3.3 (Clause 18.8, ACI 318-95), but was included in all calculations. The nominal flexural capacity of the 100%S PS section was computed to be 670 kN-m (5935 k-in.), well in excess of the required strength of 525 kN-m (4650 k-in.).

The 100%U PS section satisfied the strength requirements with six 12.7 mm (0.5") dia. prestressing strands. The 100%U PS section was also provided with two #3 bars (9.5 mm dia.) in the tension zone to aid construction of the reinforcement cages. This steel was included in all calculations. The calculated flexural capacity was 529 kN-m (4685 k-in.) for this section.

The level of prestress for the intermediate section was determined by computing the necessary mild steel reinforcement to meet strength requirements in conjunction with the selected number of strands (in this case 4 strands). A mild steel area of 800 mm² (1.24 in²) was required to provide the necessary flexural capacity. For this combination of strands and mild steel reinforcement, the level of prestress was calculated as 66.7% (2/3 PS). It was decided to use a constant number of mild steel bars for the 2/3 PS section and the Non-PS section in an attempt to emphasize the amount of prestress as the significant factor for crack widths. Four #4 bars (12.7 mm dia.) and four #3 bars (9.5 mm dia.) were selected to provide the necessary steel area.

The nominal strength requirements for the Non-PS section were met with a mild steel area of 1960 mm² (3.04 in.²). Keeping the total number of bars at eight, six #6 bars (19 mm dia.) and two #4 bars (12.7 mm dia.) were selected.

The reinforcement details are shown in Figure 2.3 for the four section types and are summarized in Table 2.1. Bar sizes are shown in customary U.S. sizes, with metric equivalents listed below the table. Complete construction details of the four sections are shown in the detailed drawing set in Appendix A.

Non-Prestressed

Compression Steel:
2 - #5's (15.9 mm dia.)

Tension Steel:
6 - #6's (19 mm dia.) and
2 - #4's (12.7 mm dia.)

2/3 Prestressed

Compression Steel:
2 - #5's (15.9 mm dia.)

Tension Steel:
4 - #3's (9.5 mm dia.) and
4 - #4's (12.7 mm dia.)

Prestressing Steel:
4 - 12.7 mm dia. strands

100% Prestressed
Strength Design

Compression Steel:
2 - #5's (15.9 mm dia.)

Tension Steel:
2 - #3's (9.5 mm dia.)
(not required by design)

Prestressing Steel:
6 - 12.7 mm dia. strands

100% Prestressed
Allowable Stress Design

Compression Steel:
2 - #5's (15.9 mm dia.)

Tension Steel:
2 - #3's (9.5 mm dia.)
(not required by design)

Prestressing Steel:
8 - 12.7 mm dia. strands

Figure 2.3 - Section Reinforcement Details

Table 2.1 - Summary of Section Details

Section	Prestressing Strands	Effective Prestress (after all losses)	Mild Steel Bars (tension)	Nominal Capacity
Non-PS	None	n/a	6-#6 and 2-#4	529 kN-m
2/3 PS	4 – 12.7 mm	$0.60f_{pu} = 1116$ MPa	4-#4 and 4-#3	536 kN-m
100%U PS	6 – 12.7 mm	$0.60f_{pu} = 1116$ MPa	2-#3	529 kN-m
100%S PS	8 – 12.7 mm	$0.56f_{pu} = 1042$ MPa	2-#3	670 kN-m

Bar Sizes: #6 – 19 mm dia.   Conversion Factors: 1 in.   = 25.4 mm
            #4 – 12.7 mm dia.   1 ksi   = 6.895 MPa
            #3 – 9.5 mm dia.   1 k-in. = 0.11298 kN-m

Shear Reinforcement

Shear reinforcement was proportioned for the shear force corresponding to development of the nominal flexural capacity of the sections. Stirrup layouts for all members are shown in Appendix A.

Anchorage Zone Reinforcement

General zone reinforcement for the post-tensioning anchorage forces was designed according to the recommendations of Breen et al. General zone reinforcement was provided with closed stirrups according to the spacing shown in Appendix A. Local zone anchorage reinforcement in the form of spirals was based on the guidelines of the post-tensioning hardware supplier. Anchorage zone details and anchorage hardware are shown in Appendix A.

Post-Tensioning System

All prestressed sections utilized the same draped tendon profile (depression points at third points) shown in Figure 2.2 and Figure 2.4. As described in the previous section, this profile was chosen to satisfy allowable stresses at the ends of the 100%S PS members. The draped profile also ensures that all strands within the tendon are in contact (electrically), as this contact may influence corrosion behavior.

Figure 2.4 - Tendon Layout for Post-Tensioned Beams

The VSL Corporation Type E anchorage system was used for all post-tensioned beams. The smallest available configuration in the Type E system is for a three-strand tendon. This configuration (Type E5-3) was used for the 100%U PS and 2/3 PS sections. For the 2/3 PS section with only two strands per tendon, the E5-3 was used with the third strand opening unused. The 100%S PS section used the Type E5-4 configuration. The basic hardware for the E5-4 anchorage is shown in Figure 2.5. The anchorages were located inside a recessed pocket at both ends of the beams, as shown in Figure 2.4. Grouting was performed using grout tubes at both ends of the duct. Grout sleeves and tubes were used for the 100%U PS and 100%S PS beams. The grout tube location is shown in Figure 2.4 for these section types. Grout tubes were placed through the third opening in the E5-3 anchor head for grouting the 2/3 PS beams. The duct profiles, grout tube locations and end pocket details are shown in Appendix A for each of the post-tensioned beam types.
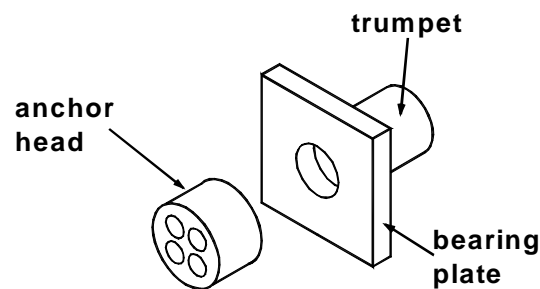
Figure 2.5 - VSL Type E5-4 Anchorage

2.2.3   Analysis of Section Behavior

Once the section details were defined, each section was thoroughly analyzed to determine its moment curvature behavior and applied moment - crack width behavior. Guidelines proposed by Armstrong et al for crack width prediction in cracked prestressed members were used with the Gergely-Lutz crack width expression to estimate the surface crack widths. The recommendations of Armstrong et al and the Gergely-Lutz expression are described in Research Report 1405-1 under this project. The cracking moment for each section was computed based on the uncracked transformed section. The section was then analyzed as a cracked section at that moment to estimate the crack width immediately after cracking. Several additional points were calculated to define the applied moment - crack width relationship up to a maximum crack width of 0.46 mm (0.018 in.).

The sections were analyzed using the layer-by-layer strain compatibility section analysis technique. A spreadsheet was developed by Jeff West to automate the task of performing repeated analyses on the different section types. Moment-curvature and crack width analysis were performed neglecting long-term material behavior. The basic assumptions for the analysis are listed below.

Concrete: $\varepsilon_{cmax} = 0.0038$

Hognestad parabolic stress-strain relationship

no tension stiffening

Prestressing Steel:

bonded prestressing steel, low-relaxation seven-wire strand

stress-strain relationship modeled using a Ramberg-Osgood function

Mild Steel: stress-strain relationship linear elastic to f_y, perfectly plastic to $\varepsilon_{sh} = 0.010$, strain hardening given by cubic polynomial

The material stress-strain curves and expressions are shown in Figure 2.6, Figure 2.7 and Figure 2.8. The computed moment-curvature and moment-crack width curves are shown in Figure 2.9 and Figure 2.10 for the control concrete (TxDOT Class C Concrete). The computed moment-curvature curves are shown in Figures 2.11 and 2.12 for the fly ash concrete and high performance concrete respectively. (See Section 2.3.3.1 for more information on concrete types.)

$$f_c = f'_c \left[\left(\frac{2\varepsilon_c}{\varepsilon_o} \right) - \left(\frac{\varepsilon_c}{\varepsilon_o} \right)^2 \right] ; \varepsilon_c \leq \varepsilon_o$$

$$f_c = f'_c \left[1 - 0.15 \left(\frac{\varepsilon_c - \varepsilon_o}{\varepsilon_{max} - \varepsilon_o} \right) \right] ; \varepsilon_o \leq \varepsilon_c \leq \varepsilon_{max}$$

$$\varepsilon_o = \frac{2f'_c}{E_c} \qquad \varepsilon_{max} = 0.0038$$

$$E_c = 12,411 + 3.17f'_c \quad (MPa)$$
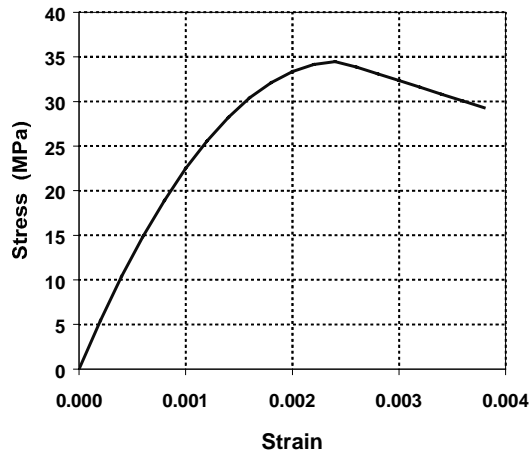
Figure 2.6 - Concrete Stress-Strain Curve

$$f_s = 200,000\varepsilon_s ; \varepsilon_s \leq \varepsilon_y$$

$$f_s = 400\,MPa ; \varepsilon_y < \varepsilon_s \leq 0.010$$

$$f_s = 297 + 13052\varepsilon_s - 143292(\varepsilon_s)^2 + 520200(\varepsilon_s)^3 ; \varepsilon_s > 0.01$$
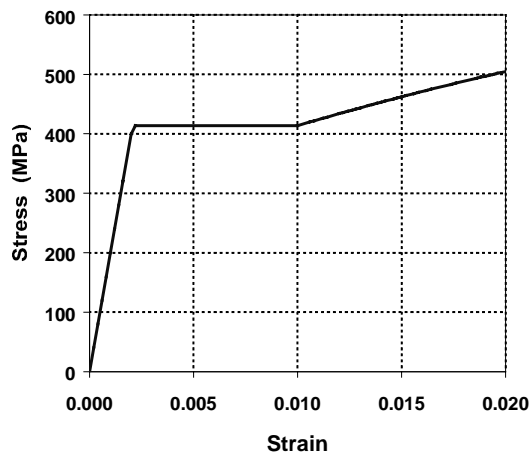
Figure 2.7 - Mild Steel Reinforcement Stress-Strain Curve

$$f_{ps} = 200,000\varepsilon_{ps}\left(0.025 + \frac{0.975}{\left[1 + \left(118\varepsilon_{ps}\right)^{10}\right]^{0.10}}\right)$$

$$\leq 1860 \text{ MPa}$$
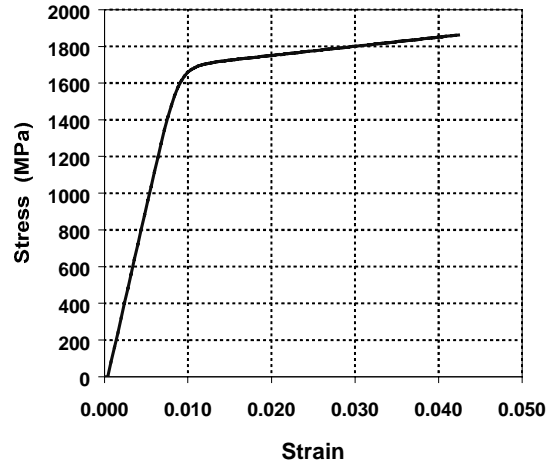
Figure 2.8 - Prestressing Strand Stress-Strain Curve
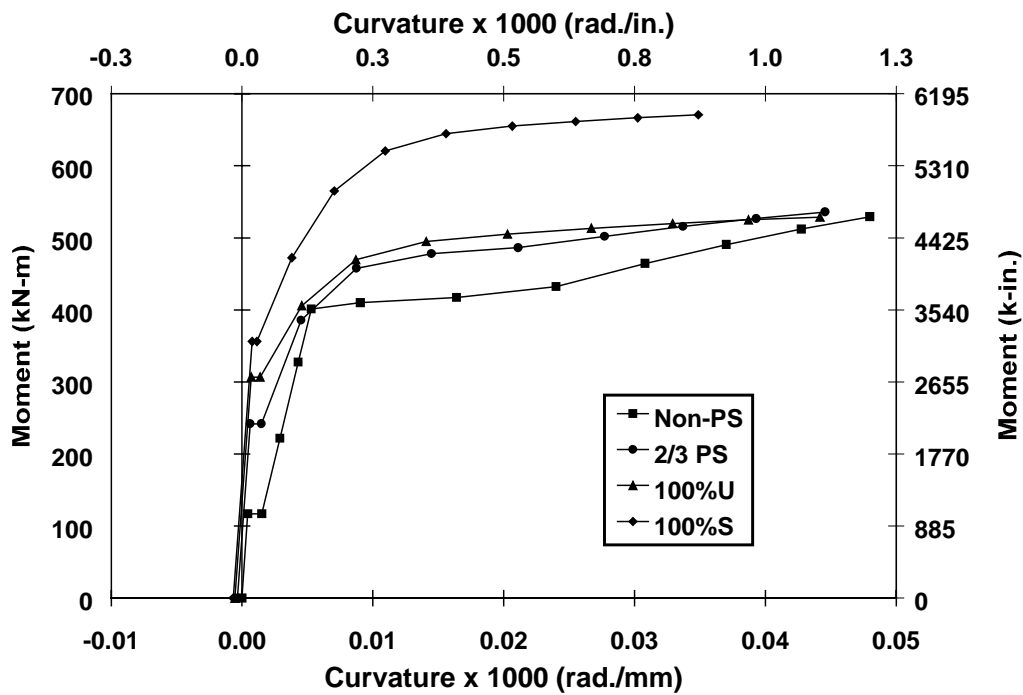
Figure 2.9 - Moment Curvature Behavior for All Sections
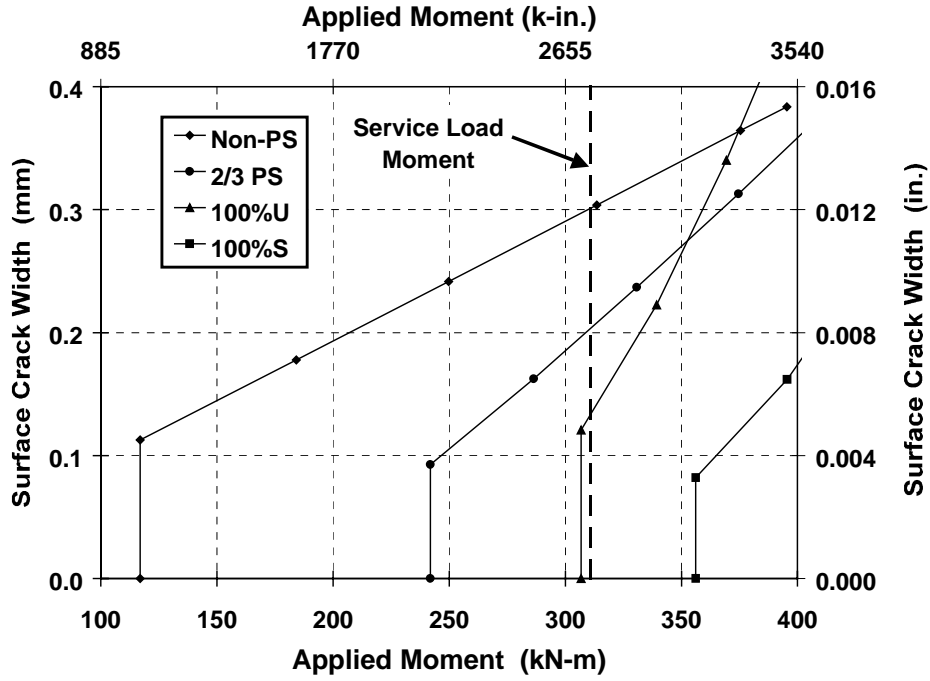
Figure 2.10 - Applied Moment – Estimated Crack Width Behavior for All Sections
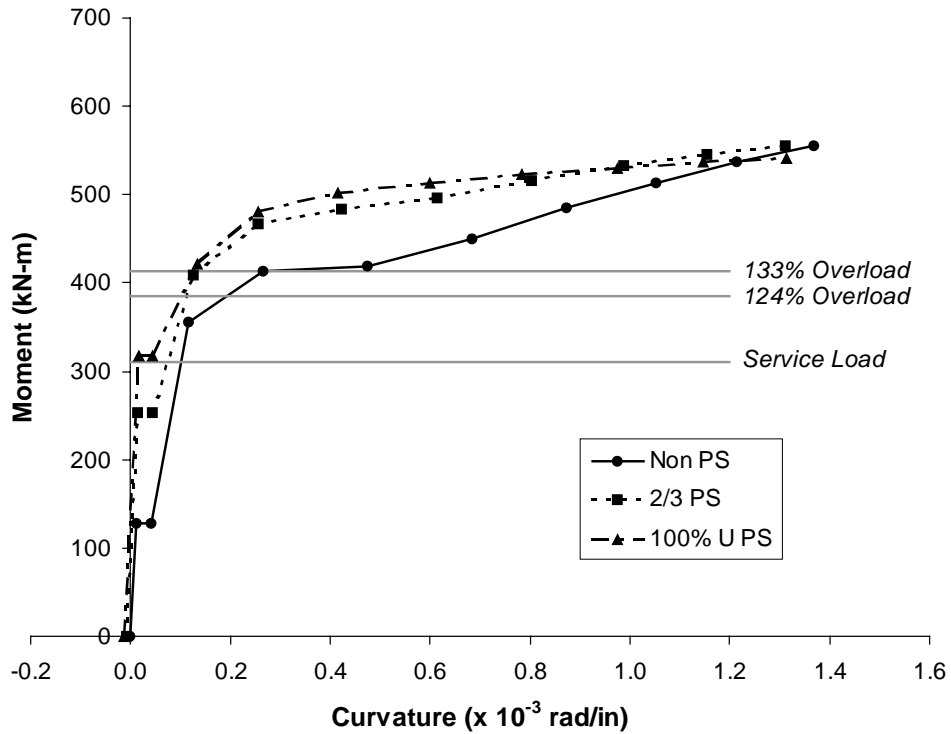
Figure 2.11 - Calculated Moment-Curvature for Fly Ash Concrete Specimens
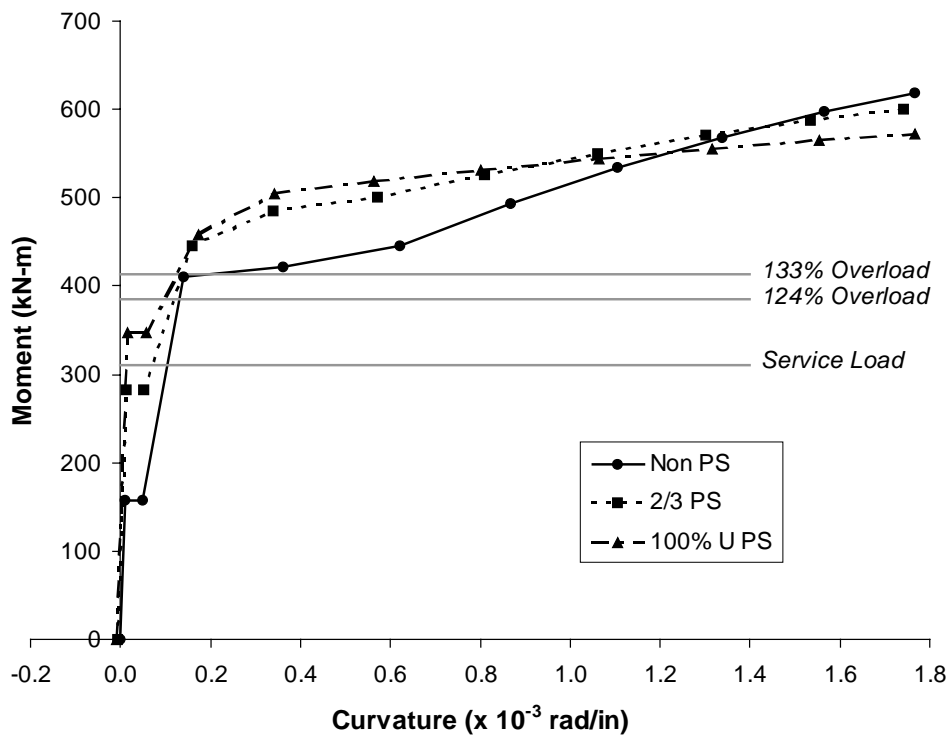
Figure 2.12 - Calculated Moment-Curvature for High Performance Concrete

Long-term behavior of all sections was calculated according to the procedure proposed by Ghali and Favre. This procedure uses basic equilibrium and strain compatibility without the use of empirical relationships. The procedure is general and can be applied to fully prestressed members (uncracked), cracked prestressed sections, sections with a combination of mild steel reinforcement and prestressed reinforcement and nonprestressed sections. This method was chosen to calculate long-term prestress losses because the effect of nonprestressed reinforcement and/or the effect of cracking is directly included in the calculations of prestress losses. The procedure is analogous to the displacement method of structural analysis and has four main steps:

1. Compute the initial stresses and strain profile for the section under the action of initial prestress forces and sustained loading.

2. Determine the hypothetical change in strain distribution due to creep and shrinkage of the concrete if they were free to occur during the time interval being considered. Determine the amount of relaxation of the prestressed reinforcement during the time interval.

3. Determine the total axial force (ΣN) and moment (ΣM) that would be required to restrain the deformations due to creep, shrinkage and relaxation (Step 2) using the age-adjusted modulus of elasticity of the concrete.

4. Eliminate the artificial restraint (Step 3) by applying $-\Sigma N$ and $-\Sigma M$ on the section using the age-adjusted section properties. The strain distribution at the end of the time increment is the sum of the strains computed in Steps 1 and 4. The corresponding stresses are determined by summing the stresses calculated in Steps 1, 3 and 4.

The procedure presented by Ghali and Favre is simple in concept but can be complicated to implement, particularly for cracked sections. The procedure was adapted by Jeff West to use the layer-by-layer compatibility section analysis technique to determine stresses and resultant forces at the various steps. The adapted approach was programmed into a spreadsheet to allow rapid analysis of long-term behavior for sections with any cross section and combination of prestressed and mild steel reinforcement. The recommendations of

ACI Committee 209 were used to predict creep and shrinkage. An aging coefficient is used in the analysis when computing ΣN and ΣM to reflect that these forces would be introduced gradually as the time dependent deformation occurs. Relaxation of the prestressing steel was predicted using the reduced relaxation approach to account for the gradual reduction in prestress due to concrete creep and shrinkage.

The results of the long-term analysis for each section are shown in Figure 2.13 through Figure 2.16. These figures show the initial strain profile and the strain profile after a duration of four years. The locations of the prestressing steel and mild steel reinforcement are indicated on the figures. A long-term prestress loss (creep, shrinkage, relaxation) of 4.7% was calculated for the 100%S PS section. Prestress force increases of 5% and 4.3% were calculated for the 100%U PS and 2/3 PS sections, respectively, after four years of sustained loading. Prestress force increases rather than losses are obtained since these sections are cracked prior to and during sustained loading. This behavior is similar to that of reinforced concrete members under sustained loading (see Figure 2.16).

F$_{pi}$ = 817 kN (initial)
F$_{pe}$ = 778 kN (t = 4 yrs)
ΔF$_p$ = - 4.7% (loss)
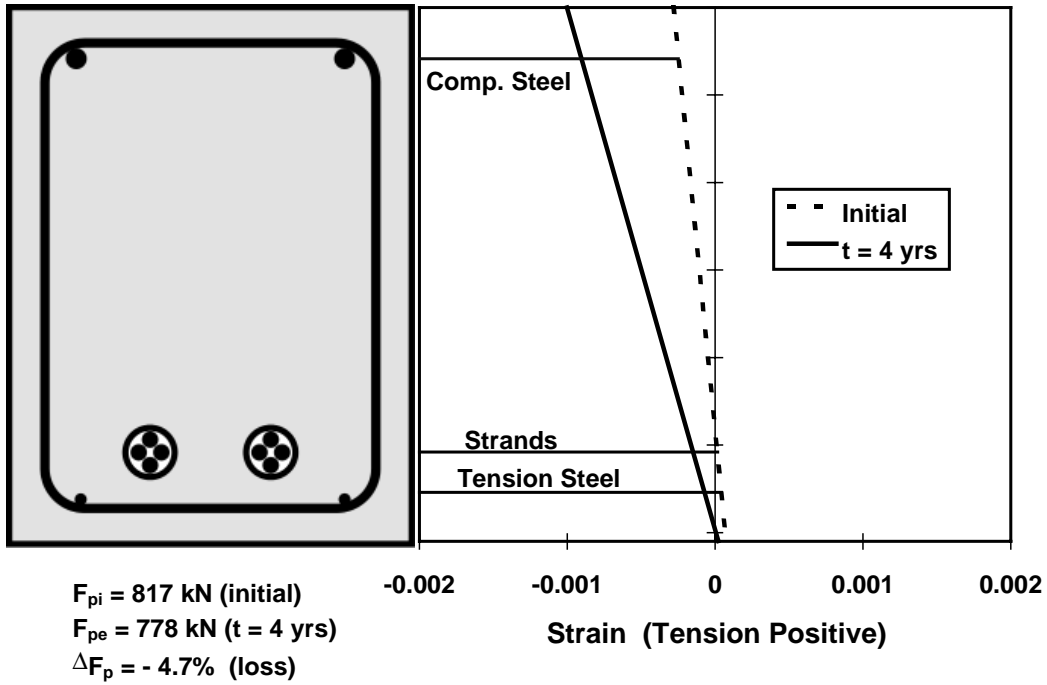
Figure 2.13 - Initial and Long-Term Strain Profiles for 100%S PS Section

F$_{pi}$ = 723 kN (initial)
F$_{pe}$ = 760 kN (t = 4 yrs)
ΔF$_p$ = 5.0% (increase)
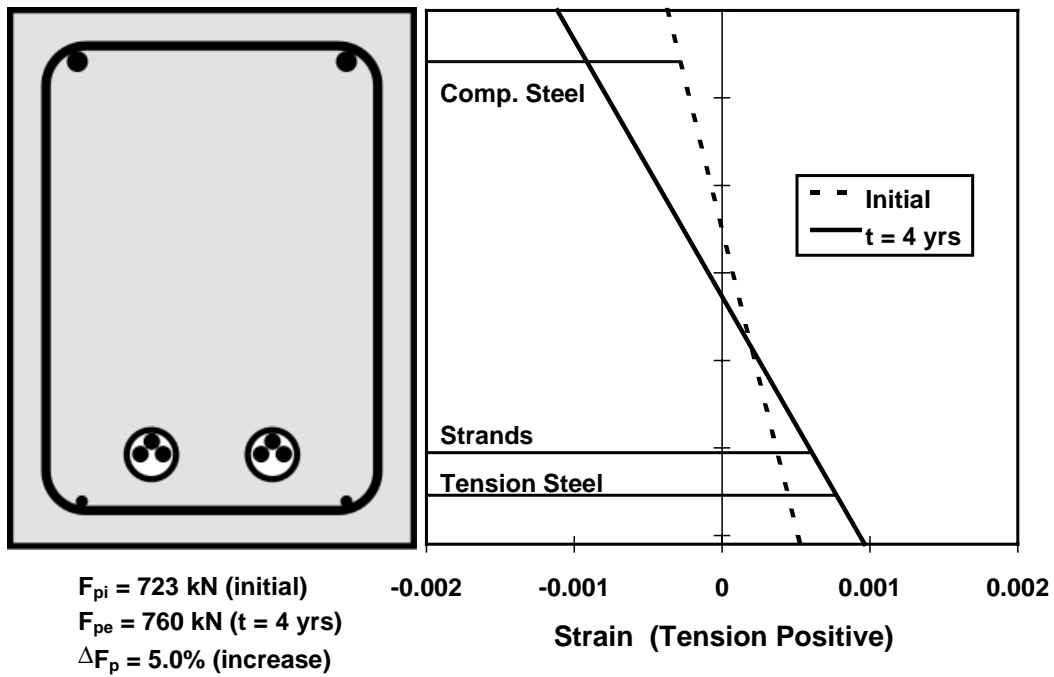
Figure 2.14 - Initial and Long-Term Strain Profiles for 100%U PS Section

F_pi = 522 kN (initial)
F_pe = 544 kN (t = 4 yrs)
ΔF_p = 4.3% (increase)
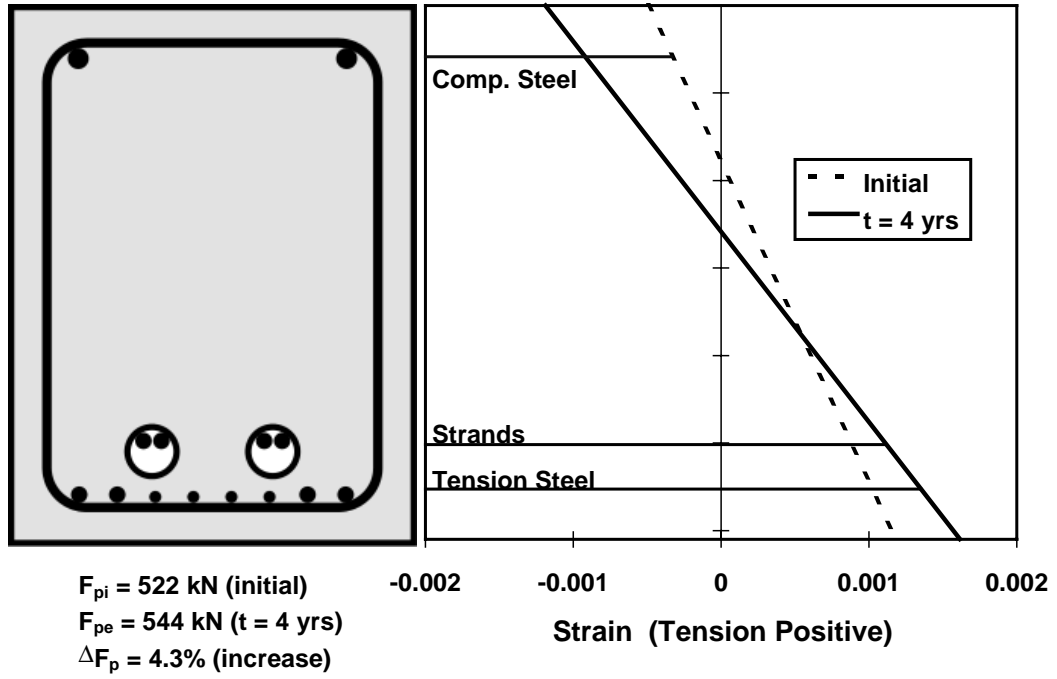
Figure 2.15 - Initial and Long-Term Strain Profiles for 2/3 PS Section
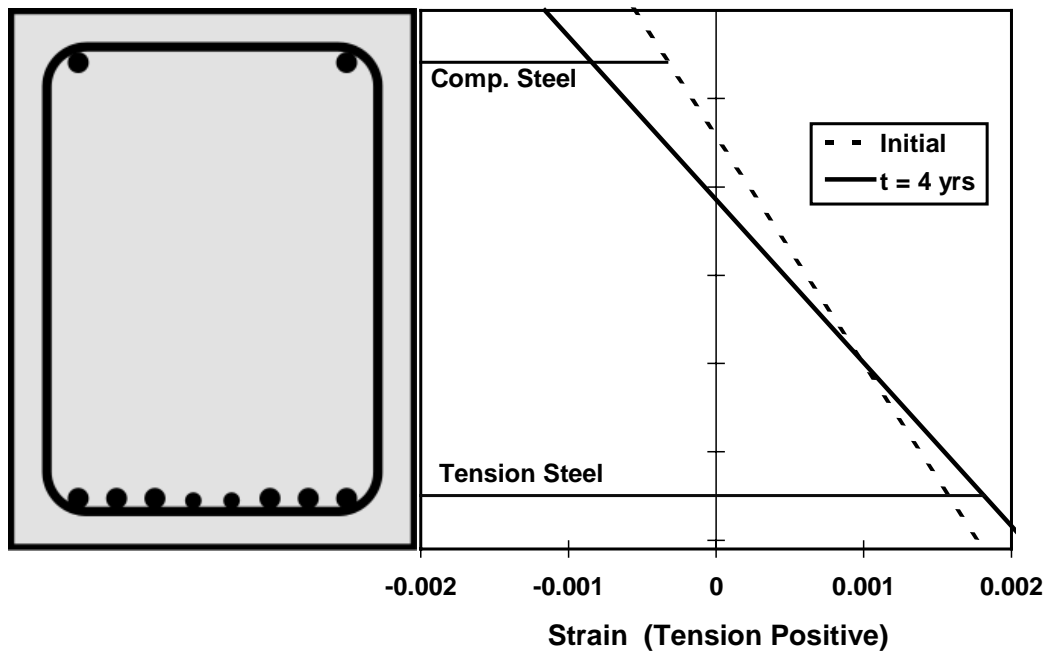
Figure 2.16 - Initial and Long-Term Strain Profiles for Non-PS Section

2.3 VARIABLES

A very broad scope of variables was selected for evaluation in the beam testing program. The variables fall into four main categories: level of prestress and crack width, concrete type, prestressing strand coatings and post-tensioning hardware protection. In addition to these variables, different post-tensioning duct splices are evaluated within the other variable categories.

The testing program was implemented in two phases. The first phase includes all of the specimens in the first category of variables (level of prestress and crack width), one specimen with high performance grout, and the evaluation of duct splices. The second phase includes the remaining three categories of variables and the duct splice evaluation.

2.3.1 Control Variables

Standard variables based on typical current practice were defined to represent control cases. These include concrete mix design, concrete clear cover, cement grout, duct and anchorage protection. Details of each are given below.

Concrete: based on TxDOT Specification Item 421

TxDOT Class C concrete for bridge substructures

maximum w/c ratio = 0.533 (actual w/c will be closer to 0.45 based on slump requirements)

Type I cement

slump = 100 mm (4 in.)

maximum coarse aggregate size = 19 mm (3/4 in.)

retarder, Rheocrete 300-R

entrained air admixture

50 mm (2 in.) clear cover to main steel

Cement Grout: based on TxDOT Specification Item 426.3.4a

w/c ratio = 0.44

Type I cement

expanding admixture, Intraplast-N

PT Duct: rigid galvanized steel duct

Anchor. Protection: based on TxDOT guidelines

Type V State epoxy bonding compound

nonshrink grout patch (Euclid NS grout)

2.3.2 Phase I Variables

2.3.2.1 Level of Prestressing, Loading and Cracking

The inter-related effects of cracking and amount of prestressing on corrosion are given considerable emphasis in this experimental program. The effect of cracking is primarily investigated using standard variables and the three sections that would be expected to crack under service loads (Non-PS, 2/3 PS and 100% U). The range of crack widths investigated in this program is based on a survey of relevant literature regarding critical crack widths for corrosion and recommended allowable crack widths. Consideration was also given to the applied moment - crack width behavior computed for the sections (Figure 2.10). A broad range of crack widths was selected to provide a suitable evaluation of the effect of cracking on corrosion. The selected crack widths are 0.05 mm (0.002 in.), 0.1 mm (0.004 in.), 0.2 mm (0.008 in.), 0.3 mm (0.012 in.), and uncracked. To obtain this crack width range, the four cases shown in Table 2.2 were developed. This information is also presented in

Figure 2.17. A total of eleven specimens are required to address the four loading cases. The four specimens under constant service load (loading case 1) are duplicated, giving a total of fifteen specimens in this category of variables.

Table 2.2 - Planned Crack Widths, Prestress Amounts and Loading

Loading Case	Crack Widths	Applicable Sections	Loading
1.) Constant Service Load	uncracked	100%S PS	service load
	0.1 mm	100%U PS	service load
	0.2 mm	2/3 PS	service load
	0.3 mm	Non-PS	service load
2.) Very Small Crack	0.05 mm	2/3 PS & 100%U PS	as needed and hold
3.) Unloaded	uncracked	Non-PS & 100%U PS	none
4.) Overload & Return to Service	as measured	Non-PS, 2/3 PS & 100%U PS	up to 1.33 x service load, then return to service load

Due to the large number of variables and uncertain nature of cracking, it was expected that some deviation from the planned crack width and loading combinations would occur. This deviation is discussed in Section 2.7.
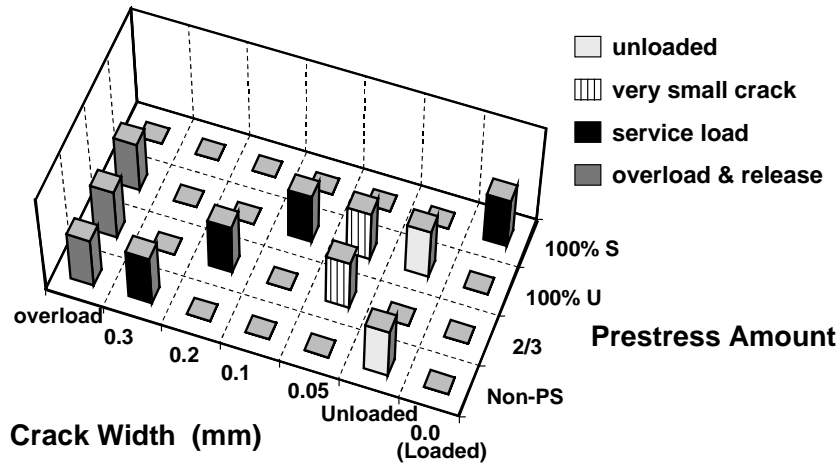
Figure 2.17 - Variables: Level of Prestress and Crack Widths

2.3.2.2   Duct Splices for Galvanized Steel Duct

In most practical applications, the post-tensioning ducts must be spliced at some location. It was decided to compare industry standard splices to heat shrink splices and unspliced duct. The effect of damaged splices was also examined. The two splices are shown in Figure 2.18. The industry standard splice consists of a 300 mm (1 ft) length of oversized duct. Concrete is prevented from entering the splice by wrapping the ends with duct tape. The heat shrink splice consists of an 200 mm (8 in.) length of heat shrink tubing. The original diameter of the heat shrink tubing is 100 mm (4 in.). No mechanical connection was made between the two ducts being connected. For the damaged condition, poor or incomplete duct taping was used on the industry standard splice. For the damaged heat shrink splice, a 25 mm (1 in.) cut was made in the heat shrink tubing at the location where the ducts meet.
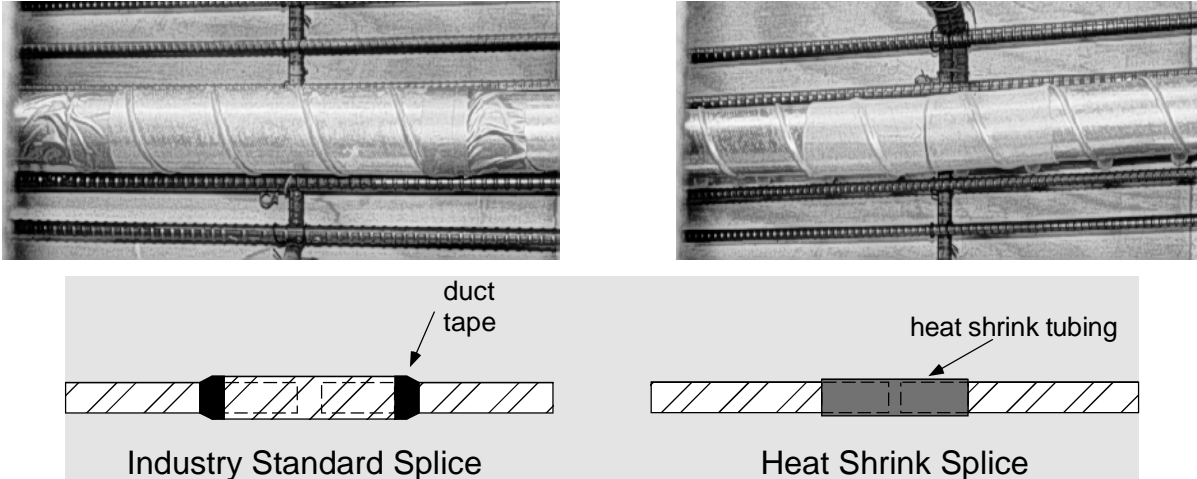
Figure 2.18 - Duct Splices

Three different comparisons were made for the duct splices:

1) Industry standard versus heat shrink

2) Industry standard versus unspliced

3) Effect of damage for industry standard and heat shrink splices

The configurations of the three splice comparisons are shown in Figure 2.19. Details of the splices and their locations for the various configurations are shown in Appendix A.
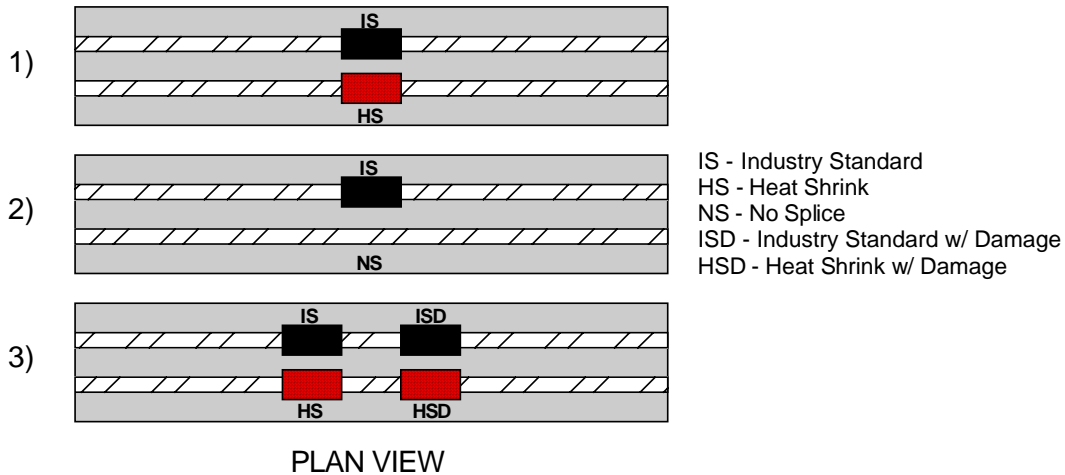
Figure 2.19 - Duct Splice Configurations

2.3.2.3   High Performance Fly Ash Grout

Two high performance grouts (a fly ash grout and an antibleed grout) recommended from the evaluation of grouts described in Research Report 1405-2 under this project were used to evaluate corrosion performance under field conditions. The fly ash grout was evaluated in Phase I while the antibleed grout was included in Phase II.

The fly ash grout has a water-cement ratio of 0.35 with 30% cement replacement, by weight, using fly ash. This grout required a superplasticizer dosage of 4 milliliters per kilogram of cementitious material to meet fluidity requirements.

2.3.3   Phase II Variables

2.3.3.1   Concrete Durability

Concrete plays an important role in corrosion protection of steel reinforcement. A tremendous amount of research has investigated the use of high performance concrete to improve corrosion protection. One of the objectives of this research program is to evaluate the effectiveness of high performance concrete as a function of cracking. The effect of cracking is important since the majority of past research on the effects of cracking on corrosion used poor or average concrete by modern standards. It is possible that cracking may have a more significant effect on the corrosion protection provided by high quality, low permeability concrete. The concrete selected for investigation in this research was based on practical considerations and a review of current literature. It was important to consider current and future trends in concrete technology in Texas to ensure that possible recommendations would be adopted by TxDOT and could be supplied by ready-mix concrete producers within the state. For this reason, it was decided to use fly ash based high performance concrete rather than silica fume or blast furnace slag. Although concrete using these pozzolanic admixtures have been shown to improve corrosion protection and durability, they are very uncommon in Texas, where fly ash is widely used and readily available. Two different concrete mixes were selected for comparison to the standard substructure concrete. Each is described below.

TxDOT Class C Concrete with 25% Fly Ash

Partial cement replacement with fly ash has been shown to improve most aspects of concrete durability (see Report 1405-1). Replacement amounts of 20% to 35% (by volume) are permissible under TxDOT Standard Specifications. Cement replacement with fly ash is common practice in Texas bridges, normally at the contractor's request due to the low cost of fly ash in comparison to cement.

Traditionally, ASTM Class C fly ash has been readily available in Texas as a by-product of burning lignite and/or sub-bituminous coals for electricity production within the state. However, due to recent increased construction and demand for fly ash, some ready-mix concrete producers have begun to use ASTM Class F fly ash from North Eastern states where bituminous coals are predominant. From a durability standpoint, ASTM Class F fly ash normally provides better durability performance through slightly lower permeability and better resistance to sulfate attack.

Due to the increasing use of fly ash in concrete, it was decided to investigate its effect on corrosion protection when fly ash is simply used as partial cement replacement and no other changes are made to the mix design. It was decided to use the standard TxDOT concrete for bridge substructures and to replace 25% of the cement (by weight) with fly ash. No other significant changes were made to the concrete mix, and the ratio of water to total cementitious materials was 0.44. At the time of construction, only Class F fly ash was available from local ready-mix suppliers, so Class F fly ash was used.

High Performance Concrete

High performance concretes are quickly gaining popularity for use in Texas bridges. Concretes rated as high performance for durability have very low permeability and make an interesting comparison with the standard TxDOT concretes. Concretes rated as high performance for strength may not give better corrosion protection alone, but may give rise to favorable situations for corrosion protection such as the absence of cracking at service loads for post-tensioned members. Higher strength concretes may also allow a higher level of post-tensioning and more slender members that may help to justify the additional cost of these mixes. A mix classified as high performance for both strength (around 68.9 MPa [10,000 psi]) and durability was chosen. The mix design chosen was similar to that used for a cast-in-place bridge deck in San Angelo, Texas, with a modification of a maximum aggregate size of 19 mm (¾"). The mix contained 25% cement weight replacement fly ash (water-cement ratio around 0.29) batched to a slump of 25-50 mm (1-2") with additional superplasticizer added on site to reach a slump of about 200 mm (8"). The original San Angelo mix design strength was 41.3 MPa (6 ksi), but cylinder strengths were around 68.8 MPa (10 ksi) due to the low water-cement ratio. Details of the mix designs are included in Appendix B.

Effect of Cracking

In order to evaluate the effect of cracking, the two concrete types were each used with the Non-PS, 2/3 PS and 100%U PS sections at a constant service load level to produce a range of crack widths. A total of six specimens were required for this category of variables (3 sections x 2 variables).

2.3.3.2 Strand Type

The two types of corrosion resistant strand considered are an epoxy-coated strand and a galvanized strand. Both were obtained from Florida Wire and Cable. Representative elongation curves and properties are included in Appendix A. Both strand types were 13 mm diameter, 1860 MPa (0.5", 270 ksi) stress relieved strand. The epoxy-coated strand had grit impregnated coating for improved bond (Flo-Bond™ strand).

When examining coated steel for corrosion resistance, it is important to also consider the effect of damaged coating. To examine this effect, the specimen with epoxy-coated strand contains one damaged tendon and one undamaged tendon. The damaged tendon has 6 by 6 mm squares of epoxy removed at five selected locations along the length of each strand. The locations of the damage are shown in Figure 2.20. Three of the damage locations coincide with the centerline crack and the cracks located 300 mm on each side of the centerline. The remaining two damage locations coincide with the bends in the parabolic duct. A continuous length of sheet metal is rolled into a helical shape to form the galvanized duct (a close-up photograph of the duct is shown in Figure 2.18). When the duct is bent to form the desired shape, small gaps may occur between the overlapping metal. Gaps in the duct allow chlorides to penetrate to the grout surface more quickly, so these areas may be of interest. One strand in the damaged tendon is repaired with an epoxy patch repair kit provided by Florida Wire and Cable and the other strand is left damaged.
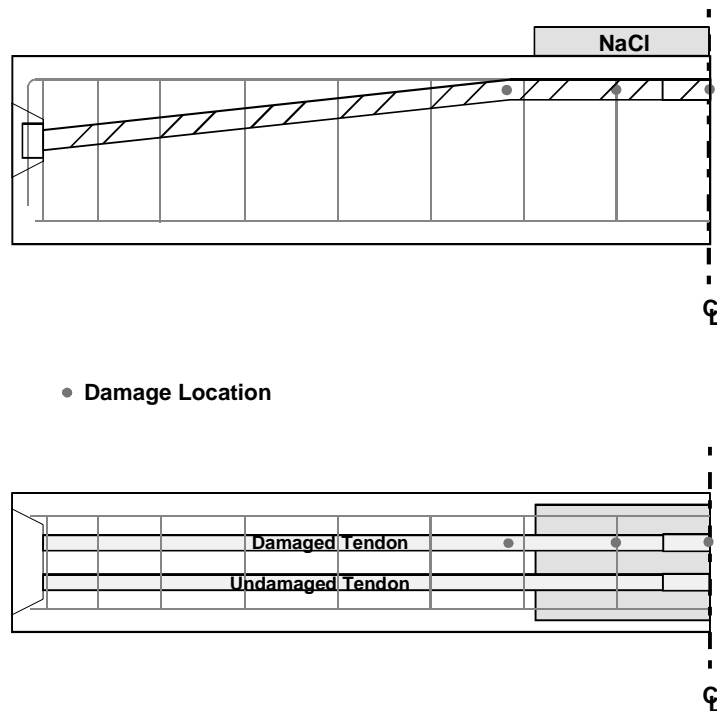
Figure 2.20 - Locations of Intentional Damage to Epoxy-Coated Strand

2.3.3.3 Duct Type and End Anchorage Protection

Plastic ducts have been found to increase durability for post-tensioned structures as both a barrier for chloride penetration as well as by resisting duct corrosion that may cause further chloride ingress due to concrete cracking and spalling from corrosion product buildup. The specifications released by the United Kingdom to remove the restrictions on grouted post-tensioned construction require plastic ducts and do not allow galvanized ducts that are common in U.S. post-tensioned construction.

The plastic duct chosen for testing was a polyethylene duct that is part of VSL Corporation's VSLAB+™ system. The duct is oval in cross section and can accommodate two strands. The smallest round plastic duct commercially available was intended for 5-12 strands and was too large for the beam specimens. Therefore, the two-strand slab system was chosen.

The PT-Plus system also allowed the investigation of an encapsulated system for end anchorage protection. Figure 2.21 shows the end protection provided by the system. The end trumpet with the bearing plate clips directly onto the duct and a cap and gasket is provided that screws on over the end anchor head. A grout inlet is prefabricated into the end trumpet. This system is basically air and water tight. The original intention was to evaluate an electrically isolated system, but such a system was not commercially available. An electrically isolated system has the added benefit of protection of the tendon from stray currents and protection from the development of corrosion cells with other metal in the proximity.
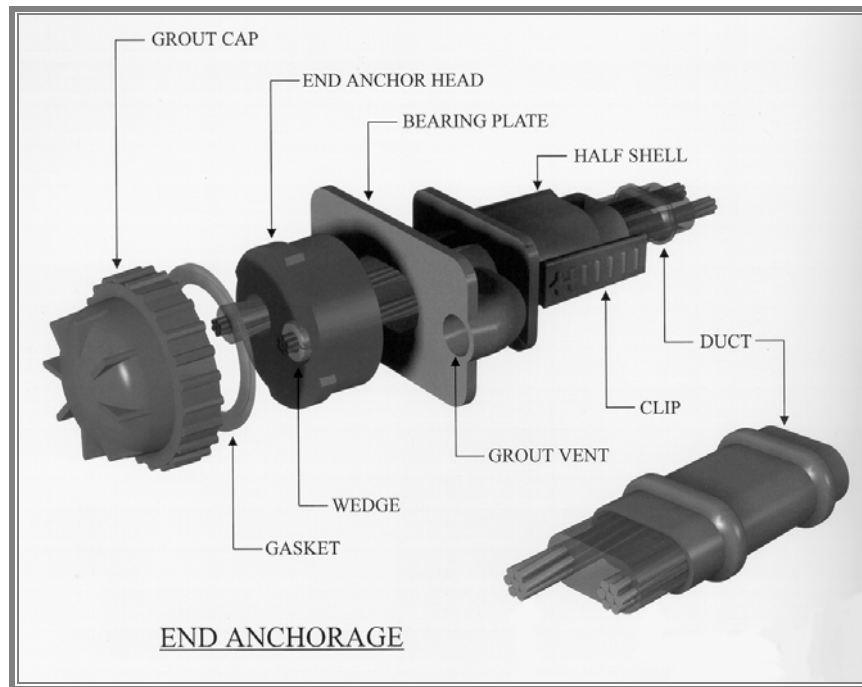
Figure 2.21 - VSLAB+™ System

2.3.3.4   High Performance Antibleed Grout and Poor Grouting Procedures

As mentioned in Section 2.3.2.3, two high performance grouts (a fly ash grout and an antibleed grout) were selected from the research described in Research Report 1405-2 under this project to evaluate corrosion performance under field conditions. The fly ash grout was included in Phase I (see Section 2.3.2.3).

The antibleed grout has a water-cement ratio of 0.33 with 2% cement weight of antibleed admixture. The profile duct used in the beam specimens has only a small vertical rise, so bleed should not be a significant problem. The antibleed grout was chosen so that its corrosion protection properties could be compared with the fly ash grout and TxDOT grout. Upon autopsy, the tendons will also be evaluated for presence of voids in comparison with the TxDOT standard grout.

One specimen was chosen to simulate the effect of poor grouting procedures. This specimen had one tendon grouted by the standard method and one tendon poorly grouted. The grouting procedure for this specimen is discussed in Section 2.6.3.

2.4   EXPERIMENTAL PROGRAM

A total of twenty-seven specimen types were developed to address the selected variables. The complete testing program is summarized in Table 2.3. A simple numbering scheme to identify each specimen is used in the table. The testing program was implemented in two phases, with sixteen specimens in Phase I and eleven specimens in Phase II. Schematics of the beams in each phase are shown in Figure 2.22 and Figure 2.23. The duct splice locations and types for each beam are shown in the figures. The relative positions of the various specimens outside of Ferguson Lab are shown in Figure 2.24.

Table 2.3 - Beam Experimental Program

	Main Variable	Non-PS	2/3 PS	100%U	100%S
			Section Type		
Phase I	Unloaded	1.1		3.1	
	Very Small Crack		2.1	3.2	
	Constant Service Load	1.2	2.2	3.3	4.1
	Constant Service Load (duplicate)	1.3	2.3	3.4	4.2
	Overload and Return to Service	1.4	2.4	3.5	
	High Performance Fly Ash Grout		2.11		
Phase II	Standard Concrete with 25% Fly Ash	1.5	2.5	3.6	
	High Performance Fly Ash Concrete	1.6	2.6	3.7	
	Epoxy-Coated Strands		2.7		
	Galvanized Strands		2.8		
	Poor Grouting Procedures		2.9		
	High Performance Antibleed Grout		2.10		
	Encapsulated System w/ Plastic Duct		2.12		

Non-Prestressed Beams

Beam 1.1: Unloaded

Beam 1.2: Service Load (cracked)

Beam 1.3: Service Load (cracked)

Beam 1.4: Overload & Return to Service

2/3 Prestressed Beams

Beam 2.1: Very Small Crack
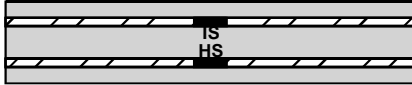
Beam 2.2: Service Load (cracked)
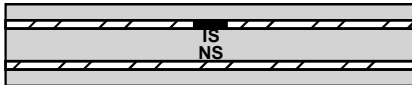
Beam 2.3: Service Load (cracked)
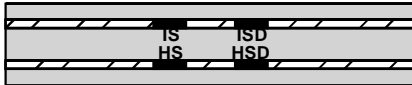
Beam 2.4: Overload & Return to Service
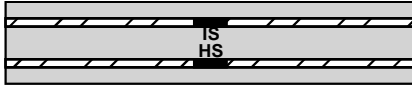
Beam 2.11: Service (Fly Ash Grout)
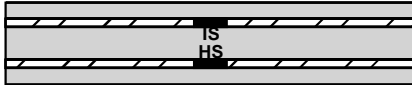
100%U Prestressed Beams

Beam 3.1: Unloaded
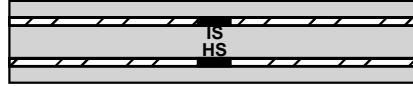
Beam 3.2: Very Small Crack
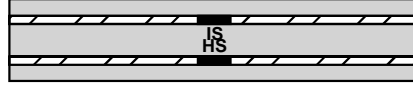
Beam 3.3: Service Load (cracked)
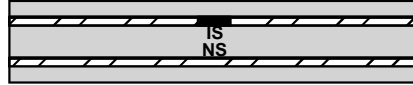
Beam 3.4: Service Load (cracked)
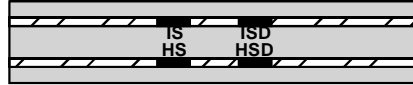
Beam 3.5: Overload & Return to Service
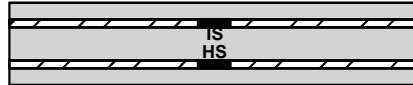
100%S Prestressed Beams

Beam 4.1: Service Load (uncracked)
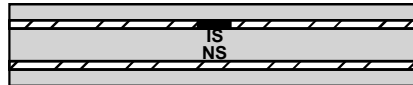
Beam 4.2: Service Load (uncracked)
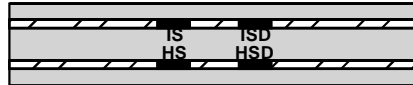
SPLICE DESCRIPTIONS:
IS - Industry Standard
HS - Heat Shrink
NS - No Splice
ISD - Industry Standard w/ Damage
HSD - Heat Shrink w/ Damage

Figure 2.22 - Phase I Beams

Non-Prestressed Beams

Beam 1.5: Fly Ash Concrete

Beam 1.6: High Performance Concrete

100%U Prestressed Beams

Beam 3.6: Fly Ash Concrete
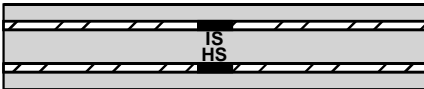
Beam 3.7: High Performance Concrete
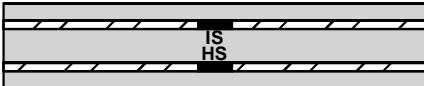
Splice Descriptions:
IS - Industry Standard
HS - Heat Shrink

2/3 Prestressed Beams

Beam 2.5: Fly Ash Concrete
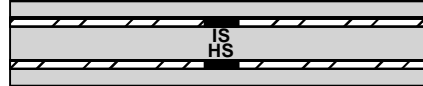
Beam 2.6: High Performance Concrete
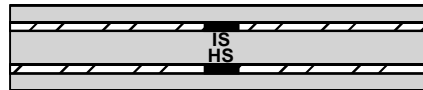
Beam 2.7: Epoxy Coated Strands
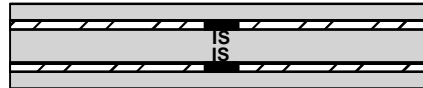
Beam 2.8: Galvanized Strands
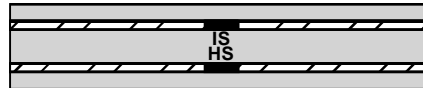
Beam 2.9: Poor Grouting
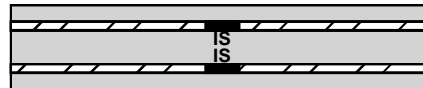
Beam 2.10: Anti-Bleed Grout
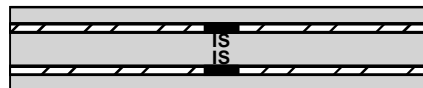
Beam 2.12: Enc. System / Plastic Duct
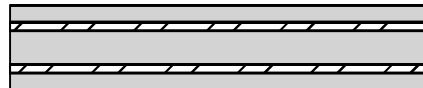
Figure 2.23 - Phase II Beams

Beam Placement
North End of Ferguson Laboratory

PG: Poorly Grouted	I: Industry Standard Splice	D: Damaged Splice End
SG: Standard Grouting	H: Heat Shrink Splice	G: Undamaged Splice End
C: Coating Damaged	U: Undamaged Coating	X: Saltwater End Drippers

Figure 2.24 - Beam Arrangement Outside of Ferguson Laboratory

2.5   EXPERIMENTAL SETUP

The experimental setup required the ability to subject the test specimens to sustained structural loading and corrosive environment. The sustained loading involved forces in excess of 225 kN (50 kips) applied on the beams. The exposure conditions were selected as wet-dry cycling with a 3.5% salt (NaCl) solution. The salt concentration is based on the recommendations of ASTM G109. The salt solution is applied on the cracked region of the elements for a period of two weeks, followed by a dry period of two weeks to complete one wet-dry cycle. Wet-dry cycling is expected to be continued for several years at this site. The large specimen size, number of specimens and long testing duration required a large outdoor area for exposure testing. The selection of an experimental setup was based on consideration of the following criteria:

Space: Total area required for placement of test specimens.

Volume of Concrete: Total volume of concrete for test specimens (and reaction beams if required).

Number of Specimens: Total number of specimens required to consider desired variables. Consideration given to the use of multiple variables in some specimens (strand and anchorage protection), where possible, depending on specimen orientation.

Construction Time: Time required for construction of test specimens (and reaction beams if required).

Salt Water Application: Ease of application, collection and removal of NaCl solution. Consideration given to sophistication of application/collection system (cost, construction time and reliability).

Exposure Surface: Coverage of cracked region with NaCl solution and protection from environment (wind, rain, limit evaporation).

Support System: Complexity (cost, construction time and reliability) of support system for test specimens.

Crack Measurement: Ease of taking measurements on cracked surfaces.

Control of Cracking During Loading: Ability to attain desired crack widths in a given specimen during application of loading.

The selection of an experimental setup and test procedure was based primarily on the concern for the application, collection and removal of the salt water solution. Due to the frequency of cycling and the considerable duration of the testing, a simple and reliable system and procedure was desired. In addition, environmental regulations require all of the NaCl solution to be collected and disposed of in a sanitary sewer. Thus, the method for application and removal of the NaCl solution must minimize potential for leakage and spillage to the ground. For these reasons, a ponding system was selected over a system where the solution was pumped over the cracked region and collected in drip pans below the specimen. To accommodate this exposure method, it was decided to test the specimens in a typical negative moment tendon orientation, as shown in Figure 2.25. Other benefits of testing in this orientation include better control during loading, ease of crack measurements and the opportunity to evaluate multiple tendons in one specimen. In the latter case, the two tendons/ducts allows variables such as duct splices, strand coatings and coating damage to be compared to the control cases in a single specimen. This comparison is not possible when the specimens are tested on their sides.

32
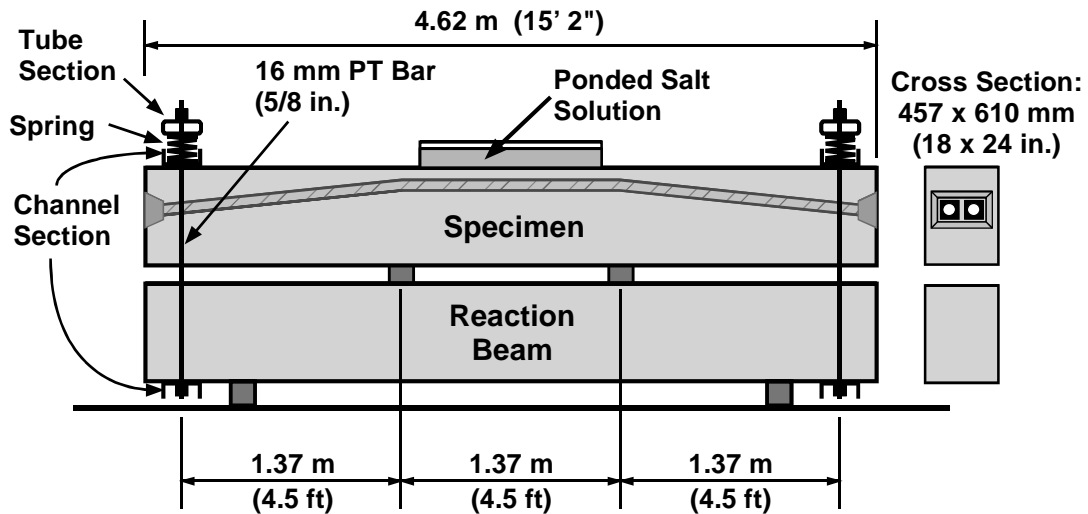
Figure 2.25 - Test Setup

The specimen is oriented tension side up and is paired with a reinforced concrete reaction beam. Salt water is ponded directly on the tension side over the middle third of the member using a plastic dike adhered to the concrete surface with marine sealant/adhesive. A wet-dry shop vacuum is used to remove the salt solution at the end of the wet period. The ponded region is covered during the wet cycle to prevent contamination of the NaCl solution and to limit evaporation.

Loading is applied through a system of post-tensioning bars and railroad springs at the ends of the member and reactions at the third points along the member length. The railroad springs were used to minimize force losses due to time dependent deflections of the members. The spring stiffness was selected to limit force loss to 5% during the first year of sustained loading, with calculations based on the Non-PS beam section. It was decided not to use traditional methods to monitor the force in the loading system due to the cost of using load cells and due to the questionable long-term reliability of strain gauges in an exterior exposure. Periodic re-loading of the beams will be necessary to ensure load levels remain within expected limits.

The reaction beam was designed as reinforced concrete. Other options investigated included prestressed concrete beams and steel beams. The decision to use nonprestressed, reinforced concrete beams was based on cost and construction time. The dimensions of the reaction beam were identical to the beam specimens. Reinforcement for the reaction beams was proportioned to provide excess strength in comparison to the specimens and to limit crack widths at service load levels. The nominal strength of the reaction beam was 700 kN-m (6180 k-in.). Maximum surface crack widths at the specimen service load level were computed as 0.2 mm (0.008 in.). Detailed drawings of the reaction beam are included in Appendix A.

The paved area at the north end of the Ferguson Structural Engineering Laboratory was selected for storage and testing of the beams, as shown in Figure 2.26. Figure 2.27 shows a top view of the beams with plywood covers on the ponded region of the beams.

Figure 2.26 - Beam Test Setup at North End of Ferguson Laboratory
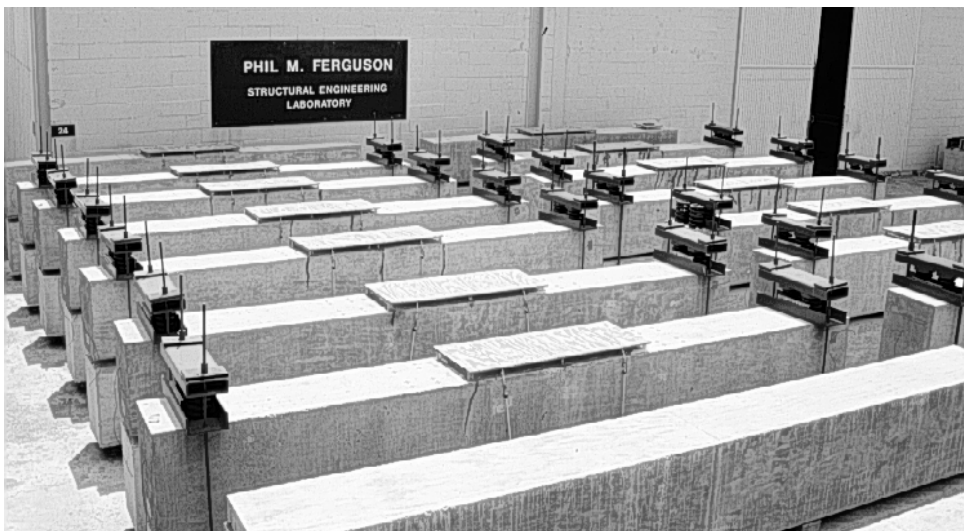
Figure 2.27 - Top View of Beams Showing Ponded Area (Covered)

In addition to the saltwater ponding, three specimens were selected to investigate the effects of chloride ingress at the end anchorage. Specimen 2.12 (encapsulated system / plastic duct), Specimen 2.7 (epoxy-coated strand), and Specimen 2.9 (poorly grouted) were chosen for the end exposure testing. Specimen 2.9 contains one tendon grouted with standard procedures that can be used as a control. A dripper system was used to trickle saltwater over the beam ends as shown in Figure 2.28. The drippers were run for an 8-hour duration at 2-week intervals.

Figure 2.28 - Beam End Dripper System

2.6   FABRICATION

2.6.1   *Beam Fabrication*

All reaction beams and beam specimens were fabricated at Ferguson Laboratory. Forms were built at the laboratory with end walls customized for each section type. All bars used in the specimens were uncoated and in "bright" condition (free from rust) in order to eliminate surface condition as a variable in testing. A photograph of a completed cage prior to attaching the end walls is shown in Figure 2.29. Close-ups of the reinforcing cage end detail for a 2/3 PS section are shown in Figure 2.30. The spiral reinforcement was slightly overlapped to accommodate the small width of the beam specimens. The pocket forms and end trumpets were attached to the end form walls and then aligned with the ducts in the completed cage. Once in place, the end trumpets were sealed to the ducts with duct tape. Figure 2.31 shows the end form wall and the end of the specimen after removal of the form wall and pocket. Figure 2.32 shows a beam form just prior to casting.
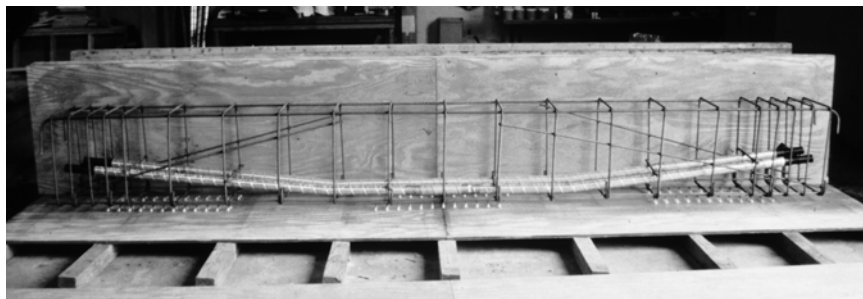
Figure 2.29 - Reinforcing Cage
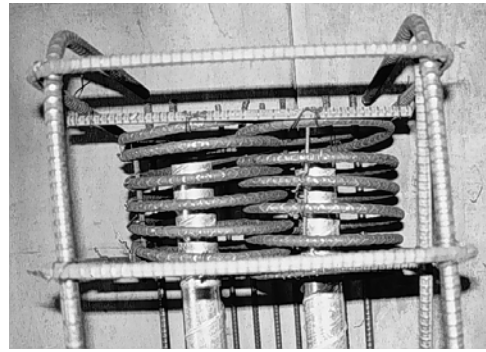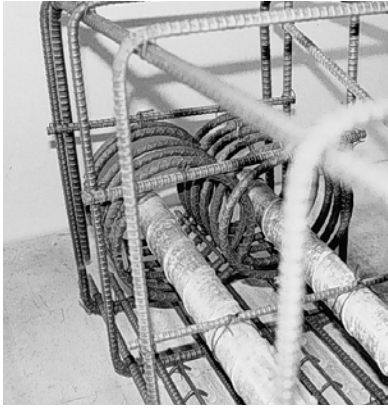
Figure 2.30 - End Detail of Reinforcing Cage for a Post-Tensioned Beam
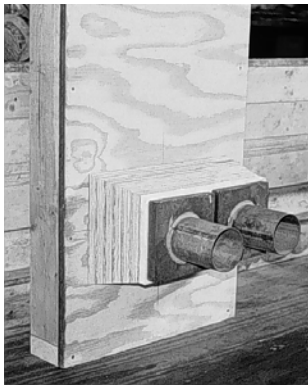
end form wall   completed end pocket

Figure 2.31 - Forming of the End Pocket

Figure 2.32 - Beam Formwork

Concrete was ordered from Capitol Aggregates in Austin, Texas. Typically three beam specimens were cast at one time along with two ponding block specimens for chloride samples. Prior to casting the high performance concrete specimens, a test truck was ordered to evaluate the mix. This mix required a batched slump of 25-50 mm (1-2") at the plant with addition of superplasticizer on site until a slump of approximately 200 mm (8") was reached. Concrete compressive strengths for all concrete batches are given in Appendix A. The average 28-day strengths for each batch are shown in Table 2.4, with a corresponding plot showing differences in the TxDOT Class C batches given in Figure 2.33. Figure 2.34 shows a comparison between the average TxDOT Class C strengths and the fly ash and high performance concretes.

Table 2.4 - Average 28-Day Compressive Strengths

Mix Design	Specimens	28-day Strength (MPa)	Average (MPa)	Average (psi)
TxDOT Class C	1.1,1.2, 1.3	35.9		
	1.4, 2.1, 2.2	33.2		
	2.3, 2.4, 2.11	41.4		
	3.1, 3.2, 3.3	37.0	36.8	5270
	3.4, 3.5	39.7		
	4.1, 4.2	33.1		
	2.7, 2.8, 2.10	39.9		
	2.9, 2.12	34.0		
TxDOT Class C with Fly Ash	1.5, 2.5, 3.6	42.7	42.7	6200
High Performance	1.6, 2.6, 3.7	64.3	64.3	9300
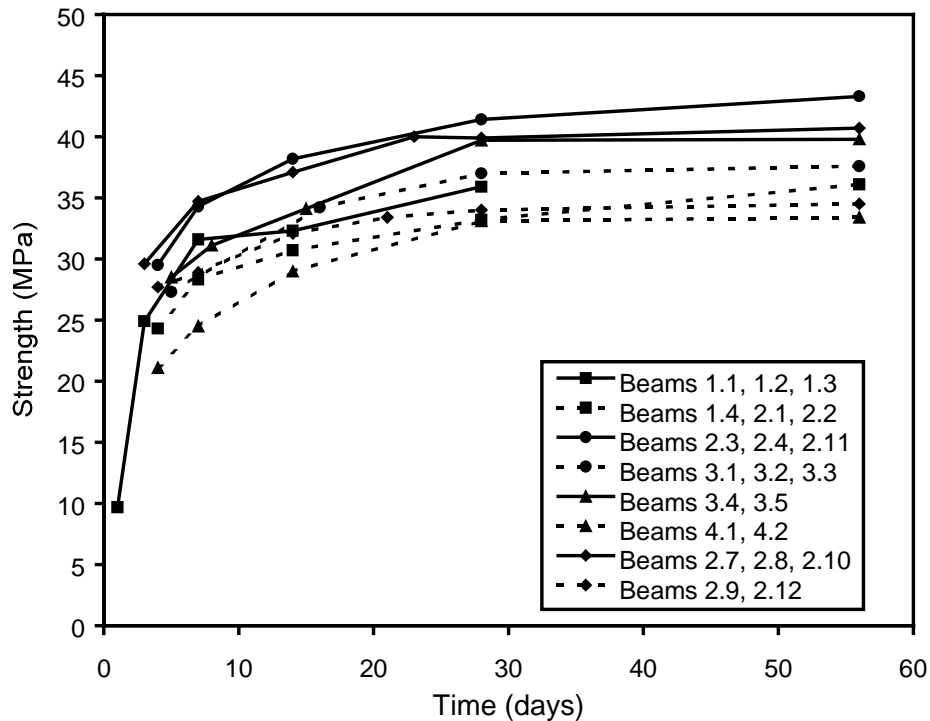
Figure 2.33 - TxDOT Class C Compressive Strengths

37
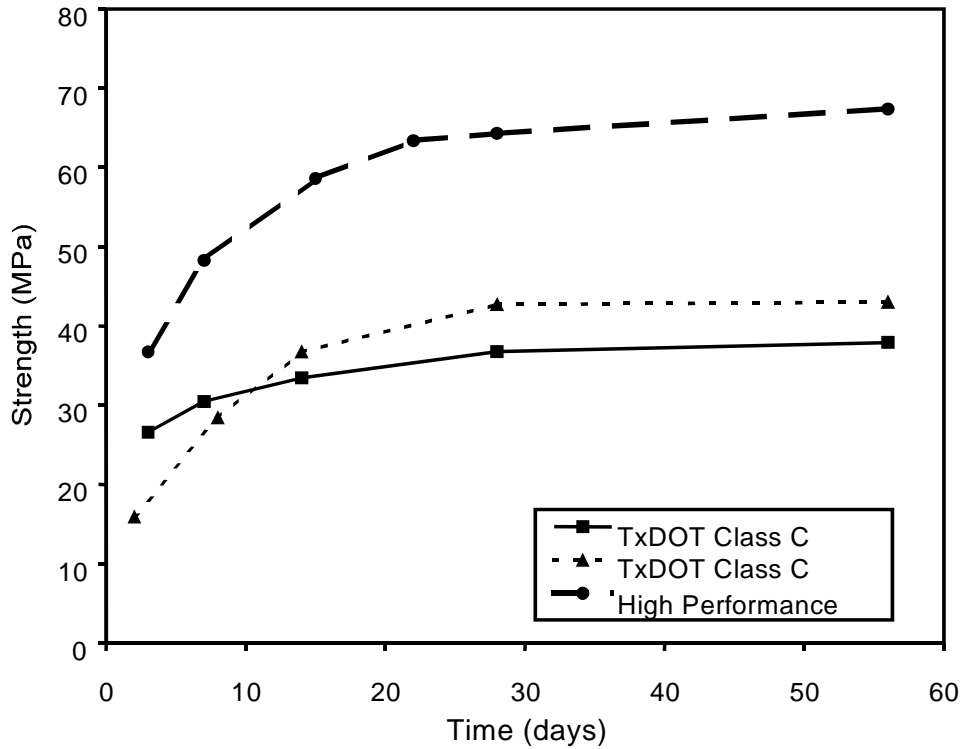
Figure 2.34 - Compressive Strength Comparison

2.6.2   Post-Tensioning

2.6.2.1   Prestress Losses

Elastic shortening, friction losses and anchorage seating were considered in the calculation of the post-tensioning jacking forces for each section type.

Elastic Shortening

Staged post-tensioning was used to minimize prestress losses due to elastic shortening. The post-tensioning sequence is shown in Figure 2.35. The final elastic shortening loss occurs in Tendon 1 as Tendon 2 is stressed from two thirds of the jacking force up to the total jacking force, T_j.
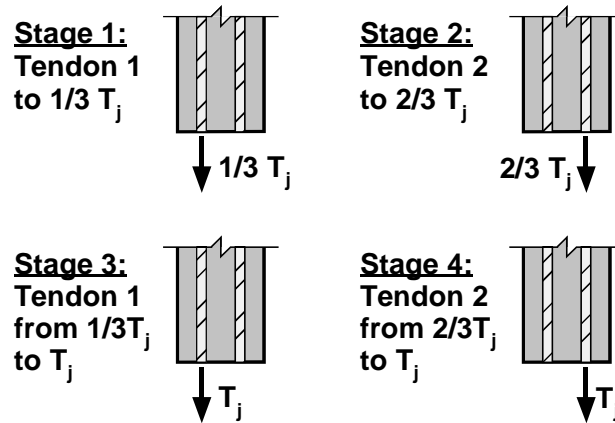
Figure 2.35 - Staged Post-Tensioning Sequence

Friction

Friction losses were small due to the short length of the beams and small variation in tendon path. The prestress loss due to friction at the midspan of the beams was computed to be 2.5% of the jacking force.

Anchorage Seating

Prestress losses due to anchorage seating were very critical due to the short beam length. Common practice is to use shims to compensate for anchorage seating losses in short tendons. The use of shims in the beam specimens was not practical due to the details of the anchorages and beam end pockets. Therefore, it was necessary to power seat the wedges to minimize seating losses. Most commercially available post-tensioning equipment has power seating capabilities incorporated into the stressing rams. However, for tendon sizes smaller than four strands and ram capacities less than 450 kN (100 kips), power seating is not available. It was decided to use the available hydraulic rams at the Ferguson Laboratory in a configuration that would allow stressing and power seating of the wedges. Post-tensioning equipment is described in more detail in Section 2.6.2.3.

It was necessary to accurately determine the amount of anchorage seating loss for the anchorage hardware, tendon length and post-tensioning equipment to be used. A large, heavily reinforced concrete stressing block with the same length as the beams was available from a previous project at Ferguson Laboratory. Several pull off tests were used with the anchorage hardware and stressing equipment to determine necessary power seating forces to limit seating losses to tolerable levels. The setup for the pull off tests is shown in Figure 2.36. The procedure is as follows:

1. Stress the tendon to a trial jacking force based on the desired initial prestress and an assumed seating loss.

2. Power seat the wedges to a trial seating force.

3. Release the stressing ram.

4. Perform a pull off test to determine the actual force in the tendon. This determination is made by plotting the jacking force and stroke of the stressing ram as the tendon is re-stressed. A distinct slope change on a plot of T_j versus Δ will occur when the force in the stressing ram overcomes the force in the tendon.

5. Based on the trial jacking force and measured tendon force, determine the prestress loss and anchorage seating value. If unsatisfactory, de-tension the tendon, remove the wedges, and repeat the process using new values of assumed seating loss and power seating force.
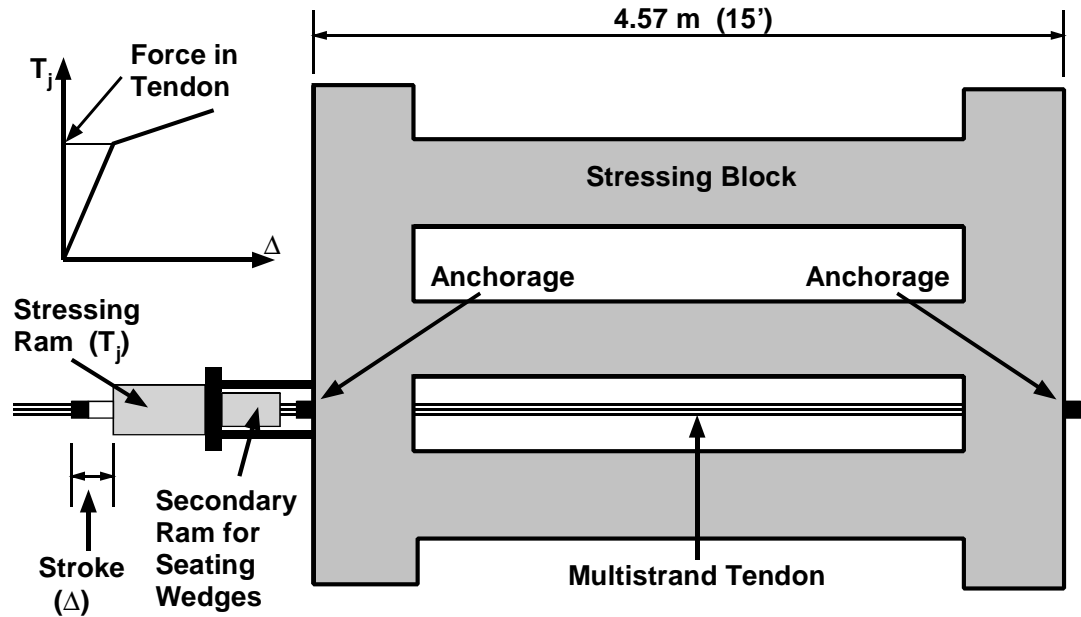
Figure 2.36 - Pull Off Test for Determining Anchorage Seating Loss

The pull off tests determined a wedge seating force of approximately 80 kN (18 kips) would limit anchorage seating to 3.2 mm (1/8 in.). This seating loss could be easily accommodated by adjusting the jacking force.

The prestress losses, jacking forces and initial prestress for each of the post-tensioned beam types are summarized in Table 2.5. The total prestress loss due to elastic shortening, friction and seating was rounded up to 172 MPa (25 ksi) for each section type. Due to the small magnitude of the elastic shortening loss, it was decided to use the same jacking force for both tendons in a beam.

2.6.2.2 Epoxy-Coated Strand

Epoxy-coated strand has some unique considerations for post-tensioning. PCI (Prestressed Concrete Institute) has published *Guidelines for the Use of Epoxy-Coated Strand* to address these considerations. Special wedges are used that can bite through the protective epoxy coating. These wedges are larger than standard wedges and proper anchor heads were fabricated to accommodate the wedges. Figure 2.37 shows a comparison of wedges for bare and epoxy strand. The strand in the center of the figure shows the bite marks that are inflicted on the coating by the wedges. Standard anchor heads were obtained from VSL Corporation, and anchor heads for the epoxy-coated strand were machined at Ferguson Laboratory.

Initial tension of 45 kN (10 kips) was used to remove slack from the strand. This force is small enough not to cause major damage to the strand, so the wedge can be moved before final stressing. Higher forces may contaminate the wedge jaws with epoxy and damage the strand coating, so the final stressing must be performed in a single tensioning step. Therefore, each tendon with epoxy-coated strands was stressed to the full force of T_o in one stage.

Epoxy-Coated Strand

Standard Wedge

Epoxy Wedge

Figure 2.37 - Comparison of Post-Tensioning Wedges

Anchor head seating losses are considerably larger for epoxy-coated strand than for bare strand. This loss has been reported to be approximately double the loss for bare strand when power seating is not used. Anchor seating losses are reduced for both bare and epoxy-coated strand when power seating is used, but the power seating may not be as effective on the epoxy-coated strand. Pull-off test data for the epoxy-coated strands was not available and therefore assumed anchorage end movements of 8 mm (5/16 in) for the epoxy-coated strand were used to calculate the necessary adjustments to the jacking force. The resulting jacking stress was at the AASHTO Code limit of $0.8f_{pu}$. Total losses for tendons with epoxy-coated strand were estimated at 378 Mpa (54.8 ksi). Calculated post-tensioning forces and stresses are listed in Table 2.5.

During seating, the coating was somewhat damaged on the live end, and the power seating was significantly less effective on the epoxy-coated strands. The resulting elongations after post-tensioning were lower than anticipated which indicates an expected average tendon stress of around 145 ksi instead of the targeted 162 ksi.

Bare steel is exposed at the cuts at the end of the strands. After stressing and prior to grouting, the ends are patched with the same epoxy-repair compound used for repairing damaged strand. The epoxy patch liquid is inserted into a small plastic end cap that is fitted over the end of the strand. Any damaged areas at the strand end were also painted with the epoxy patch repair.

Table 2.5 - Calculated Post-Tensioning Forces and Stresses

	2/3 PS		100% U PS	100% S PS
	2-strand tendon		3-strand tendon	4-strand tendon
	Epoxy-Coated Strand	*Bare Strand*	*Bare Strand*	*Bare Strand*
Initial Prestress, f_{pi}	1117 MPa *(162 ksi)*	1117 MPa *(162 ksi)*	1117 MPa *(162 ksi)*	1041 MPa *(151 ksi)*
Total Estimated Losses	378 MPa *(55 ksi)*	172 MPa *(25 ksi)*	172 MPa *(25 ksi)*	172 MPa *(25 ksi)*
Jacking Stress, f_{pj}	1495 MPa *(217 ksi)* $0.8\ f_{pu}$	1289 MPa *(187 ksi)* $0.69\ f_{pu}$	1289 MPa *(187 ksi)* $0.69\ f_{pu}$	1114 MPa *(176 ksi)* $0.65\ f_{pu}$
Jacking Force	296 kN *(66.4 k)*	255 kN *(57.2 k)*	383 kN *(87.2 k)*	480 kN *(108 k)*

2.6.2.3 Post-Tensioning Equipment

All equipment for post-tensioning was adapted from Ferguson Laboratory hydraulic equipment. The setup used for the 100%S PS beams is shown in Figure 2.38. Additional details are shown in Appendix A. The chair for post-tensioning was fabricated from a 50 mm (2 in.) thick steel plate and four 35 mm (#11) reinforcing bars. The stressing ram for the 100%S PS section had a capacity of 1335 kN (300 kips). This large ram was selected based on its internal diameter that could accommodate the four-strand tendon. A smaller ram with 535 kN (120 kips) capacity was used for the 2/3 PS and 100%U PS beams. A system of two smaller rams and transfer bracket were used to power seat the anchorage wedges. The post-tensioning equipment was mounted on an electric forklift for ease of movement and height adjustment.
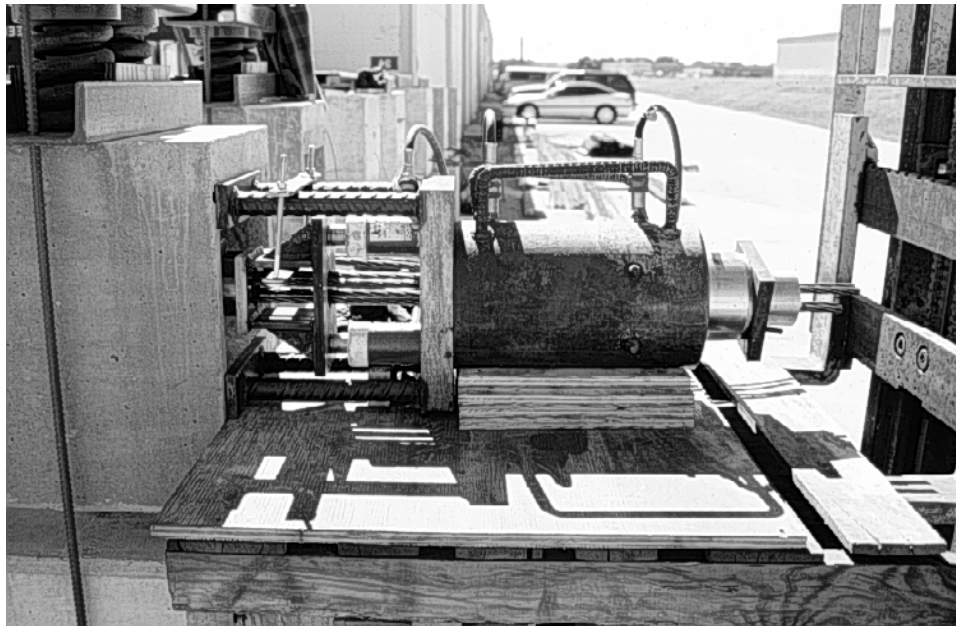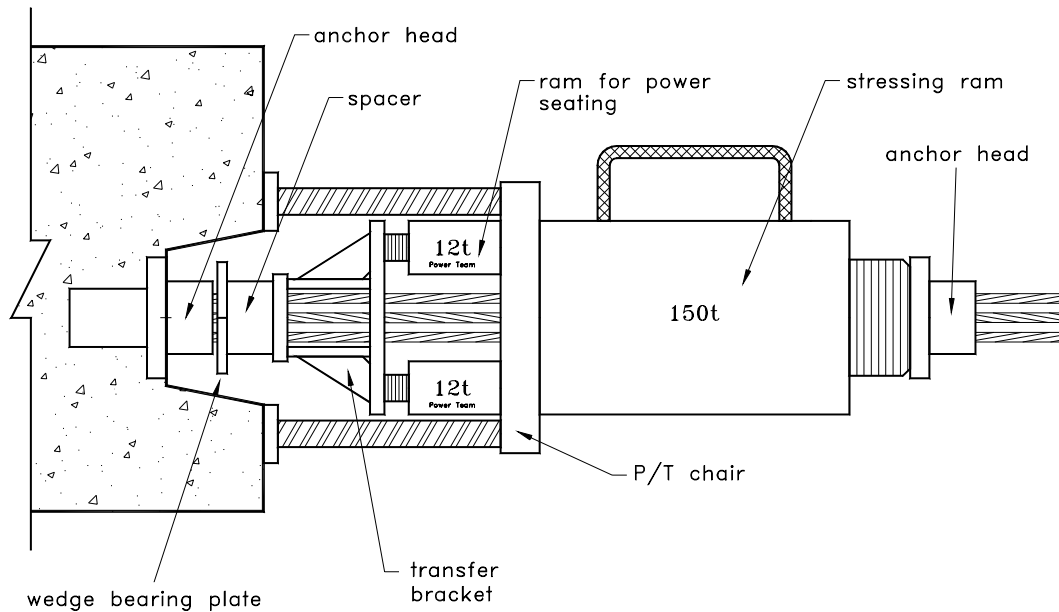
Figure 2.38 - Post-Tensioning Equipment for 100%S PS Beams

2.6.2.4 Post-Tensioning Procedure

Post-tensioning procedures were based on TxDOT Specifications Item 426.9 and AASHTO LRFD Construction Specifications. The main steps in the process are as follows:

1. Each individual strand was given an initial tension of approximately ten percent of the jacking force (per strand) to remove slack. Initial tensioning was performed using a small 107 kN (24 kip) ram.

2. After initial tensioning, all strands of the tendon were given a reference mark to measure elongation.

3. The tendons were stressed using a staged post-tensioning procedure, as described in Section 2.6.2.1. Prestress force was monitored using a pressure gauge on the hydraulic pump. At each stage, stressing ram stroke and tendon elongation were measured to confirm force levels. Wedges were power seated at each stage.

4. At the completion of the four stressing stages, final tendon elongation was checked. If acceptable, equipment was removed and the strand ends were trimmed to 25 mm (1 in.) (none of the tendons required re-tensioning).

The 100%S PS sections required a small amount of preload before post-tensioning to keep concrete stresses within tolerable ranges. The preload was applied using the post-tensioning bar and spring loading system described in Section 2.5 and shown in Figure 2.25. The necessary applied moment was 56.5 kN-m (500 k-in.). This moment was below the cracking moment for the section (before post-tensioning).

2.6.3 Grouting

Grouting procedures followed those recommended by the Post-Tensioning Institute. All post-tensioned beams were grouted with the TxDOT standard grout except Specimens 2.10 and 2.11 that contain the high performance grouts. The TxDOT standard grout has a 0.44 water-cement ratio with 0.9% Intraplast-N (superplasticizer / expansive admixture). The specifics for the fly ash and antibleed grouts are included in Sections 2.3.2.3 and 2.3.3.4 and in Research Report 1405-2.

Vents were provided toward the end of the intermediate rise in the duct. Silicone was added around the wedges to prevent excessive leakage of grout or water. The 2/3 PS sections were grouted through the third wedge opening. The grout tube in the third wedge opening is shown in Figure 2.39. The 100% U PS and 100% S PS sections were grouted through a grout tube connected to the duct behind the end trumpet and cast into the concrete as shown in Figure 2.40. The encapsulated system specimen was grouted through a prefabricated connection in the end trumpet.
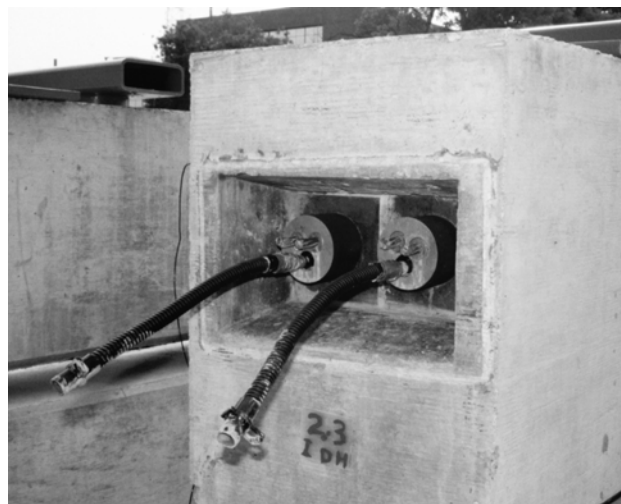
Figure 2.39 - Grouting Tubes for 2/3 PS Specimens

Figure 2.40 - Grouting Tubes for 100% U PS and 100% S PS Sections

Grout was mixed with a portable mixer and then transferred to the holding bin of a grout pump. Grout in the holding bin was continuously agitated. Grout cube specimens were cast from a representative batch of grout for each set of beam specimens. Average 28-day strengths are shown in Table 2.6.

Table 2.6 - Average 28-Day Grout Strengths

Mix Design	Specimens	28-day Strength (MPa)	Average (MPa)	Average (psi)
TxDOT Class C	4.1, 4.2 2.1, 2.2, 2.3, 2.4 3.1, 3.2, 3.3 3.4, 3.5 2.5, 2.6, 3.6, 3.7 2.9, 2.12 2.7, 2.8	30.7 28.1 24.9 30.4 27.2 26.0 31.7	28.4	4130
0.35 w/c, 30% Fly Ash	2.11	43.5	43.5	6310
0.33 w/c, 2% Antibleed	2.10	55.4	55.4	8050

After grouting, bleed water leaked from the ends of the strand and around the wedges, even though silicone was applied to the wedge openings. The encapsulated system also had leakage from one end cap. This cap may not have been fully in the "locked" position, but there was no indication that it was not securely in place before grouting. The other caps showed no signs of leakage.

Specimen 2.9 was used to investigate poor grouting procedures. One tendon of the specimen was grouted using standard procedures, but during grouting of the other tendon the pump was turned off twice during pumping to allow possible pockets of air in the line. The pump was left off for approximately 10 minutes at one point

during grouting to allow the grout already pumped into the tendon to reach a different consistency than that of the grout in the pumping chamber that was continuously agitated. The far end grout tube was closed at the first appearance of grout instead of letting the grout flow reach a continuous stream.

2.6.4 Anchorage Protection

Corrosion protection for the anchorages and strand ends was provided by filling the anchorage pockets with a nonshrink grout. Procedures and materials were based on TxDOT Specifications.

After grouting was completed, all exposed surfaces including the anchorage heads, bearing plates and sides of the pockets were cleaned with a wire brush to remove grout and rust. Each end pocket was photographed to provide a record of its condition before capping. This photo will provide a basis for comparison during forensic examination of the specimens at a later date. A sample photo is shown in Figure 2.41. Ground clamps were used to attach a lead wire to one strand in each tendon. This lead wire is used for half-cell potential and corrosion rate measurements during testing. Ground clamps were attached on both tendons, one at each end of the beam.
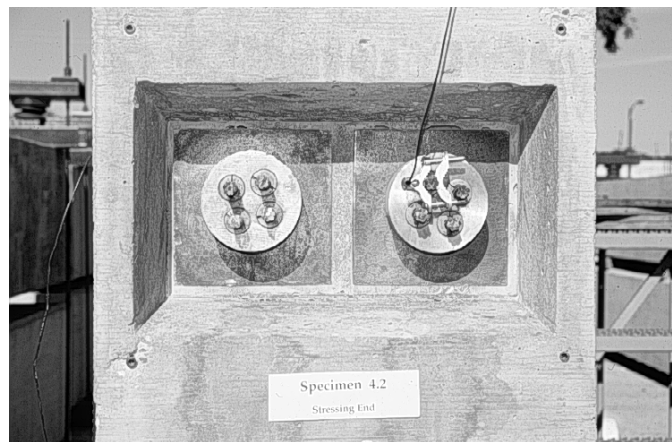
Figure 2.41 - Anchorage Pocket Immediately Before Capping

All exposed surfaces were coated with an epoxy bonding compound immediately prior to capping. After epoxy application, the end pockets were closed in with plywood. Silicone sealant was used to prevent leakage around the plywood. The pockets were with filled with a nonshrink grout mixture by pouring it through a tube as shown in Figure 2.42. The premixed grout contained silica sand and a nonshrink admixture. After the grout had hardened, the plywood was removed. In some cases, a small void remained at the top of the pocket. The entire beam end was rubbed with a mixture of cement, sand and latex bonding agent to provide a uniform finish and fill any voids in the end pocket.
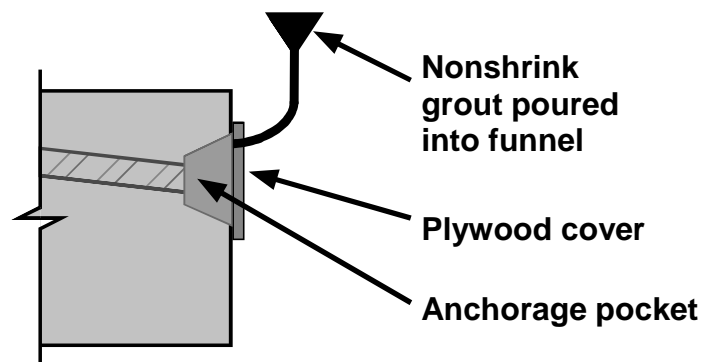
Figure 2.42 - Capping End Anchorages

2.7 SPECIMEN LOADING AND INITIAL CRACK WIDTH MEASUREMENTS

2.7.1 Specimen Load History

Loading was applied according to the planned loading cases (see Section 2.3.2.1 and Table 2.2). Due to variations in the concrete modulus of rupture and the inherent variability in crack prediction, some deviation from the planned loading cases occurred during loading. The actual loading histories for the Phase I beams are listed in Table 2.7. Beams 1.1 and 3.1 were not loaded and are not listed in the table. Loading Step 1 corresponded to the actual (measured) cracking moment for the beam, with the exception of beams 3.2, 4.1 and 4.2 which were uncracked at service load levels.

Deviation from the planned loading cases occurred for Beams 3.2, 3.3 and 3.4. In all cases, the changes were required because the cracking moment was higher than predicted and exceeded the service load moment. The computed cracking moment for the 100%U PS beams was 305 kN-m based on the commonly assumed modulus of rupture of $0.623\sqrt{f'_c}$ MPa $(7.5\sqrt{f'_c}$ psi$)$. The actual cracking moments for Beams 3.3, 3.4 and 3.5 were 310 kN-m, 356 kN-m and 338 kN-m, respectively. Because the effect of cracking is one of the main objectives for the Phase I beam specimens, it was decided to temporarily increase loading on some of the 3 Series beams to produce the desired cracking patterns and levels. The planned and actual loading cases for the 3 Series beams (100%U PS) are shown in Table 2.8.

Table 2.7 - Beam Specimen Loading Histories

Beam No.	1 (M_{cr})	2	3	4	5	6	Note
			Loading Step				**Note**
Phase I Beams							
1.2	0.48 x M_s	0.55 x M_s	0.77 x M_s	1.0 x M_s			
1.3	0.46 x M_s	0.55 x M_s	0.77 x M_s	1.0 x M_s			
1.4	0.48 x M_s	0.55 x M_s	0.77 x M_s	1.0 x M_s	1.25 x M_s		
2.1	0.84 x M_s						
2.2	0.79 x M_s	0.90 x M_s	1.0 x M_s				
2.3	0.82 x M_s	0.91 x M_s	1.0 x M_s				
2.4	0.85 x M_s	0.92 x M_s	1.0 x M_s	1.25 x M_s	1.0 x M_s		
2.11	0.82 x M_s	0.91 x M_s	1.0 x M_s				
3.2	1.0 x M_s						2
3.3	1.0 x M_s	1.1 x M_s	1.15 x M_s	1.25 x M_s	1.0 x M_s		3
3.4	1.15 x M_s	1.25 x M_s	1.0 x M_s	1.25 x M_s	1.33 x M_s	1.0 x M_s	3
3.5	1.09 x M_s	1.16 x M_s	1.25 x M_s	1.0 x M_s			
4.1	1.0 x M_s						1
4.2	1.0 x M_s						1
Phase II Beams							
1.5	0.56 x M_s	0.78 x M_s	1.0 x M_s				
1.6	0.53 x M_s	0.76 x M_s	1.0 x M_s				
2.5	0.92 x M_s	1.0 x M_s					
2.6	0.97 x M_s	1.0 x M_s					
2.7	0.80 x M_s	0.90 x M_s	1.0 x M_s				
2.8	0.97 x M_s	1.0 x M_s					
2.9	0.92 x M_s	0.96 x M_s	1.0 x M_s				
2.10	0.92 x M_s	0.96 x M_s	1.0 x M_s				
2.12	0.89 x M_s	0.95 x M_s	1.0 x M_s				
3.6	1.0 x M_s						4
3.7	1.11 x M_s	1.25 x M_s	1.0 x M_s				

Notes: 1. Beam is uncracked at service load (as designed)
2. Loading case changed from very small crack to Constant Service Load (Uncracked)
3. Loading case changed from Constant Service Load to Overload and Return to Service
4. First cracking at service load ($M_{cr} = M_S$)

Table 2.8 - Planned and Actual Load Cases for Phase I 100%U PS Beams

Beam	Planned Load Case	Actual Load Case	Comment
3.1	Unloaded	Unloaded	No change.
3.2	Very Small Crack	Constant Service Load (Uncracked)	Since the cracking moment for other 3 Series beams had exceeded the service moment, it was decided to leave this beam uncracked at service load. Comparisons can be made with Beams 3.1, 4.1 and 4.2.
3.3	Constant Service Load (Cracked)	Overload and Return to Service	A 25% temporary overload was required to produce three cracks in this beam. ($M_{cr} = 1.0M_{serv}$)
3.4	Constant Service Load (Cracked)	Overload and Return to Service	A 33% temporary overload was required to produce three cracks in this beam. ($M_{cr} = 1.15M_{serv}$)
3.5	Overload and Return to Service	Overload and Return to Service	No change. ($M_{cr} = 1.09M_{serv}$)

2.7.2 *Loading Procedure and Measurement of Crack Widths*

The beam specimens were loaded using two 535 kN (120 kip) hydraulic rams, one at each end of the beam. The loading hardware is shown in Figure 2.43. The ram reacts against a steel spreader beam, compressing the springs. Once the desired level of loading is attained, the force is locked in by tightening the nuts on the post-tensioning bars. An air driven pump was used to apply loading. Load levels were monitored using a pressure gauge on the pump.

Loading was applied according to the load histories listed in Table 2.7. At each loading stage, surface crack widths were measured on the tension face using a crack microscope. Five reference lines were drawn on the tension face of the beams as shown in Figure 2.44. Crack widths were measured where each crack crossed the five reference lines. The crack location was measured relative to the center of load application at one end of the beam.
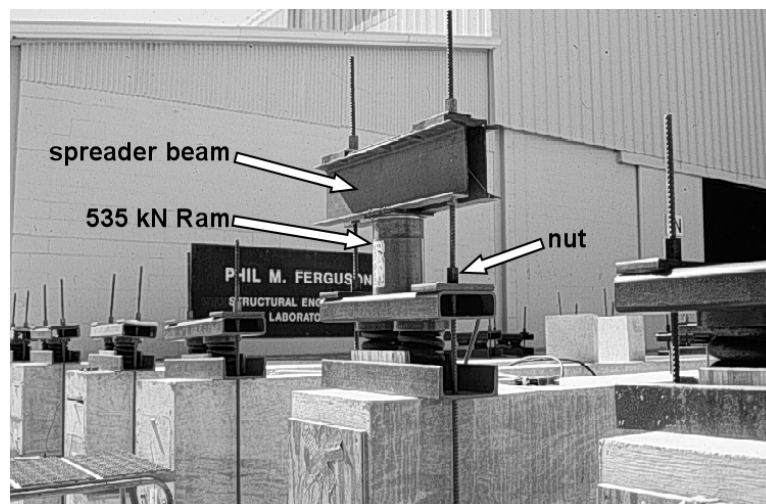
Figure 2.43 - Beam Loading Apparatus
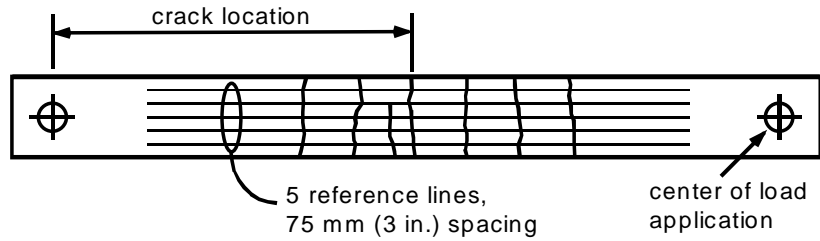
Figure 2.44 - Crack Width Measurement Locations

2.7.3   Measured Crack Widths

Figure 2.45 shows typical crack patterns for each of the three cracked section types. The cracks are traced in the photograph so that they can be clearly seen. The Non-PS section shows a textbook type cracking pattern and a large number of cracks. The 2/3 PS section has fewer cracks that are more confined toward the maximum moment region. The 100% U PS section has only 3 cracks that are confined to the maximum moment region, and the 100% S PS section remains uncracked. Crack patterns for each specimen are included in Appendix A along with plots of final measured crack widths at service load.
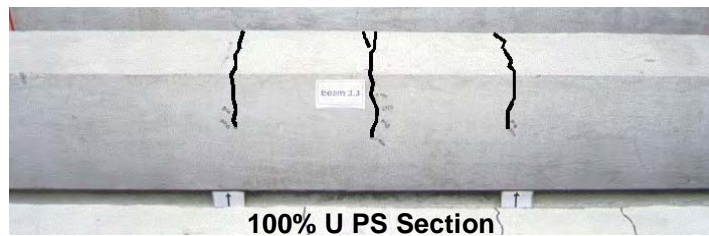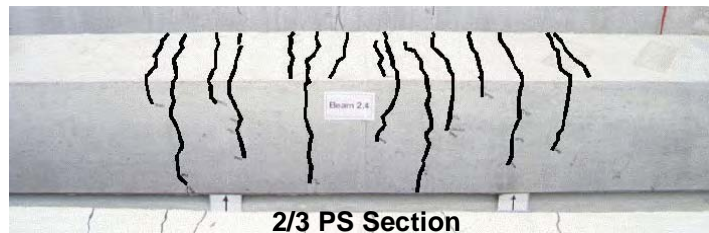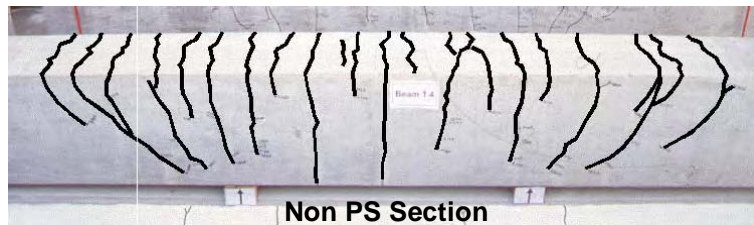
Figure 2.45 - Typical Crack Patterns for Each Section Type

Plots of measured maximum crack width versus moment for each section type are shown in Figure 2.46-Figure 2.48. The descending branch of the curve for overload and return to service load cases is omitted for clarity. Separate plots for specimens with similar reinforcement and concrete type are shown in Figure 2.49-Figure 2.61. Included in each of these plots are the estimated maximum crack widths predicted by the Gergely-Lutz method with modifications for post-tensioned sections. The calculated maximum crack width versus moment curves in these figures are based on the average cylinder strengths for the specimens included in each chart.

Agreement is generally very good for the Non-PS sections as shown in Figure 2.46. The only major variance is seen in Beam 1.2, the first specimen loaded in the testing program. Beam 1.2 was reloaded several times during refinement of the loading system. The measured crack widths compare fairly well with the calculated values as shown in Figure 2.49-Figure 2.51.

A comparison of the moment versus crack width plots for the 2/3 PS sections is shown in Figure 2.47. These specimens represent a large number of variables including concrete type, grout type and strand type. The specimens with TxDOT standard concrete and control variables show excellent agreement with the calculated crack width values as shown in Figure 2.52. The plots for the fly ash concrete and high performance concrete specimens are shown in Figure 2.53 and Figure 2.54. The two members with different strand types are compared in Figure 2.55. A plot for the epoxy-coated strand specimen with the calculated curve that takes into account the lower post-tensioning stress in this member is shown in Figure 2.56. The comparisons for the specimens with different grouting procedures and grout types are shown in Figure 2.57, and the plastic duct/encapsulated system member is shown in Figure 2.58.

The comparison of moment versus crack width for the 100% U PS sections is given in Figure 2.48. Crack width measurements were not as consistent between specimens for this series as they were for the Non-PS beams. Generally, the slope of the curve for the measured values was steeper than the calculated slope as shown in Figure 2.59 and Figure 2.61. The fly ash specimen reached its cracking moment at service load as seen in Figure 2.60.
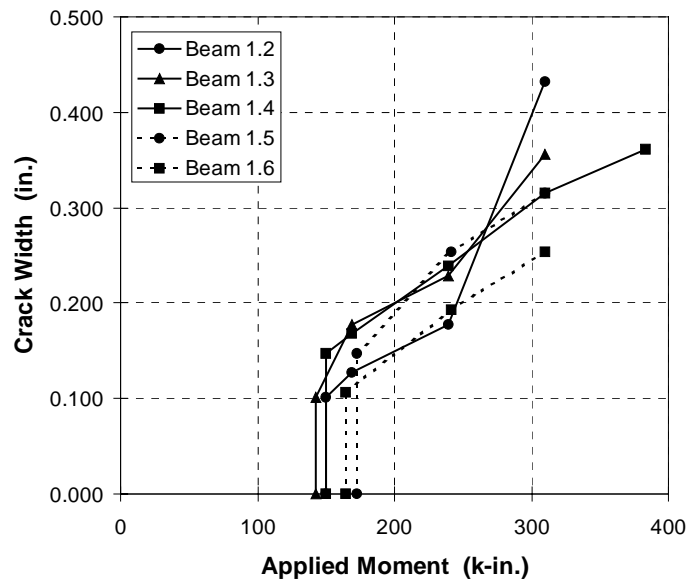
Figure 2.46 - Non-PS Sections – Measured Maximum Crack Widths
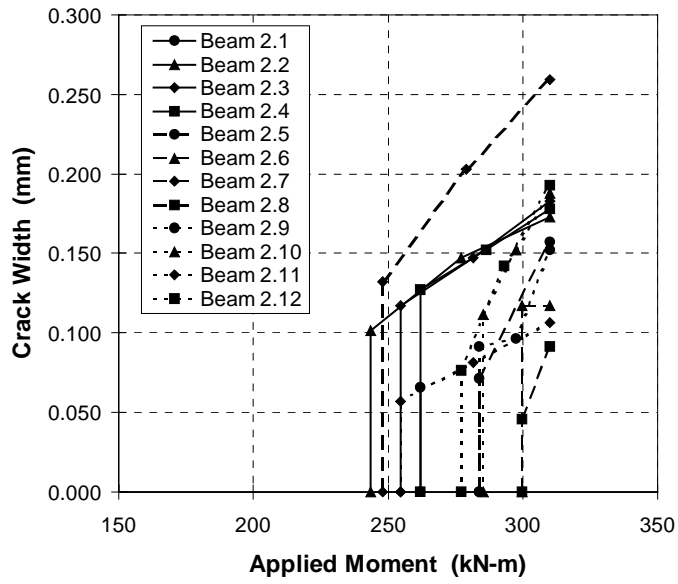
Figure 2.47 - 2/3 PS Sections – Measured Maximum Crack Widths
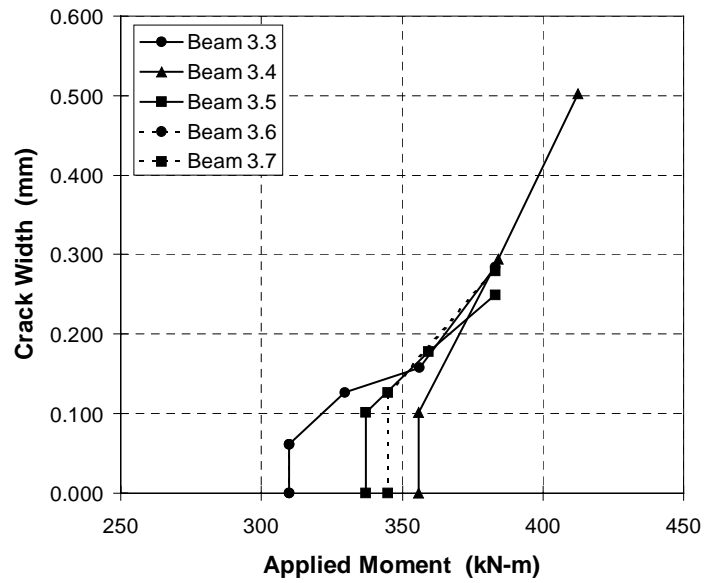
Figure 2.48 - 100% U PS Sections – Measured Maximum Crack Widths
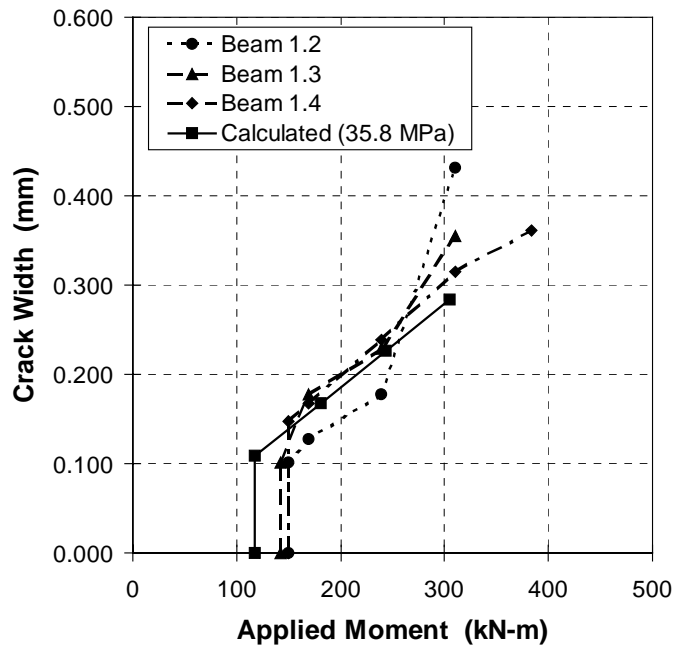
Figure 2.49 - TxDOT Standard Specimens (Non-PS) – Maximum Crack Widths
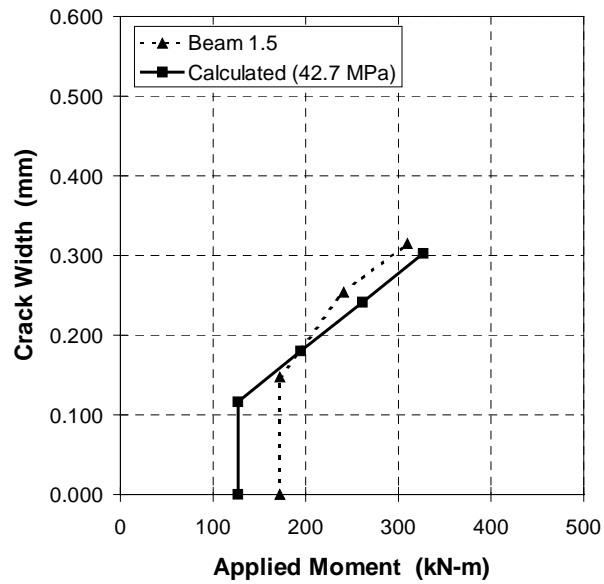
Figure 2.50 - Fly Ash Concrete Specimens (Non-PS) – Maximum Crack Widths
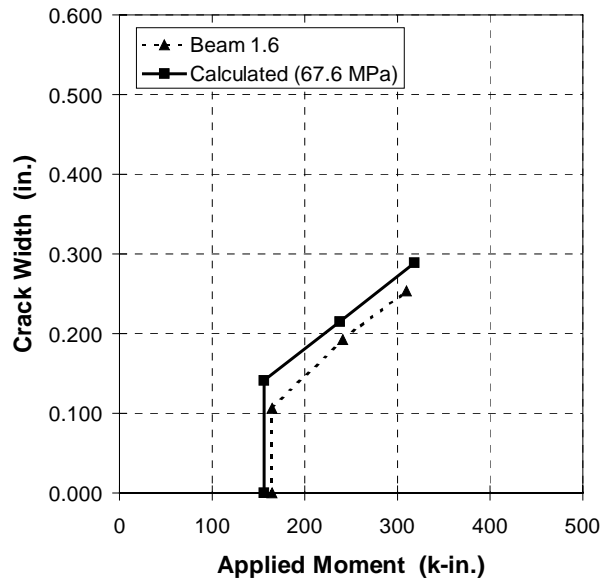
Figure 2.51 - High Performance Concrete Specimens (Non-PS) – Maximum Crack Widths
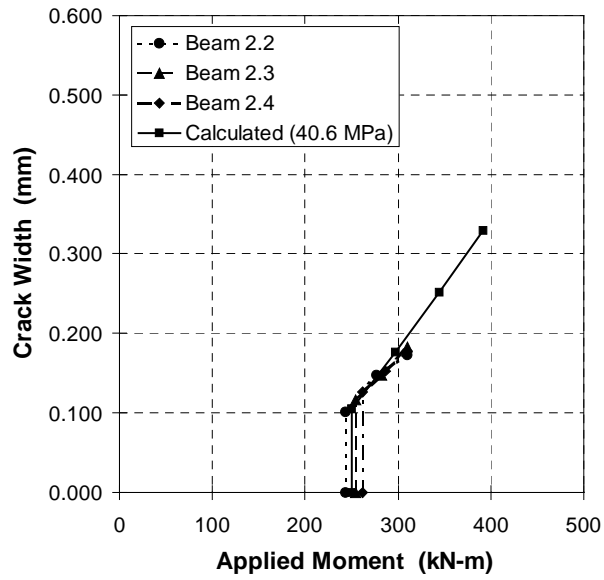
Figure 2.52 - TxDOT Standard Specimens (2/3 PS) – Maximum Crack Widths
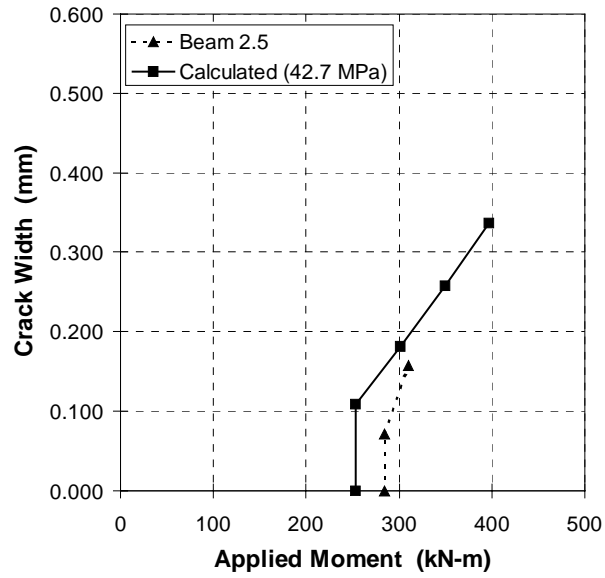
Figure 2.53 - Fly Ash Concrete Specimen (2/3 PS) – Maximum Crack Widths
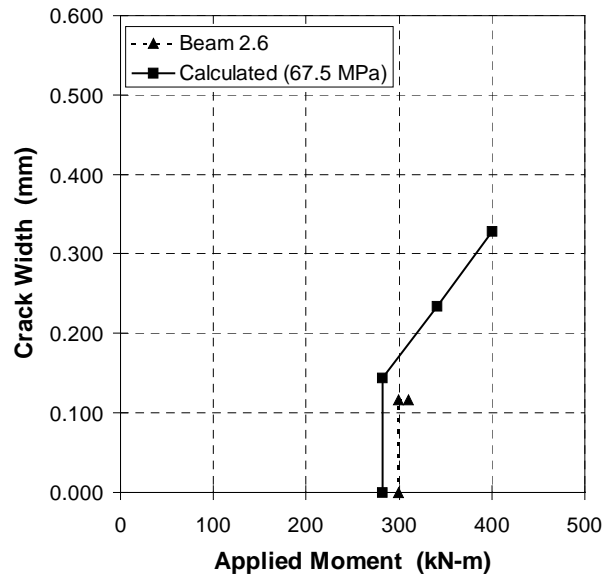
Figure 2.54 - High Performance Concrete Specimen (2/3 PS) –Maximum Crack Widths
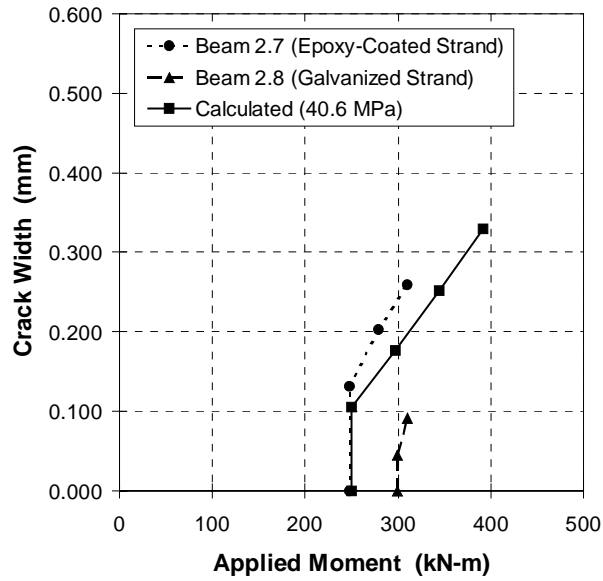
Figure 2.55 - Strand Variable Specimens (2/3 PS) – Maximum Crack Widths
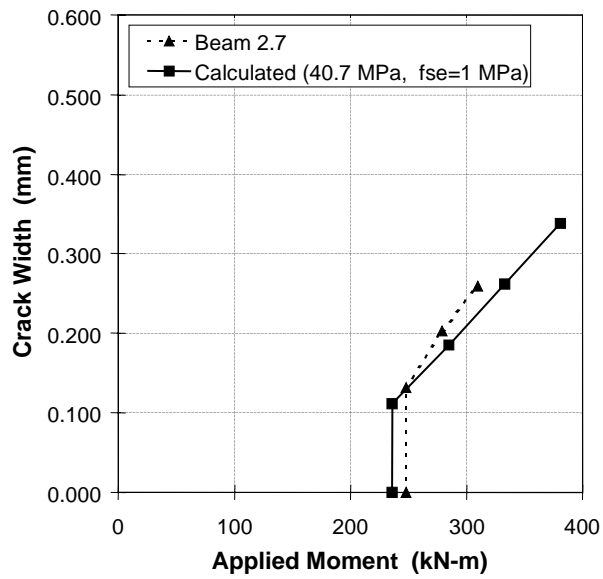
Figure 2.56 - Epoxy-Coated Strand Specimen (2/3 PS) – Maximum Crack Widths
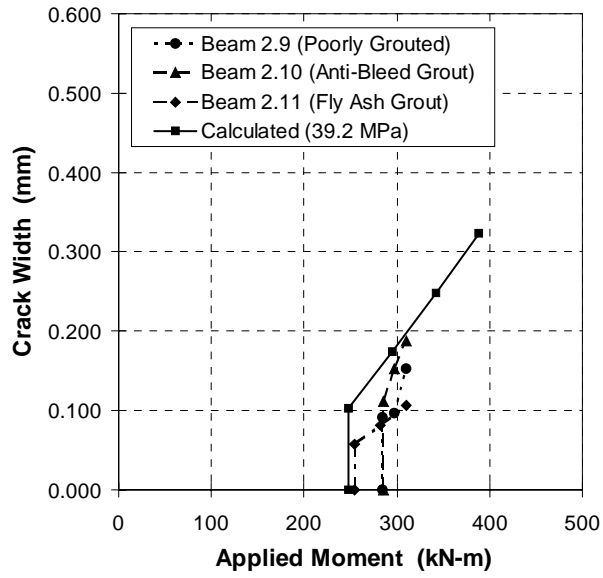
Figure 2.57 - Grout Variable Specimens (2/3 PS) – Maximum Crack Widths
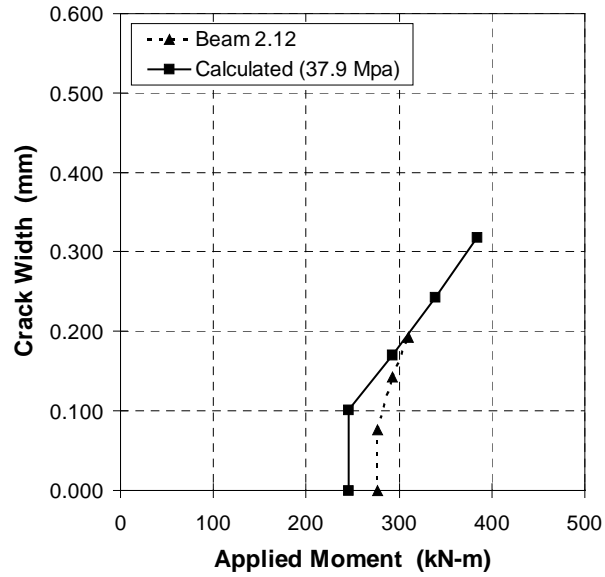
Figure 2.58 - Plastic Duct Specimen (2/3 PS) – Maximum Crack Widths
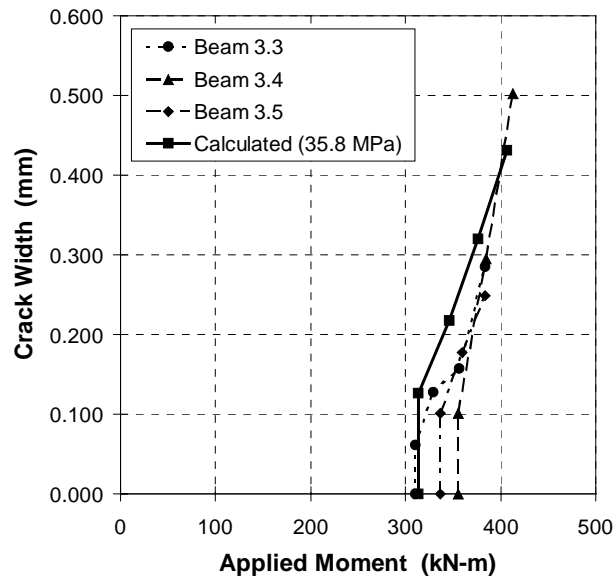
Figure 2.59 - TxDOT Standard Specimens (100% U PS) –
Maximum Crack Widths
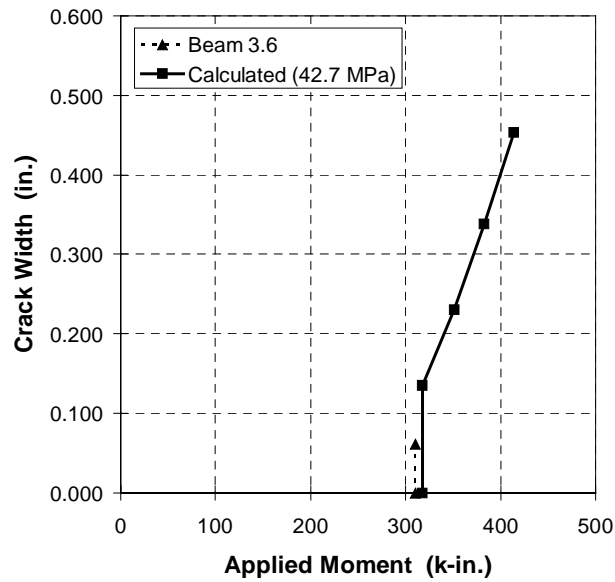
Figure 2.60 - Fly Ash Concrete Specimen (100% U PS) –
Maximum Crack Widths
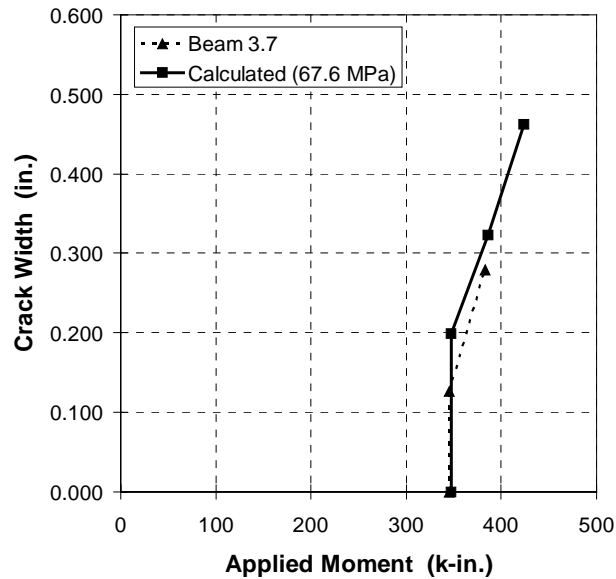
Figure 2.61 - High Performance Concrete Specimen (100% U PS) – Maximum Crack Widths

The crack data plotted in the preceding figures and the photos in Figure 2.45 clearly illustrate the effect of post-tensioning on cracking. The measured crack data show the following trends:

- The number of cracks and extent of cracking is drastically reduced as the level of prestress increases. The Non-PS beams show a large number of cracks well distributed over a large area extending well outside the third points of the beam. The 2/3 PS beams show reduced cracking, confined primarily to the maximum moment region in the middle one-third of the beam. The 100%U PS beams have only three cracks, one near midspan and one near each support location.

- The extent of cracking along the beam is well predicted by the cracking moments for the three beam types. Figure 2.62 shows the service load bending moment diagram with the computed cracking moments for the three section types that are cracked under service load.
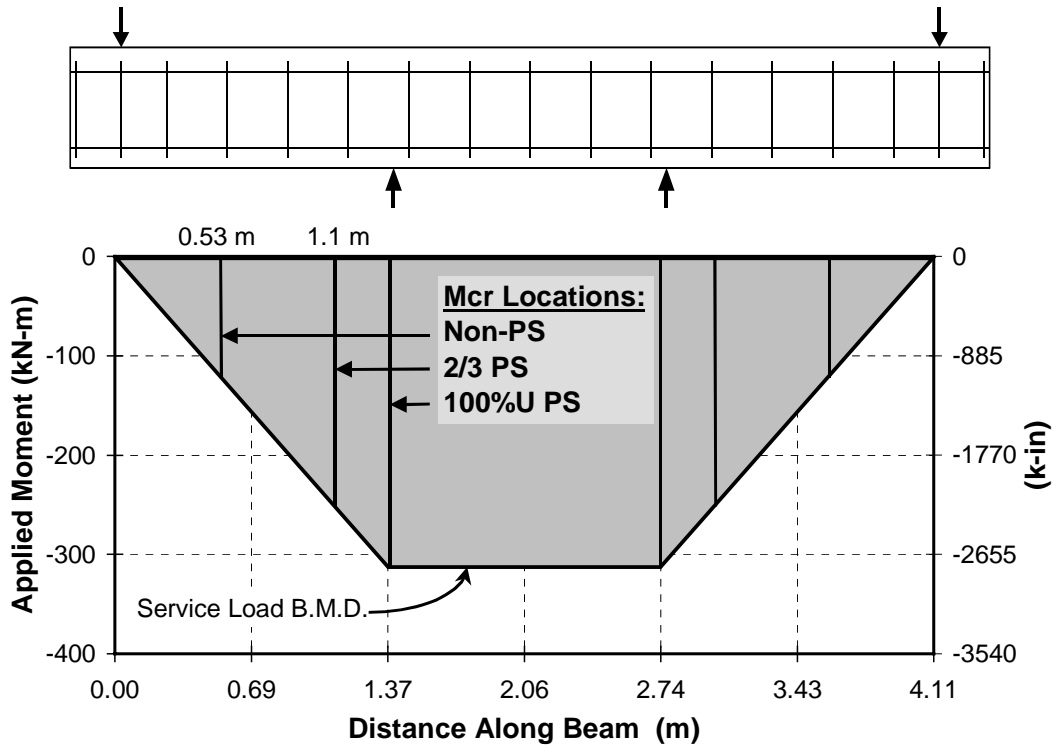
Figure 2.62 - Cracking Moment Locations along Beam Length

- Cracks commonly occurred at stirrup locations. In many cases, the first cracks to form were located at stirrups, and in general cracks located at stirrups had larger crack widths than adjacent cracks.

2.8   LONG-TERM MONITORING DATA AND RESULTS

Specimen condition and corrosion activity are regularly monitored by collecting four forms of data: half-cell potential readings, chloride penetration and corrosion rate measurements. Each is described below.

2.8.1   Half-Cell Potential Readings

Half-cell potential readings can provide two forms of information regarding the condition of the beam specimens:

- The magnitude of half-cell potential readings indicate the probability of corrosion at a given location.
- The time at which corrosion initiation occurred can be determined from regular potential readings taken during testing.

Half-cell potential readings require a reference electrode, voltmeter and electrical connection to the reinforcement. Common reference electrode types include copper-copper sulfate and saturated calomel. Saturated calomel electrodes (SCE) are used in this testing program. As mentioned in Section 2.6.4, ground clamps were used to attach a wire to the prestressing tendons before capping the anchorages. In addition, two ground wires were attached to the reinforcement for each beam before placing concrete. The entire system of the reinforcement cage, ducts and prestressing tendons was found to be electrically continuous, and half-cell potential measurements using any of the lead wires should produce the same results.

The numerical significance of the half-cell potential readings (saturated calomel electrode) is shown in Table 2.9. The values reported in Table 2.9 were developed for uncoated reinforcing steel in concrete are not necessarily appropriate for post-tensioned concrete. In general, half-cell potential readings are not an effective method for monitoring corrosion activity in bonded post-tensioned structures. In structures with galvanized steel ducts, the prestressing tendon will be in contact with the duct in most cases and half-cell potentials taken

on the prestressing tendon may reflect the potential of the zinc on the galvanized steel duct. Because the potential of the zinc will be more negative than that of the tendon, this difference in potential could lead to erroneous results and conclusions. However, due to the lack of other nondestructive methods for monitoring corrosion activity in post-tensioned concrete, it was decided to use regular half-cell potentials to monitor specimen condition. By considering both the magnitude and variation of the readings during testing it still may be possible to detect the onset of corrosion activity.

Table 2.9 - Interpretation of Half-Cell Potentials for Uncoated Reinforcing Steel

Measured Potential (vs SCE)	Probability of Corrosion
more positive than –130 mV	less than 10% probability of corrosion
Between -130 mV and –280 mV	corrosion activity uncertain
more negative than –280 mV	greater than 90% probability of corrosion

Half-cell potential readings are measured using a saturated calomel reference electrode at the end of each wet cycle (once every four weeks). The readings are taken along points on a grid that covers the central 1.8 m (6') of the length of the beam as shown in Figure 2.63. The spacing of the grid is 152 mm (6") in the long direction and the spacing along the width varies depending on the section type. Figure 2.64 indicates the location of the measurements taken for each section type along the width of the beam.
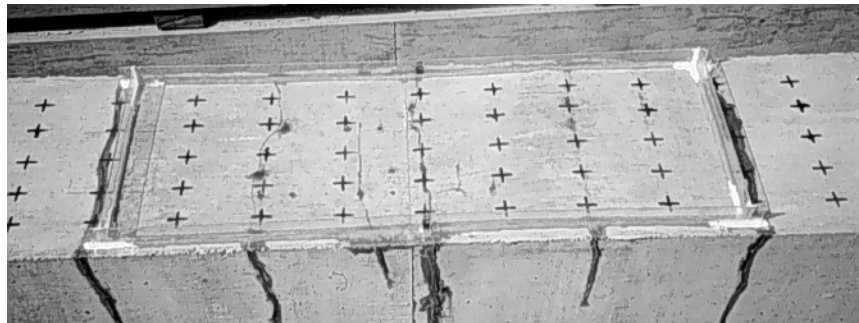
Figure 2.63 - Half-Cell Potential Readings Grid
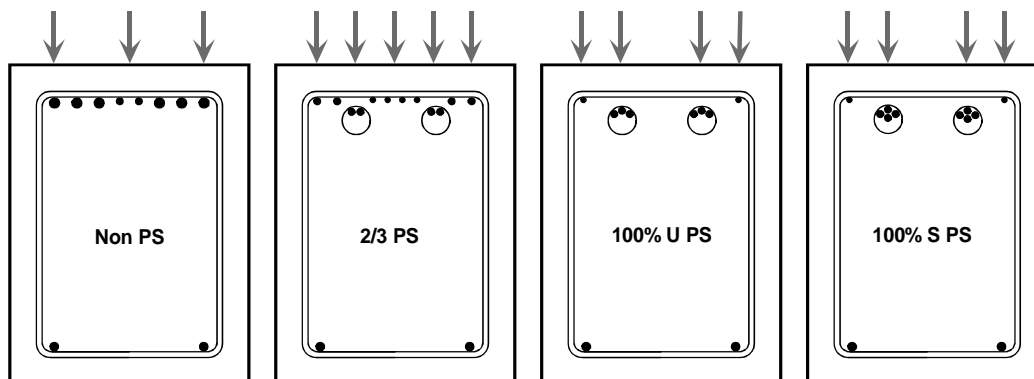
Figure 2.64 - Half-Cell Reading Locations

2.8.1.1   Phase I Specimens

Phase I specimens began exposure testing in December of 1997. Plots of potential readings through the end of April 1999 (498 days) are given in Figure 2.65-Figure 2.71. The potentials plotted are the high value for a given specimen on a given day. The average half-cell potentials from the ponded region and the high values follow the same trends. Additional plots that include average ponded values are given in Appendix A. ASTM 876, *Standard Test Method for Half-Cell Potentials of Uncoated Reinforcing Steel in Concrete*, gives a corrosion threshold of -280 mV$_{SCE}$ for a greater than 90% probability of corrosion and a threshold of -130 mV$_{SCE}$ for a less than 10% probability of corrosion. These values are included on the plots for reference, but past research has shown that half-cell potentials taken on submerged concrete are often higher than expected due to the restriction of oxygen, and therefore the trend of the values is more important than the actual values. Since all of the beams are undergoing the same type of exposure testing, the values can be compared among beams. Initiation of corrosion activity can also be indicated by a sudden increase in half-cell potentials.

Figure 2.65-Figure 2.68 show the effect of loading (cracking) on the half-cell potentials of beams of the same section and concrete type. The highest half-cell potential readings for each specimen are plotted. A comparison of half-cell potentials for the Non-PS sections is shown in Figure 2.65. Each of the three loaded specimens has significantly higher readings than the unloaded specimen as would be expected due to the extensive cracking in the loaded specimens. The readings for the 2/3 PS sections shown in Figure 2.66 are very close in value, with the lowest values from the specimen with the smallest crack widths. The half-cell potentials for the 100% U PS sections are relatively low as shown in Figure 2.67. The uncracked sections have the lowest readings, although the difference between the cracked and uncracked specimens is small. The two 100% S PS sections also have low half-cell potential readings as seen in Figure 2.68.

Figure 2.69-Figure 2.71 show the effect of post-tensioning by comparing different section types with the same loading. The unloaded section potential readings shown in Figure 2.69 are both low, with slightly lower values for the prestressed section. Figure 2.70 shows half-cell potential readings for the service loaded specimens. The Non-PS and 2/3 PS sections are grouped together with higher potential readings, while the 100% U PS and 100% S PS sections are grouped together with lower readings. It is interesting that the readings are so similar for both the 100% U PS and 100% S PS sections. The 100% S PS section has 33% more prestressing steel than the 100% U PS section, but the benefit for corrosion protection from the additional prestressing appears to be minimal above the level of 100% prestressing for ultimate strength. A comparison of overload specimens is shown in Figure 2.71. The highest half-cell potential readings are for the specimens with the least amount of prestressing and the lowest readings are from the 100% U PS sections. Table 2.10 gives a summary of the half-cell potential readings for each Phase I specimen.
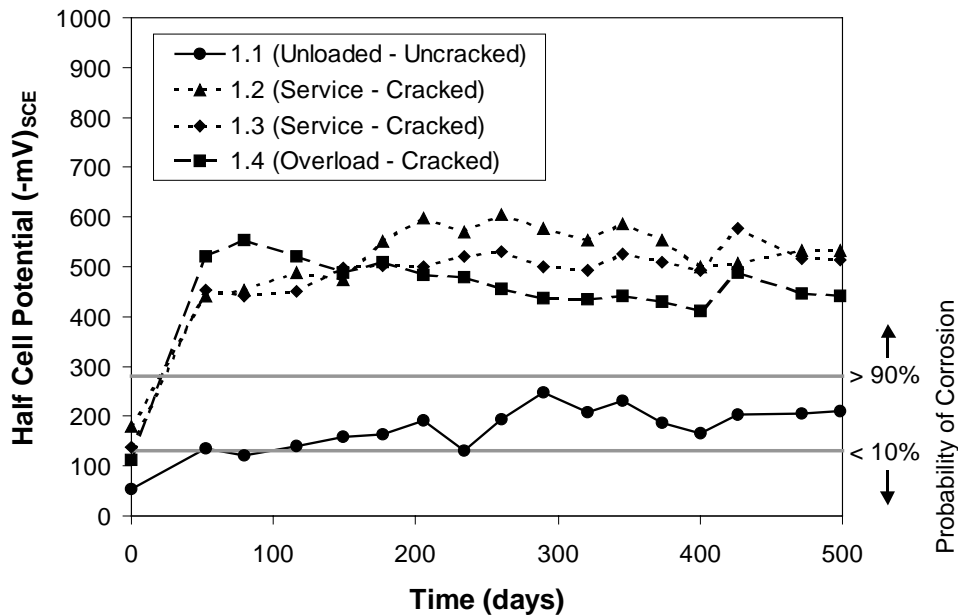
Figure 2.65 - Half-Cell Potential Readings – Non-PS Sections
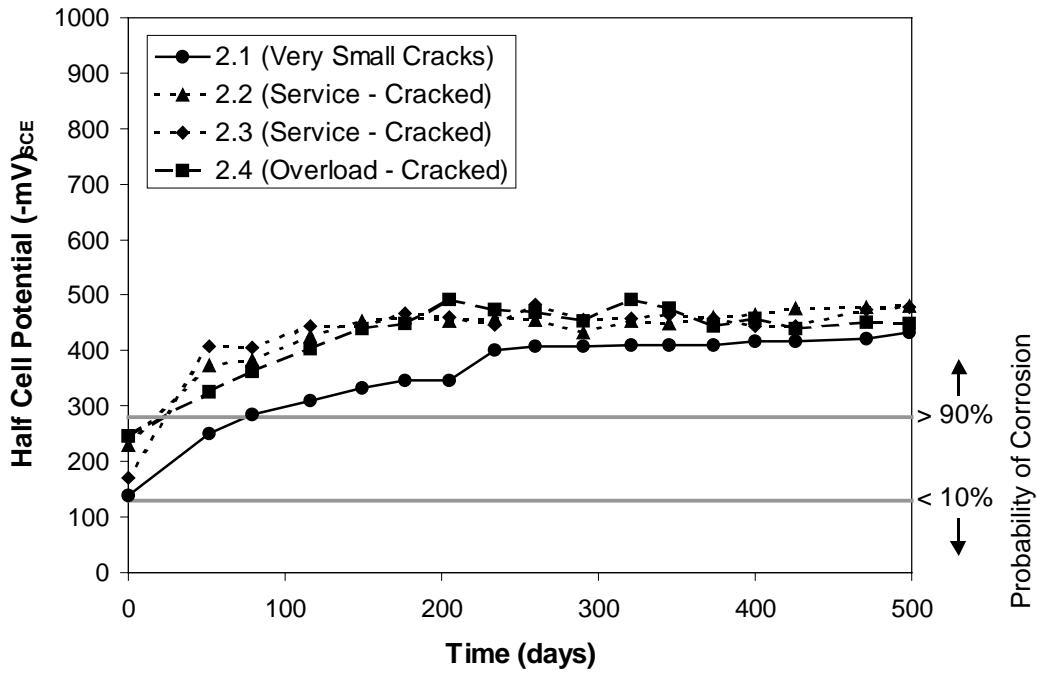
Figure 2.66 - Half-Cell Potential Readings – 2/3 PS Sections
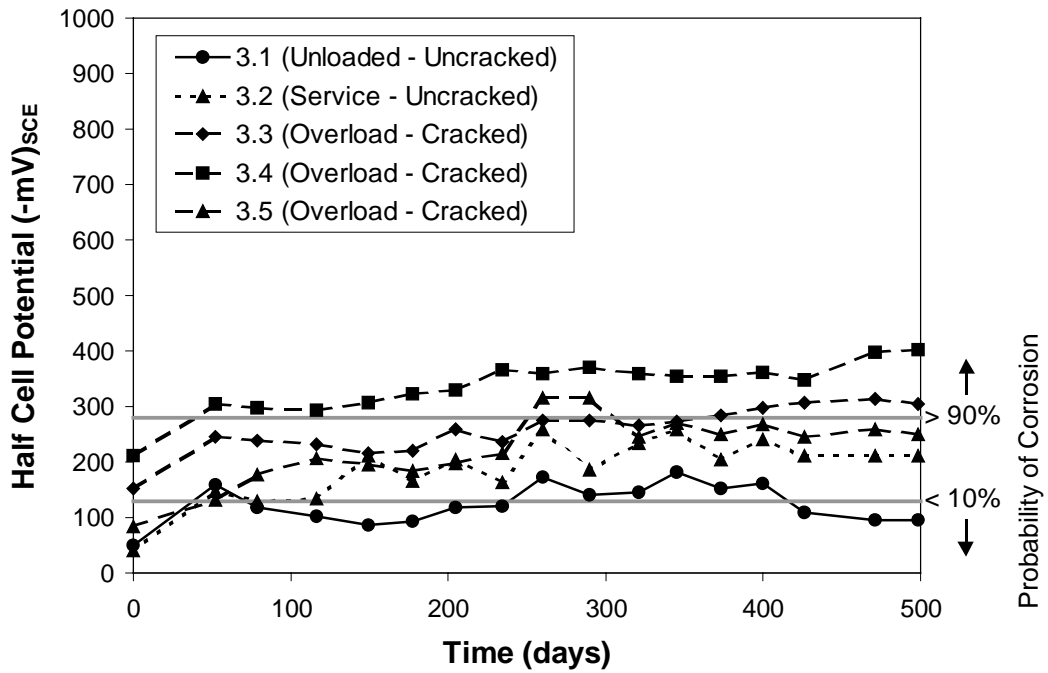
Figure 2.67 - Half-Cell Potential Readings – 100% U PS Sections
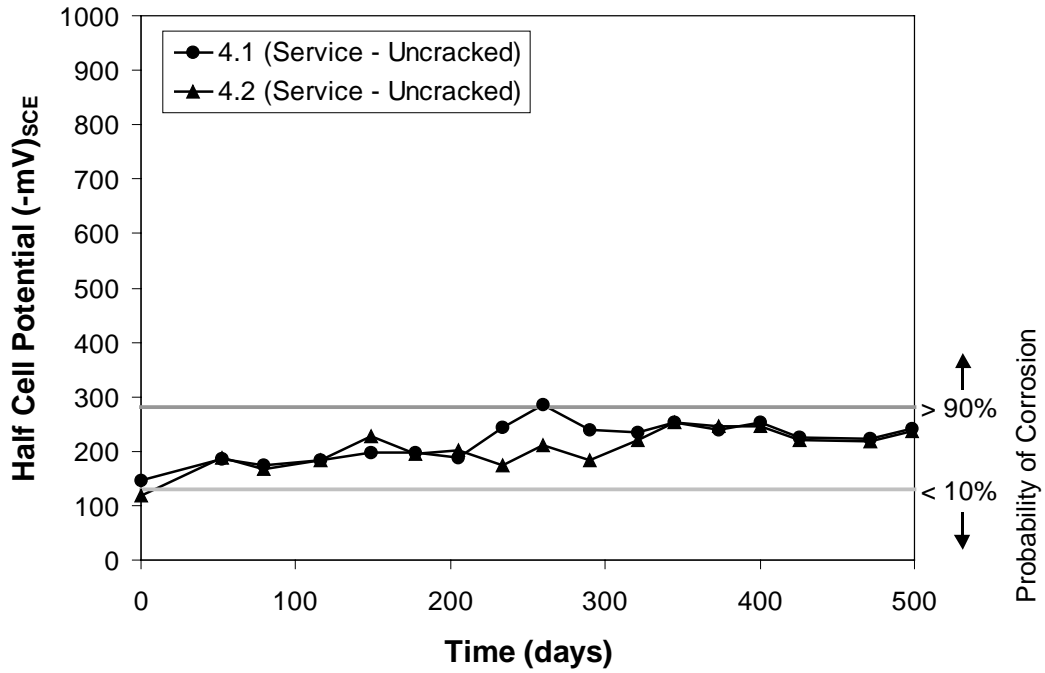
Figure 2.68 - Half-Cell Potential Readings – 100% S PS Sections
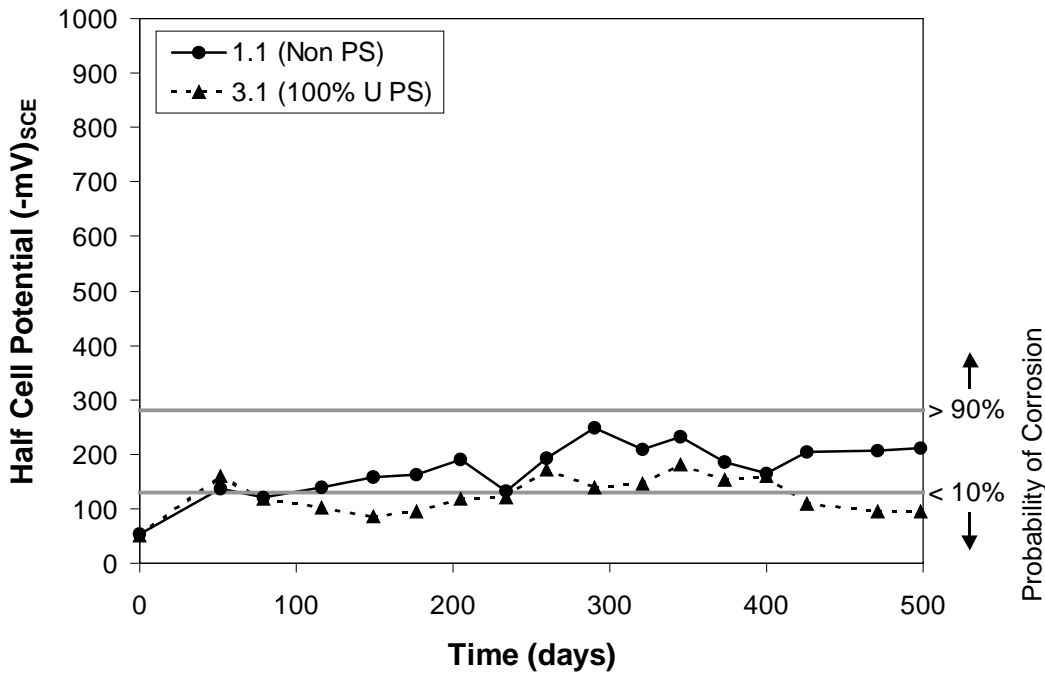
Figure 2.69 - Half-Cell Potential Readings – Unloaded Specimens
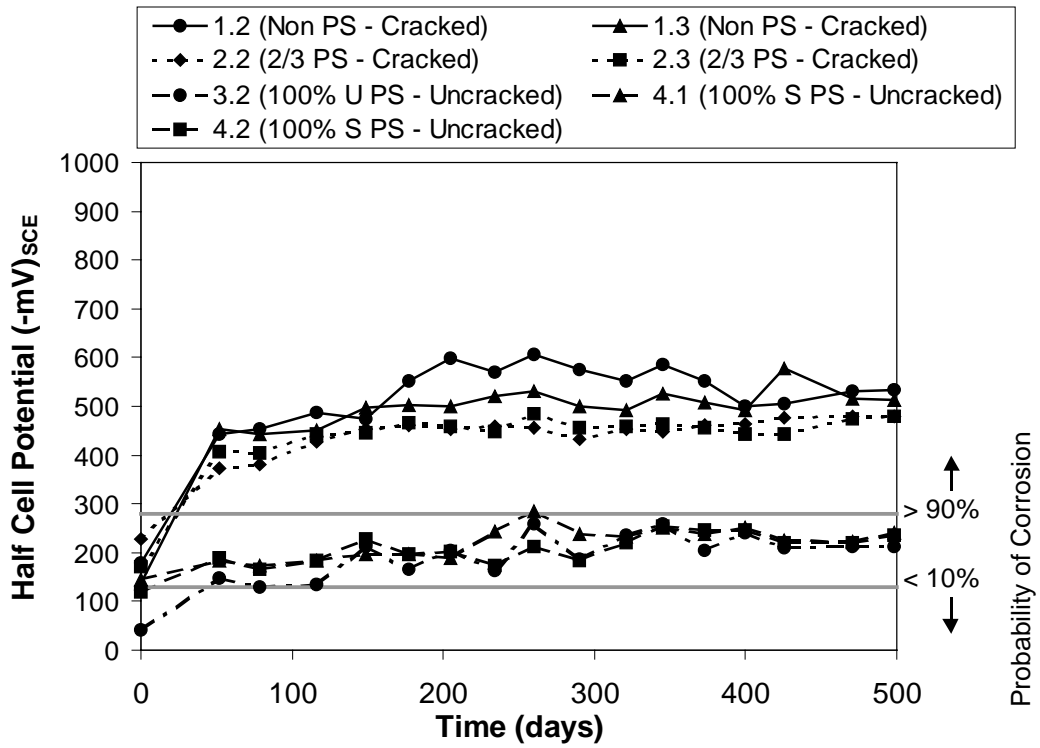
Figure 2.70 - Half-Cell Potential Readings – Service Load Specimens
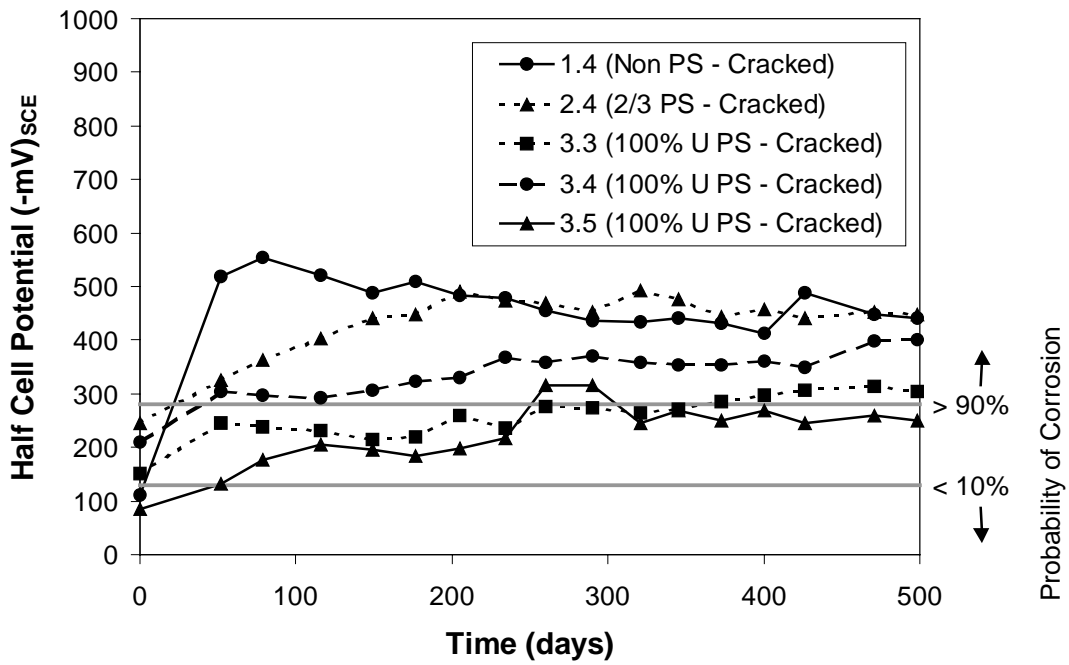
Figure 2.71 - Half-Cell Potential Readings – Overload Specimens

Table 2.10 - Phase I Beam Half-Cell Readings Summary
(Highest HC Potential Readings)

Specimen	Main Variable	Probability of Corrosion*
Non-PS		
1.1	unloaded	uncertain
1.2	constant service load	high
1.3	constant service load	high
1.4	overload	high
2/3 PS		
2.1	very small cracks	high
2.2	constant service load	high
2.3	constant service load	high
2.4	overload	high
2.11	fly ash grout (service load)	high
100% U PS		
3.1	unloaded	low
3.2	constant service load	uncertain
3.3	overload (124% service)	high
3.4	overload (133% service)	high
3.5	overload (124% service)	uncertain
100% S PS		
4.1	constant service load	uncertain
4.2	constant service load	uncertain

* Refers to ASTM C876

An interesting comparison can also be made of the value and distribution of potential readings across the surface of the beam for different amounts of post-tensioning. Figure 2.72 shows readings at 498 days as a contour plot over the grid area. The dashed box superimposed on the contour plot represents the area of saltwater ponding. Blue areas indicate a low probability of corrosion (by ASTM), yellow areas are uncertain (possible corrosion), and orange areas indicate a high probability of corrosion. The red areas indicate extremely high half-cell potentials. The "1 series" beams (labeled 1.x) are the Non-PS beams, the "2 series" beams are the 2/3 PS beams, the "3 series" beams are the 100% U PS beams, and the "4 series" beams are the 100% S PS beams. The effect of prestress level and cracking is evident from this figure. A service load specimen from each section type is singled out in Figure 2.73 to show the effect of the level of prestressing. As discussed in the previous section, the Non-PS and 2/3 PS beams have very high probability of corrosion, while the 100% U PS and 100% S PS sections have uncertain to low probabilities of corrosion. The difference between the 2/3 PS section (4 prestressing strands) and the 100% U PS section (6 strands) is significant. However, at this point in exposure testing there is little difference between the 100% U PS section (6 strands) and the 100% S PS section (8 strands). These preliminary results may indicate that the benefit to cost ratio favors the 100% U PS section rather than the more costly 100% S PS section. The 100% U specimen shown in Figure 2.73 is uncracked, but readings are similar or only slightly higher for the 100% U specimens that were cracked with an overload (shown in Figure 2.72). The advantage of an uncracked specimen (100% S) at service load may become more apparent as the exposure testing continues.

Certain Phase I specimens (2.1, 2.4, 2.11, 3.2, 3.3, 3.4, 3.5) had the saltwater ponds divided into two sections due to unevenness in the top surface. This division caused a slight discrepancy in half-cell potential values between the two sides of the pond for some specimens as evident in Figure 2.72 for Specimens 2.11 and 3.3 where the values fell on different sides of the corrosion probability lines.

1.1 - Unloaded (uncracked)

2.11 - Service (cracked)

1.2 - Service (cracked)

3.1 - Unloaded (uncracked)

1.3 - Service (cracked)

3.2 - Service (uncracked)

1.4 - Overload (cracked)

3.3 - Overload (cracked)

2.1 - Very Small Cracks

3.4 - Overload (cracked)

2.2 - Service (cracked)

3.5 - Overload (cracked)

2.3 - Service (cracked)

4.1 - Service (uncracked)

2.4 - Overload (cracked)

4.2 - Service (uncracked)

■ -430 to -580 V_{SCE}

■ -280 to -430 V_{SCE}

□ -130 to -280 V_{SCE}

■ +20 to -130 V_{SCE}

Figure 2.72 - Contour Plots of Half-Cell Potential Readings at 498 Days

1.2 - Service (cracked)

2.2 - Service (cracked)

3.2 - Service (uncracked)

4.2 - Service (uncracked)

- ■ -430 to -580 V_{SCE}
- ▨ -280 to -430 V_{SCE}
- □ -130 to -280 V_{SCE}
- ▨ +20 to -130 V_{SCE}
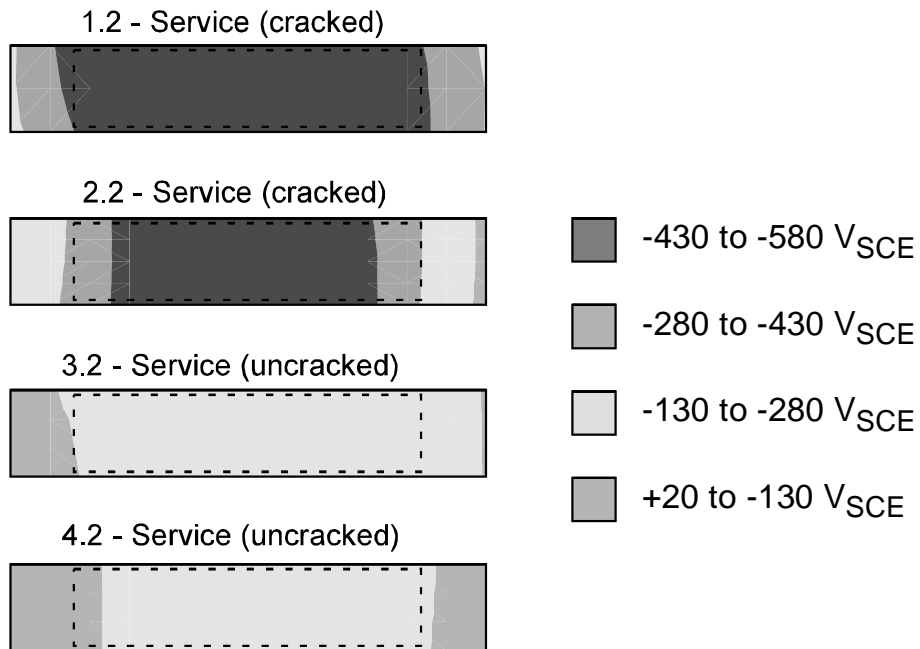
Figure 2.73 - Half-Cell Potentials – Prestress Level
Comparison at Service Load

2.8.1.2 Phase II Specimens

Phase II specimens began exposure testing in December of 1998. Figure 2.74-Figure 2.80 give the half-cell potential data through April of 1999 (139 days). Additional plots of half-cell potentials for each specimen are given in Appendix B. Table 2.11 gives a summary of the half-cell potential readings for each Phase I specimen.

Although it is too early in the exposure testing to make many conclusions from the half-cell data, some general trends are taking shape. Figure 2.74-Figure 2.76 give comparisons between specimens for a given level of prestressing. The 1 series beams (Non-PS) and the 2 series beams (2/3 PS) are generally showing half-cell potentials in the high range, except for the high performance concrete specimen that has readings in the medium range. The 3 series beams are showing the opposite behavior. These differing indications are likely due to the difference in the number of cracks in these two specimens. The fly ash specimen was loaded to service load and held at this load level. At service load, the fly ash specimen had two cracks. The high performance concrete specimen showed no cracks at service load, so the specimen was overloaded to produce cracks. In this case, three cracks were produced, and the specimen was then returned to service load.

Figure 2.77-Figure 2.80 separate the half-cell readings by post-tensioning protection variables. The specimens containing fly ash concrete are showing lower half-cell potentials with increasing levels of post-tensioning. The specimens containing the high performance concrete are not showing lowered half-cell potentials with increased post-tensioning. This difference is likely due, once again, to the overloading of Specimen 3.7 that caused larger crack widths in this specimen than in Specimens 1.6 and 2.6. Figure 2.79 shows a comparison of the specimens with different grout types. The fly ash grout specimen from Phase I is included in the figure for comparison. At this point, the specimen with the antibleed grout and the specimen with the fly ash grout are showing slightly better corrosion performance than the poorly grouted specimen. The specimens with different strand and duct types are shown in Figure 2.80. All three of the specimens are showing high half-cell potential values. Coated steel and steel within a plastic duct may give inaccurate readings, so these values may not be indicating corrosion.
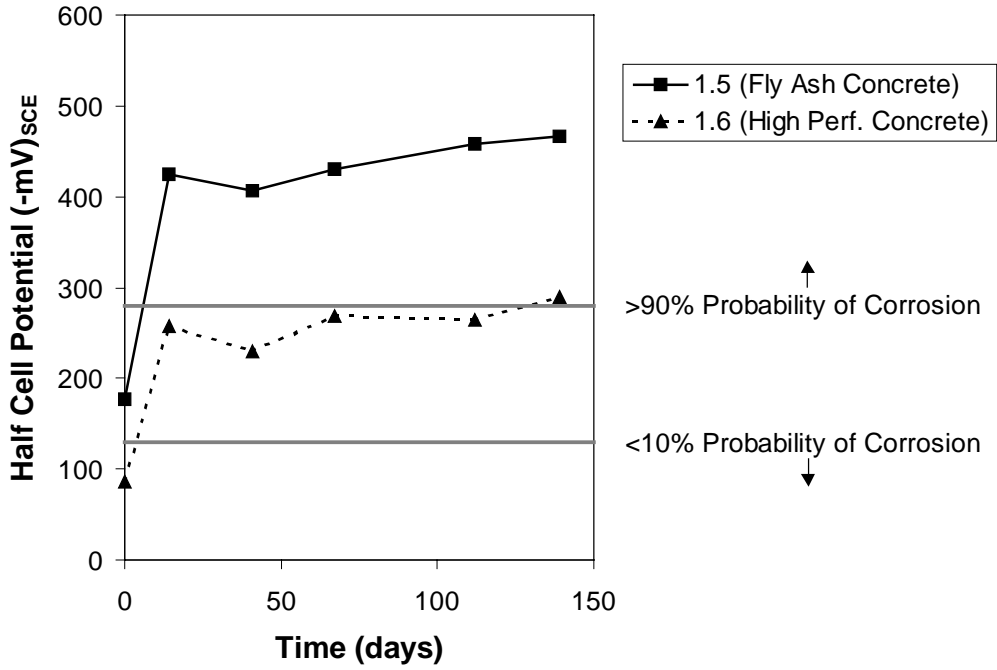
Figure 2.74 - Half-Cell Potential Readings – Non-PS Sections
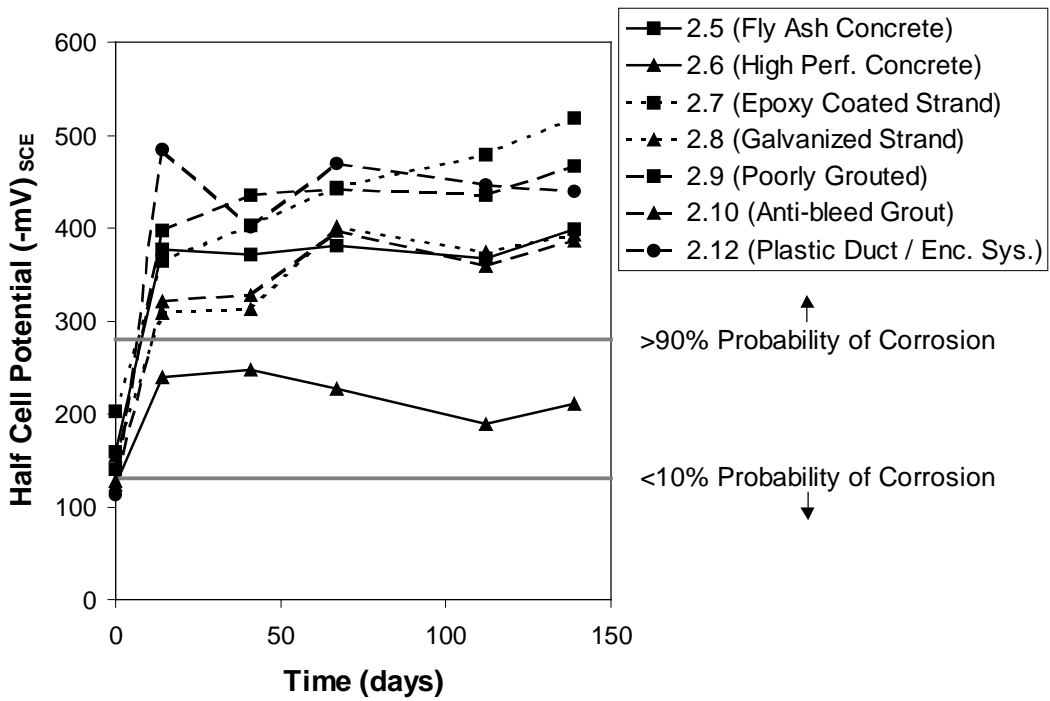
Figure 2.75 - Half-Cell Potential Readings – 2/3 PS Sections
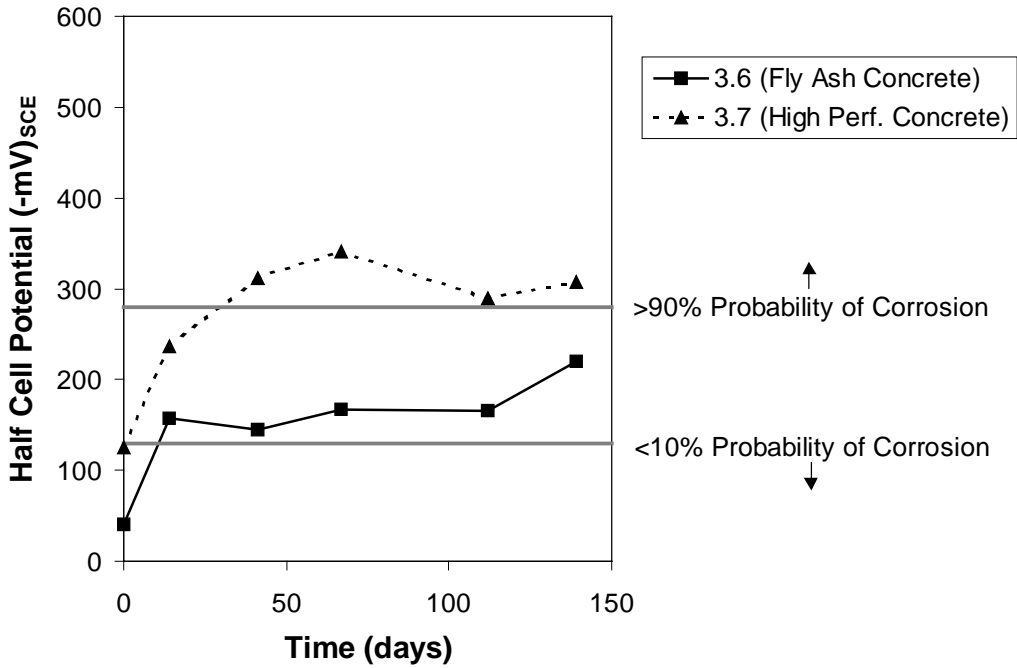
Figure 2.76 - Half-Cell Potential Readings – 100% U PS Sections
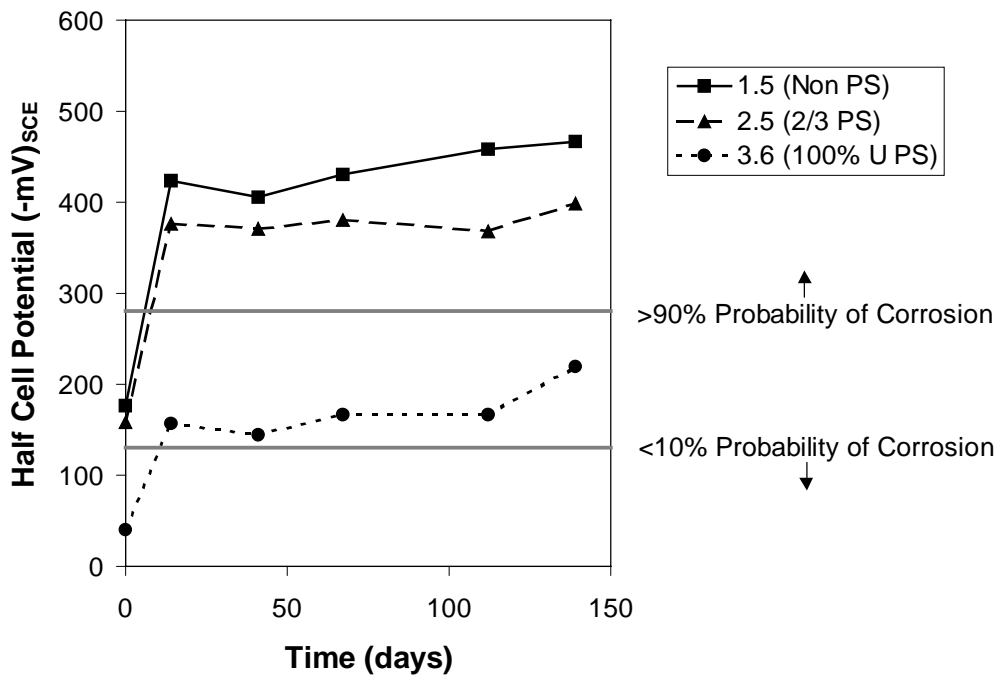
Figure 2.77 - Half-Cell Potential Readings – Fly Ash Concrete

68
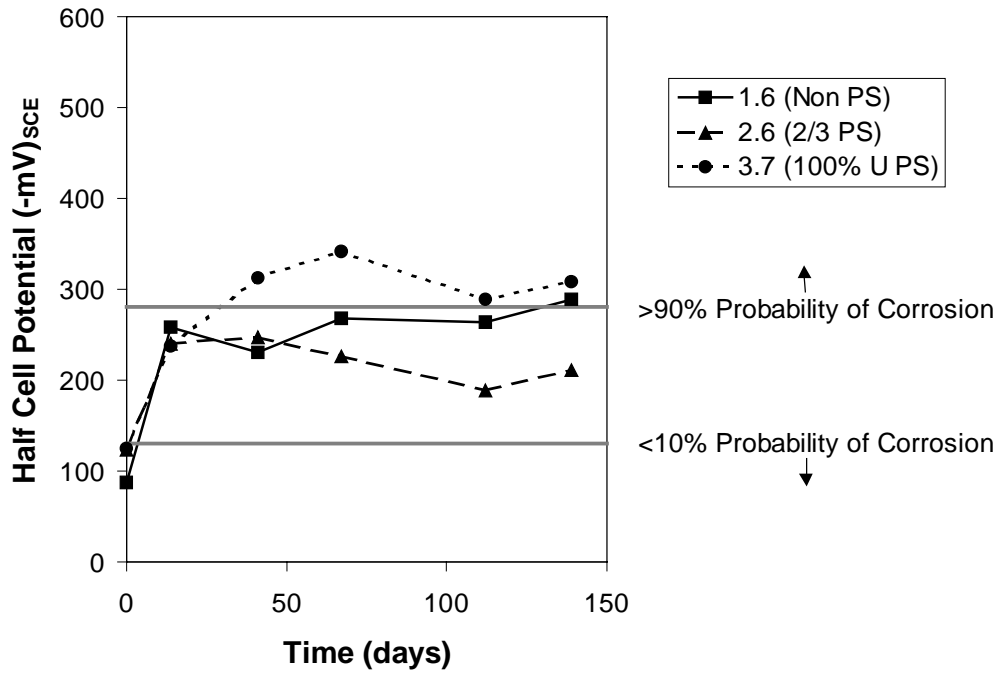
Figure 2.78 - Half-Cell Potential Readings – High Performance Concrete
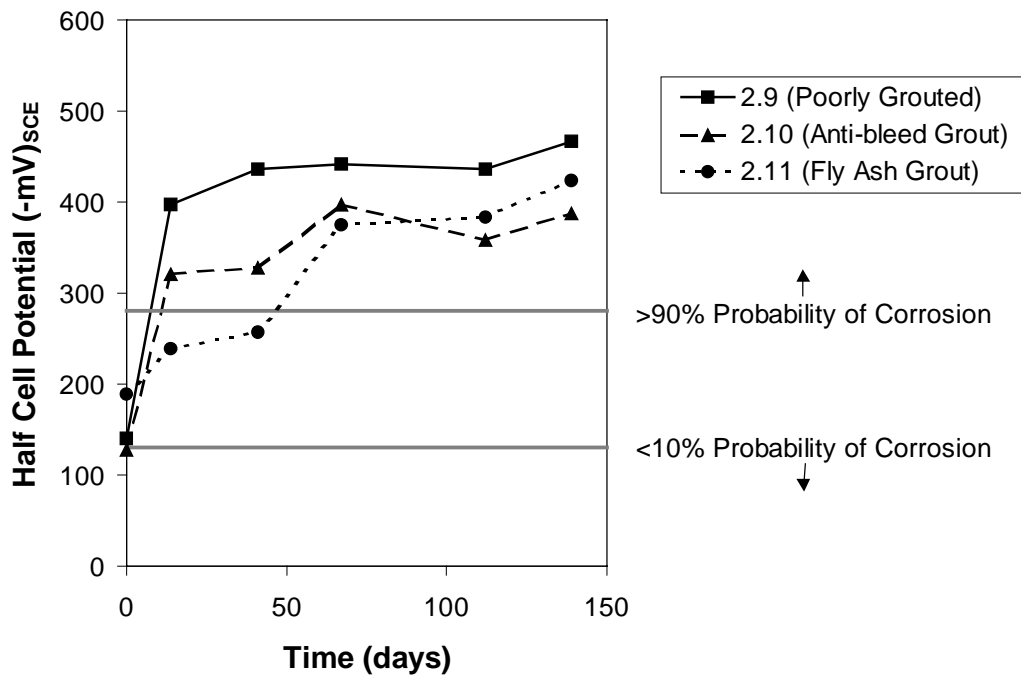
Figure 2.79 - Half-Cell Potential Readings – Grout Types
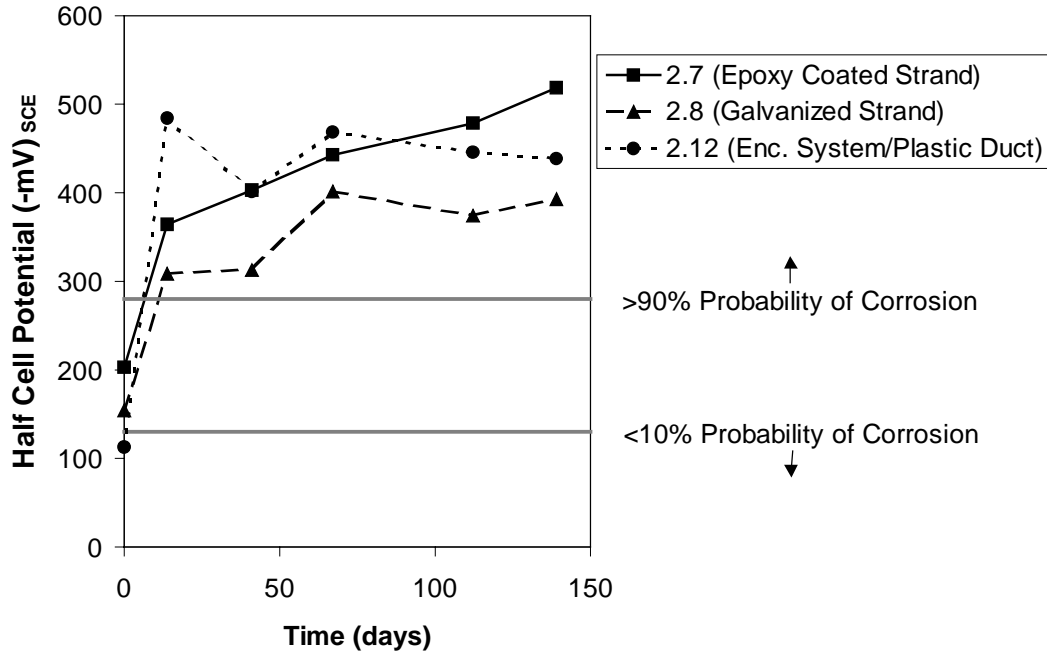
Figure 2.80 - Half-Cell Potential Readings – Strand and Duct Types

Table 2.11 - Phase II Beam Half-Cell Readings Summary
(Highest HC Potential Readings)

Specimen	*Main Variable*	*Probability of Corrosion**
Non-PS		
1.5	fly ash concrete	high
1.6	high performance concrete	uncertain
2/3 PS		
2.5	fly ash concrete	high
2.6	high performance concrete	uncertain
2.7	epoxy-coated strand	high
2.8	galvanized strand	high
2.9	poorly grouted	high
2.10	antibleed grout	high
2.12	plastic duct / encapsulated system	high
100% U PS		
3.6	fly ash concrete	uncertain
3.7	high performance concrete	high

* Refers to ASTM C876

The contour plots of the half-cell potentials at 139 days are shown in Figure 2.81. The figure illustrates the distribution of the half-cell potential readings across the top surface of the beam in and around the ponded region. Two of the high performance concrete specimens are showing the lowest readings. The validity of the high readings recorded from the epoxy-coated strand specimen and the plastic duct specimen will be investigated during autopsy.

70

1.5 - Fly Ash Concrete

2.9 - Poor Grouting Procedures

1.6 - High Performance Concrete

2.10 - Anti-Bleed Grout

2.5 - Fly Ash Concrete

2.12 - Encapsulated System / Plastic Duct

2.6 - High Performance Concrete

3.6 - Fly Ash Concrete

2.7 - Epoxy Coated Strand

3.7 - High Performance Concrete

2.8 - Galvanized Strand

-430 to -580 V_{SCE}

-280 to -430 V_{SCE}

-130 to -280 V_{SCE}

+20 to -130 V_{SCE}
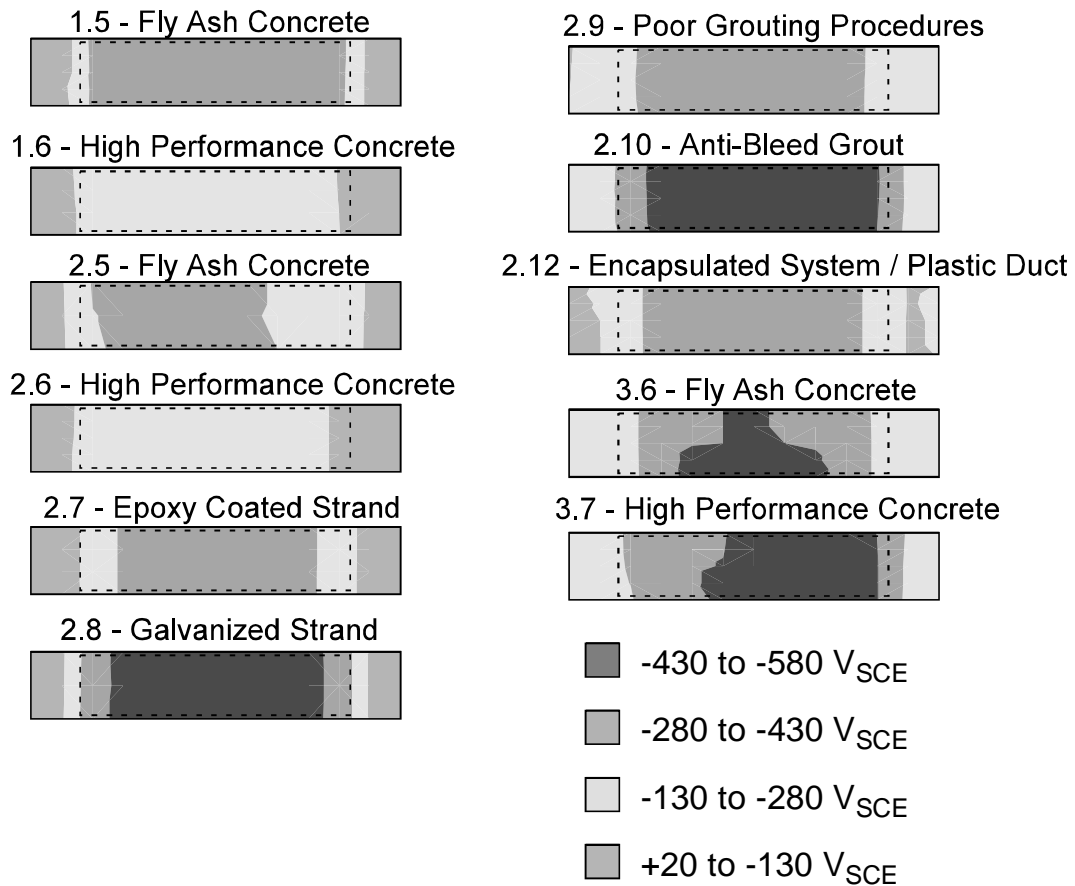
Figure 2.81 - Contour Plot of Half-Cell Potential Readings at 139 Days

2.8.2   Chloride Penetration

Two ponding blocks were cast with each set of beam specimens. The ponding blocks have a top surface of 300 by 300 mm and a depth of 150 mm. One of the ponding blocks for each set is a control and remains outside with the beam specimens but does not undergo saltwater ponding. The other ponding block undergoes the same cycle of saltwater ponding as the beam specimens. Figure 2.82 shows several of the ponding blocks and control blocks. At approximately 7-month intervals, chloride samples are taken from the ponding blocks to monitor the ingress of chlorides in each batch of concrete.   Samples of the control blocks are taken at 14-month intervals for comparison. After chloride sampling, the drill holes were filled with epoxy.

Powder samples were taken for three depths: 13 mm (7-19 mm drilled sample), 25 mm (19-32 mm drilled sample), and 50 mm (45-57 mm drilled sample). The 50 mm (2") depth data represent the chloride concentration at the bar level. Each sample is taken from two locations and the powder is combined to give a representative sample. From a representative sample, several acid-soluble chloride tests are run and the results are averaged.
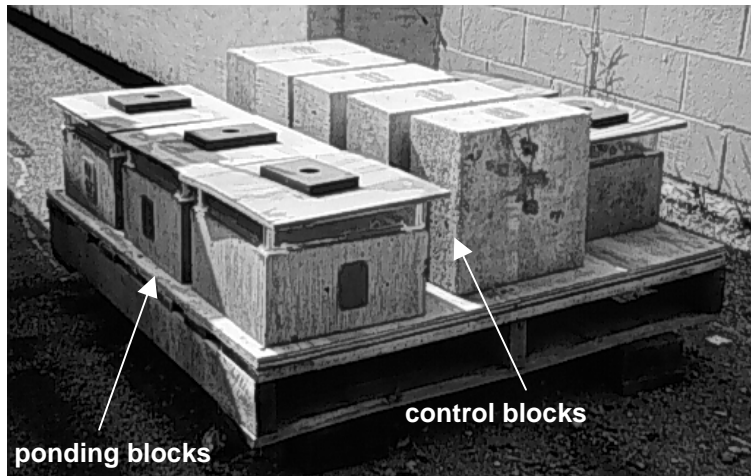
Figure 2.82 - Ponding and Control Blocks

Phase I ponding blocks have had two sets of chloride samples taken to date: July 1998 (7 months) and February 1999 (14 months). Phase II ponding blocks will have chloride samples taken in August of 1999.

Figure 2.83 shows the chloride data at 7 months for the Phase I specimens. All specimens were cast with TxDOT Class C concrete and the chloride threshold level for corrosion initiation for this type of concrete is shown in the figure. Corrosion thresholds depend on many variables besides chloride levels, and these threshold values are shown for illustration only. At the 13 mm (0.5") depth, the majority of specimens had chloride levels above the threshold value. At the 25 mm (1") depth, most specimens had negligible chloride contents and all specimens had chloride contents below the threshold level. At the 50 mm (2") depth, all specimens had negligible chlorides. The values at this depth represent the penetration of chlorides at bar level in uncracked concrete. The uncracked control specimens showed no chlorides at all depths.

Figure 2.84 shows the chloride data at 14 months for the Phase I specimens. The majority of the values are higher than at 7 months as would be expected. However, some of the samples are slightly lower which is likely due to the variance in collection locations. Samples must be drilled from new locations for each test. Although powder from two locations is mixed for each set of samples, and drilling for later samples is near the original locations, some variation is expected. At 14 months, all ponded blocks showed some level of chlorides at the 13 mm depth. At the 25 mm depth, most specimens had negligible chloride contents. At bar level (50 mm), all specimens continued to have negligible chloride contents. These data indicate that chloride penetration in uncracked concrete has yet to reach the level of the reinforcement in the beam specimens and that the main route of chloride ingress in the specimens at this time is through cracks. Samples from the control blocks are taken only once every 14 months as a comparison, so samples were not taken for this cycle.

Acid Soluble Chloride Content
(% by weight of concrete)
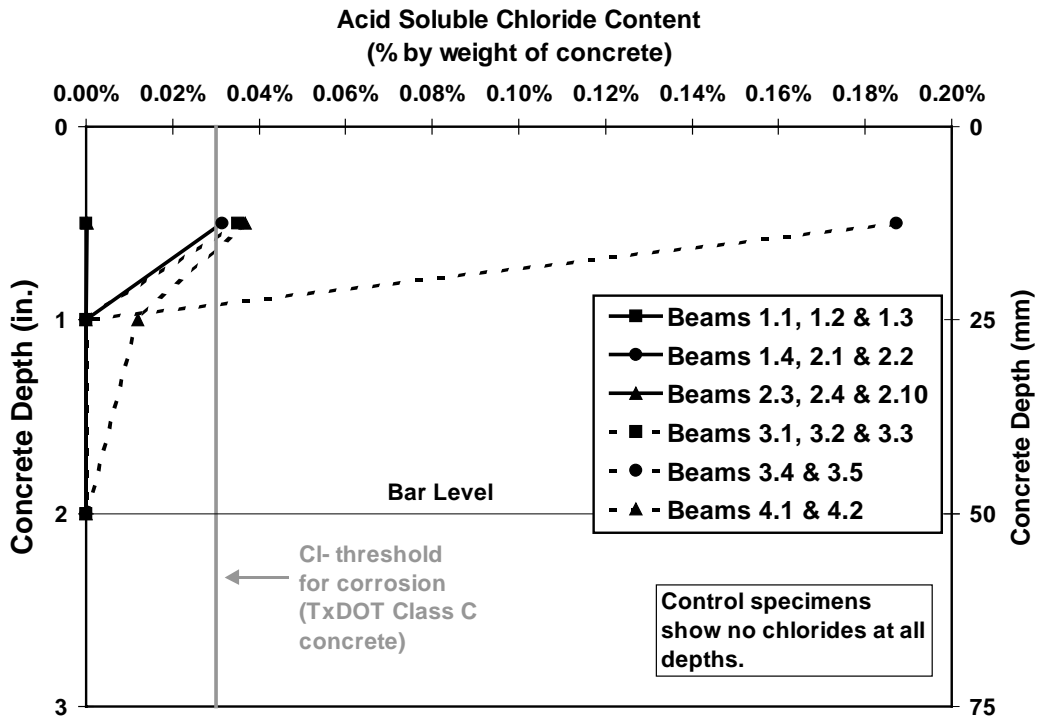
Figure 2.83 - Chloride Penetration at 7 Months, Phase I Beam Specimens

Acid Soluble Chloride Content
(% by weight of concrete)
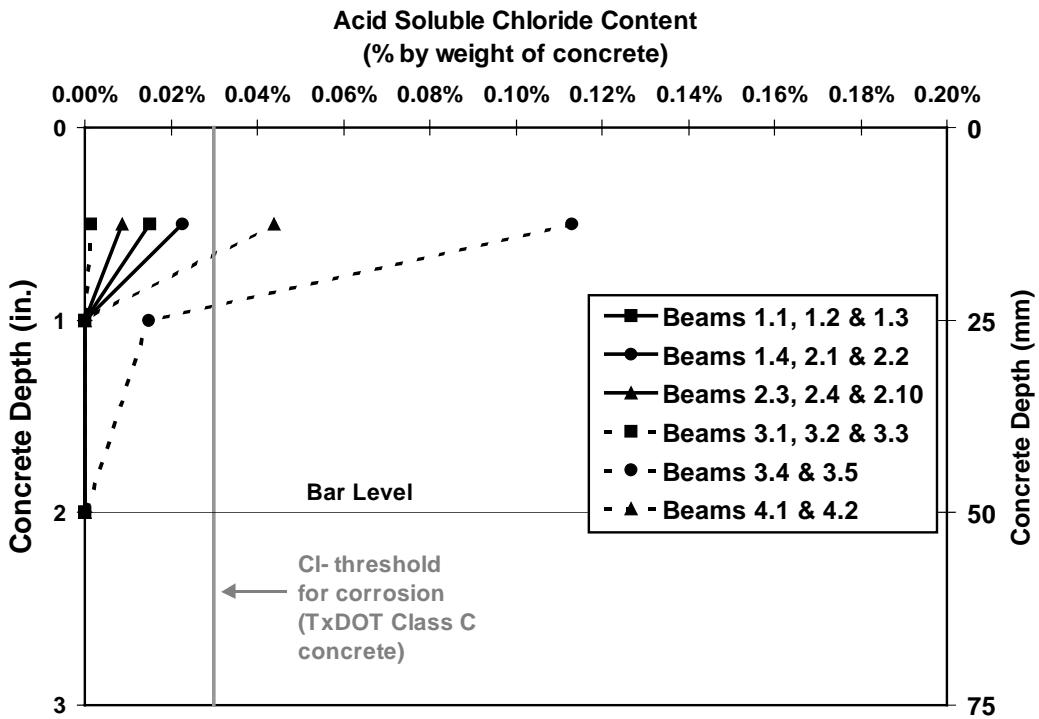
Figure 2.84 - Chloride Penetration at 14 Months, Phase I Beam Specimens

2.8.3   Corrosion Rate Measurement

Polarization resistance is a useful technique for measuring instantaneous corrosion rates under laboratory and field conditions. Polarization measurements are rapid, highly sensitive, nondestructive and can be performed repeatedly. The theory behind this technique is detailed in many references. The theory states that within a small range of overvoltage (+/- 10 to 15 mV from the free corrosion potential), there is a linear relationship between applied current and electrode potential. The slope of the curve of ΔE versus $\Delta I_{applied}$ at the origin is defined as the polarization resistance, R_p (see Figure 2.85). The polarization resistance is inversely proportional to corrosion current, which in turn is directly proportional to corrosion rate. The computed corrosion rate can be compared to established guidelines to relate corrosion rate to corrosion damage. This method for corrosion rate measurements is often referred to as linear polarization or the polarization resistance method.
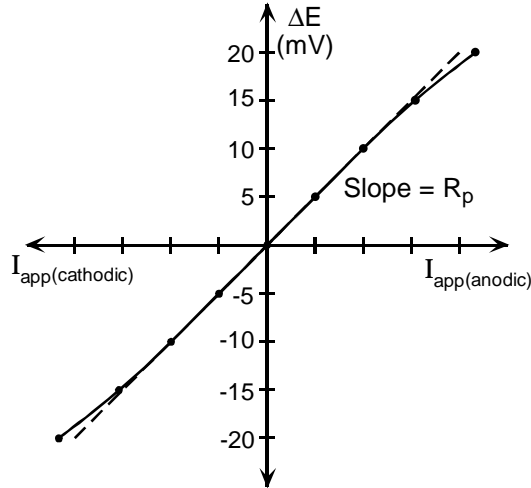
Figure 2.85 - Applied Current Linear Polarization Curve

The instantaneous corrosion current is related to the polarization resistance by the Stern-Geary equation shown below.

$$i_{corr} = \frac{\beta_a \beta_c}{2.3(\beta_a + \beta_c)} \times \frac{1}{R_p}$$ *Eq. 2.1*

where

i_{corr} = corrosion current, mA

β_a = anodic Tafel constant, mV

β_c = cathodic Tafel constant, mV

R_p = polarization resistance, Ohms

The rate of corrosion in terms of corrosion current density, i, can be calculated by dividing the corrosion current, i_{corr}, by the area of polarized steel, A_p.

$$i = \frac{i_{corr}}{A_p}$$ *Eq. 2.2*

The term containing the Tafel constants in Eq. 2.1 is often replaced by a proportionality constant, B, as follows:

$$i_{corr} = \frac{B}{R_p}$$

Eq. 2.3

where,

$$B = \frac{\beta_a \beta_c}{2.3(\beta_a + \beta_c)}$$

In order to accurately calculate the corrosion current, the anodic and cathodic Tafel constants must be known. The polarization resistance is primarily influenced by the corrosion current, I_{corr}, and is relatively insensitive to changes in the Tafel constants. The value of the proportionality constant, B, ranges from 26 for actively corroding mild steel reinforcement in concrete to 52 for passive mild steel reinforcement in concrete. There is no reported research on values of the constant B for prestressing steel in concrete.

2.8.3.1 Measurement of Polarization Resistance

The polarization resistance, R_p, can be measured using several different techniques. The two most common methods used for reinforced concrete are the three-electrode procedure and electrochemical impedance spectroscopy (sometimes referred to as AC impedance). Each method has advantages and disadvantages. The three-electrode method is most common due to its simplicity and low equipment cost.

The basic components of the equipment for the three-electrode method are shown in Figure 2.86. The working electrode is the steel reinforcement for which the corrosion rate is to be measured. The counter electrode is used to apply the polarizing current to the steel. The reference electrode measures the free corrosion potential of the working electrode and the change in potential of the working electrode due to the applied current from the counter electrode. The process of measuring the polarization resistance begins with measuring the free corrosion potential or open-circuit potential of the tested area of steel reinforcement (working electrode). The working electrode is then polarized in uniform increments from the free corrosion potential and the associated current is measured. The polarization resistance is taken as the slope of the curve when ΔE versus $\Delta I_{applied}$ is plotted (see Figure 2.85). This relationship is normally linear for a range of up to +/- 10 mV from the free corrosion potential. When corrosion activity is low, small changes in applied current will produce a large change in potential and the polarization resistance will be large. When corrosion activity is high, large changes in applied current are needed to produce the desired potential increment, resulting in a low polarization resistance.
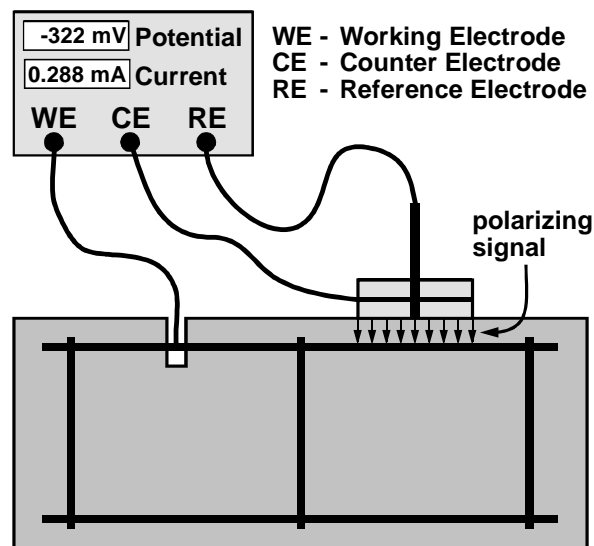
Figure 2.86 - Polarization Resistance Apparatus (Schematic)

2.8.3.2   Errors in Corrosion Rates based on Polarization Resistance Measurements

The polarization resistance technique and apparatus were developed to measure corrosion rates of mild steel reinforcement in "regular" concrete. For this application in the laboratory setting, the polarization resistance technique provides excellent results when compared to direct corrosion rate measurements in macrocell corrosion specimens. In field applications, the results are felt to be somewhat less accurate, but still reliable. The inaccuracies may arise from several sources:

- **Ohmic Electrolyte Resistance:**   The configuration of the three-electrode procedure for polarization resistance measurements in concrete results in a separation between the reference electrode and working electrode (see Figure 2.86).   The separation provided by the concrete cover introduces an error in the measurements due to ohmic electrolyte resistance, that is the resistance of the concrete. This resistance is also referred to as the solution resistance. The total resistance measured by the three-electrode procedure is the sum of the polarization resistance, R_p and the solution resistance, R_s:

$$R_{tot} = R_p + R_s \qquad\qquad \textit{Eq. 2.4}$$

  In situations where the concrete resistance or solution resistance is high and the reference electrode cannot be located close to the working electrode, the error introduced by solution resistance can be significant. The error introduced by solution resistance is unconservative since it increases the apparent polarization resistance, resulting in lower corrosion rates.

- **Uncertain polarized area:**   Calculation of the corrosion rate or current density requires an accurate estimation of the polarized area of the working electrode (see Eq. 2.2). Normally, the polarized area is assumed to be that directly below the counter electrode, but it may unknowingly be smaller or larger. The use of a guard electrode has been shown to confine the current path between the counter electrode and the reinforcement, improving the accuracy of the corrosion rate measurement. Other bars in the vicinity of the counter electrode may also affect the accuracy of the measurements. Diffusion of the current path also will result in larger polarized steel areas as the concrete cover increases. Research has also shown that only the top half of the rebar (closest to the counter electrode) is effectively polarized. This finding suggests that the polarized area is normally overestimated by a factor of two.

- **Uncertain Tafel constants:**   Accurate calculation of corrosion current requires accurate values for the anodic and cathodic Tafel constants (see Eq. 2.1). However, because the Tafel constants β_a and β_c appear in both the numerator and denominator of the Stern-Geary equation (Eq. 2.1), the corrosion current is primarily a function of the polarization resistance and is relatively insensitive to changes in the Tafel constants. For this reason, the values of the proportionality constant, B, proposed earlier are normally deemed sufficient. Inaccuracies resulting from uncertain Tafel constants may be avoided by using the results of polarization resistance measurements for relative comparisons of corrosion activity measured under similar conditions.

- **Prestressed concrete:** Prestressed concrete introduces several factors that may produce errors in corrosion rates determined using the polarization resistance technique.

  - **prestressing strand** - affects Tafel constants, and area of polarized steel is uncertain because of seven wires in close proximity.

  - **prestressing strand inside duct** - may make potential measurements very small (possibly too small or erratic to be useful). Also affects Tafel constants. If duct is plastic, measurements cannot be taken.

- **Erratic or very small polarization resistance:**   Some situations and conditions may lead to unusable values of polarization resistance due to limitations in the technique and equipment. These include:

  - **epoxy coated reinforcement** - may make potential measurements very small (possibly too small or erratic to be useful). Also affects Tafel constants.

- **large cover to reinforcement** - may make potential measurements very small (possibly too small or erratic to be useful).

- **concrete with high resistivity or low permeability** - may make potential measurements very small (possibly too small or erratic to be useful). Concrete containing silica fume is an example of this.

- **cracked concrete** – affects signal distribution in concrete.

2.8.3.3 Corrosion Measurements on Phase I Beam Specimens

There is no published work to date on using polarization resistance to monitor corrosion rates in pre-tensioned or post-tensioned concrete. Some of the factors listed above may have a significant influence on the usefulness of the technique in prestressed concrete. In spite of these potential limitations, it was decided to use polarization resistance as an evaluation method in this testing program since qualitative information and comparisons may still be possible. Relative corrosion rate measurements can provide an indication of relative corrosion rates between specimens with different variables. For example, the relative effectiveness of different corrosion protection measures may be evaluated by comparing corrosion rates with those from "control" specimens. Also, regular measurements may indicate the onset of corrosion through increases in corrosion rate.

Corrosion rate measurements were taken on the Phase I specimens three times during the first fifteen months of exposure testing. Measurements after seven months were performed using the PR-Monitor equipment. Measurements after one year of testing were performed using the 3LP equipment. Both the 3LP and PR Monitor were used to measure corrosion rate after fifteen months exposure. Both types of equipment use the three-electrode technique. Two corrosion rate measurements were taken on each beam, one at midspan and one at 305 mm (12 in.) from midspan, as shown in Figure 2.87. The electrodes were centered over a stirrup at these locations. In the Non-PS and 2/3 PS beams, the electrode also covered several bars of the tension reinforcement.
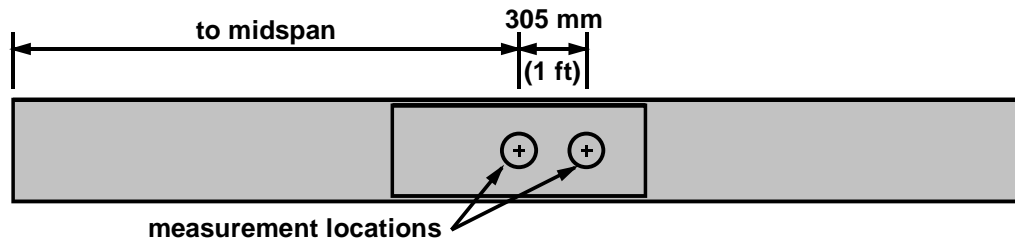
Figure 2.87 - Corrosion Rate Measurement Locations

The polarization resistance technique requires a direct electrical connection (ground connection) to the steel for which the corrosion rate is being measured. As mentioned in Section 2.8.1, ground wires were attached to the mild steel reinforcement and prestressing tendons during construction. Corrosion rate measurements require the concrete to be initially dry. A wetting solution is used to moisten the concrete surface immediately prior to testing.

2.8.3.4 PR-Monitor for Corrosion Rate Measurement

Corrosion rate measurements taken after seven and fifteen months of exposure testing were performed using the CORRTEST PR-Monitor Model IN-4500. The PR-Monitor device uses a portable computer to control the corrosion rate measurement process. The PR-Monitor compensates for the concrete resistance (IR drop) and has a guard electrode to confine the polarization signal. The default polarization scan uses six steps of 5 mV, starting at -15 mV from the free corrosion potential and ending at +15 mV. The starting and ending potentials and voltage increment may be adjusted by the user in situations where the solution resistance is large in comparison to the polarization resistance. The increased potential range for the polarization scan can improve the accuracy of the measured polarization resistance when the solution resistance is high. At the end of the polarization scan, the concrete resistance or solution resistance is measured using AC impedance. A high frequency, low voltage AC signal is used to isolate the solution resistance. The computer performs a linear regression analysis on the polarization scan data and computes the total resistance, R_{tot}, as the slope of ΔE versus $\Delta I_{applied}$. The solution resistance, R_s, is subtracted from the total resistance to obtain the polarization

resistance, R_p (see Eq. 2.4). The corrosion current is calculated assuming a proportionality constant, B, of 26 mV. When all measurements and calculations are complete, the computer displays the free corrosion potential, polarization resistance, concrete resistance and corrosion rate in mils per year. This information and the polarization scan data is also written to an output file. The corrosion rate can be converted to current density by dividing the corrosion rate in mils per year by 0.4568. The corrosion current density can also be calculated using the measured polarization resistance and assumed polarized area. The corrosion severity is assigned based on the ranges listed in Table 2.12.

Table 2.12 - PR-Monitor Corrosion Severity Based on Current Density

Corrosion Current Density	Corrosion Severity
Less than 0.1 $\mu A/cm^2$	Passive
Between 0.1 and 0.5 $\mu A/cm^2$	Low
Between 0.5 and 1.0 $\mu A/cm^2$	Moderate
Greater than 1.0 $\mu A/cm^2$	High

The guard ring is assumed to confine the polarized area of reinforcement to that of a circle with 152 mm (6 in.) diameter directly under the electrodes. The polarized steel surface area necessary to compute corrosion rate was calculated by multiplying the bar circumference by the lengths of the bars directly under the 152 mm (6 in.) diameter circle, as shown in Figure 2.88. In the post-tensioned beams, twice the horizontal projection of the duct area under the circle was included when determining the polarized area. Calculated surface areas for each beam type are indicated in the figure. The wider duct spacing in the 100%S PS beams decreases the polarized area in comparison to the 100%U PS beams.

extent of polarized area

Non-PS:
4 bars + stirrup
A_p = 24,850 mm^2
= 38.5 in^2

100%U PS:
stirrup + duct
A_p = 13,300 mm^2
= 20.6 in^2

2/3 PS:
4 bars + stirrup + duct
A_p = 29,350 mm^2
= 45.5 in^2

100%S PS:
stirrup + duct
A_p = 8660 mm^2
= 13.4 in^2
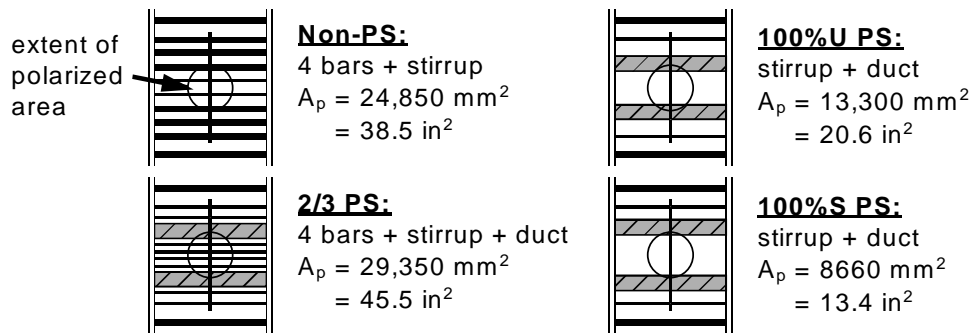
Figure 2.88 - Polarized Steel Surface Areas for PR-Monitor

2.8.3.5   3LP Equipment for Corrosion Rate Measurement

Corrosion rate measurements were taken on the Phase I specimens after twelve and fifteen months of exposure testing using the 3LP Equipment developed by Kenneth C. Clear, Inc., USA. The 3LP device is manually operated, and polarization scan data is recorded by hand. The counter electrode is rectangular and current confinement is not provided. The equipment measures the half-cell potential of the reinforcement (working electrode) and the applied polarization current. The polarization scan uses three steps of 4 mV, starting at the free corrosion potential and ending at +12 mV. The concrete resistance is not measured by the 3LP device. The linear regression analysis on the polarization scan data must be performed using a hand calculator or computer to determine the total resistance, R_{tot}, as the slope of ΔE versus $\Delta I_{applied}$. No correction is made for the concrete resistance, and the polarization resistance, R_p, is simply taken as equal to the total resistance. The manufacturer recommends a proportionality constant, B, of 40.76 mV for calculating corrosion current. The manufacturer also provides guidance for relating corrosion current densities to expected corrosion damage. The SHRP Procedure Manual for Condition Evaluation of Bridges indicates a proportionality constant, B, of 26 mV can be used with the 3LP device. The interpretation guidelines listed in Table 2.12 are appropriate for the 3LP device if B = 26 mV is used.

The counter electrode for the 3LP device is rectangular with dimensions of 178 mm by 76 mm (7 x 3 in.). The polarized steel surface area was calculated by multiplying the bar circumference by the bar length directly under counter electrode, as shown in Figure 2.89. Calculated surface areas for each beam type are indicated in the figure. The counter electrode was positioned such that it was not located over the ducts in the post-tensioned beams.

Non-PS:
2 bars + stirrup
A_p = 16,720 mm^2
    = 25.9 in^2

2/3 PS:
2 bars + stirrup
A_p = 13,300 mm^2
    = 20.6 in^2

100%U PS:
stirrup
A_p = 3040 mm^2
    = 4.7 in^2

100%S PS:
stirrup
A_p = 3040 mm^2
    = 4.7 in^2

extent of polarized area
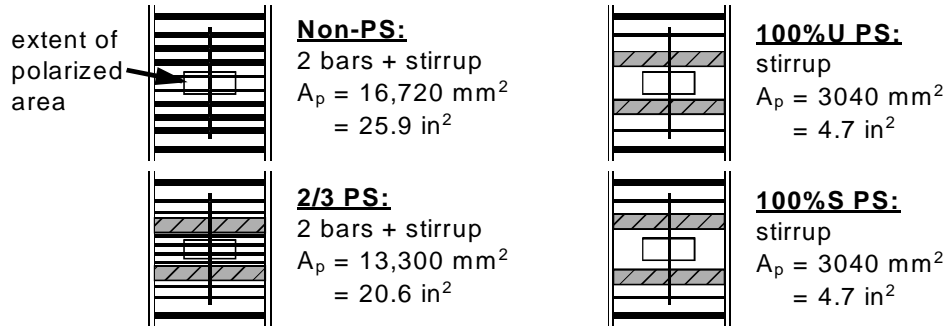
Figure 2.89 - Polarized Steel Surface Areas for 3LP

2.8.4   Corrosion Rate Measurements

2.8.4.1   Seven-Month Exposure Duration

Corrosion rate measurements were performed after seven months of exposure testing using the PR-Monitor equipment (see Section 2.8.3.4). Readings were taken midway (one week) through the dry portion of the exposure cycle. Corrosion rate readings in terms of corrosion current density are plotted in Figure 2.90 and listed in Table 2.13 for all specimens. Two readings were performed on each beam, one at midspan and one 305 mm (12 in.) from midspan. Corrosion currents for most beams are in the range of moderate and high corrosion activity. The corrosion rate for uncracked Beam 1.1 (nonprestressed, unloaded) is in the range of low corrosion activity. In general, the measured corrosion rates for the 100%U PS and 100%S PS beams are higher than those for the 2/3 PS and Non-PS beams. This trend in corrosion activity is contradictory to the half-cell potential readings.
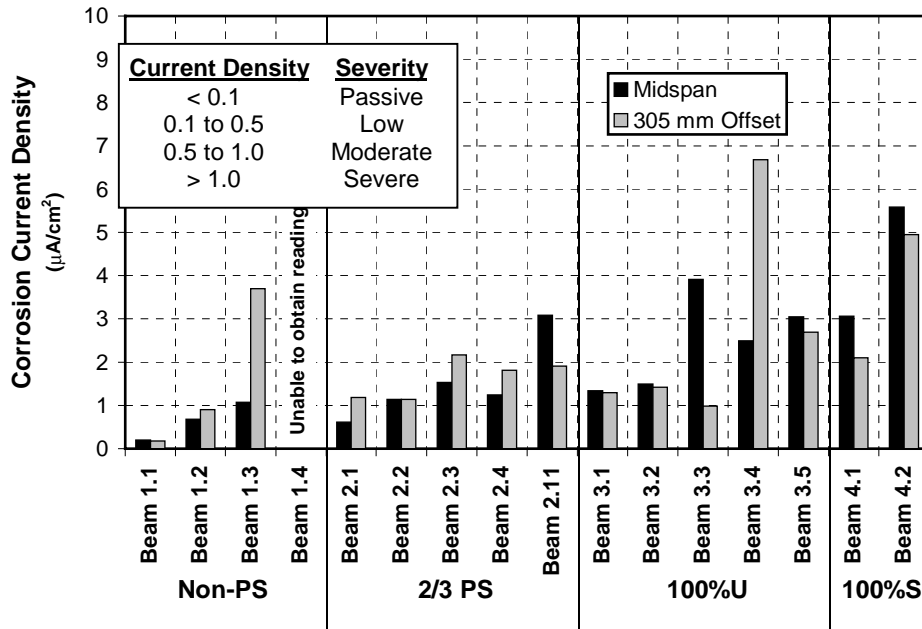
Figure 2.90 - Phase I Beam Measured Corrosion Rates – Seven-Month Exposure Duration
(PR Monitor Equipment)

2.8.4.2 Twelve-Month Exposure Duration

Corrosion rate measurements were performed after twelve months of exposure testing using the 3LP equipment (see Section 2.8.3.5). Readings were taken on day five of the two-week dry portion of the exposure cycle. Corrosion rate readings in terms of corrosion current density are plotted in Figure 2.91 (note the greatly expanded scale in comparison to Figure 2.90) and listed in Table 2.13 for all specimens. Readings were taken at the same locations used with the PR-Monitor after seven months exposure. Corrosion rates for all beams except Beam 1.1 are very high. Although considerably lower than the other beams, the 3LP corrosion rate for Beam 1.1 has exceeded the threshold for severe corrosion activity. The relative corrosion rates between specimens show trends comparable to the data measured after seven months using the PR-Monitor. The measured corrosion rates for the 100%U PS and 100%S PS beams are again higher than those for the 2/3 PS and Non-PS beams, contrary to the relative corrosion activity indicated by the half-cell potential readings.
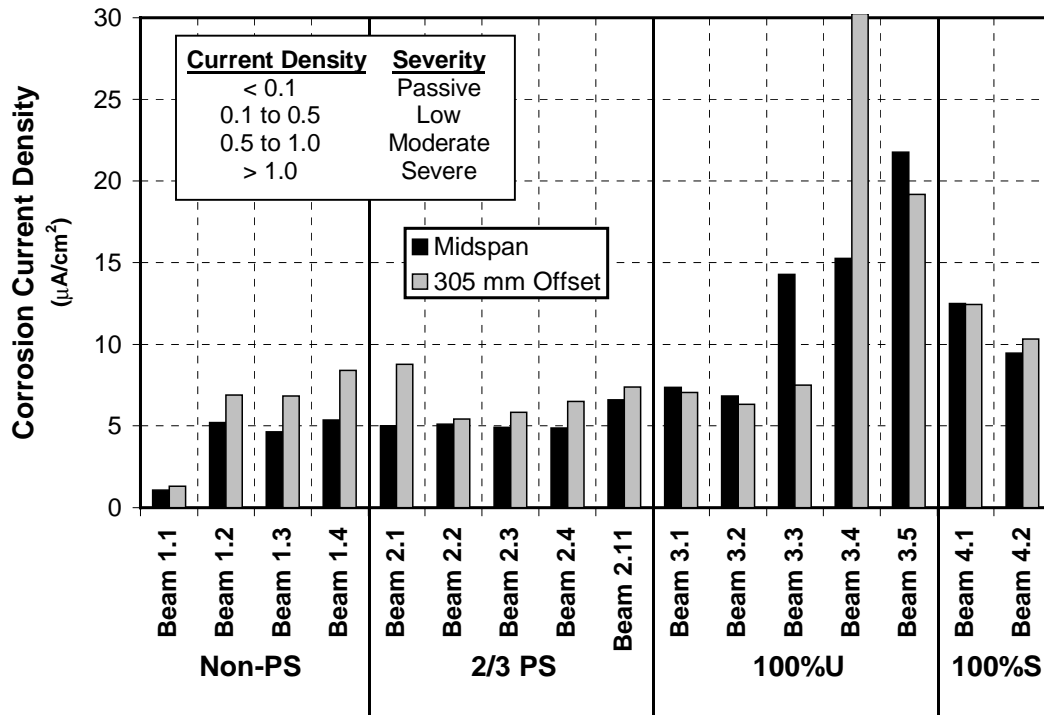
Figure 2.91 - Phase I Beam Measured Corrosion Rates – Twelve-Month Exposure Duration
(3LP Equipment)

2.8.4.3 Fifteen-Month Exposure Duration

Corrosion rate measurements were repeated after fifteen months of exposure testing using both the 3LP equipment and PR Monitor. Readings were taken sixteen days after the start of the dry portion of the exposure cycle (the dry period was extended beyond the normal two weeks because work was being performed on the beams). Corrosion current densities are plotted in Figure 2.92 and Figure 2.93 for the PR Monitor and 3LP, respectively (again, note the expanded scale in Figure 2.93 in comparison to Figure 2.92). All measured corrosion rates are summarized in Table 2.13.
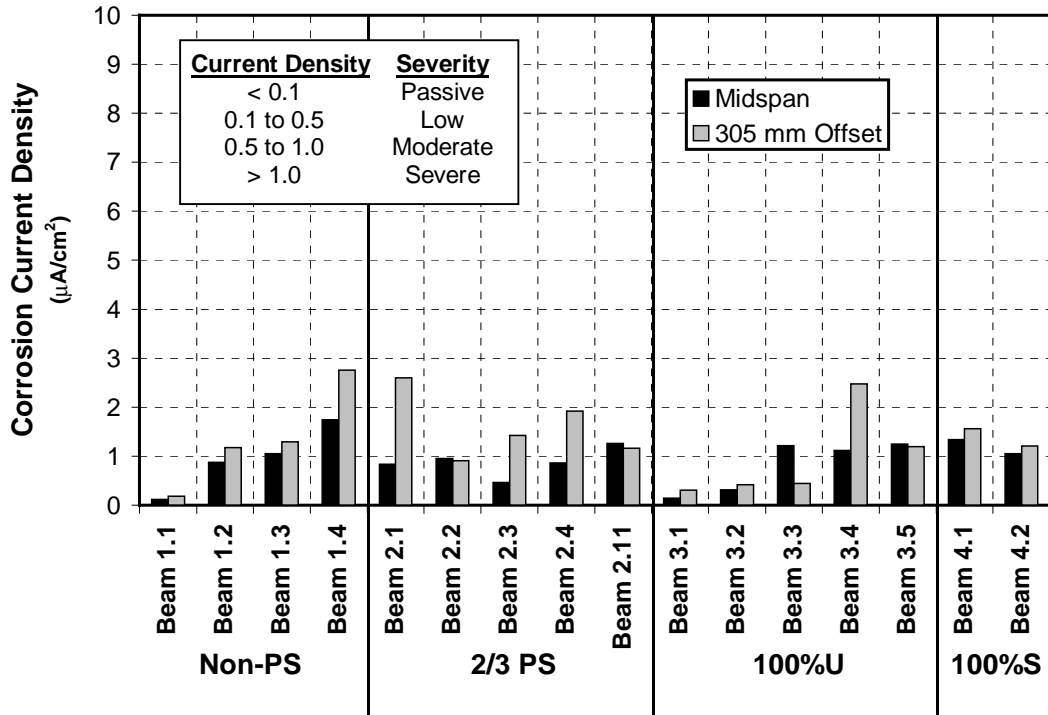
Figure 2.92 - Phase I Beam Measured Corrosion Rates – Fifteen-Month Exposure Duration (PR Monitor Equipment)
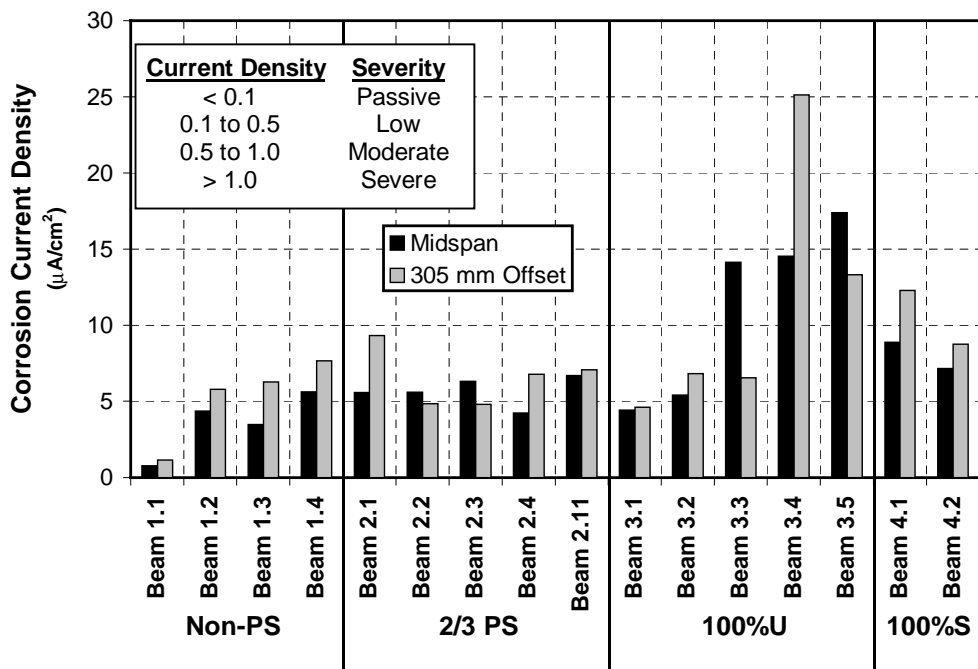
Figure 2.93 - Phase I Beam Measured Corrosion Rates – Fifteen-Month Exposure Duration (3LP Equipment)

81

PR Monitor corrosion rates are high for many of the beams. Low corrosion activity is indicated in Beams 1.1, 3.1 and 3.2 and for some readings in other beams. The fifteen-month data can be compared to the seven-month PR Monitor data shown previously in Figure 2.90. While many relative trends are similar (Beam 1.1 is very low and corrosion rates for the 100%U PS and 100%S PS beams are comparable to or higher than those for the 2/3 PS and Non-PS beams), the differences between the groups are much smaller. The corrosion rates for the 100%U PS and 100%S PS beams are greatly reduced from the seven-month values.

The fifteen-month 3LP data shows very high corrosion rates for all beams with the exception of Beam 1.1. Measured corrosion rates at fifteen months have decreased for several beams in comparison to the twelve-month data shown previously in Figure 2.91. In general, the 3LP data is much more consistent between the twelve and fifteen-month data. The overall trends in relative corrosion rates between beams at fifteen months are comparable to the data measured after twelve months.

Table 2.13 - Summary of Phase I Beam Corrosion Current Density Measurements

		7 months	12 months	15 months	
Specimen	**Location**	**PR Monitor**	**3LP**	**PR Monitor**	**3LP**
		$\mu A/cm^2$	$\mu A/cm^2$	$\mu A/cm^2$	$\mu A/cm^2$
Beam 1.1	Midspan	0.18	1.09	0.12	0.76
	Offset	0.17	1.31	0.19	1.15
Beam 1.2	Midspan	0.65	5.22	0.88	4.37
	Offset	0.85	6.89	1.18	5.79
Beam 1.3	Midspan	1.01	4.64	1.06	3.50
	Offset	3.70	6.83	1.29	6.29
Beam 1.4	Midspan	no reading	5.37	1.74	5.64
	Offset	no reading	8.39	2.75	7.66
Beam 2.1	Midspan	0.47	5.00	0.84	5.58
	Offset	0.89	8.76	2.60	9.32
Beam 2.2	Midspan	0.85	5.12	0.95	5.61
	Offset	0.86	5.43	0.91	4.86
Beam 2.3	Midspan	1.15	4.93	0.47	6.32
	Offset	1.64	5.85	1.43	4.79
Beam 2.4	Midspan	0.94	4.88	0.86	4.25
	Offset	1.36	6.50	1.92	6.78
Beam 2.11	Midspan	2.33	6.61	1.26	6.70
	Offset	1.43	7.39	1.16	7.08
Beam 3.1	Midspan	0.61	7.37	0.14	4.44
	Offset	0.59	7.06	0.31	4.62
Beam 3.2	Midspan	0.68	6.84	0.31	5.43
	Offset	0.65	6.33	0.42	6.83
Beam 3.3	Midspan	1.78	14.27	1.21	14.14
	Offset	0.45	7.50	0.45	6.56
Beam 3.4	Midspan	1.14	15.25	1.12	14.53
	Offset	3.05	30.26	2.47	25.14
Beam 3.5	Midspan	1.40	21.77	1.24	17.41
	Offset	1.23	19.18	1.19	13.31
Beam 4.1	Midspan	2.14	12.51	1.34	8.88
	Offset	1.46	12.44	1.56	12.28
Beam 4.2	Midspan	3.90	9.47	1.06	7.16
	Offset	3.45	10.31	1.21	8.75

2.9 AUTOPSY

2.9.1 Limited Autopsy

In order to monitor the progression of corrosion without completely removing specimens from the testing program, selected beams were chosen for an invasive inspection by limited autopsy. The data from this inspection were used to check the condition of the beams and to correlate the half-cell potential readings with actual reinforcement condition.

Invasive inspections were performed on three beams. The 1 series (Non-PS) and the 3 series (100% U PS) beams each contained one duplicate beam. Specimens 1.2 and 1.3 have the same variables and Specimens 3.3 and 3.5 have the same variables. Half-cell potential readings were very similar for the identical specimens. Specimens 1.3 and 3.3 were chosen for the limited autopsies. Specimen 3.4 was also inspected at one location where heavy surface staining was evident and where high corrosion rates had been measured.

2.9.1.1 Chloride Samples

Concrete powder samples were taken from Specimens 1.3 and 3.3 at several locations to monitor chloride ingress. Three main locations were chosen to compare variation between cracked and uncracked regions and distance from the ponded region. The locations chosen are indicated by letters A through C in Figure 2.94. Location A is at the centerline crack in the ponded region, while location B is in an uncracked area in the ponded region. Location C is used to examine the migration of chlorides outside of the ponded region. Samples were taken from two holes at each location. The samples were then mixed to obtain a representative sample.

Side View
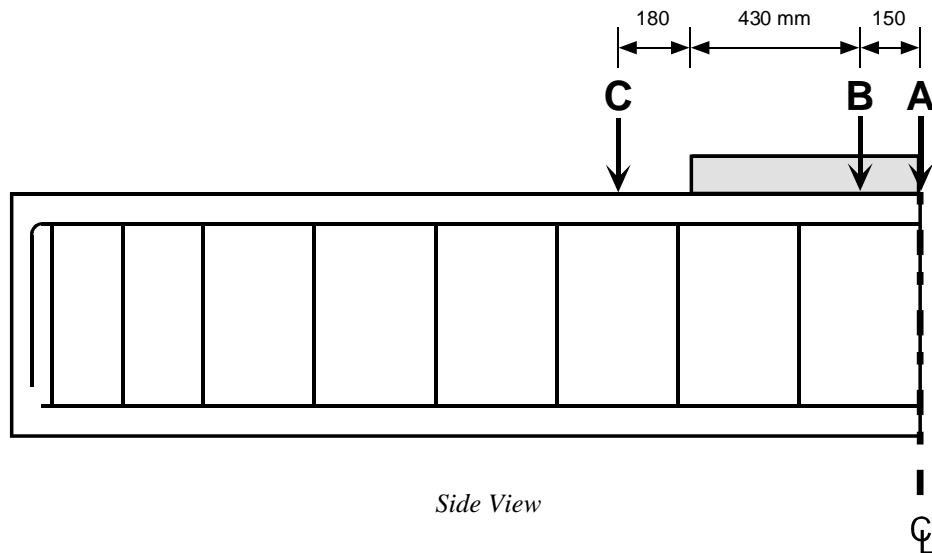
Figure 2.94 - Chloride Sample Locations

Each sample was taken at a depth of 13 mm (7-19 mm drilled sample) and 25 mm (19-32 mm drilled sample). Samples were not taken at the 50 mm (2") depth so that the reinforcing bars were not damaged. Results from the chloride samples taken at the inspection locations are shown in Figure 2.95. Both beams had negligible chlorides outside of the ponded region. The chloride levels in the ponded region away from a crack were significantly lower than the levels at a crack. The chloride levels were higher near the surface in the post-tensioned Specimen 3.3 at both locations than they were for the non post-tensioned Specimen 1.3. However, the chloride levels were lower for the post-tensioned Specimen 3.3 at the 25 mm (1") depth than they were for the non post-tensioned Specimen 1.3. The maximum crack width at the centerline was 0.33 mm (0.013") for the non post-tensioned Specimen 1.3 and 0.18 (0.007") for the post-tensioned Specimen 3.3. The post-tensioned specimen with the smaller crack widths has reduced chloride penetration compared with the non-PS section at both the uncracked and especially at the cracked region.

Acid Soluble Chloride Content
(% by weight of concrete)
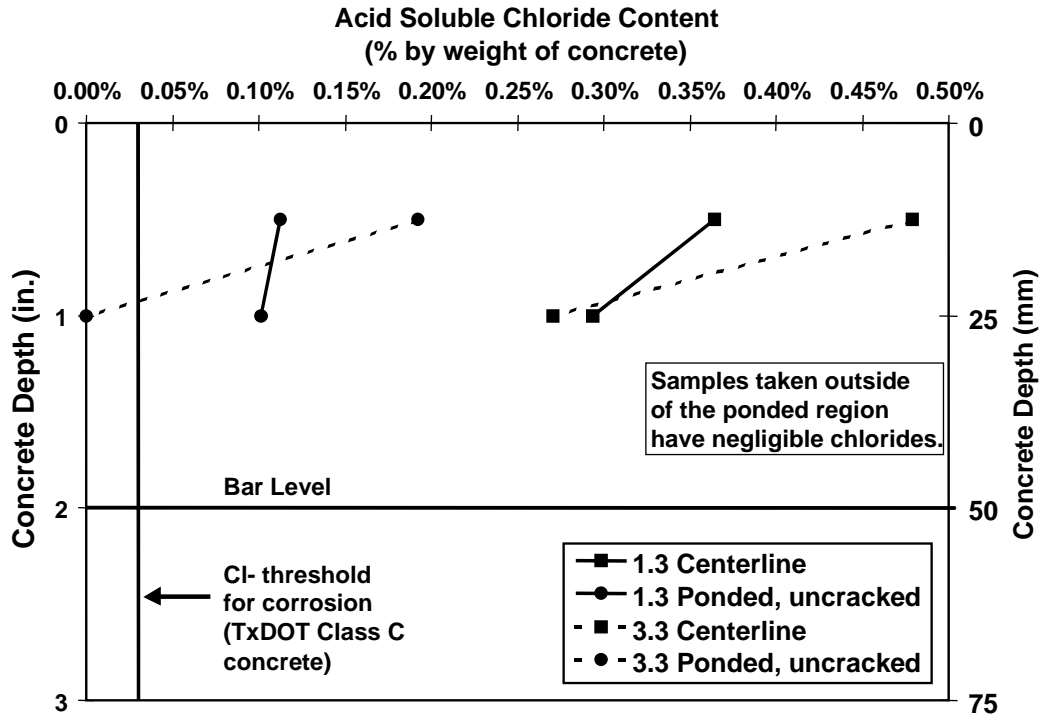
Figure 2.95 - Chloride Penetration at Limited Autopsy Locations

2.9.1.2   Inspection of Reinforcement

<u>Specimen 1.3</u>

This non post-tensioned specimen has heavy staining as shown in Figure 2.96 (top surface of the beam). Holes were drilled at two locations (Figure 2.97) to evaluate the condition of the reinforcing bars. Crack locations in the ponded region were highlighted with a marker for the photograph shown in Figure 2.97. Location 1 coincides with the centerline crack and also coincides with a large patch of staining. Location 2 is away from a crack. First, small holes were drilled to collect powder for chloride samples. A 30 mm (1 ¼") hole was then drilled in the same location, and the remaining concrete above the steel was chipped away carefully by hand. Once a portion of the steel was exposed, the hole was widened by a combination of careful drilling and hand chipping to uncover the reinforcement. After completion of the inspection, holes were coated with epoxy and filled with a nonshrink grout.
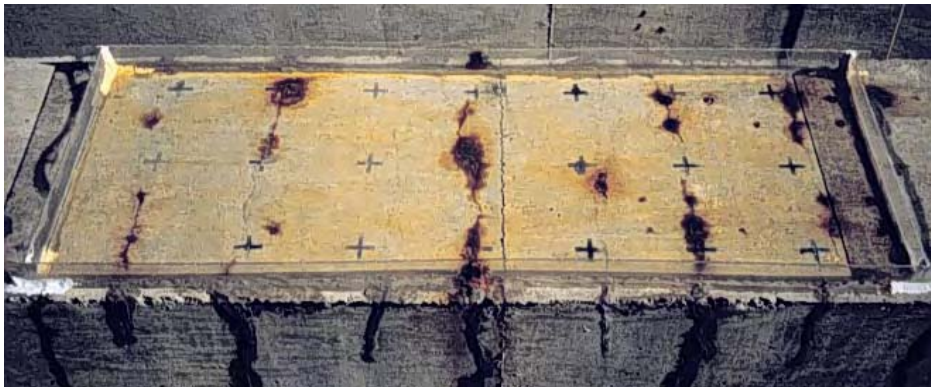
Figure 2.96 - Staining on Specimen 1.3
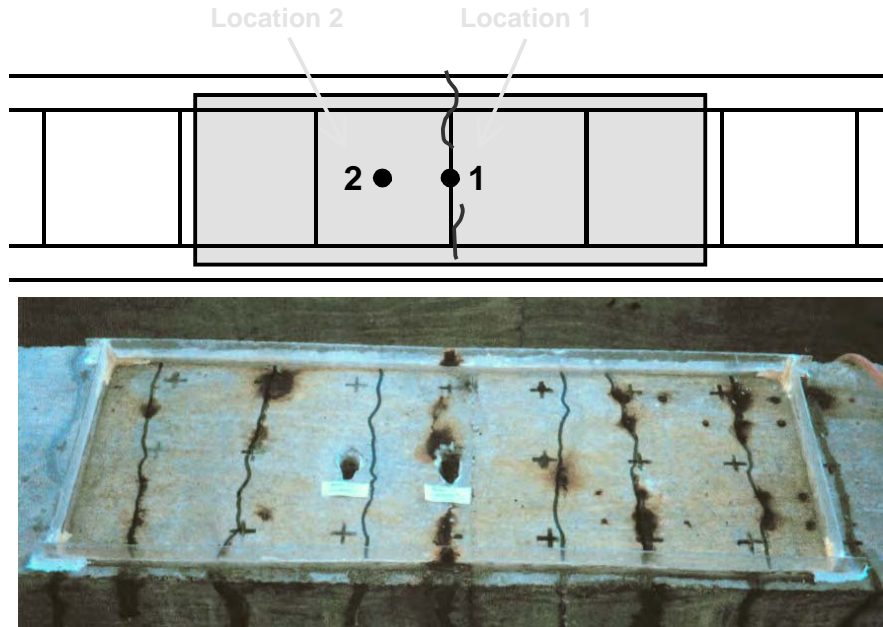
Figure 2.97 - Invasive Inspection Locations, Specimen 1.3

The stirrup exposed under location 1 showed light pitting extending all along the steel where it intersected with the crack. Two pockets of heavier pitting were also found as shown in Figure 2.98. The longitudinal reinforcement exposed under location 2 showed one area of pitting as illustrated in Figure 2.99, but otherwise showed little sign of corrosion.
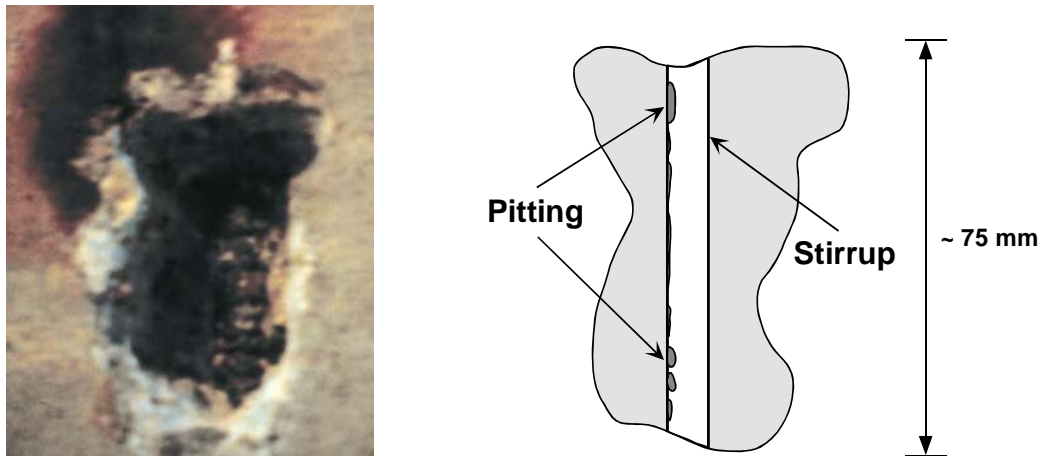
Figure 2.98 - Reinforcing Bar Condition under Crack, Specimen 1.3
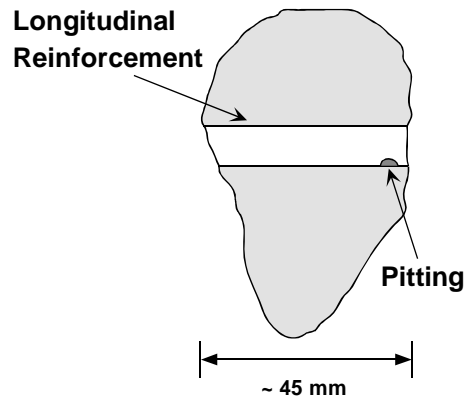
Figure 2.99 - Reinforcing Bar Condition Away from Crack, Specimen 1.3

Specimen 3.3

The condition of the duct and strand was evaluated at two locations for this post-tensioned specimen. Holes were drilled over the duct at two locations as shown in Figure 2.100. Location 1 coincides with the centerline crack and only the stirrup was inspected at this location. Concrete removal followed the same process as for Specimen 1.3. Location 2 was used to inspect the duct. The downstream grouting direction was chosen for location 2 since there was more likelihood of voids in this part of the duct. The duct containing no splice was chosen for drilling at location 2 so as not to interfere with the splice comparisons by penetrating the duct at a splice location. Extreme care was used during hand chipping to avoid damaging the duct.
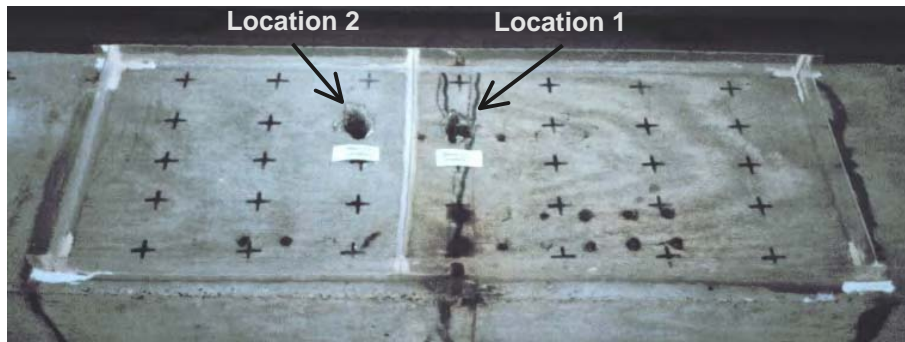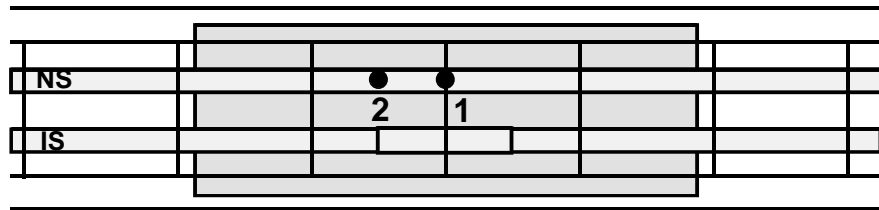
Figure 2.100 - Invasive Inspection Locations, Specimen 3.3

The stirrup at location 1 showed no signs of corrosion, and there was little staining along the crack in this location. The only significant staining on this beam appeared to be from the bolster strips. The duct at location 2 also showed no signs of corrosion. After the condition of the duct was examined, a shallow hole was carefully drilled into the duct to check for voids in the grout. The duct at the drill location was completely filled with grout. The inspection stopped at this level, since there were no signs that the strand was corroding and further excavation risked damage to the strand. A schematic of the concrete removal process for location 2 is shown in Figure 2.101. After the completion of the inspection, the holes were coated with epoxy and filled with a nonshrink grout.

86
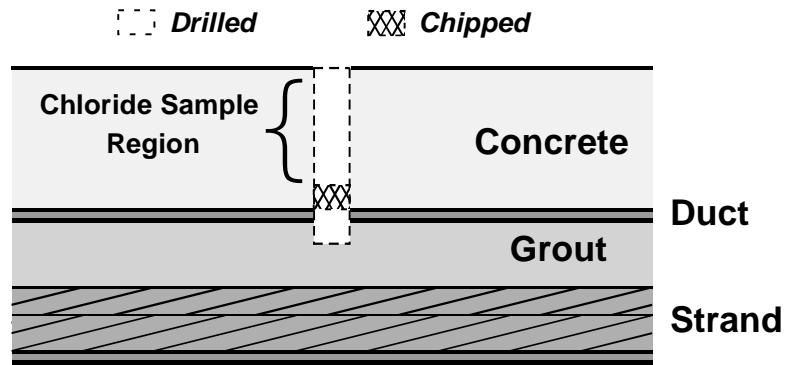
Figure 2.101 - Details for Post-Tensioning Duct Inspection

Specimen 3.4

Post-tensioned Specimen 3.4 has a different crack pattern than the other specimens and did not develop a centerline crack during loading. The typical cracking pattern for the 100% U PS specimens is three cracks (as seen in Figure 2.100 for Specimen 3.3), but Specimen 3.4 developed a crack over the stirrups on either side of the centerline. The maximum crack width for this crack measured 0.25 mm (0.010") compared with 0.18 mm (0.007") for Specimen 3.3. A patch of heavy staining was observed near a crack in Specimen 3.4. For this reason, location 1 as shown in Figure 2.102 was chosen for invasive inspection of the stirrup. The stirrup showed extensive light pitting on the west side where the crack intersected the steel. Two pockets of deeper pitting were also found on the bar as shown in Figure 2.103. The overall condition of the stirrup was similar to the condition of the stirrup in Specimen 1.3.
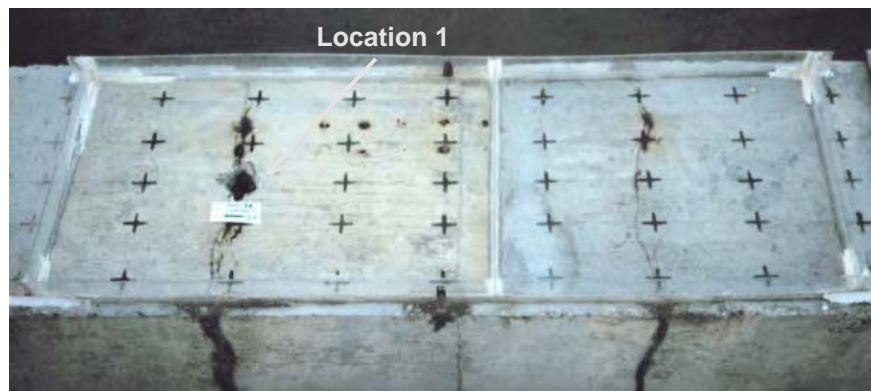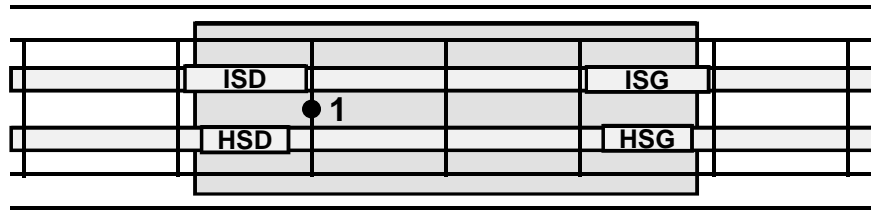
Figure 2.102 - Invasive Inspection Location, Specimen 3.4
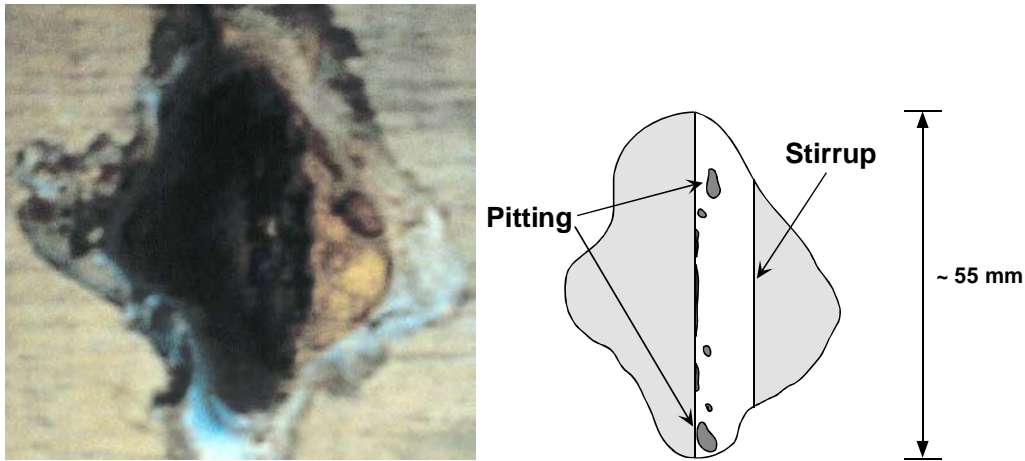
Figure 2.103 - Reinforcing Bar Condition under Crack, Specimen 3.4

2.9.2 *Plans for Full Autopsy*

When half-cell potentials and condition evaluations indicate the onset of severe corrosion, beam specimens will undergo full autopsy. To this point, half-cell potential values have been fairly constant, but a sudden increase in value often indicates the onset of corrosion. At this stage the corrosion protection provided by the different variables can be fully investigated and correlated with the half-cell potential data. The autopsies will include chloride samples and inspection of the reinforcing bars, strand, duct, and end anchorage hardware.

2.9.2.1 Chloride Samples

Future concrete powder samples will be taken at several locations to monitor chloride ingress. Four main locations were chosen to compare variation between cracked and uncracked regions and distance from the ponded region. These locations are shown in Figure 2.104. Additional samples may be taken in areas slightly away from the reinforcing steel so samples can be taken at deeper depths. The 2" depth samples will give an indication of the chloride concentration at the level of the tension steel and at the post-tensioning duct in the ponded region.
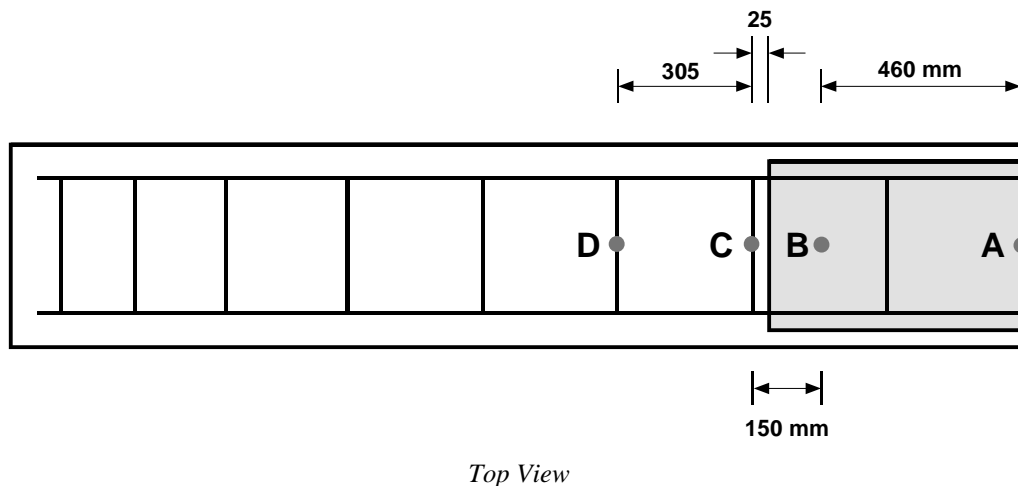
Top View

Figure 2.104 - Chloride Sample Locations

For the post-tensioned sections, grout samples from within the duct will also be taken. These samples will be taken from points along the length of each duct as indicated by the locations A through C in Figure 2.105. Grout powder samples will be obtained by removing pieces of grout from the desired area above the strand bundle and crushing the pieces with a mortar and pestle. The representative sample will then be taken from the mixture of powder from one location. The sample from location A will be used to investigate penetration of chlorides at the splice location. Location B will be used to check the chloride level under the ponded region, but away from the splice location. Location C will investigate the effect at the kink in the duct. Galvanized steel duct is formed by wrapping a long, thin sheet of metal in a spiral pattern. The duct is not watertight along these seams, and when the duct is bent, some of the seams may be forced open.

Top View

Side View
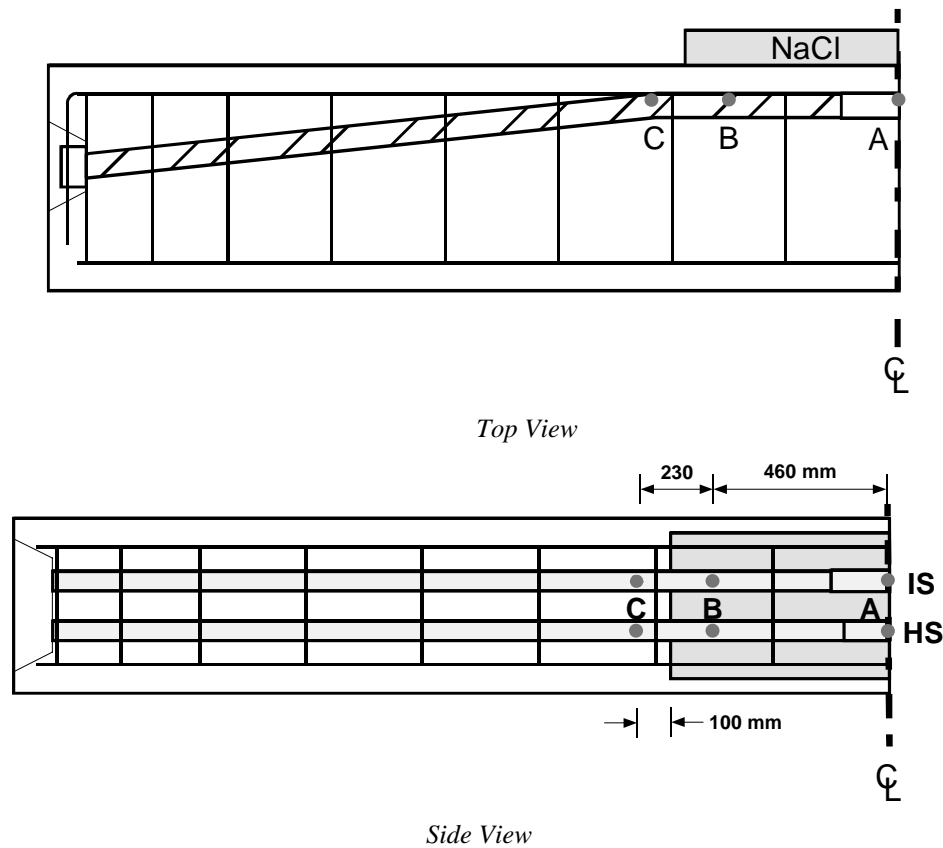
Figure 2.105 - Duct Chloride Sample Locations

2.9.2.2   Inspection of Reinforcement and Post-Tensioning System

The condition of the reinforcing cage, duct, prestressing strand and end anchorage will be inspected thoroughly. In order to facilitate handling, the specimen will be cut into several pieces along its length. Nonprestressed specimens will be cut into relatively equal segments and then a cut will be made along the tops of the segments to expose the tension steel. Remaining concrete will then be removed to expose the reinforcing cage in its entirety. Prestressed sections will be cut into segments with care taken to place cuts away from locations where grout chloride samples will be taken. Cuts will be made to expose the tension steel and post-tensioning duct. The post-tensioning duct will be carefully removed and then cut open to obtain grout samples and inspect the prestressing steel. Planned cut locations for nonprestressed and prestressed sections are shown as dashed lines in Figure 2.106.

Nonprestressed specimen

Prestressed specimen
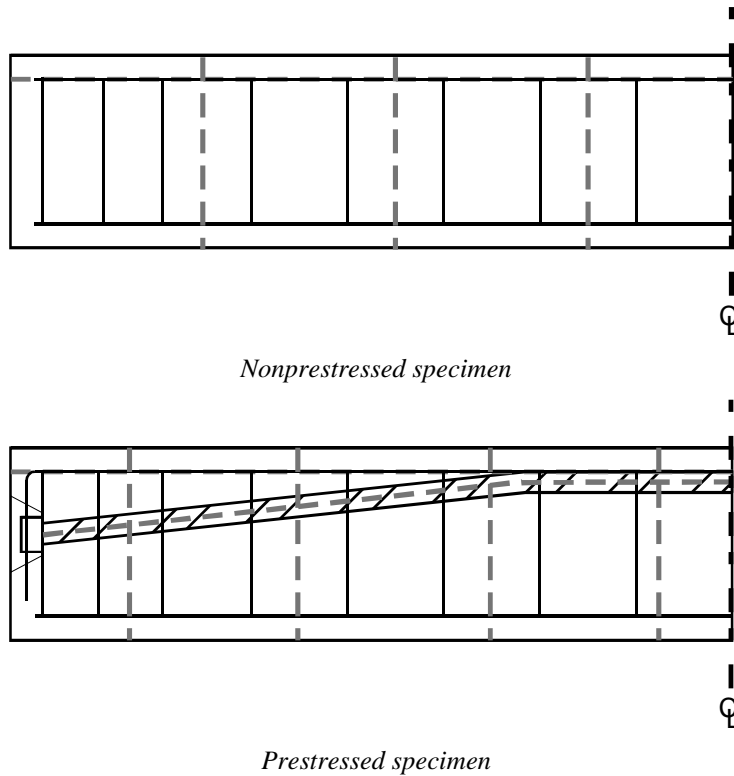
Figure 2.106 - Autopsy Cut Locations – Side View

2.10 ANALYSIS AND DISCUSSION OF RESULTS

2.10.1 Cracking Due to Applied Loading

The cracking behavior of the various beam types was described in Section 2.7.3. The prediction of the cracking moment and surface crack widths is discussed in more detail in the following sections.

2.10.1.1 Cracking Moment Prediction

The modulus of rupture for concrete is normally calculated based on the concrete cylinder strength as follows:

$$
\begin{aligned}
f_r &= 0.62\sqrt{f'_c} \quad \text{(MPa)} \\
&= 7.5\sqrt{f'_c} \quad \text{(ksi)}
\end{aligned}
$$

Eq. 2.5

The cracking moment for each beam specimen was computed using the calculated using the average concrete cylinder strength for each beam and the calculated modulus of rupture (Eq. 2.5). Concrete strength and cracking moment data is shown in Table 2.14 for all beams. Eq. 2.5 is a conservative estimate of modulus of rupture, and as a result, the calculated cracking moments were consistently lower than the cracking moments obtained during testing. Measured cracking moments ranged from very close to the estimated value to 31% higher than the estimated values. On average, the measured values were 1.11 times the estimated cracking moments.

The measured cracking moments were used to back-calculate the apparent modulus of rupture for each beam. This data is also listed in Table 2.14. The ratio of the modulus of rupture to the square root of the cylinder strength is normally taken as 7.5 in U.S. Customary Units (see Eq. 2.5). The corresponding value in metric is 0.62. Calculated values of this ratio are shown in Table 2.14. For metric units, the calculated ratio ranges from 0.62 to 0.86. In U.S. units, the range is 7.5 to 10.4. Given this range, it appears that the accepted values used in Eq. 2.5 are conservative and appropriate.

90

Table 2.14 - Cracking Moments and Concrete Strengths for All Beams

Beam	Cylinder Strength, f'_c (MPa)	f_r (Eq. 3.5) (MPa)	Cracking Moment			Apparent f_r (MPa)	$f_r / \sqrt{f'_c}$
			Calculated (kN-m)	Measured (kN-m)	Meas/Calc		
1.2	35.9	3.7	118.9	150.3	1.26	4.7	0.79
1.3	35.9	3.7	118.9	142.9	1.20	4.5	0.75
1.4	33.2	3.6	115.0	150.3	1.31	4.7	0.81
2.1	33.2	3.6	239.9	262.7	1.10	4.3	0.75
2.2	33.2	3.6	239.9	244.0	1.02	3.7	0.65
2.3	41.4	4.0	251.2	255.3	1.02	4.1	0.64
2.4	41.4	4.0	251.2	262.7	1.05	4.4	0.68
2.11	41.4	4.0	251.2	255.3	1.02	4.1	0.64
3.3	37.0	3.8	310.5	310.7	1.00	3.8	0.62
3.4	39.7	3.9	314.3	356.7	1.13	5.4	0.86
3.5	39.7	3.9	314.3	337.8	1.07	4.7	0.75
				Avg.	1.11	Avg.	0.723
				Std. Dev.	0.10	Std. Dev.	0.076

2.10.1.2 Surface Crack Width Prediction

The measured applied moment – crack width relationship is plotted in Figure 2.107 and Figure 2.109 for the Phase I Non-PS, 2/3 PS and 100%U PS beams, respectively. Also shown in the plots are estimated crack widths using several different methods, including Gergely-Lutz, CEB-FIP 1978 and 1990 Model Codes, Batchelor and El Shahawi, and Suri and Dilger. The Batchelor and El Shahawi and Suri and Dilger expressions were developed for partially prestressed concrete members only and thus were not compared to the data for the Non-PS beams (Series 1).

The Gergely-Lutz expression provides a very good estimate of maximum surface crack width in the Non-PS beams (Series 1), as shown in Figure 2.107. The CEB-FIP 1978 Model Code (MC 78) underestimates crack widths at low load levels and overestimates crack widths at service load levels. The CEB-FIP 1990 Model Code (MC 90) consistently underestimates the crack widths and is unconservative.
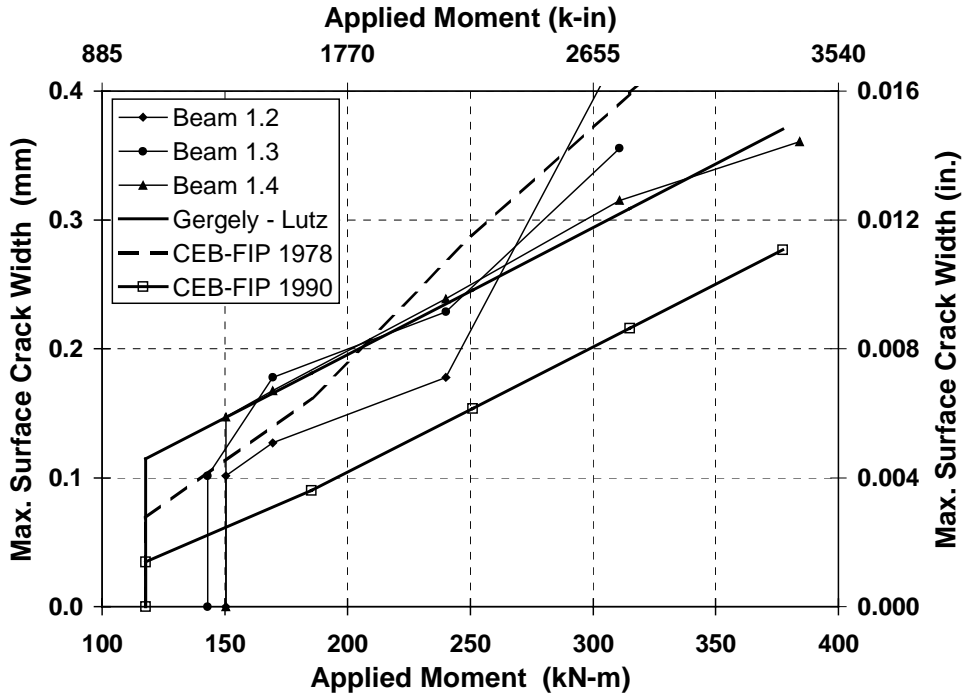
Figure 2.107 - Moment – Crack Width Relationship for Non-PS Beams
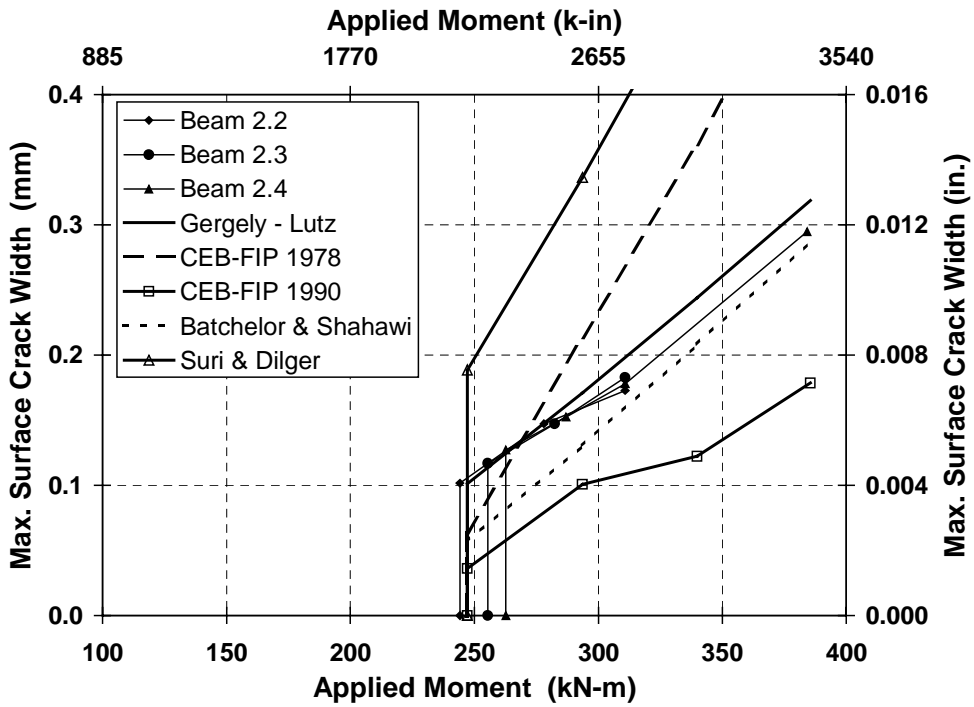
Figure 2.108 - Moment – Crack Width Relationship for 2/3 PS Beams
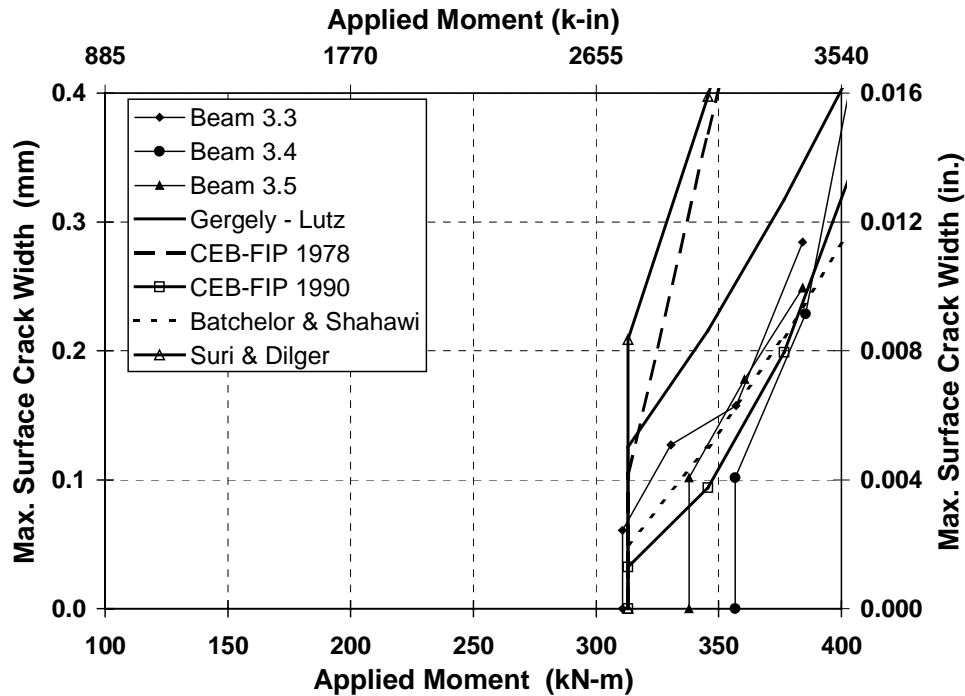
Figure 2.109 - Moment – Crack Width Relationship for 100%U PS Beams

The Gergely-Lutz expression provides an excellent estimation of surface crack width for the 2/3 PS beams. The MC 78 method and Suri and Dilger expression significantly overestimate the surface crack widths and do not appear to be appropriate. The MC 90 method again underestimates crack widths by a sizeable margin. The Batchelor and El Shahawi expression provides a reasonably good prediction for crack widths, particularly at higher load levels.

The Batchelor and El Shahawi expression and MC 90 method provide the most accurate prediction of surface crack widths for the 100%U PS beams. The Gergely-Lutz expression overestimates the crack widths by a moderate margin. The MC 78 method and Suri and Dilger expression significantly overestimate the surface crack widths and do not appear to be appropriate for the 100%U PS beams.

2.10.1.3 Evaluation of Prediction Methods

The basis for each of the crack width prediction methods is listed Table 2.15. Many crack width prediction methods are based on a statistical analysis of test data, including three of the five methods evaluated.

Table 2.15 - Crack Prediction Methods

Method	Basis	Variables Used
Gergely-Lutz	regression analysis	stress in nonprestressed reinforcement, concrete cover, area of concrete in tension around each reinforcing bar
CEB-FIP 1978 Model Code	basic principles (refined using test data)	avg. tension steel strain (accounting for tension stiffening), crack spacing, concrete cover, bar spacing, bar diameter, tension steel area, area of concrete in tension, strain profile in tension zone, tensile strength of concrete
CEB-FIP 1990 Model Code	basic principles (refined using test data)	length over which slip between steel and concrete occurs, difference between average steel and concrete strains (within length of slip), tension steel area, area of concrete in tension, tensile strength of concrete, bar diameter, bond stress
Batchelor and El Shahawi	regression analysis	stress in nonprestressed reinforcement
Suri and Dilger	regression analysis	stress in nonprestressed reinforcement, concrete cover, total tension steel area, area of concrete in tension

The accuracy of models based on regression analysis is highly dependent on the data considered and statistical methods used. It is apparent from Table 2.15 that the variables used in the regression models differ considerably in some cases. The CEB-FIP 1978 Model Code estimates crack width as a function of the average crack spacing and the average strain in the tension steel, accounting for tension stiffening of the concrete. The CEB-FIP 1990 Model Code takes a slightly different approach, using the length of steel near a crack over which slip between the concrete and steel occurs instead of average crack spacing and using the difference between the average steel and concrete strains within the length of slip.

The differences between the crack prediction methods can lead to large differences in results, as apparent in Figure 2.107, Figure 2.108 and Figure 2.109. In some cases it is possible to identify probable sources of error between the predicted and measured crack widths. Each crack prediction method is examined below.

Gergely-Lutz Expression

The Gergely-Lutz crack width expression is based on a statistical analysis of a large set of test data from six different experimental investigations. All of the test data was for reinforced (nonprestressed) concrete members. The Gergely-Lutz expression provided an excellent estimation of maximum surface crack width for the Non-PS and 2/3 PS beam types in this testing program. Maximum crack widths for the 100%U PS beam type were overestimated by a moderate margin. The most likely source of error in prediction of crack widths for the 100%U PS beam type is the effective area of concrete in tension surrounding the tension reinforcement. Some of the calculation data is shown in Table 2.16 for the three section types. The Gergely-Lutz expression is shown in Eq. 2.6. The effective area of concrete in tension, A_e, is considerably larger for the 100%U PS section due to the smaller effective depth of tensile reinforcement (nonprestressed and prestressed steel). It is possible that the effective area of concrete in tension is overestimated, leading to an overestimation of crack width. The height of the effective area of concrete in tension is almost one-third of the section depth for the 100%U PS section. Other crack width prediction methods, including MC 90, limit the height of the effective area of

concrete in tension to $(h - c)/3$. It is possible that the Gergely-Lutz method could be overestimating the effective area of concrete in tension for the 100%U PS beam type.

$$w = 0.076 \frac{h_2}{h_1} f_s (d_c A)^{1/3} = 0.076 \left(\frac{h-c}{d-c} \right) f_s \left(d_c \frac{A_e}{m} \right)^{1/3} \quad \text{(units of 0.001 in.)} \qquad \textit{Eq. 2.6}$$

w   =   tensile face surface crack width, in.

A_e =   2b(h-d):   effective area of concrete in tension surrounding tensile reinforcement (in^2) as illustrated in Figure 2.110

m   =   total number of nonprestressed reinforcing bars in the tension zone plus one fictitious nonprestressed bar for each bonded prestressing strand present

b'   =   width of beam at centroid of tensile reinforcement, in.

h   =   overall depth of beam

d   =   effective depth of beam to centroid of tensile reinforcement calculated based on the primary flexural reinforcement, including mild steel reinforcement and prestressed reinforcement, in.

d_c =   thickness of concrete cover measured from the extreme tension fiber to center of bar located closest thereto, in.

f_s =   stress in nonprestressed reinforcement calculated by elastic cracked section theory accounting for the presence of prestressing forces and prestressed reinforcement, ksi

c   =   distance from neutral axis to compression face, in.
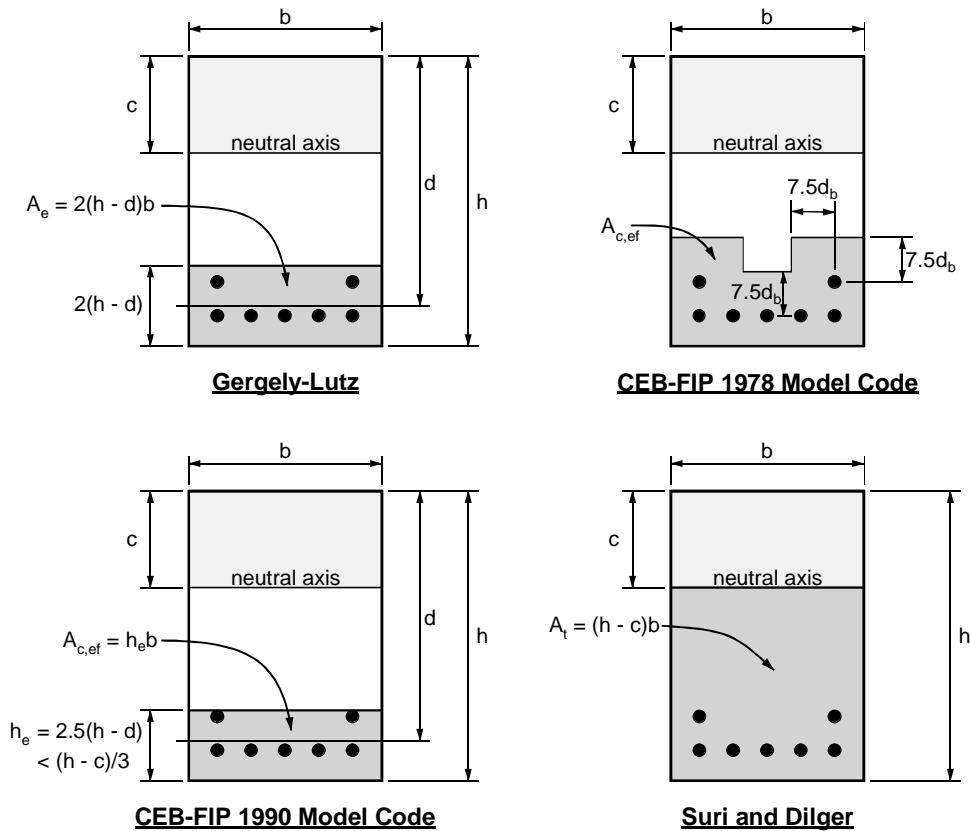
Figure 2.110 - Calculation of Effective Concrete Area in Tension for Various Models

Table 2.16 - Calculation Data for Gergely-Lutz Crack Width Expression

Variable	Non-PS	2/3 PS	100%U PS
effective area, A_e	55,742 mm^2	69,677 mm^2	83,613 mm^2
effective depth, d	549 mm	536 mm	515 mm
height of effective area: 2(h - d)	121 mm (0.20h)	148 mm (0.24h)	190 mm (0.31h)
# bars and strands, m	8 bars	8 bars + 4 strands	2 bars + 6 strands
A_e/m	274 mm	229 mm	411 mm

CEB-FIP Model Code 1978

The CEB-FIP Model Code 1978 (MC 78) method overestimated crack widths at most load levels for the three section types investigated. The MC 78 crack width model is based on the average crack spacing and average steel strain (accounting for tension stiffening), as shown in Eq. 2.7. Selected measured and calculated crack width data is shown in Table 2.17.

$$w_k = S_m \varepsilon_{sm} \qquad \qquad \textit{Eq. 2.7}$$

where:

w_k = characteristic crack width, mm

S_m = average crack spacing, mm

ε_{sm} = mean steel strain for reinforcement situated in the effective embedment section, taking into account the contribution of the concrete in tension

with:

$$S_m = 2\left(c + \frac{s}{10}\right) + \kappa_1 \kappa_2 \frac{\phi}{\rho_r}$$

$$\varepsilon_{sm} = \frac{\sigma_s}{E_s}\left[1 - \beta_1\beta_2\left(\frac{M_{cr}}{M}\right)^2\right] \geq 0.4\frac{\sigma_s}{E_s}$$

where:

c = concrete cover, mm

s = spacing of reinforcing bars, mm ($\leq 15\phi$)

ϕ = bar diameter, mm

κ_1 = coefficient for bond properties of steel

     = 0.4 for deformed reinforcing bars

     = 0.8 for smooth reinforcement, including prestressing strand

κ_2 = coefficient for strain profile within effective embedment zone

     = $0.25(\varepsilon_1 + \varepsilon_2)/2\varepsilon_1$

ε_1 = concrete strain at top of effective embedment zone

ε_2 = concrete strain at bottom of effective embedment zone

ρ_r = $A_s/A_{c,ef}$

A_s = total steel area within $A_{c,ef}$, including bonded prestressing steel, mm^2

$A_{c,ef}$ = effective embedment zone, mm^2: zone of concrete in tension where the reinforcement can effectively influence the crack widths. $A_{c,ef}$ is determined as shown in Figure 1.??. The procedure is to superimpose a square with dimensions of 15ϕ centered on each reinforcing bar/strand to determine the extent of $A_{c,ef}$. In slabs, the height of $A_{c,ef}$ is bounded by (h – c)/2.

σ_s = stress in nonprestressed reinforcement calculated for a cracked section under the combination of actions being considered, MPa

E_s = elastic modulus of steel, MPa

β_1 = coefficient for bond properties of steel

  = $1/(2.5\kappa_1)$

β_2 = coefficient for influence of loading duration/application

  = 1 for first loading

  = 0.5 for sustained or repeated loading

M_{cr} = cracking moment for the section under consideration, kN-m

M = applied moment for the combination of actions being considered, kN-m

Table 2.17 - Selected Data for MC 78 Crack Width Expression

Variable	Non-PS	2/3 PS	100%U PS
applied moment	310 kN-m	310 kN-m	360 kN-m[**]
calculated crack spacing, S_m	167 mm	183 mm	295 mm
measured crack spacing, S_{meas}	135 mm	312 mm	574 mm
average steel strain, ε_{sm}	0.00137	0.00087	0.00092
maximum steel strain, ε_{s2}	0.00160	0.00107	0.00105
calculated crack width, w_c	0.39 mm	0.27 mm	0.46 mm
measured crack width, w_{meas}	0.36 mm	0.18 mm	0.19 mm
w_{meas}/S_{meas}	0.00267	0.00058	0.00033

** Note: The higher load level for the 100%U PS section corresponds to the moment required for multiple crack formation.

The relationship between measured crack width, measured crack spacing and calculated average steel strain is not a direct relationship for the three section types (levels of prestress) investigated in this testing program. As the level of prestress increases, the error in calculated crack width increases. If the measured crack spacing is substituted for the calculated crack spacing, the error in calculated crack widths will be even larger.

MC 78 appears to have two major deficiencies that make it unsuitable for estimating crack widths for a combination of mild steel and prestressed reinforcement. First, the average crack spacing is increasingly underestimated as the level of prestress increases. The error was almost 100% for the 100%U PS section. Second, the approach seems to be fundamentally flawed in that a direct relationship between crack width, crack spacing and average steel strain does not exist over a range of prestress.

CEB-FIP Model Code 1990

The CEB-FIP Model Code 1990 (MC 90) method provided a very good estimate of crack widths for the 100%U PS section. Calculated crack widths for the Non-PS and 2/3 PS sections were consistently underestimated. The MC 90 crack width model is based on the length over which slip occurs between the steel and concrete near a crack and the difference between the average steel and concrete strains within this length, as shown in Eq. 2.8. The term $(\varepsilon_{s2} - \beta\varepsilon_{sr2})$ represents the difference between steel and concrete strains within the length of slip, accounting for tension stiffening. Selected calculated and measured crack width data is shown in Table 2.19.

$$w_k = L_{max}(\varepsilon_{sm} - \varepsilon_{cm})$$
$$= L_{max}(\varepsilon_{s2} - \beta\varepsilon_{sr2})$$

Eq. 2.8

where:

w_k = characteristic crack width, mm

L_{max} = length over which slip between the steel and concrete occurs, mm

ε_{sm} = average steel strain within L_{max}

ε_{cm} = average concrete strain within L_{max}

ε_{s2} = steel strain at the crack, calculated for a cracked section under the combination of actions being considered

β = empirical factor to assess average strain within L_{max} (see Table 2.18)

ε_{sr2} = steel strain at the crack, under forces causing f_{ctm} within $A_{c,ef}$. ε_{sr2} is analogous to the cracked section steel strain calculated at the cracking moment and is approximated in MC 90 by the following expression. ε_{sr2} should not be taken greater than ε_{s2}.

$$\varepsilon_{sr2} = \frac{f_{ctm}}{\rho_{s,ef}E_s}\left(1 + \alpha_e\rho_{s,ef}\right)$$

f_{ctm} = mean value of concrete tensile strength at the time of cracking, MPa

$\rho_{s,ef}$ = effective reinforcement ratio, $A_s/A_{c,ef}$

A_s = steel area within $A_{c,ef}$, mm^2

$A_{c,ef}$ = effective area of concrete in tension, as illustrated in Figure 2.110, mm^2

α_e = E_s/E_c (E_c at the time of cracking)

Table 2.18 - Values of β and τ_{bk} for MC 90

	Single Crack Formation		Stabilized Cracking	
	β	τ_{bk}	β	τ_{bk}
Short term/instantaneous loading	0.6	$1.8f_{ctm}$	0.6	$1.8f_{ctm}$
Long term/repeated loading	0.6	$1.35f_{ctm}$	0.38	$1.8f_{ctm}$

The length of slip, L_{max}, is dependent on the phase of cracking for the combination of actions being considered. Slightly different provisions are provided for reinforced concrete and prestressed concrete, but some simplifications are permissible to give a generalized form.

Single Crack Formation Phase

The single crack formation phase is defined as follows:

$\rho_{s,ef}\sigma_{s2} \le f_{ctm}\left(1 + \alpha_e\rho_{s,ef}\right)$ for reinforced concrete members

$\Delta F_{s+p} \le f_{ctm}A_{c,ef}$ for prestressed concrete members

where:

σ_{s2} = steel stress at the crack, calculated for a cracked section under the combination of actions being considered, MPa

ΔF_{s+p} = force in tensile reinforcement after decompression, kN

= $A_s\sigma_s + A_p\Delta\sigma_p$ (expressions are provided in MC 90 to estimate σ_s and $\Delta\sigma_p$, or they may be calculated using first principles)

$$L_{max} = \frac{1}{\lambda}\left[\frac{\sigma_{s2}\phi_s}{2\tau_{bs,k}} + \frac{\Delta\sigma_p\phi_p}{2\tau_{bp,k}}\right] \quad \textit{for single crack formation}$$

where:

λ = 1 for reinforced concrete

= 2 for combinations of mild steel reinforcement and prestressing steel

ϕ_s = reinforcing bar diameter, mm

ϕ_p = prestressing steel diameter, mm

$\tau_{bs,k}$ = characteristic bond stress for deformed reinforcing bars, MPa

= $1.8f_{ctm}$

$\tau_{bp,k}$ = characteristic bond stress for prestressing steel, MPa

= $0.36f_{ctm}$ for post-tensioning tendons with smooth bars or wires

= $0.72f_{ctm}$ for post-tensioning tendons with strands or indented wires

	=	1.08f_{ctm} for post-tensioning tendons with ribbed bars
	=	1.08f_{ctm} for pretensioned tendons with ribbed bars
	=	0.72f_{ctm} for pretensioned tendons with strands

Stabilized Cracking Phase

The stabilized cracking phase is defined as follows:

$$\rho_{s,ef}\sigma_{s2} > f_{ctm}\left(1+\alpha_e\rho_{s,ef}\right) \qquad \text{for reinforced concrete members}$$

$$\Delta F_{s+p} > f_{ctm}A_{c,ef} \qquad \text{for prestressed concrete members}$$

$$L_{max} = \frac{\phi_s}{3.6(\rho_{s,ef}+\xi_1\rho_{p,ef})} \qquad \textit{for stabilized cracking}$$

where:

$\rho_{p,ef}$ = effective prestressed reinforcement ratio, $A_p/A_{c,ef}$

A_p = prestressed steel area within $A_{c,ef}$, mm^2

ξ_1 = $(\tau_{bp,k}\phi_s)/(\tau_{bs,k}\phi_p)$

The basic concept for the MC 90 model appears more appropriate for mixed reinforcement elements than the MC 78 model. The length of slip (L_{max}) approach appears to better represent the actual cracking behavior for the levels of prestress investigated, particularly at higher prestress levels. The MC 90 model recognizes two different cracking conditions: single crack formation and stabilized cracking. Looking at the data in Table 2.19, the Non-PS beam type reaches the stabilized cracking condition soon after exceeding the cracking moment. In contrast, the 100%U PS section remained in the single crack formation condition over the range of loading investigated. This predicted behavior correlates well with observed crack formation where the Non-PS beams rapidly developed a large number of closely spaced cracks and the 100%U PS beams developed only three widely spaced cracks. The MC 90 expressions for determining L_{max} also account for the different bond properties of mild steel bars and prestressing steel.

Table 2.19 - Selected Data for MC 90 Crack Width Expression

$M_{applied}$ (kN-m)		L_{max} (mm)	Crack Type	ε_{s2}	ε_{sr2}	w_{calc} (mm)	w_{meas} (mm)
Non-PS							
M_{cr}	117.6	144	Single	0.00060	0.00079	0.035	0.070
	185.1	188	Stabilized	0.00095	0.00079	0.090	0.186
	250.9	188	Stabilized	0.00129	0.00079	0.154	0.264
M_{serv}	310.7	188	Stabilized	0.00160	0.00079	0.212	0.318
	377.1	188	Stabilized	0.00194	0.00079	0.277	0.367
2/3 PS							
M_{cr}	247.1	169	Single	0.00054	0.00147	0.036	0.107
	293.5	274	Single	0.00092	0.00164	0.101	0.160
M_{serv}	310.7	231	Stabilized	0.00107	0.00164	0.099	0.178
	339.8	231	Stabilized	0.00132	0.00164	0.122	0.206
	385.5	257	Stabilized	0.00174	0.00181	0.178	0.245
100%U PS							
$M_{cr,serv}$	313.0	163	Single	0.00050	0.00775	0.032	0.067
	345.5	262	Single	0.00089	0.00870	0.094	0.123
	376.6	372	Single	0.00134	0.00870	0.199	0.222
	406.7	484	Single	0.00182	0.00965	0.353	0.392

In spite of providing a better representation of the actual cracking behavior in terms of crack formation, the MC 90 model underestimates crack widths for the Non-PS and 2/3 PS beam types. As a concept, the MC 90 approach appears very good. However, many simplifications have been made in the model to facilitate hand calculation. Most notable are ε_{sr2} (cracked section steel strain at M_{cr}) and the steel stresses (σ_{s2} and $\Delta\sigma_p$) under the desired loading. In addition, some of the calculations were derived for tension members and have been simply applied to flexural members. It is not clear whether the model has been calibrated for the simplified hand calculations. The simplification of the calculations could possibly lead to errors if more precise methods are used to determine the necessary stresses and strains.

Another possible source of difference between the estimated and measured crack widths is the strains used in Eq. 2.8. Many assumptions and approximations were necessary for the development of the tension stiffening model used to determine the strains influencing cracking. The term ($\varepsilon_{s2} - \beta\varepsilon_{sr2}$) in Eq. 2.8 represents the difference between the average steel and concrete strains within the length of slip. The variable β is an integration factor for the steel strain along the slip length and is taken as 0.6 in most situations. Based on the calculated values of L_{max}, it appears that the value of β could range from zero to 0.6. Test data for each beam type is plotted in Figure 2.111, Figure 2.112 and Figure 2.113 along with calculated crack widths using $\beta = 0$ and $\beta = 0.6$. The range of β provides an upper and lower bound for the measured data for each of the three beam types.

Conceptually, the CEB-FIP 1990 Model Code method for crack width prediction is appealing, as it addresses many factors often overlooked. However, in its present form the estimated crack widths were unconservative for most of the beams testing in this research program.

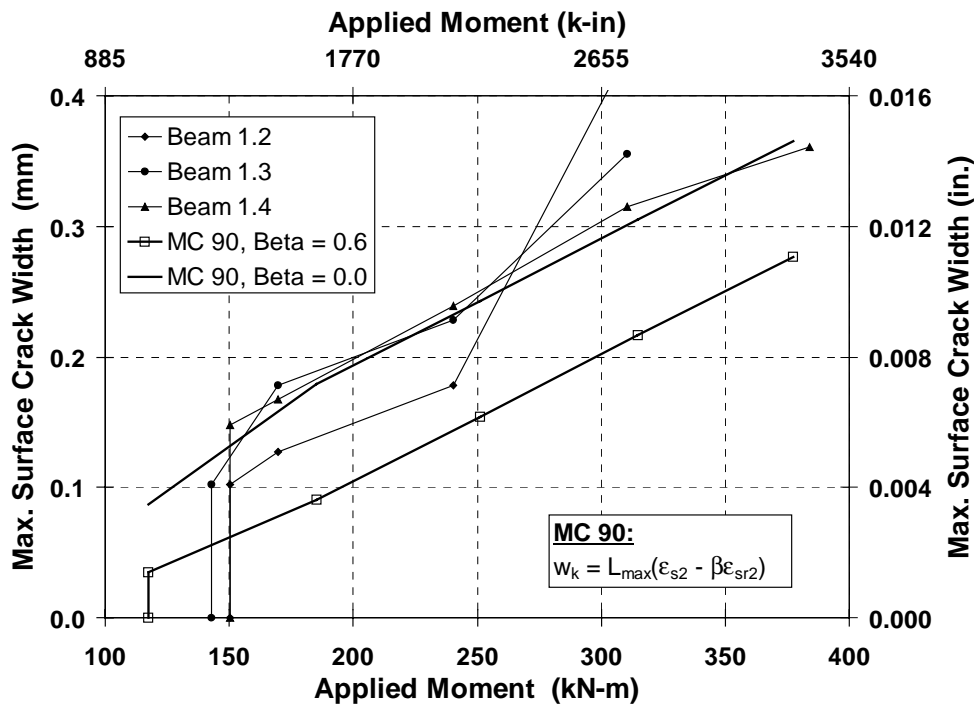

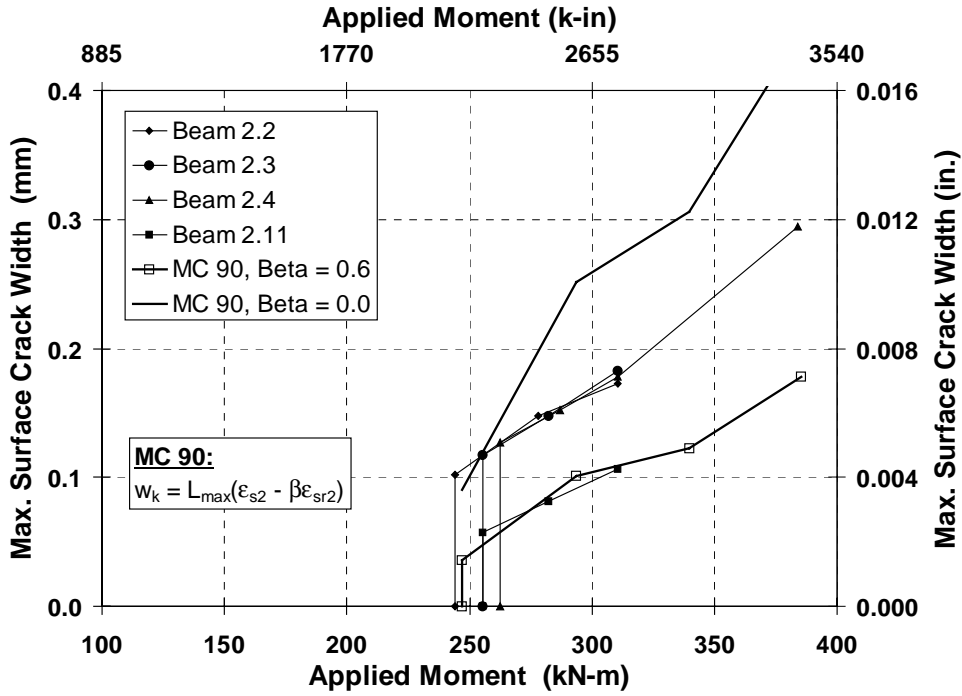*Figure 2.111 - MC 90: Upper and Lower Bound Crack Prediction for Non-PS Beams*

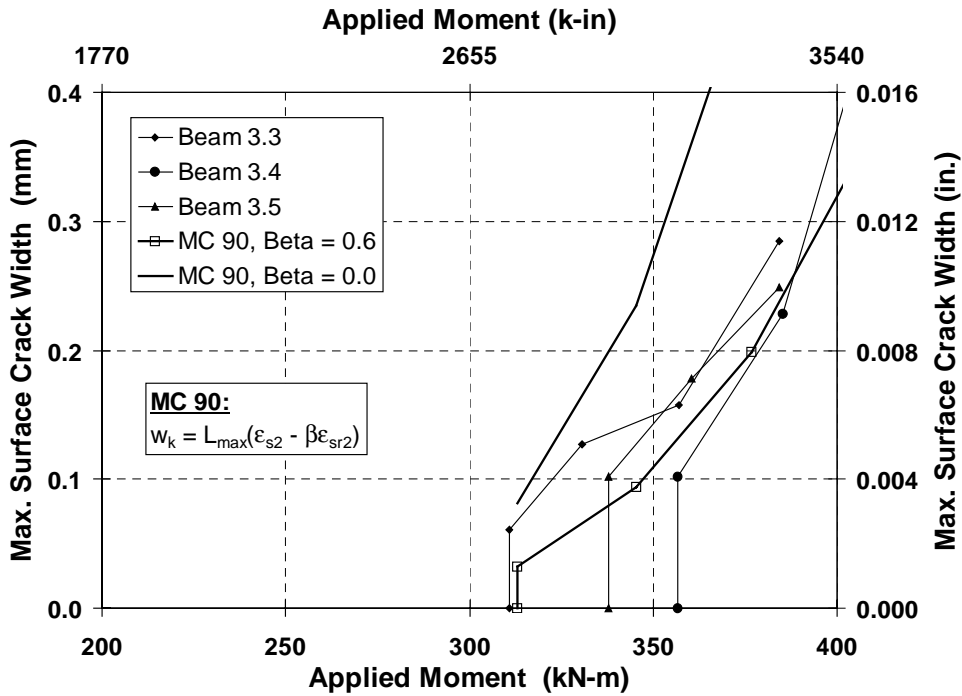*Figure 2.112 - MC 90: Upper and Lower Bound Crack Prediction for 2/3 PS Beams*

Figure 2.113 - MC 90: Upper and Lower Bound Crack Prediction for 100%U PS Beams

Batchelor and El Shahawi Expression

The Batchelor and El Shahawi crack width expression is based on a statistical analysis of test data from five different experimental investigations of cracking in partially prestressed members. The Batchelor and El Shahawi expression, shown in Eq. 2.9, provided an excellent estimation of maximum surface crack width for the 2/3 PS and 100%U PS beam types. Batchelor and El Shahawi selected the simple form of Eq. 2.9 after concluding that the very large scatter of the test data did not justify a more complicated model. This simple model appears to be more than adequate for crack width prediction for the 2/3 PS and 100%U PS beam types.

$$w_{max} = \frac{0.96f_s - 46}{1000} \quad (mm) \qquad\qquad Eq.\ 2.9$$

where:

w_{max} = maximum surface crack width, mm

f_s = stress in nonprestressed reinforcement calculated for a cracked section under the combination of actions being considered, MPa

Suri and Dilger Expression

The Suri and Dilger crack width expression is based on a statistical analysis of test data from 245 beams in eighteen different experimental investigations of cracking in partially prestressed members. The Suri and Dilger expression, shown in Eq. 2.10, significantly overestimated crack widths for the 2/3 PS and 100%U PS beam types.

$$w_{max} = k\,f_s\,c\left(\frac{A_t}{A_s + A_p}\right)^{0.5} \quad (mm) \qquad\qquad Eq.\ 2.10$$

w_{max} = maximum surface crack width, mm
k = factor to account for different bond properties of various steels
    = 2.55×10^{-6} for combinations of reinforcing bars and prestressing strands
    = 3.51×10^{-6} for combinations of reinforcing bars and prestressing wires
    = 2.65×10^{-6} for prestressing strands only
    = 4.50×10^{-6} for prestressing wires only
f_s = stress in nonprestressed reinforcement calculated for a cracked section under the combination of actions being considered, MPa
c = concrete cover from the tensile face to the center of the nearest bar, mm
A_t = area of concrete in tension below the neutral axis (see Figure 2.110), mm^2
A_s = area of mild steel reinforcement in tension zone (A_t), mm^2
A_p = area of prestressing steel in tension zone (A_t), mm^2

It is difficult to determine any reasons for the poor performance of the Suri and Dilger expression. One possible explanation could be the variable A_t: the area of concrete in tension below the neutral axis. Most crack width prediction methods define the area of concrete in tension as only a portion of the concrete area below the neutral axis as shown in Figure 2.110. MC 90 limits the effective area of concrete in tension to one-third of the concrete below the neutral axis. Overestimation of the concrete area in tension could account for overestimation of crack widths in the Suri and Dilger expression. In its present form, the Suri and Dilger does not appear to be suitable for the beam types investigated in this testing program.

2.10.2 Corrosion Rate Measurements

Several observations based on the corrosion rate measurements performed on the Phase I beams after seven, twelve and fifteen months of exposure testing are listed below. Discussion of the observations is provided in the following sections.

1. Moderate to high corrosion rates are indicated in the majority of test specimens by both the 3LP and PR Monitor equipment.

2. PR Monitor measurements at seven and fifteen months are similar in magnitude, as shown in Figure 2.114. The percent change from seven to fifteen months is plotted in Figure 2.115. Fifteen-month data shows lower corrosion rates for several beams, particularly Beams 2.11, 3.1, 3.2 and 4.2.

3. 3LP measurements at twelve and fifteen months are also similar in magnitude, as shown in Figure 2.114 and indicate very high corrosion rates. Similar to the PR Monitor data, fifteen-month corrosion rates are lower for several beams in the 3 and 4 series (100%U PS and 100%S PS). The percent change from twelve to fifteen months is plotted in Figure 2.115. In general, the 3LP data is more consistent over time than the PR Monitor data.
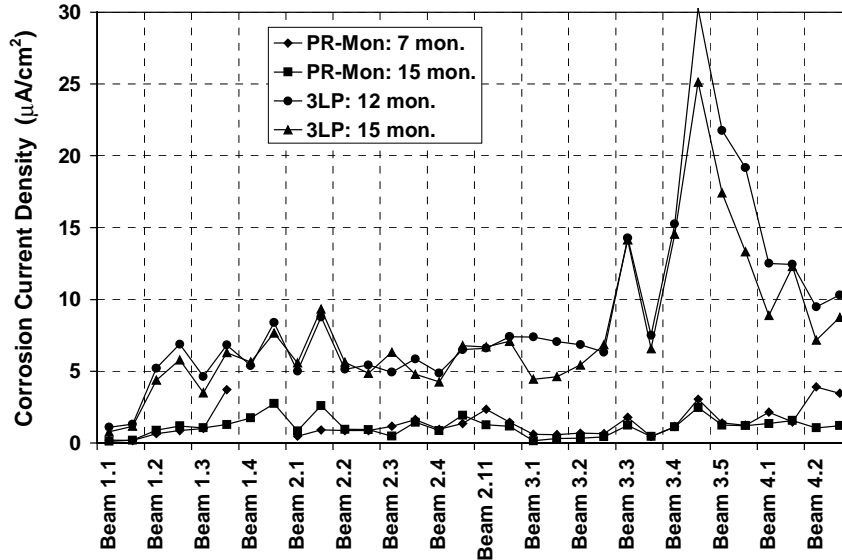

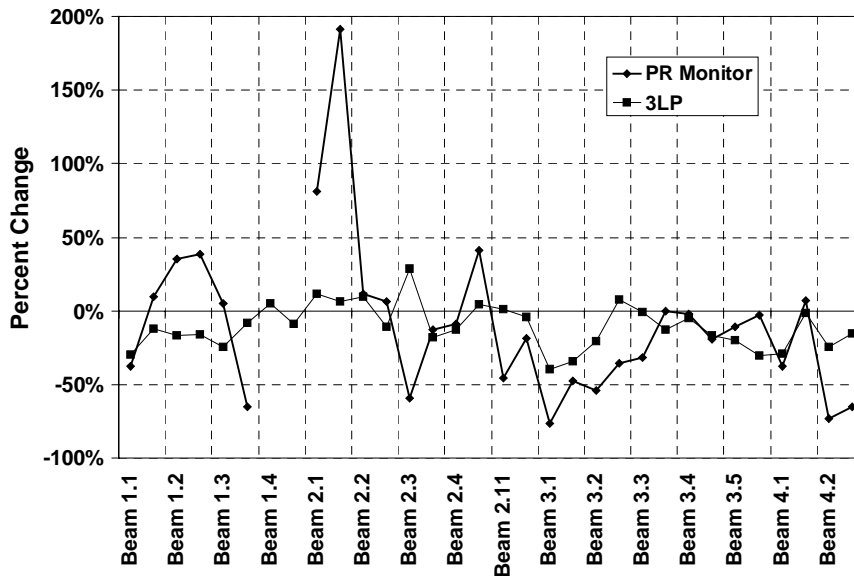*Figure 2.114 - Comparison of 3LP and PR Monitor Data*

Figure 2.115 - Change in Measured Corrosion Rates Over Time
(PR Monitor 7 to 15 months, 3LP 12 to 15 months)

103

4. 3LP corrosion rates are consistently higher than PR Monitor corrosion rates, as shown in Figure 2.114. This observation, and observations 2 and 3 above, suggest that the 3LP data should not be directly compared to the PR Monitor data.

5. The measured corrosion rates indicate that corrosion activity is related to cracking. However, the data presents contradictory relationships:

- Comparing the four series (levels of prestress), the measured corrosion rates tend to be highest in the specimens with more prestress and less cracking (Series 3 and 4, 100%U PS and 100%S PS respectively). These results are not intuitive and contradict the corrosion activity indicated by the half-cell potential readings.

- Examining each series (level of prestress) individually, the results indicate that higher corrosion rates are associated with cracked concrete. These results are most pronounced in Series 1 and 3. Within the Non-PS beams (Series 1), the corrosion rate for Beam 1.1 (unloaded and uncracked) is much lower than the corrosion rates for the remaining Series 1 beams that are loaded and cracked. In 100%U PS beams (Series 3), Beam 3.1 and 3.2 are uncracked, while Beams 3.3, 3.4 and 3.5 are cracked. Measured corrosion rates for Beams 3.1 and 3.2 are considerably lower than measured rates for the other Series 3 beams.

- Corrosion rate measurements on individual beams show higher corrosion rates at crack locations in comparison to uncracked locations. In Beams 2.1, 3.3, 3.4 and 3.5, crack patterns resulted in one reading at a crack location and one reading on uncracked concrete. In each case, the corrosion rate was higher for the measurement at the crack location. Seven- and twelve-month data is shown in Figure 2.116. These trends were also shown for fifteen-month data.

Corrosion Rates ($\mu A/cm^2$)		
Beam 2.1	**Midspan**	**Offset**
7 month	0.465	**0.893**
12 month	5.00	**8.76**
Beam 3.3	**Midspan**	**Offset**
7 month	**1.78**	0.447
12 month	**14.3**	7.50
Beam 3.4	**Midspan**	**Offset**
7 month	1.14	**3.05**
12 month	15.2	**30.3**
Beam 3.5	**Midspan**	**Offset**
7 month	**1.40**	1.23
12 month	**21.8**	19.2
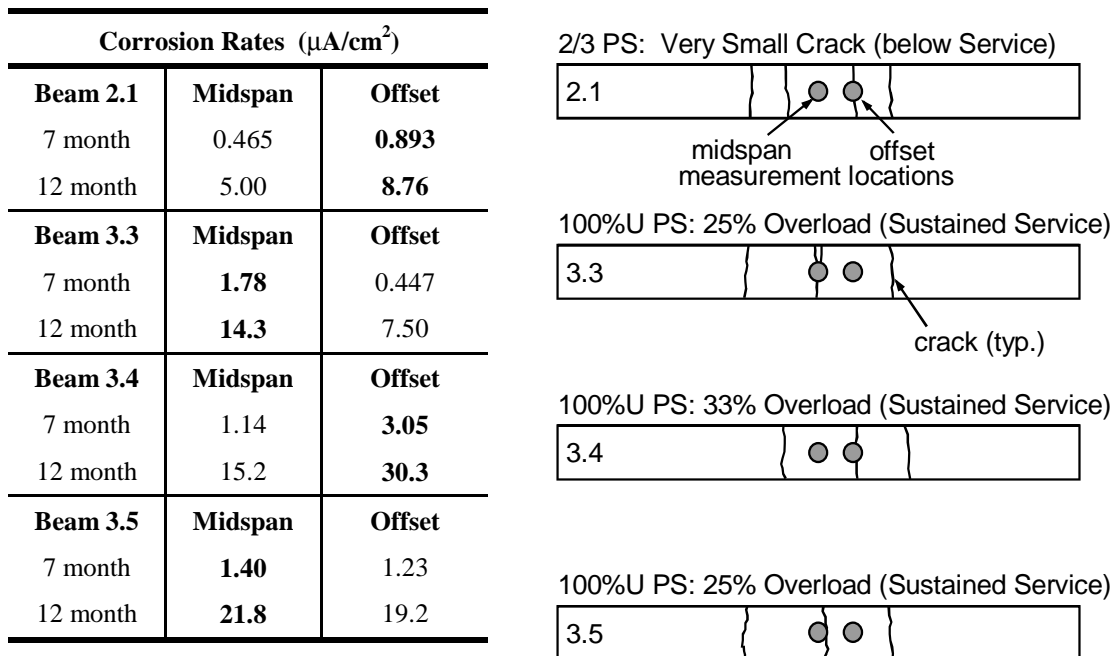
Figure 2.116 - Effect of Crack Location on Measured Corrosion Rate

2.10.2.1 High Corrosion Rates

Measured corrosion rates were very high, particularly those obtained using the 3LP device. The corrosion rate data illustrates the severe exposure conditions used in the test method. However, it is possible that the short dry period could contribute to overestimate corrosion rates if the moisture content of the concrete remained high during this short period. Elevated moisture content will decrease the resistivity of the concrete, leading to higher corrosion rate measurements. Corrosion rates will decrease as the concrete dries out.

2.10.2.2 Changes in Corrosion Rates Over Time

The changes in corrosion rate over time can be examined by comparing the seven and fifteen-month PR Monitor data (see Figure 2.114) and by comparing the twelve and fifteen-month 3LP data (see Figure 2.114). The percent change for the PR Monitor and 3LP were shown previously in Figure 2.115.

The changes in measured corrosion rates over time are generally within +/- 50%, with corrosion rates decreasing more frequently than increasing. The largest measured increase occurred in Beam 2.1, where increases were almost 200% at the offset location. The 3LP data appears to be more consistent over time. This increased consistency may be influenced by the shorter time period between readings for the 3LP readings. As mentioned previously, both the 3LP and PR Monitor data indicated a notable decrease in corrosion rate for several specimens, particularly Beams 3.1, 3.2 and 4.2. The changing moisture contents during the dry portion of the exposure cycle could possibly explain these lower corrosion rates at fifteen months. The fifteen-month data was collected at the end of the two-week dry portion of the exposure cycle, whereas the seven and twelve-month data was collected midway through the dry period. It is possible that the longer dry period before the fifteen-month measurements resulted in higher measured resistances and decreased corrosion activity in some specimens. This effect could be more pronounced for the uncracked specimens, including 3.1, 3.2 and 4.2.

The changes in measured corrosion rates for different specimens highlights the importance of regular measurements. In spite of the controlled environment (in comparison to structures in service), some corrosion rates increased and others decreased. Conclusions based on a single set of corrosion rate data should not be relied on to assess the condition of a specimen or structure.

### 2.10.2.3 Differences Between 3LP and PR Monitor Measured Corrosion Rates

The 3LP corrosion rates are significantly higher than the PR Monitor corrosion rates. The average difference for the fifteen-month data was more than 700%, with maximum and minimum increases of 2968% and 178%, respectively (measured corrosion rates for all specimens are listed in Table 2.13). The trends in corrosion activity indicated by the two devices are similar. This similarity in trends suggests that the large discrepancy in magnitude is likely due to inherent differences between the two devices.

The PR Monitor and 3LP equipment both use the three-electrode technique for measuring polarization resistance. However, several differences exist between the two pieces of equipment. The 3LP equipment represents the first generation of polarization resistance equipment for measuring corrosion rates of steel in concrete. The PR Monitor reflects several advancements, including the use of a guard ring electrode to confine the polarizing signal of the counter electrode and measurement of the concrete resistance to compensate for solution resistance. The possible effects of these differences are discussed below.

Polarized Area

The polarized area and the effect of the guard ring electrode could produce a significant difference between the 3LP and PR Monitor measurements. The unconfined counter electrode of the 3LP could lead to diffusion of the polarizing signal and a larger than expected polarized steel area. A larger polarized area would require more current to obtain the desired overvoltages, resulting in a lower polarization resistance and larger corrosion current, i_{corr}. If diffusion of the polarizing signal occurs but the polarized area is assumed to be that of the counter electrode, the corrosion rate or current density will be overestimated as shown in Figure 2.117.

The relationship between the polarized area and the measured polarization resistance is inversely proportional for a bar that is corroding uniformly. Thus, the error in the measured current density corresponds directly to the difference between the assumed polarized area and the actual polarized area. That is, if the actual polarized area is 50% larger than the assumed polarized area, the current density will be overestimated by 50%.

counter electrode

possible diffusion of polarizing signal

Ap1

Ap2

uniformly corroding bar current density = i
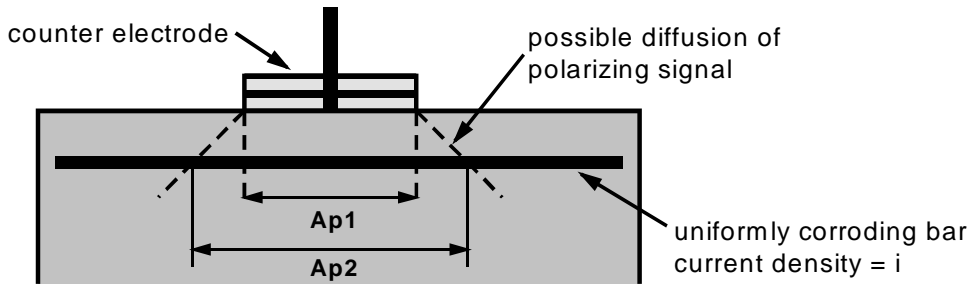
Case 1: Polarized area is A_{p1}

ΔE (mV)

20
15
10
5

Slope = R_{p1} > R_{p2}

-5
-10
-15
-20

I_{app}

ΔI_1

Case 2: Assumed polarized area is A_{p1}, but actual polarized area is A_{p2}

ΔE (mV)

20
15
10
5

Slope = R_{p2}

-5
-10
-15
-20

I_{app}

$\Delta I_2 > \Delta I_1$
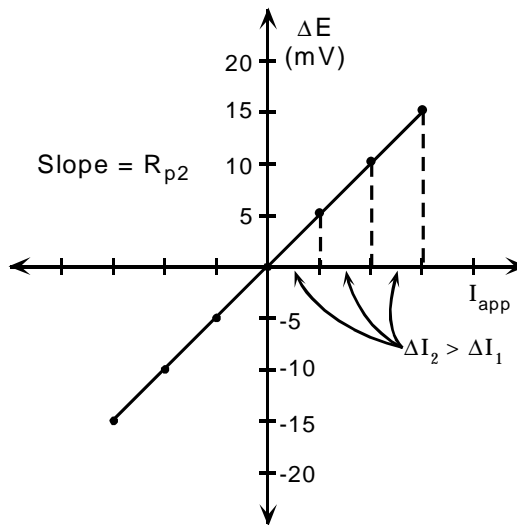
Since the polarized area is larger, more current is needed to polarize the steel. This increase results in a lower polarization resistance. As an example, assume $R_{p1} = 1.5 \, R_{p2}$.

corrosion current, $\quad i_{corr1} = \dfrac{B}{R_{p1}}$

current density, $\quad i_1 = \dfrac{i_{corr1}}{A_{p1}} = \dfrac{B}{R_{p1} \, A_{p1}}$

$i_{corr2} = \dfrac{B}{R_{p2}} = \dfrac{1.5\,B}{R_{p1}}$

$i_2 = \dfrac{1.5\,B}{R_{p1} \, A_{p1}} \quad (A_{p1} \text{ assumed})$

$i_2 = 1.5 \times i_1$ __50% error__

Figure 2.117 - Overestimation of Corrosion Rate due to Unconfined Polarization

The unconfined signal in the 3LP equipment will almost certainly lead to an overestimation of the corrosion rate. The effect of diffusion of the polarizing current can be explored by assuming different diffusion profiles. Figure 2.118 shows the 100%U PS section with the 3LP counter electrode located directly over a stirrup. Projection lines are used to illustrate the assumed polarized area if diffusion of the polarizing signal occurred at 30 and 45 degrees. Figure 2.118 is not intended to suggest that the polarizing signal would diffuse linearly, but rather to indicate the effect of diffusion for polarized areas defined in this manner. The projected areas listed in Figure 2.118 are taken at a depth of 64 mm (2.5 in.) (clear cover to duct). The resulting polarized steel areas are listed in Table 2.20 for all four section types. The polarized areas for the 100%U PS and 100%S PS sections increase significantly since some portion of the ducts are now included. The last column of Table 2.20 lists the average difference between the 3LP and PR Monitor corrosion rates at fifteen months.

Table 2.20 - Polarized Steel Areas Assuming Diffusion of the Polarizing Signal

Section	No Diffusion	Polarized Steel Area (mm^2)				Avg. Corr. Rate Increase**
		30 deg. Projection	% increase	45 deg. Projection	% increase	
Non-PS	16,720	55,738	233%	67,392	303%	361%
2/3 PS	13,300	78,540	490%	146,438	1001%	483%
100%U PS	3,040	48,137	1483%	109,956	3517%	1440%
100%S PS	3,040	30,873	915%	109,956	3517%	612%

** Percent increase, 3LP over PR Monitor at 15 months exposure.

The data in Table 2.20 indicates that diffusion of the polarizing signal over an area equivalent to a 30 degree projection of the counter electrode could approximately account for the large difference between the 3LP and PR Monitor measurements. Although it is difficult to make any firm conclusions from the limited data, it does appear that diffusion of the polarizing signal in the 3LP equipment could have a significant effect on overestimation of the corrosion rates and could possibly account for the very large difference between 3LP and PR Monitor measurements.

3LP Equipment:

Counter Electrode Area:
178 x 76 mm (7"x 3")
Ap = 3,040 sq.mm

30 deg. Projected Area:
254 x 152 mm (10"x 6")
Ap = 48,140 sq.mm

45 deg. Projected Area:
305 x 203 mm (12"x 8")
Ap = 109,960 sq.mm

Top View

3LP counter electrode

45° 30°
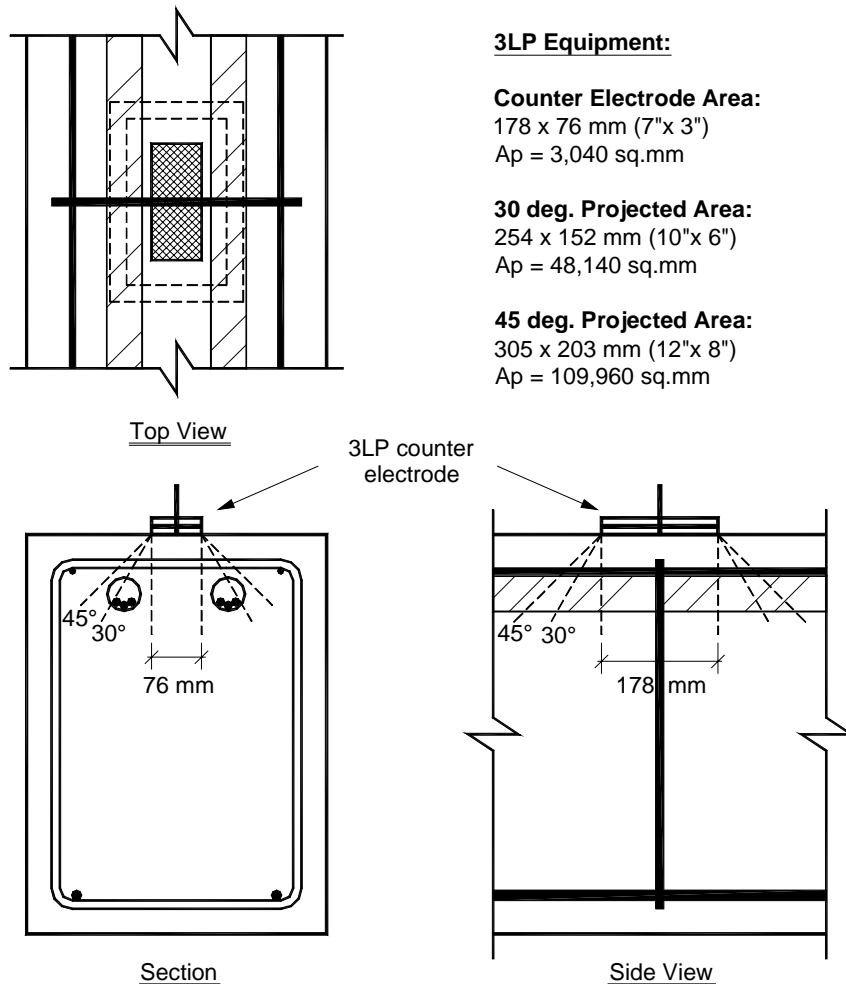
76 mm

Section

45° 30°

178 mm

Side View

Figure 2.118 - 100%U PS Beam Type: Projected Areas for 3LP Counter Electrode

The importance of signal confinement can be further illustrated using the PR Monitor. A limited data set was collected to assess the effect of the guard ring electrode in the PR Monitor. Two corrosion rate measurements, one with the guard ring enabled and one with it disabled, were taken on two beams from each series. The measured corrosion rates are listed in Table 2.21. Measurements were taken at the beam midspan of the selected specimens. Additional measurements were taken at a 1.2 m (4 ft.) offset from midspan in two of the beams. For Beams 1.2 and 2.4, the effect of the guard ring was negligible. However, for the remainder of the beams listed in Table 2.21, the effect of the guard ring is appreciable and the corrosion rates are considerably overestimated when the guard ring electrode is off. The effect is most pronounced in the 3 Series (100%U PS), where the error ranges from 67% to 124%. This result supports the previous conclusion that the unconfined polarizing signal of the 3LP is possibly leading to overestimated corrosion rates.

Table 2.21 - PR Monitor: Effect of Guard Ring Electrode

Beam	Location	Corrosion Rate ($\mu A/cm^2$)		% Difference
		Guard Ring On	Guard Ring Off	
Beam 1.2	Midspan	0.83	0.84	1.6%
Beam 1.4	Midspan	1.22	1.63	34.4%
Beam 1.4	1.2 m Offset	0.35	0.50	41.0%
Beam 2.2	Midspan	0.53	1.03	94.2%
Beam 2.4	Midspan	0.78	0.81	3.7%
Beam 3.2	Midspan	0.39	0.65	66.6%
Beam 3.5	Midspan	1.10	2.47	124.1%
Beam 3.5	1.2 m Offset	0.22	0.45	100.9%
Beam 4.1	Midspan	1.69	2.19	29.9%
Beam 4.2	Midspan	1.66	1.95	17.5%

Concrete Resistance Compensation

The PR Monitor uses AC impedance to assess the concrete or solution resistance and adjusts the measured polarization resistance to account for this error (see Section 2.8.3.2). The 3LP equipment does not account for concrete resistance, and thus solution resistance could be a possible source of difference between the measured corrosion rates.

PR Monitor: $\quad R_p = R_{tot} - R_s \qquad (R_s = \text{solution resistance})$

3LP: $\quad\quad\quad R_p = R_{tot}$

Measured corrosion current and current density are inversely proportional to polarization resistance (see Eq. 3.1). If the solution resistance is not accounted for (as in the case of the 3LP), the assumed polarization resistance will be higher than the actual polarization resistance. This higher resistance will result in a measured corrosion rate lower than the actual rate. This complication would suggest that corrosion rate measurements obtained using the 3LP equipment could be too low or unconservative. However, the polarization resistances measured using the 3LP were consistently lower than those obtained with the PR Monitor, as shown in Figure 2.119 (data shown at fifteen months exposure). Since the corrosion rates obtained using the 3LP where significantly larger than those obtained using the PR Monitor (with compensation for solution resistance), it is difficult to make any conclusions regarding the effect of solution resistance on the measured corrosion rates. It is possible that the relatively moist condition of the concrete at the time of testing minimized the effect of solution resistance.

Relationship Between 3LP and PR Monitor Data

Other research and field experience with various devices for corrosion rate measurement has consistently shown that the 3LP equipment indicates corrosion rates higher than other devices. A number of corrosion rate measurements were performed on several bridges in Texas using the 3LP and PR Monitor. The 3LP corrosion rates were consistently higher than the PR Monitor corrosion rates. A regression analysis indicated a linear relationship between the two data sets. However, due to the extremely limited data, it is not prudent to use this data further.

Another research study compared measured corrosion rates from several devices, including the 3LP, to known corrosion rates for laboratory test specimens. A device known as GECOR (three-electrode linear polarization device with solution resistance compensation) had corrosion rates very close to the actual rates. The 3LP device gave the highest corrosion rates. The researchers found a linear relationship between the logarithms of corrosion current measured by the two devices:

$$\log(i_{GECOR}) = 0.92 \log(i_{3LP}) - 0.90 \qquad\qquad \textbf{\textit{Eq. 2.11}}$$
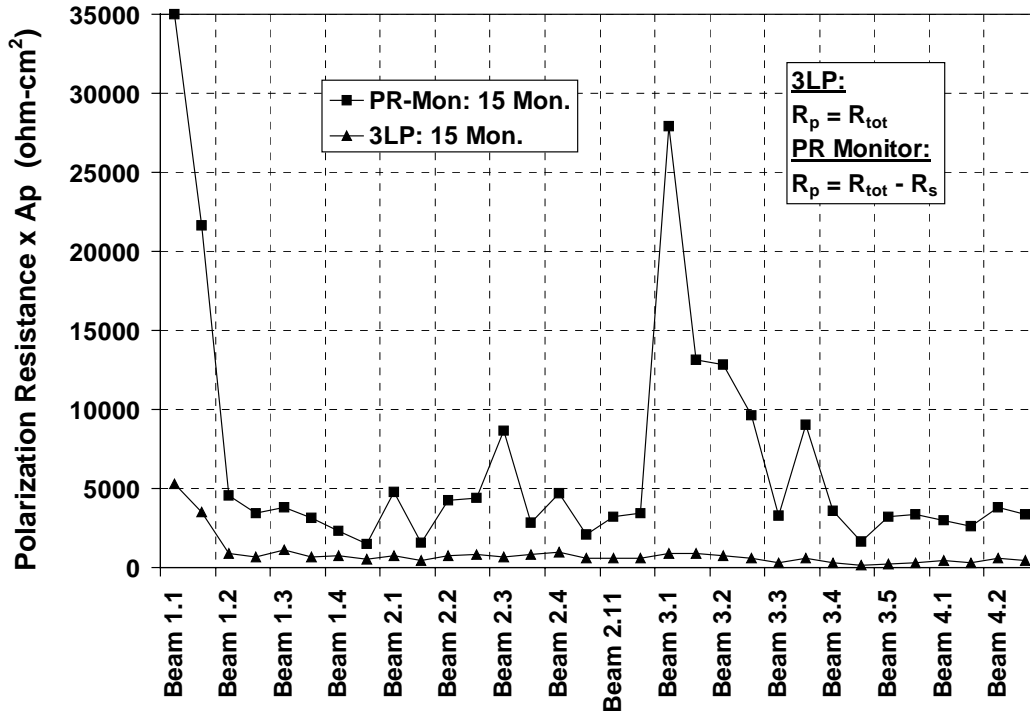

Figure 2.119 - Normalized Polarization Resistance Measured Using 3LP and PR Monitor

The corrosion rate data collected at fifteen months provides the opportunity for a direct comparison between the 3LP and PR Monitor data. When the entire data set is examined for a relationship between the two devices, the correlation is very poor. However, if each Beam Series is examined individually an approximate relationship can be determined. A linear regression analysis provided the best results. Correlation for the Non-PS and 2/3 PS beams is satisfactory, while correlation for the 100%U PS and 100%S PS beams is good. The calculated expressions are listed below.

Series 1, Non-PS:	$i_{PR} = 0.3136 (i_{3LP}) - 0.2277$	$(\mu A/cm^2)$	***Eq. 2.12***
Series 2, 2/3 PS:	$i_{PR} = 0.3099 (i_{3LP}) - 0.5560$	$(\mu A/cm^2)$	***Eq. 2.13***
Series 3, 100%U PS:	$i_{PR} = 0.1022 (i_{3LP}) - 0.2618$	$(\mu A/cm^2)$	***Eq. 2.14***
Series 4, 100%S PS:	$i_{PR} = 0.09612 (i_{3LP}) + 0.4014$	$(\mu A/cm^2)$	***Eq. 2.15***

Using Eq 2.11 and 2.12 through 2.15, calculated corrosion rates i_{GECOR} and i_{PR} were obtained using the 3LP data measured after fifteen months. The calculated corrosion rates are plotted together with the PR Monitor

measured corrosion rates after fifteen months in Figure 2.120. The calculated PR Monitor values (i_{PR}) are similar to the measured data, indicating the reasonable accuracy of Eq. 2.12 to 2.15. The calculated GECOR values (i_{GECOR}) are lower than the measured PR Monitor data for Series 1 and 2, but similar for Series 3 and 4. The good correlation between the calculated GECOR and measured PR Monitor data lends credibility to the PR Monitor results, since the GECOR device had previously been found to give the best estimation of corrosion rates.
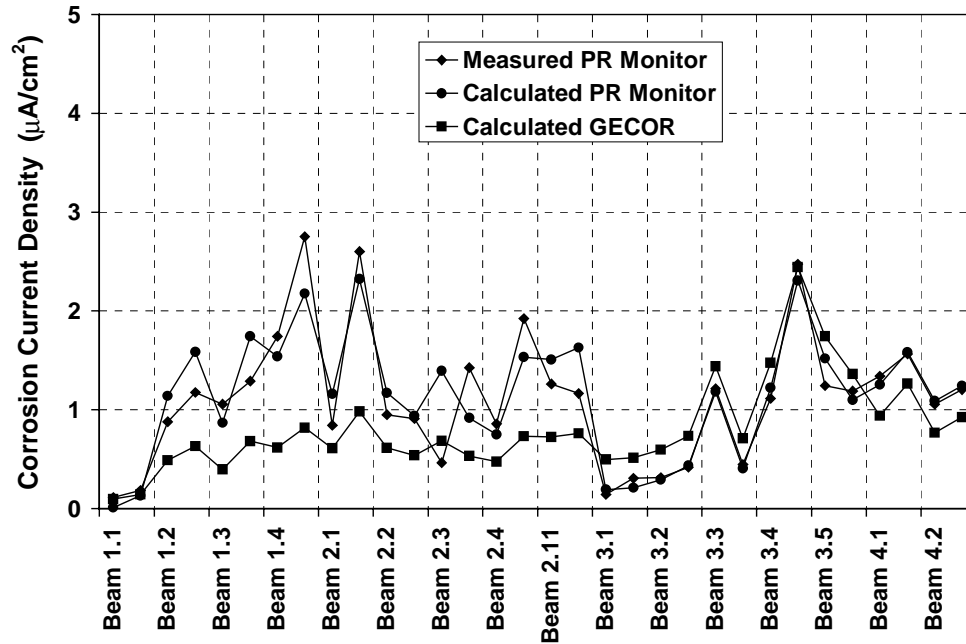

Figure 2.120 - Comparison of Measured and Calculated Corrosion Rates at 15 Months

The comparison of measured and calculated results makes it tempting to "correct" past and future 3LP data using Eq. 2.12 to 2.15. Figure 2.121 shows measured PR Monitor data at seven and fifteen months with calculated PR Monitor data at twelve months. The calculated twelve-month data is based on the twelve-month 3LP data and Eq. 2.12 to 2.15. The twelve-month data significantly overestimates the corrosion currents for the Series 3 and 4 beams, illustrating the shortcomings of this approach. The conclusion to be drawn from this comparison of data is that it is best to use a corrosion rate device with signal confinement, and it is important to account for solution resistance. That is, the PR Monitor should be used for future measurements. If it is not possible to use the PR Monitor, the 3LP device could be used and the results "corrected" using the equations listed above. Correction of the 3LP data will improve the estimated corrosion rates, but it would be preferable to use the PR Monitor.
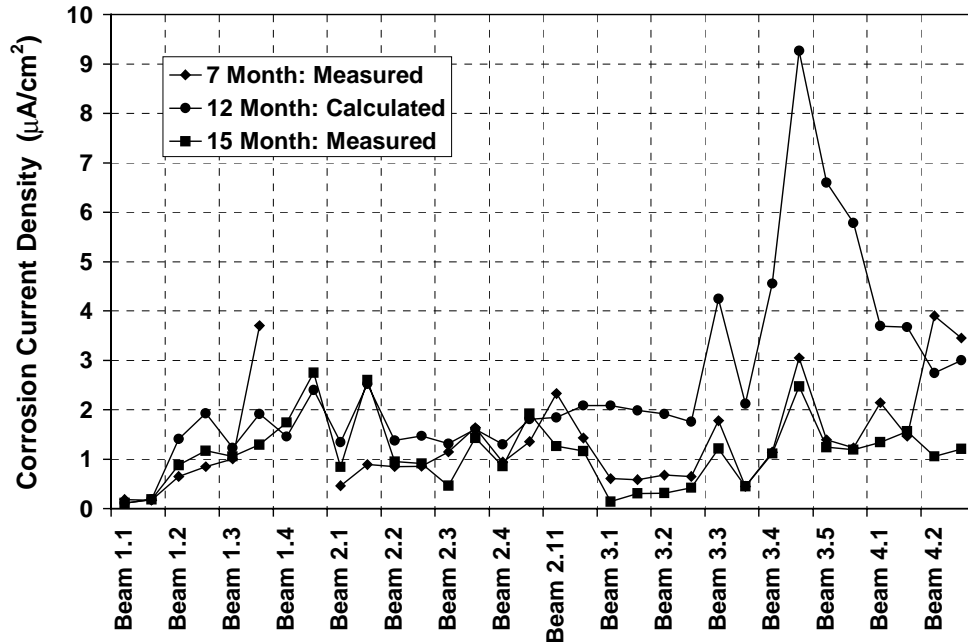
Figure 2.121 - Measured and Calculated PR Monitor Corrosion Rates

2.10.2.4 Effect of Cracks on Solution Resistance Measurement

The presence of cracks could affect the accuracy of the polarization resistance (total resistance) and the solution resistance measurements. Most guidelines for corrosion rate measurement suggest performing the tests on uncracked concrete. The solution resistance measurements obtained from the PR Monitor appear to be influenced by the presence of cracks. Table 2.22 shows values of measured solution resistance for all specimens. Measured resistances at crack locations are consistently lower than readings at uncracked locations. This trend is apparent by comparing cracked and uncracked beams and also by comparing midspan and offset measurements on Beams 2.1, 3.3, 3.4 and 3.5.

In several cases, high corrosion rates measured by the PR Monitor occurred when the solution resistance was very close to the total measured resistance. Since the polarization resistance is computed as the difference between the measured total resistance and solution resistance, the polarization resistance was very low in these cases, leading to high corrosion rates. Errors in either the total resistance or solution resistance could lead to inaccurate corrosion rates and conclusions. The presence of cracks clearly has an effect on measurement of the polarization resistance and solution resistance. However, it is difficult to assess the effect of cracks on the accuracy of the estimated corrosion rates in the test data.

Table 2.22 - Effect of Cracking on Measured Solution Resistance (PR Monitor)

Beam	Location	Condition	Solution Resistance (Ohms)	
			7 Month	**15 Month**
Beam 1.1	**Midspan**	*Uncracked*	**1560**	**2904**
	Offset	*Uncracked*	**1339**	**1886**
Beam 1.2	Midspan	Cracked	605	644
	Offset	Cracked	424	598
Beam 1.3	Midspan	Cracked	397	580
	Offset	Cracked	No data	459
Beam 1.4	Midspan	Cracked	No data	249
	Offset	Cracked	No data	194
Beam 2.1	**Midspan**	*Uncracked*	**747**	**553**
	Offset	Cracked	508	291
Beam 2.2	Midspan	Cracked	573	460
	Offset	Cracked	471	514
Beam 2.3	Midspan	Cracked	459	602
	Offset	Cracked	427	536
Beam 2.4	Midspan	Cracked	618	654
	Offset	Cracked	330	336
Beam 2.11	Midspan	Cracked	350	401
	Offset	Cracked	322	326
Beam 3.1	**Midspan**	*Uncracked*	**1547**	**4216**
	Offset	*Uncracked*	**1118**	**3066**
Beam 3.2	**Midspan**	*Uncracked*	**923**	**1738**
	Offset	*Uncracked*	**942**	**1553**
Beam 3.3	Midspan	Cracked	652	796
	Offset	*Uncracked*	**1137**	**1682**
Beam 3.4	**Midspan**	*Uncracked*	**757**	**910**
	Offset	Cracked	367	480
Beam 3.5	Midspan	Cracked	524	685
	Offset	*Uncracked*	**641**	**894**
Beam 4.1	**Midspan**	*Uncracked*	**1166**	**1365**
	Offset	*Uncracked*	**877**	**1197**
Beam 4.2	**Midspan**	*Uncracked*	**753**	**833**
	Offset	*Uncracked*	**1062**	**1353**

2.10.3   Effect of Cracking and Level of Prestress

2.10.3.1 Half-Cell Potential Readings

The reported half-cell readings indicate that the level of corrosion activity is related to the amount of cracking. The measured potentials have been averaged for each series (prestress level) in Phase I and are plotted in Figure 2.122. The highest (most negative) half-cell potentials were measured for the Non-PS beams under service loading. Potentials become less negative as the level of prestress is increased. These measurements suggest that control of cracking can reduce corrosion activity and improve corrosion protection. This finding is based on short-term data, and it will be important to see if this trend continues over long-term exposure.
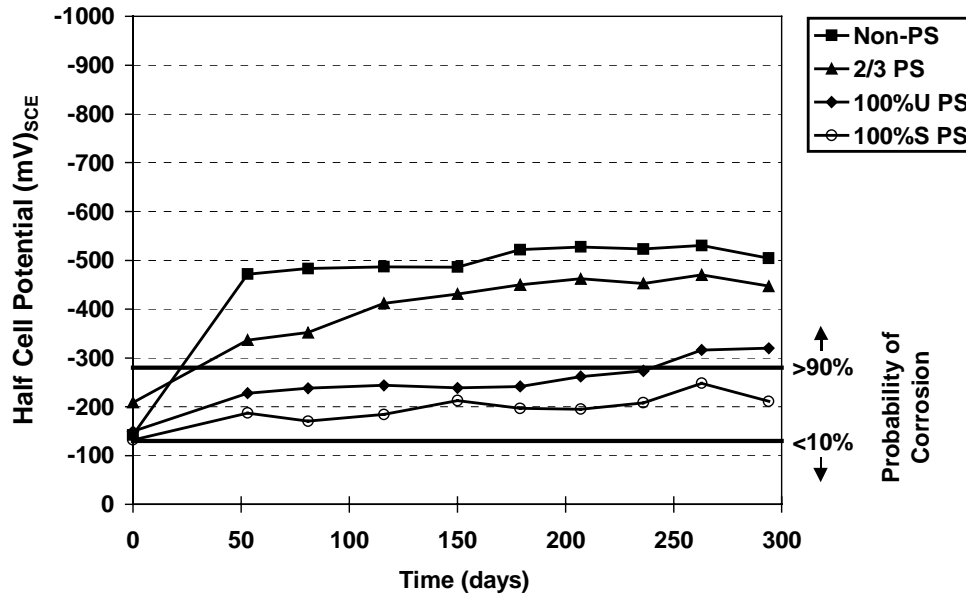
Figure 2.122 - Average Half-Cell Potentials for Each Series (Prestress Level) – Phase I Specimens

The effect of post-tensioning in members that are not cracked is illustrated in Figure 2.123. Average half-cell potentials from the ponded region are plotted for the five beams that are uncracked. Several comparisons can be made:

- Beams 1.1 and 3.1 are unloaded. Measured potentials are similar in magnitude, with Beam 1.1 slightly more negative. These results suggest no significant effect of prestress on corrosion activity in unloaded beams.

- Beams 3.1 and 3.2 are 100%U PS, with 3.1 unloaded and 3.2 subjected to service loading (uncracked). Measured potentials for Beam 3.2 are more negative, suggesting a possible increase in corrosion activity due to loading. Although no visible cracks are present in Beam 3.2, concrete tensile stresses are present (by calculation) at the ponded surface. It is possible that this tensile stress state results in a higher concrete permeability in comparison to the precompressed ponded surface of Beam 3.1.

- Beams 4.1 and 4.2 are uncracked at service loading. Measured potentials for 4.1 and 4.2 are slightly more negative than Beam 3.2. This data suggests no improvement in corrosion protection is gained by increasing the prestress level from 100%U PS (nominal strength design) to 100%S PS (allowable stress design).
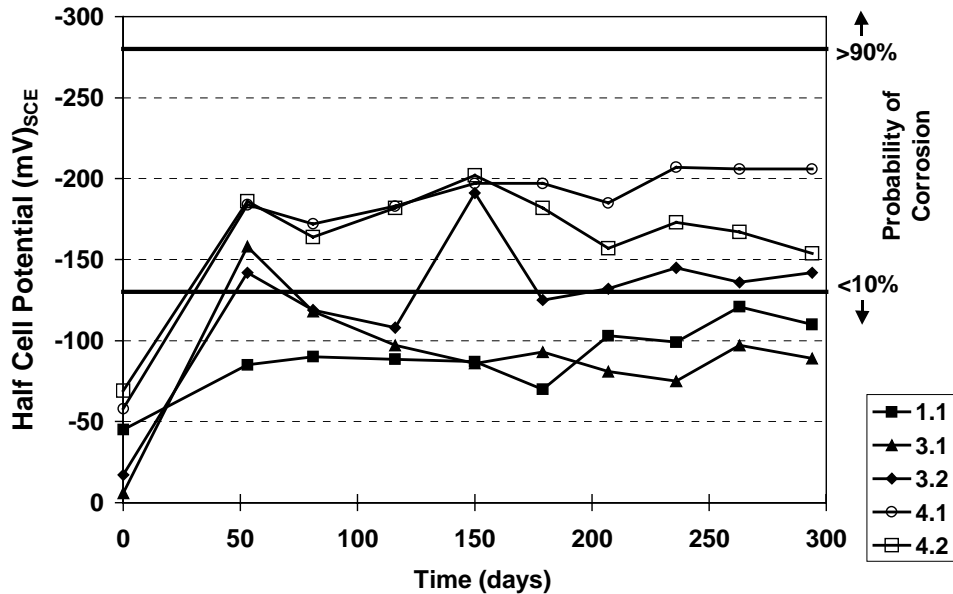
Figure 2.123 - Average Half-Cell Potentials for Phase I Uncracked Beams

2.10.3.2 Corrosion Rate Measurements

On the global scale, comparisons of corrosion rates between the different levels of prestress indicate that the 100%U PS and 100%S PS beams (Series 3 and 4) had corrosion rates comparable to or higher than Non-PS and 2/3 PS beams (Series 1 and 2). On the local scale, measured corrosion rates within Series 1, 2 and 3 indicate that higher corrosion rates are associated with cracking.   Also, corrosion rates on beams where one measurement occurred at a crack location and the other on sound concrete showed higher corrosion rates at the crack locations.

Global Scale: Corrosion Rate and Level of Prestress

The observation that measured corrosion rates (from polarization resistance equipment) for prestressed members with limited or no cracking are similar to or higher than corrosion rates for heavily cracked, nonprestressed members does not match intuition. Normally, the use of prestress would be expected to improve corrosion protection by limiting the number and width of cracks. This trend was indicated by the measured half-cell potential data. Since the corrosion rate data measured after seven, twelve and fifteen months of exposure indicates high corrosion rates for the 100%U PS and 100%S PS beams, the data warrants in-depth consideration.

It is possible that limitations or errors in the measurement of corrosion rate could explain the unexpected corrosion rates. As described in Section 2.8.3.2, many factors may introduce errors in measured corrosion rates. In this situation, the most likely errors are uncertain polarized area and unknown Tafel constants.

The effect of errors in the assumed polarized steel area was discussed in detail in Section 2.10.2.3. Underestimation of the polarized area was shown to lead to overestimation of corrosion rate. This effect was most pronounced for the 100%U PS and 100%S PS section types where diffusion of the polarizing signal could significantly increase the actual polarized area, resulting in overestimation of corrosion rates.

Calculation of the corrosion current based on measured polarization resistance requires knowledge of the Tafel constants for the conditions under investigation. The Tafel constants used in the calculations were developed for uncoated mild steel reinforcement in normal concrete. The presence of the prestressing strand and the galvanized steel duct could change the Tafel constants, affecting the accuracy of the results. Little or no research has been performed in this area, and no guidance is available at present.

Another possibility is that the intuitive assumption that prestressing will improve corrosion protection is not necessarily true, and thus the corrosion rate data is correct. Research by Schiessl and Raupach (reviewed in Research Report 1405-1 from this project) indicated that increased crack spacing would lead to higher corrosion

rates at crack locations. Their explanation was that the ratio of cathode area to anode area increased as the crack spacing increased, resulting in high anodic current densities at the crack. The crack spacing in the 100%U PS (Series 3) beams is very large compared to the Non PS and 2/3 PS beams (Series 1 and 2). Thus, the conclusions of Schiessl and Raupach could offer an explanation for the high corrosion rates in Beams 3.3, 3.4 and 3.5, particularly at crack locations. However, the work of Schiessl and Raupach does not explain the high corrosion rates in the uncracked 100%S PS (Series 4) beams. It should also be mentioned that Schiessl and Raupach's conclusions on crack spacing were based on theoretical calculations that require simplifying assumptions and were not confirmed experimentally. Continued exposure testing and invasive or forensic examinations of the beams are required to fully assess the effect of cracking and level of prestress on corrosion.

Local Scale: Corrosion Rate At Crack Locations

On the local scale, the effect of cracks is to cause increased corrosion activity in the vicinity of the crack. As mentioned previously, this effect is particularly evident for beams where one measurement was taken at a crack location and the other measurement was taken on uncracked concrete. The effect of cracking was most pronounced in Beams 2.1, 3.3 and 3.4 (see Figure 2.116), where corrosion rates at crack locations were significantly higher than rates at uncracked locations. Since all other variables are essentially equal when comparing two readings from one beam, the higher corrosion rates at crack locations can be attributed to increased penetration of chlorides at the crack.

In many cases, flexural cracks coincided with stirrup locations. Therefore, it is assumed that corrosion of the stirrups is occurring at crack locations. This assumption leads to an important observation; the corrosion rate measurement is an assessment of corrosion activity at a very local scale, in this case, the corrosion of a stirrup at a crack. This local condition could be similar whether the crack has occurred in a nonprestressed beam with many cracks, or in a prestressed beam with a very limited number of cracks. Therefore, corrosion rate measurements at cracks could be very similar for different levels of prestress and crack patterns.

The measured corrosion rate data collected in this testing program indicates that corrosion rates at cracks tend to be significantly higher than corrosion rates in uncracked concrete. This increase leads to the conclusion that the overall corrosion damage in a specimen is a function of the number of cracks in the beam. The question to debate is what criteria should be used to assess the severity of corrosion damage? Should it be the localized corrosion rate at a crack, or should it be the total amount of corrosion damage in the beam. In the latter case, post-tensioning would appear to improve corrosion protection by limiting the number of cracks and thus limiting the total amount of corrosion damage. This assumption would be an appropriate conclusion if the corrosion at the cracks was not threatening to structural integrity. Continued long-term exposure testing and invasive inspections are required to fully assess the effect of cracking.

The high corrosion rates at cracks located over stirrups warrant an additional observation. Since the crack is aligned with the stirrup, the potential for severe corrosion of the stirrup is very high. Corrosion damage to the stirrup could lead to deterioration of the shear strength of the beam. This aspect of corrosion in structural concrete is rarely considered, as most attention is given to deterioration of flexural capacity.

2.11   SUMMARY AND CONCLUSIONS

The exposure duration reported in this document will ultimately represent only a short portion of the total exposure duration the for beam corrosion tests. The preliminary test data indicates varied levels of corrosion activity, but does not suggest significant corrosion damage or corrosion related structural deterioration has occurred. Continued exposure testing and monitoring, combined with forensic examinations of the beams, will provide considerably more information and insight into corrosion in post-tensioned structural elements. The test data does present some interesting conclusions. Because the conclusions are based on preliminary data, they could be subject to change.

2.11.1 Assessing Corrosion Activity Using Half-Cell Potential Measurements

- Very negative half-cell potentials (more negative than the guidelines for high probability of corrosion) do not necessarily indicate that corrosion is occurring. Very negative half-cell potentials can result from sources other than significant corrosion activity, and therefore it is more important to consider the variation of half-cell potentials over time to assess corrosion activity.

- Although comparisons of half-cell potential data may be used with other forms of data to indicate the relative performance of the different beam types, the most important and appropriate use of the half-cell potential data is to indicate corrosion initiation by observing long-term trends in the measured data. Therefore, continued regular measurements are very important.

2.11.2 Effect of Cracking and Level of Prestress

- Half-cell potential measurements indicate that as the level of post-tensioning increases, the probability of corrosion activity decreases.

- Half-cell potentials for the 100% U PS (6 strands) and 100% S PS (8 strands) are not significantly different at this time. This similarity may indicate that the increased level of prestress obtained using the allowable stress design approach (100% S PS) may not be necessary for corrosion protection and that the 100% U PS sections will be adequate. This reduction in degree of prestressing required will result in reduced costs. The advantage of an uncracked specimen (100% S PS) may become more apparent as the exposure testing continues.

- Corrosion rate measurements indicated corrosion activity is related to cracking.

    - Corrosion rate measurements on uncracked Beams 1.1, 3.1 and 3.2 were significantly lower than measured rates on companion cracked specimens.

    - Higher corrosion rates were measured at crack locations. This finding suggests that on a local scale cracks lead to increased corrosion activity in comparison to uncracked concrete.

- Corrosion rate measurements at crack locations in post-tensioned beams were as high or higher than corrosion rates at cracks in nonprestressed beams. This finding illustrates the significance of cracking on corrosion, at least in the short term.

- Assessing the effect of post-tensioning on corrosion protection depends on the criteria used to quantify the severity of corrosion. If corrosion rates at crack locations are used as criteria, there appears to be little or no positive effect of post-tensioning. If overall corrosion damage in the structural element is considered, post-tensioning improves corrosion protection by limiting the number of cracks and thus limiting the total deterioration due to corrosion.

- Overall, the preliminary test data indicates that corrosion protection can be improved through crack control with post-tensioning.

2.11.3 Effect of Durability Variables

- Fly ash specimens have improved durability due to reduced permeability.

- High performance concrete specimens have improved durability due to reduced permeability and reduced cracking. The high performance concrete has both improved durability performance and improved strength performance. This improvement in strength may lead to structural efficiences.

- Benefits from the plastic duct, strand coatings, and encapsulated system are not likely to be fully known until final autopsy due to the difficulty in monitoring these types of materials with half-cell potentials.

2.11.4 Crack Width Prediction for Structural Concrete with Mixed Reinforcement

- Comparison of measured crack data with several crack prediction models produced widely varying results. This finding suggests that not all crack prediction methods are appropriate for structural concrete members with a combination of mild steel and prestressed reinforcement.

- The Gergely-Lutz crack width model provided an excellent prediction of maximum crack widths for the Non-PS and 2/3 PS beams and a conservative estimate for the 100% U PS beams. The Gergely-Lutz model was applied using the recommendations of Armstrong et al. This model is relatively easy to apply and is recommended for sections with mixed reinforcement.

- The Batchelor and El Shahawi crack width expression provided a very good prediction of maximum crack widths for the 2/3 PS and 100%U PS beams. This very simple model is also recommended for sections with mixed reinforcement.

2.11.5 Corrosion Rate Measurements Using Polarization Resistance

- Corrosion rate measurements were obtained using the three-electrode procedure to measure polarization resistance. Two different devices were used: 3LP and PR Monitor. The PR Monitor uses a guard electrode for signal confinement and compensates for concrete resistance.

- Corrosion rates obtained using the 3LP device were extremely high and did not correlate with specimen condition and half-cell potentials. The PR Monitor indicated lower corrosion activity than the 3LP, although moderate to high corrosion rates were indicated for most beams.

- The corrosion activity indicated by both devices, and in particular the 3LP, contradicted the half-cell potential measurements for some specimens. In general, the highest corrosion rates were obtained for the 100%U PS beams, while the most negative half-cell potentials were measured for the Non-PS beams. Numerous possible factors were investigated, but no firm conclusions could be made other than several limitations exist for the 3LP device and the polarization resistance technique in general.

- The PR Monitor appears to provide a better assessment of corrosion rate than the 3LP device. Because of differences between the devices, it is not recommended to directly compare corrosion rates obtained using the 3LP and PR Monitor.

- The 3LP device suffers from an unconfined polarizing signal. As a result, the polarized area of steel will unknowingly be larger than expected in most cases, resulting in an overestimation of corrosion rate.

- The three-electrode technique for measuring polarization resistance appears to be most useful for relative comparisons of corrosion activity rather than a quantitative assessment of corrosion rate. Relative comparisons should only be made for similar beams and similar conditions, and therefore the comparison of corrosion rates for the different levels of prestress investigated is questionable.

- In view of the preceding conclusions, corrosion rate measurements in post-tensioned concrete structures should be approached with caution and should not be relied on as a sole method to evaluate corrosion activity.

- Regular corrosion rate measurements over time are needed to assess the amount of corrosion related distress in structural concrete. Discrete measurements may occur at instances where corrosion rates are higher or lower than normal and give a false indication of the specimen or structural element condition.

- The PR Monitor is recommended for future corrosion rate measurements in this testing program. The 3LP device could be used as a second choice. 3LP corrosion rates could be "corrected" using the expressions developed in Section 2.10.2.3 for an improved estimate of corrosion rates.

2.11.6 Chloride Samples

- Chloride samples were taken from the Phase I ponding blocks at 7 and 14 months. Samples indicate negligible chlorides in the control specimens. Chloride penetration in the exposed ponding blocks is evident, but chloride content at the bar level remains negligible.

- Samples taken during the limited autopsies indicate significantly higher chloride levels in cracked regions and reduced chloride penetration in the post-tensioned specimen.

2.11.7 Limited Autopsy

- The limited autopsy revealed corrosion of a stirrup and main longitudinal reinforcement for Specimen 1.3 (Non-PS). The stirrup located under a crack showed extensive light pitting along with two concentrated areas of pitting where the crack directly intersected the steel. The longitudinal reinforcement in the location away from the crack had one isolated area of pitting.

- Specimen 3.3 (100% U PS) showed no visible corrosion at either location. The post-tensioning duct showed no signs of corrosion and was fully grouted at the inspection location.

- A stirrup under a crack was investigated in Specimen 3.4 (100% U PS) due to the staining in this location. Investigation revealed corrosion similar to that on the stirrup in Specimen 1.3.

- Staining is prevalent on many of the more heavily cracked specimens. The post-tensioned specimens, which have fewer cracks, show considerably less staining. Many of the Phase I specimens have staining in areas away from the cracks. This staining appears to be due to corrosion of the plastic-tipped bolster strips used to maintain cover during casting. The staining is unsightly and has caused spalling which reveals the plastic tips in some areas. The problem can be remedied by the use of fully plastic chairs. These chairs were used during fabrication of the Phase II specimens, and to date these specimens are showing no staining / spalling away from cracks.

- The findings from the limited autopsy indicate that corrosion is progressing in the test specimens after 15 months of exposure testing. However, to obtain beneficial comparisons between specimen types, exposure testing will need to extend for several more years for each phase of beam specimens before final autopsy.

CHAPTER 3
LONG-TERM COLUMN CORROSION TESTS

3.1   TEST CONCEPT AND OBJECTIVE

The applications of post-tensioning in bridge columns or piers have been limited in comparison to flexural members. However, some situations do exist where post-tensioning can provide an efficient structural solution. Some examples include columns or piers where large bending moments are encountered during construction or in service, or in precast segmental construction. In the latter case, post-tensioning provides continuity in the structure. Similar to flexural members, post-tensioning may have two general effects on corrosion protection in columns or piers. First, post-tensioning may improve the corrosion protection provided by the concrete by controlling cracking in the concrete. Post-tensioning may also be used to control or prevent tensile stresses across segmental joints or construction joints in columns. The second effect is that the post-tensioning system introduces additional components that may be susceptible to corrosion damage. Thus, durability design for post-tensioned columns must address how to use post-tensioning to improve corrosion protection and how to protect the post-tensioning hardware from corrosion damage.

This portion of the research project consists of long-term exposure testing of large structural concrete columns or vertical members. The specific objectives are to investigate:

1) The effect of post-tensioning on durability (corrosion protection) through precompression of the concrete and precompression of construction joints, and

2) The relative performance of various aspects of corrosion protection for post-tensioning.

The experimental program uses large-scale circular column specimens subjected to combined structural loading and aggressive exposure. The columns are cast-in-place on a large concrete foundation. The specimens are tested outside the Ferguson Structural Engineering Laboratory, and are continuously exposed to saltwater to promote corrosion activity. The majority of the columns are subjected to simulated service load conditions. The effect of post-tensioning is compared to the standard nonprestressed (reinforced concrete) column. Variables investigated are the joint between the column and foundation, loading, concrete type, prestressing bar coatings, and type of post-tensioning duct. Exposure testing began in July of 1996. This report describes the specimen design and variables, and presents exposure testing results through April of 1999.

3.2   TEST SPECIMEN

The test specimens in this experimental program are circular cast-in-place columns. The columns were patterned after standard Texas Department of Transportation (TxDOT) multicolumn substructures. Although post-tensioning would not normally be used in this type of column, it was selected for research purposes for several reasons, including constructibility, size limitations and familiarity. The column dimensions and details were selected such that covers, reinforcement sizes and post-tensioning hardware were on a similar order of magnitude as in practical applications, with consideration for construction and loading of the specimens. A nominal column diameter of 460 mm (18 in.) and height of 1.83 m (6 ft) were selected.

3.2.1   Column Design Loading
The test specimen design process began with determining the applied loading for the columns. It was decided to deviate from the design process used for the beam corrosion tests to determine the loading for the columns. In many cases, typical bridge column reinforcement is based on minimum reinforcement requirements, and the nominal capacity of the column is well in excess of the design loading dictated by analysis of the bridge. Thus, it was decided to obtain design loading for a typical TxDOT multicolumn bridge substructure. The test specimen reinforcement would be proportioned to meet minimum requirements and column capacity would be compared against the design loading. The design loading would be applied on the columns during testing. This approach would provide a more realistic representation of the typical relationship between bridge column capacity and design loading.

3.2.1.1   Prototype Substructure

The prototype bridge substructure selected for analysis was a three-column frame bent from an overpass structure, as shown in Figure 3.1. The bridge carried two lanes of traffic and one shoulder. The substructure was cast-in-place reinforced concrete (nonprestressed). The circular columns had a 762 mm (30 in.) diameter, and a clear height of 4.88 m (16 ft). The bent cap was rectangular in section with dimensions of 838 mm (33 in.) by 914 mm (36 in.). The bent was skewed to the roadway alignment at 45 degrees. The superstructure consisted of five Type C precast, pretensioned bridge girders with a 22.86 m (75 ft) span, and a 200 mm (8 in.) thick cast-in-place concrete deck.
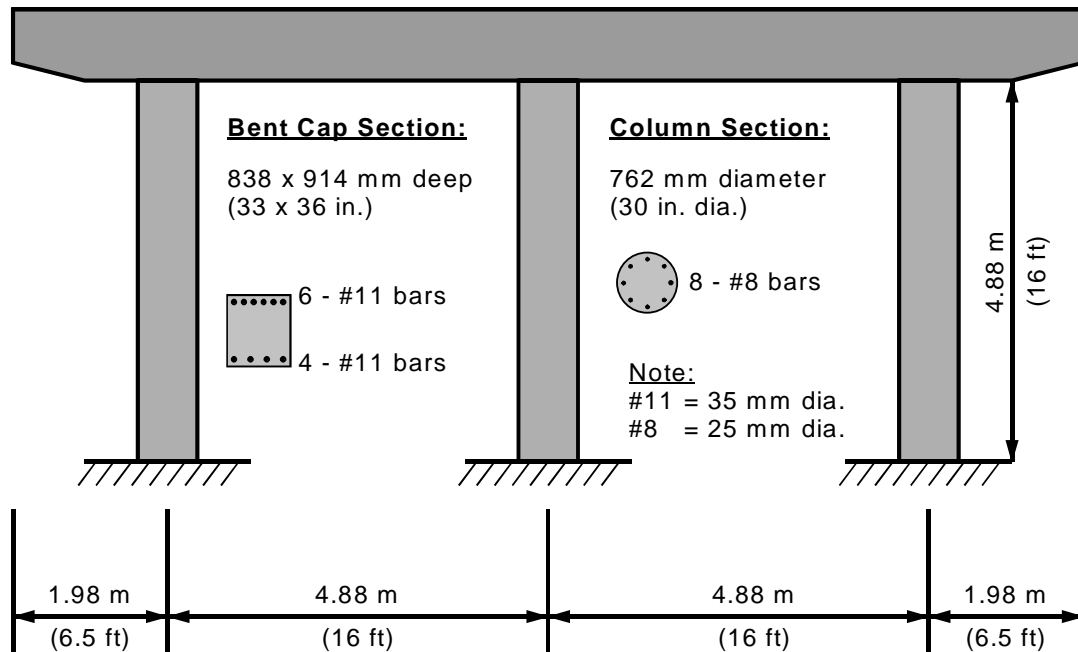
Figure 3.1 - Prototype Multicolumn Substructure

3.2.1.2   Substructure Analysis

The three-column frame bent was analyzed using a plane frame analysis program. AASHTO LRFD was used for design loading on the bridge. Elastic uncracked transformed section properties were used for the columns. The bent cap was divided into several segments and the analysis was performed assuming an initial moment of inertia of 40% of the gross moment of inertia. The initial analysis results were then used to refine the moment of inertia for each segment based on the calculated end moments for each segment. Depending on the magnitude and direction of the end moment, the gross transformed moment of inertia or elastic cracked section moment of inertia (positive or negative bending) was assigned to each end, and the average was computed for each segment. The frame was then re-analyzed and the various combinations of axial load and moment for the columns were determined. The calculated column forces are shown in Table 3.1. Columns 1 and 3 are the outside columns. Loading on the substructure was not symmetric due to the shoulder, producing different force combinations for the two columns. The critical combination was taken at the top of column 3, since this combination produced the largest eccentricity (ratio of moment to axial load).

Table 3.1 - Calculated Column Forces for Prototype Substructure (unfactored)

Location	Data	Column 1		Column 3	
Column Base	N_{max}	1781 kN	(400.4 kips)	994 kN	(223.4 kips)
	M_{max}	55.8 kN-m	(494.4 k-in.)	74.6 kN-m	(660.0 k-in.)
	e = M/N	30.5 mm	(1.2 in.)	76.2 mm	(3.0 in.)
Column Top	N_{max}	1716 kN	(385.7 kips)	**928 kN**	**(208.7 kips)**
	M_{max}	144.8 kN-m	(1281.6 k-in.)	**118.0 kN-m**	**(1044.0 k-in.)**
	e = M/N	83.8 mm	(3.3 in.)	**127 mm**	**(5.0 in.)**

The design loading from the prototype analysis was scaled for use with the column specimens. Axial forces are scaled by the square of the ratio of column diameters. Bending moments are scaled by the cube of the ratio of column diameters. Calculation of the column specimen design forces is as follows:

$$N_{specimen} = \left(\frac{D_{specimen}}{D_{prototype}}\right)^2 \times N_{prototype} \qquad M_{specimen} = \left(\frac{D_{specimen}}{D_{prototype}}\right)^3 \times M_{prototype}$$

$$= \left(\frac{457 \text{ mm}}{762 \text{ mm}}\right)^2 \times (928 \text{ kN}) \qquad = \left(\frac{457 \text{ mm}}{762 \text{ mm}}\right)^3 \times (118 \text{ kN} - \text{m})$$

$$= 334 \text{ kN} \quad (75.2 \text{ kips}) \qquad = 25.5 \text{ kN} - \text{m} \quad (225 \text{ k} - \text{in.})$$

Assuming an average load factor of 1.5, the factored design forces are:

$$N_f = 501 \text{ kN} \qquad (112.6 \text{ kips})$$

$$M_f = 38.2 \text{ kN-m} \qquad (338.6 \text{ k-in.})$$

3.2.2   Reinforced Concrete Column Design

The smallest circular column used by TxDOT is 460 mm (18 in.) diameter. This column was selected as the nonprestressed or reinforced concrete design in the research program. The 460 mm column is provided with six #6 (19 mm) bars for longitudinal reinforcement. Spiral reinforcement is #3 (9.5 mm) at a 152 mm (6 in) pitch. Clear cover to the spiral is 50 mm (2 in.). The concrete used in the columns was TxDOT Class C concrete, with a minimum compressive strength of 25 MPa (3600 psi). The reinforced concrete section is shown in Figure 3.2.
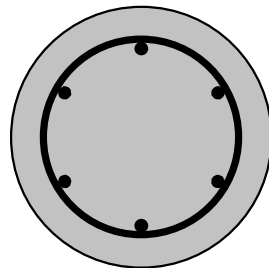
Main Reinforcement:
6 - #6 (19 mm) bars

Spiral:
#3 (9.5 mm) at
152 mm (6 in.) pitch

Column Diameter: 460 mm (18 in.)
Clear Cover to Spiral: 50 mm (2 in.)

Figure 3.2 - Reinforced Concrete Column Section Details

The reinforced concrete section was analyzed using a layer-by-layer strain compatibility section analysis technique to produce an axial force-moment interaction diagram. A spreadsheet was developed by the author to automate the analysis process. The basic assumptions for the analysis were listed previously in Section 2.2.3. The concrete compressive strength used in the calculations was 25 MPa (3600 psi) (minimum allowable for TxDOT Class C concrete). The calculated interaction diagrams are shown in Figure 3.3. Curves are plotted for the nominal capacity (N_n, M_n) and the factored resistance (ϕN_n, ϕM_n). The factored resistance is well in excess of the factored loading.

The elastic decompression moment for the column was calculated for the design service loading as follows:

$$f_{tensile} = 0 = \frac{P_{service}}{A_{tr}} - \frac{M_{decomp.}}{S_{tr}}$$

$$M_{decomp.} = \left(\frac{S_{tr}}{A_{tr}}\right)P_{serv} = \left(\frac{10.147 \times 10^6 \text{ mm}^3}{176,903 \text{ mm}^2}\right)\left(\frac{334 \text{ kN}}{1000}\right)$$

$$= 19.2 \text{ kN} - \text{m} \quad (169.4 \text{ k} - \text{in.})$$

The service load moment of 25.5 kN-m (225 k-in.) exceeds the decompression moment for the reinforced concrete column design.
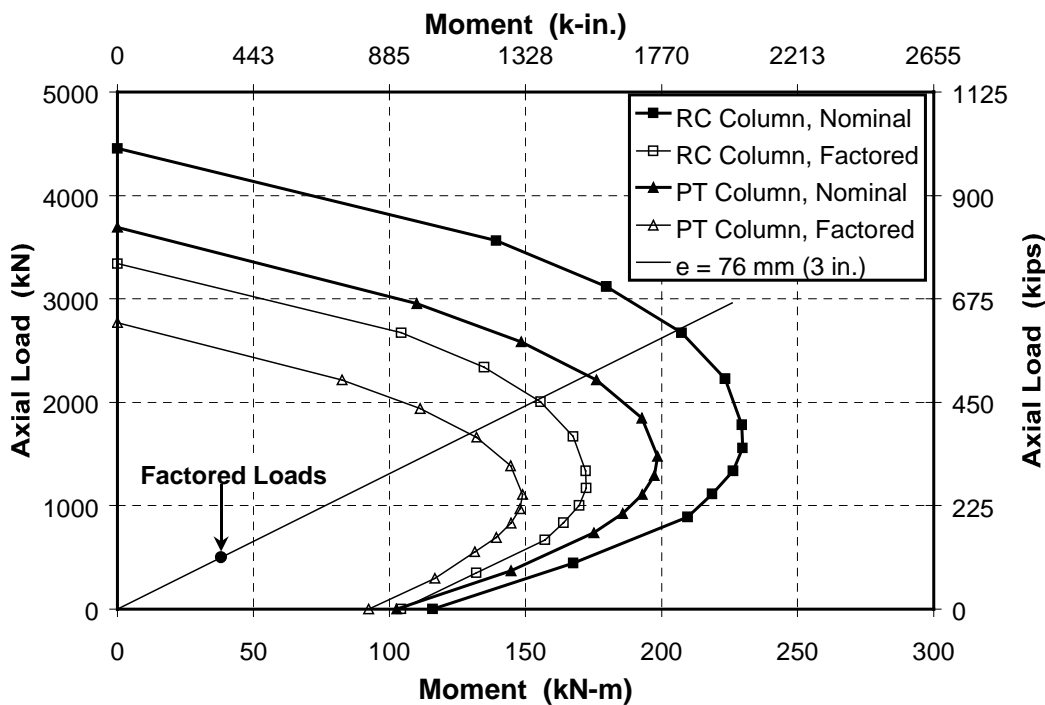
Figure 3.3 - Column Interaction Diagrams, Nominal Resistance and Factored Resistance

3.2.3   Post-Tensioned Column Design

The post-tensioned column design was based on practical considerations. The design concept for the post-tensioned column was to keep the same mild steel reinforcement from the reinforced concrete column design, and to add prestressed steel to provide continuity between the column and foundation and increase the decompression moment, which could improve durability at construction joints. The mild steel column reinforcement would not extend into the foundation or the bent cap. The longitudinal mild steel was left in the column for several reasons, including the need for confinement and concerns for creep. Due to the relatively small size of the test specimens, it was decided to use threaded prestressing bars rather than seven-wire strand for post-tensioning. The use of threadbar minimized anchorage seating losses and provided simple details for

anchoring the bars in the foundation while accommodating a construction joint at the column-foundation interface. The column-foundation joint is discussed in Section 3.3.2.

Since only the post-tensioning bars would provide continuity between the column and other elements, a minimum of four prestressing bars would be required to effectively develop flexural capacity about more than one axis. Four 16 mm (5/8 in.) prestressing bars were selected. A minimum effective prestress of 60% of ultimate ($f_{pe} = 0.6f_{pu}$) was used for design and analysis purposes. The post-tensioned column section details are shown in Figure 3.4.
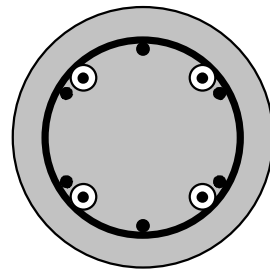
Main Reinforcement:
6 - #6 (19 mm) bars**
4 - 16 mm (5/8 in.) PT bars
$f_{pe} = 0.6f_{pu}$

Spiral:
#3 (9.5 mm) at
152 mm (6 in.) pitch

Column Diameter: 460 mm (18 in.)
Clear Cover to Spiral: 50 mm (2 in.)

** Only PT bars provide continuity to foundation

Figure 3.4 - Post-Tensioned Column Section Details

The elastic decompression moment was calculated for the post-tensioned column at the critical section (neglecting the mild steel reinforcement) as follows:

$$f_{tensile} = 0 = \frac{P_{service} + F_p}{A_{tr}} - \frac{M_{decomp.}}{S_{tr}}$$

$$M_{decomp.} = \left(\frac{S_{tr}}{A_{tr}}\right)\left(P_{serv} + F_p\right) = \left(\frac{9.382 \times 10^6 \text{ mm}^3}{164,173 \text{ mm}^2}\right)\left(\frac{334 \text{ kN} + 4(117.3 \text{ kN})}{1000}\right)$$

$$= 45.9 \text{ kN} - \text{m} \quad (406 \text{ k} - \text{in.})$$

The decompression moment for the post-tensioned column exceeds the applied service load moment of 25.5 kN-m (225 k-in.) by a considerable margin.

The post-tensioned column section was analyzed using the layer-by-layer strain compatibility section analysis technique described previously. The stress-strain curve for the high strength prestressing bars was modeled using a Ramberg-Osgood function, as shown in Figure 3.5. The concrete strength assumed for the calculations was 25 MPa (3600 psi). An axial force-moment interaction diagram was produced for the post-tensioned column at the critical section (neglecting the mild steel reinforcement). The calculated interaction diagrams are shown in Figure 3.3. Curves are plotted for the nominal capacity (N_n, M_n) and the factored resistance (ϕN_n, ϕM_n). The interaction diagram for the post-tensioned section shows a lower nominal capacity than the reinforced concrete column, particularly for axial loads higher than 500 kN. This reduction illustrates the effect of post-tensioning on the axial load carrying capacity of columns. Although the post-tensioned column had a lower strength than the reinforced concrete column, the factored resistance of the post-tensioned columns far exceeded the factored loads (Figure 3.3).

$$f_{ps} = E_{ps}\varepsilon_{ps}\left(0.01293 + \frac{0.987}{\left[1 + \left(238.5\varepsilon_{ps}\right)^8\right]^{0.125}}\right)$$

$$\leq 1035 \text{ MPa}$$

$$E_{ps} = 200,000 \text{ MPa}$$
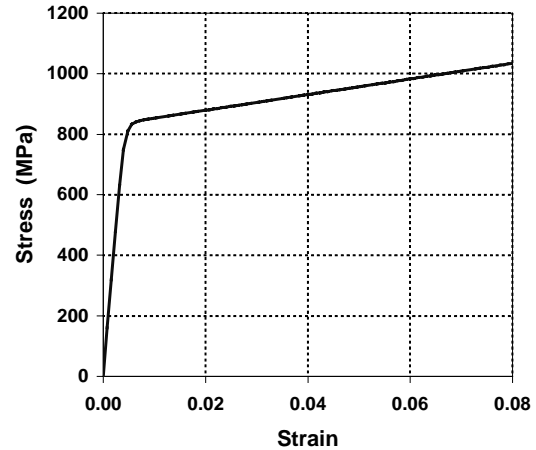
Figure 3.5 - Prestressing Bar Stress-Strain Curve

Long-term prestress losses were calculated using the approach proposed by Ghali and Favre (see Section 2.2.3). The assumed concrete strength was increased from 25 MPa (3600 psi) to 35 MPa (5000 psi) to better reflect tested cylinder strengths obtained for the columns. The column mild steel reinforcement was included the long-term analysis. Initial calculations were performed using an initial prestress value of $0.6f_{pu}$. Calculated average prestress losses under sustained service loading were approximately 10% after 1000 days. Since the desired effective prestress was $0.6f_{pu}$, it was decided to increase the initial level of prestress to $0.68f_{pu}$. Calculations were performed for periods of 500, 1000 and 1500 days, for both loaded and unloaded post-tensioned columns. The results are listed in Table 3.2. Losses are not uniform in the loaded case due to the eccentric loading. The calculated losses indicate that with an initial prestress of $0.68f_{pu}$ the effective prestress in the columns will meet or exceed the design value for an experiment duration longer than 1500 days.

The effect of the mild steel reinforcement on the prestress losses was investigated by excluding the mild steel from the prestress loss calculations. Calculations indicated an average prestress loss of 12.75% after 1500 days of loading compared to an average loss of 11% when the mild steel is included.

Table 3.2 - Long-Term Prestress Losses

Time Period	Prestress Loss	
(days)	ΔF_{p1}	ΔF_{p2}
Case 1: Loaded, $f_{pi} = 0.68f_{pu}$		
500	10.7%	8.8%
1000	11.5%	9.6%
1500	11.9%	9.9%
Case 2: Unloaded, $f_{pi} = 0.68f_{pu}$		
500	7.8%	7.8%
1000	8.4%	8.4%
1500	8.8%	8.8%
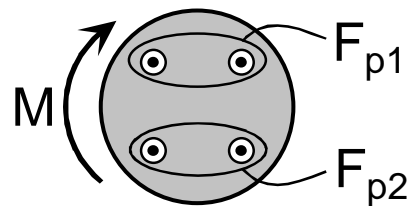
3.3   VARIABLES

A number of variables were selected for consideration column corrosion tests. The variables fall into five main categories: column to foundation joint, concrete type, loading, prestressing bar coatings and post-tensioning duct types.

3.3.1   Control Variables

Standard variables based on typical current practice were defined to represent control cases. These include concrete mix design, concrete clear cover, cement grout and post-tensioning duct. Details of each are given below.

Concrete:	based on TxDOT Specification Item 421
	TxDOT Class C concrete for bridge substructures
	maximum w/c ratio = 0.533 (actual w/c will be closer to 0.45 based on slump requirements)
	Type I cement
	slump = 100 mm (4 in.)
	maximum coarse aggregate size = 19 mm (3/4 in.)
	retarder, Rheocrete 300-R
	entrained air admixture
	50 mm (2 in.) clear cover to main steel
Cement Grout:	based on TxDOT Specification Item 426.3.4a
	w/c ratio = 0.44
	Type I cement
PT Duct:	rigid galvanized steel duct

3.3.2   Column to Foundation Connection

The construction joint between the column and foundation presents a possible weak link in corrosion protection since it represents a pre-formed crack that could open under loading. This problem is aggravated by the potential exposure conditions at the column-foundation interface, since the joint could be directly exposed to moisture and chlorides in coastal and deicing chemical exposures. One of the objectives for this research program is to investigate the influence of the column-foundation cold joint on chloride ion movement and corrosion activity. Three configurations were selected, as shown in Figure 3.6.
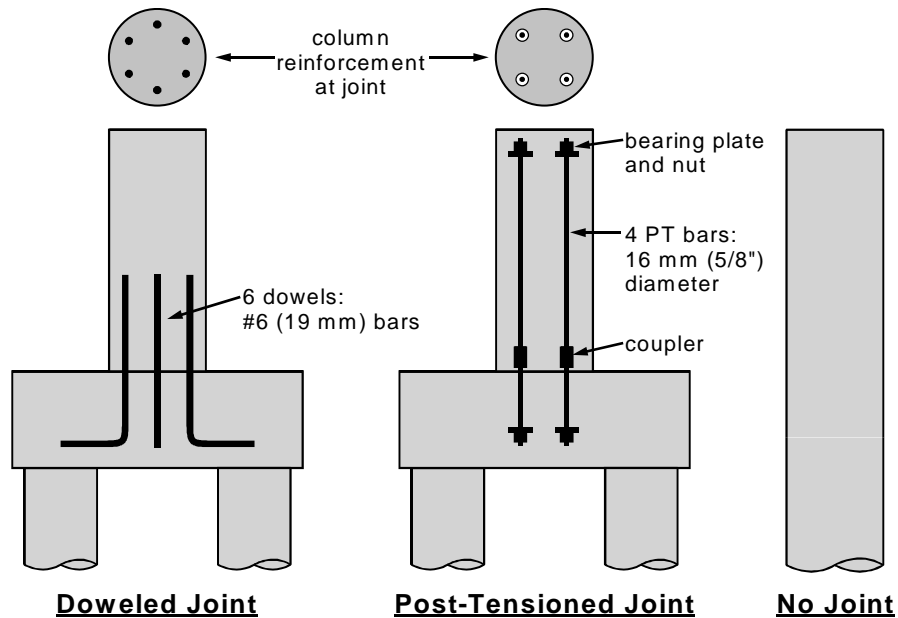
Figure 3.6 - Column-Foundation Joint Configurations

The standard doweled joint has six mild steel dowels (#6 (19 mm dia.) bars) cast into the foundation to provide continuity with the column. The column reinforcement is lapped with the dowels, and the column is cast-in-place on the foundation. In the second configuration, continuity between the column and foundation is provided with four post-tensioned bars (16 mm (5/8 in.) dia.). A short length of threadbar with bearing plate and nut is cast into the foundation for each post-tensioned bar. The bars protrude from the foundation to permit coupling with the column post-tensioning bars during column construction. After the column is cast-in-place, it is post-tensioned to the foundation. The no joint configuration represents the condition of a column or trestle pile in deep water. The column is cast-in-place on the foundation for this configuration, but no dowel steel is used and an end cover of 50 mm (2 in.) is provided for all column longitudinal reinforcement. An epoxy bonding agent was used to prepare the foundation surface immediately prior to casting the no joint type columns.

3.3.3   Loading

Two loading conditions were considered: unloaded and service load. The columns were subjected to the combined axial load and moment conditions obtained from the prototype substructure analysis for the service load condition:

$$N_{service} \quad = \quad 334 \text{ kN} \qquad (75.2 \text{ kips})$$

$$M_{service} \quad = \quad 25.5 \text{ kN-m} \qquad (225 \text{ k-in.})$$

The unloaded case was included since it could represent a worse case condition for allowing moisture and chloride penetration at the column-foundation construction joint.

3.3.4   Concrete Type

Partial cement replacement with fly ash has been shown to improve most aspects of concrete durability, as discussed in Section 2.3.3.1. Replacement amounts of 20% to 35% (by volume) are permissible under TxDOT Standard Specifications. Cement replacement with fly ash is common practice in Texas bridges, normally at the contractor's request due to the low cost of fly ash in comparison to cement.

Due to the increasing use of fly ash in concrete, it was decided to investigate its effect on corrosion protection when fly ash is simply used as partial cement replacement and no other changes are made to the mix design. It was decided to use the standard TxDOT concrete for bridge substructures in most specimens, and replace 35% of the cement by volume (31% replacement by weight) with fly ash in two columns. No other significant changes were made to the concrete mix. ASTM Class C fly ash was supplied by the ready-mix concrete supplier.

3.3.5   Prestressing Bar Coatings

Two prestressing bar coatings are investigated in the long-term column exposure tests. Epoxy-coated and zinc galvanized prestressing bars are compared to uncoated prestressing bars. The coated bars were compared directly to uncoated bars within individual specimens, as shown in Figure 3.7.
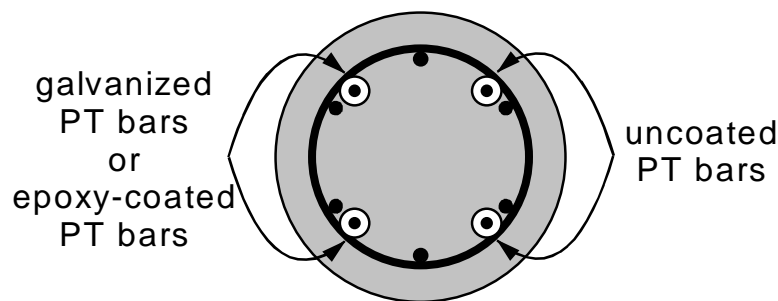
Note: all ducts are galvanized steel

Figure 3.7 - Comparison of Coated and Uncoated Prestressing Bars

3.3.5.1 Epoxy-coated Bars

High strength threaded bars commonly used for post-tensioning may be specified with epoxy coating. Epoxy-coated threadbars are coated according to ASTM A775-97, the same standard used for epoxy coating mild steel reinforcement. Anchorage hardware, including bearing plates, nuts and couplers are also epoxy-coated. Nuts and couplers are proportioned to allow free movement over the threads without damaging the epoxy coating.

3.3.5.2 Galvanized Bars

Threaded galvanized prestressing bars are commercially available in standard sizes and strengths of threadbar for prestressing. The high strength prestressing bars are galvanized according to strict specifications to minimize the potential for hydrogen embrittlement. Similar to the epoxy-coated prestressing bars, bearing plates, nuts and couplers are also galvanized. Nuts and couplers are proportioned to limit damage to the zinc coating.

3.3.6 Post-Tensioning Ducts

Impermeable plastic ducts are compared to standard galvanized steel ducts. Due to the short column height, duct splices were not necessary in the column specimens, and thus were not introduced as a test variable. The performance of plastic ducts was compared directly to galvanized steel ducts within individual specimens as shown in Figure 3.8. Uncoated post-tensioning bars were used in columns where duct type was evaluated.
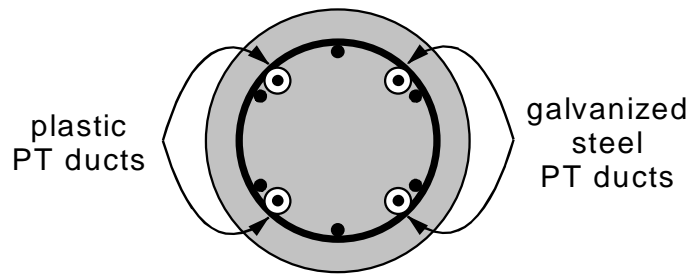
Note: PT bars are uncoated

Figure 3.8 - Comparison of Galvanized Steel and Plastic Ducts for Post-Tensioning

3.4 EXPERIMENTAL PROGRAM (SPECIMEN TYPES)

A total of ten specimen types were needed to address the selected variables. The complete experimental program is listed in Table 3.3. A specimen notation scheme used throughout the testing program is shown after the table.

Table 3.3 - Column Specimen Types and Variables

	Specimen	Foundation Connection	Concrete Type	Loading	PT Protection
1	DJ-TC-N	Doweled	Class C	Unloaded	n/a
2	PT-TC-N-PD	Post-tensioned	Class C	Unloaded	Plastic Duct
3	NJ-TC-N	No Joint	Class C	Unloaded	n/a
4	DJ-TC-S	Doweled	Class C	Service	n/a
5	PT-TC-S-PD	Post-tensioned	Class C	Service	Plastic Duct
6	NJ-TC-S	No Joint	Class C	Service	n/a
7	PT-TC-S-EB	Post-tensioned	Class C	Service	Epoxy-coated PT Bar
8	PT-TC-S-GB	Post-tensioned	Class C	Service	Galvanized PT Bar
9	DJ-FA-S	Doweled	35% Fly Ash	Service	n/a
10	PT-FA-S-PD	Post-tensioned	35% Fly Ash	Service	Plastic Duct

<div align="center">

PT-TC-S-PD

</div>

Connection Type ⟵ ⟶ PT Protection

Concrete Type ⟵ ⟶ Loading

Connection Type:
    DJ =   Doweled Joint
    PT =   Post-tensioned Joint
    NJ =   No Joint

PT Protection:
    PD =   Plastic Duct*
    EB =   Epoxy-coated PT Bar**
    GB =   Galvanized PT Bar**
    Blank = Not applicable (i.e., no PT)

Concrete Type:
    TC =   TxDOT Class C
    FA =   35% Fly Ash

Loading:
    N =   No Load
    S =   Service Load
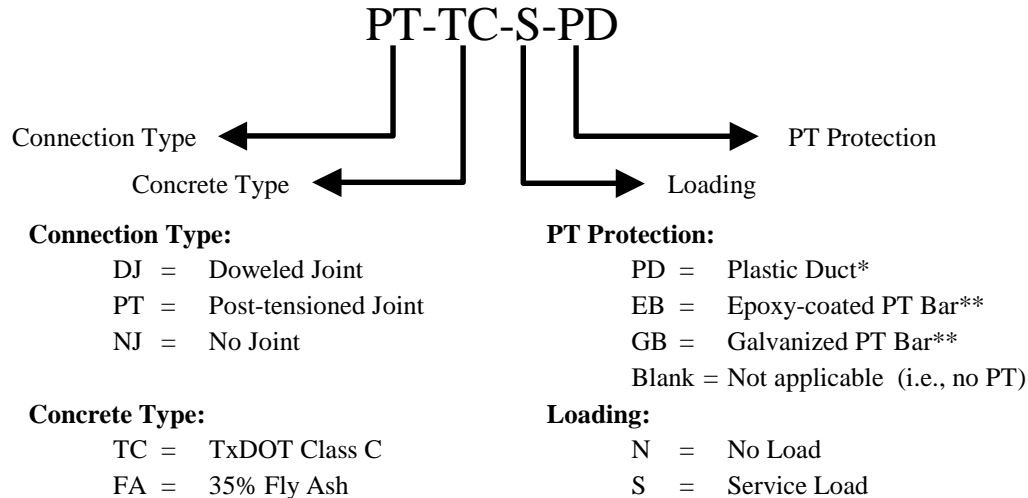
Notes:

*   plastic ducts used for bars 1 and 2, galvanized steel ducts used for bars 3 and 4
** epoxy-coated or galvanized bars used for bars 1 and 2, uncoated bars used for bars 3 and 4

3.5   EXPERIMENTAL SETUP

Due to the specimen size and expected long duration of the exposure testing, it was decided to place the column testing program outside of the Ferguson Laboratory. A suitable location was found adjacent to the Construction Materials Research Group building. The ground was leveled and a layer of gravel was placed over heavy plastic sheeting. The design requirements for the experimental setup included:

- provide simulated foundation for the column specimens,

- permit loading of the columns without requiring the lab strong floor, and

- accommodate exposure conditions consisting of saltwater continuously ponded around column base and regular application of saltwater to one face of columns.

The experimental setup is shown schematically in Figure 3.9. It was decided to use a large reinforced concrete foundation to support the columns, provide load reactions and hold ponded saltwater. The dimensions of the foundation are 4.67 m (15.33 ft) long, 915 mm (36 in.) wide and 460 mm (18 in.) high. A 152 x 152 mm (6 x 6 in.) curb was provided around the top surface of the foundation to contain ponded saltwater. The foundation size was dictated by the necessity of moving the foundation with a forklift from inside the laboratory to its final outdoor position. Each foundation accommodates five column specimens, although only two columns are shown in place in Figure 3.9. Loading is applied on the columns using a stiffened loading plate on top of the column and four 25 mm (1 in.) threaded prestressing bars. These bars have been referred to as "tie-down bars" in the figure to avoid confusion with the internal post-tensioning bars used in selected specimens. The loading system is self-reacting, as the foundation provides the reaction for both the column and prestressing bars. Eccentric loading is achieved by adjusting the level of loading in the bars to apply the desired moment and axial force. A photo of the complete experimental setup is shown in Figure 3.10. Two foundations were used to accommodate the ten specimens.

The reinforced concrete foundation was designed using a strut and tie model to resist the complex pattern of reaction forces and post-tensioning forces. All foundation reinforcement was epoxy-coated to prolong the life of the foundation. The top surface and curbs of the foundation were painted with swimming pool paint to improve water-tightness of the ponded area and to limit penetration of chlorides into the foundation. High performance concrete containing fly ash was used to further improve the durability of the foundation. Concrete for the foundations was selected from a list of design mixes supplied by a local ready-mix concrete producer. Concrete for the nonprestressed column foundation had a design strength of 55 MPa (8000 psi) and contained 30% fly ash by weight. Concrete for the post-tensioned column foundation had a design strength of 96 MPa

(14,000 psi) and contained 26% fly ash by weight. Details of the foundation concrete are listed in Table 3.4. Details of the foundation reinforcement and loading plates are included in Appendix B.
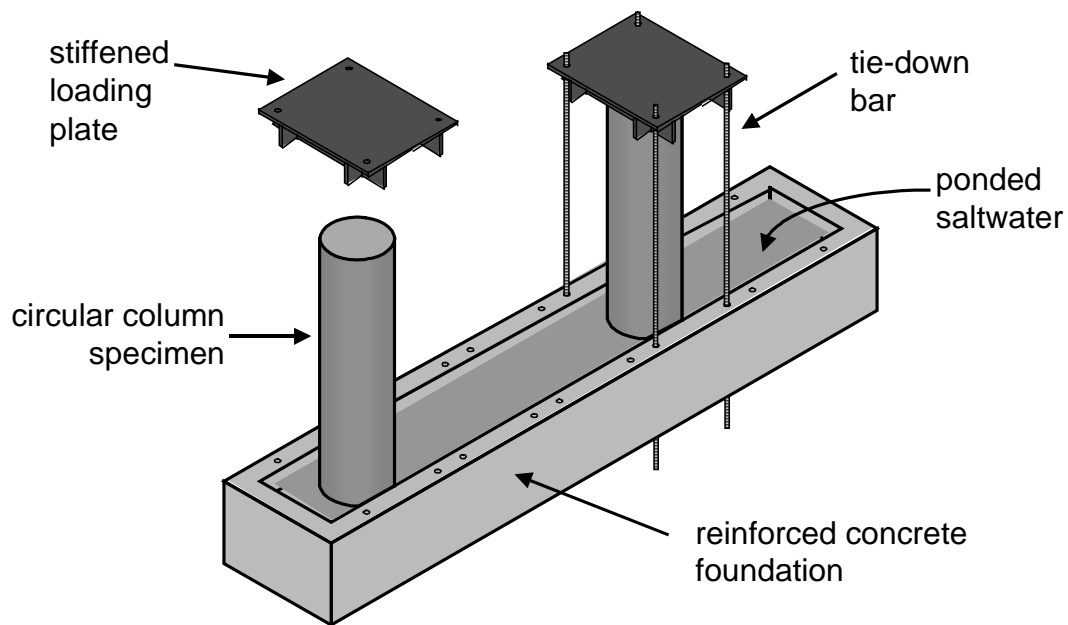
Figure 3.9 - Long-Term Column Corrosion Test Setup – Schematic

Figure 3.10 - Long-Term Column Corrosion Test Setup

The applied loading is to be sustained on the columns for the duration of exposure testing. The effect of concrete creep and shrinkage on the loading system was investigated using the procedure proposed by Ghali and Favre, (see Section 2.2.3). The loading system was treated as external prestressing in the calculations, and loading force losses were estimated for various time periods. Due to the relatively low axial force on the

column, average loading force losses (i.e., in the tie down bars) for the post-tensioned columns were only 6.6% for the period of 500 days from first loading. Losses were even lower for the reinforced concrete column, reaching 3.6% over the first 500 days of loading. Due to their small magnitude, it was decided not to complicate the loading system by introducing springs in an attempt to reduce the losses. Rather, it was decided to simply re-apply the loading forces on the columns every twelve to sixteen months. Column specimens were re-loaded in December 1997. The re-loading procedure was completed in less than one day.

3.5.1 *Exposure Conditions*

Exposure conditions for the column specimens consist of saltwater continuously ponded around the base of the columns to simulate a coastal exposure. The effect of deicing salts dripping from the superstructure or saltwater spray is simulated by trickling saltwater on one face of each column for a period of six to eight hours every two weeks. A small electric pump and system of hoses is used to provide the trickled water, as shown in Figure 3.11. Valves are used at each column to control the flow rate to provide equal flow of trickled water to each column. Flow rates are determined manually by measuring the length of time to fill a known volume. The saltwater used in this testing program is a 3.5% solution of NaCl in tap water. The salt concentration is based on the recommendations of ASTM G109.
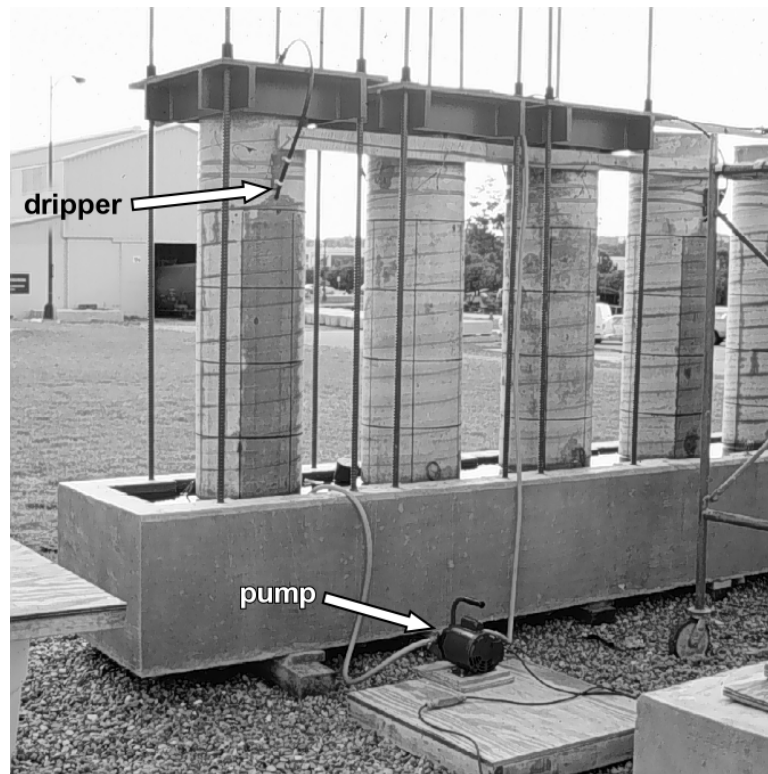
Figure 3.11 - Trickled Saltwater Exposure for Columns

3.5.2 *Specimen Locations*

The locations of the column specimens on the two foundations are shown in Figure 3.12. All references are made with respect to the North direction. The mild steel reinforcement and post-tensioning bars were numbered according to the scheme shown in Figure 3.12. The curved arrows in the figure indicate the direction of applied moment on each column. Columns without arrows were not loaded. A capital "D" is used to indicate the location of the dripper for trickled water on each column. The dripper was located on the tension side of the column for loaded columns. Plastic ducts, epoxy-coated post-tensioning bars and galvanized post-tensioning bars were placed in PT Bar Locations 1 and 2 in the appropriate specimens. Locations 3 and 4 have uncoated post-tensioning bars and galvanized steel ducts in these specimens.
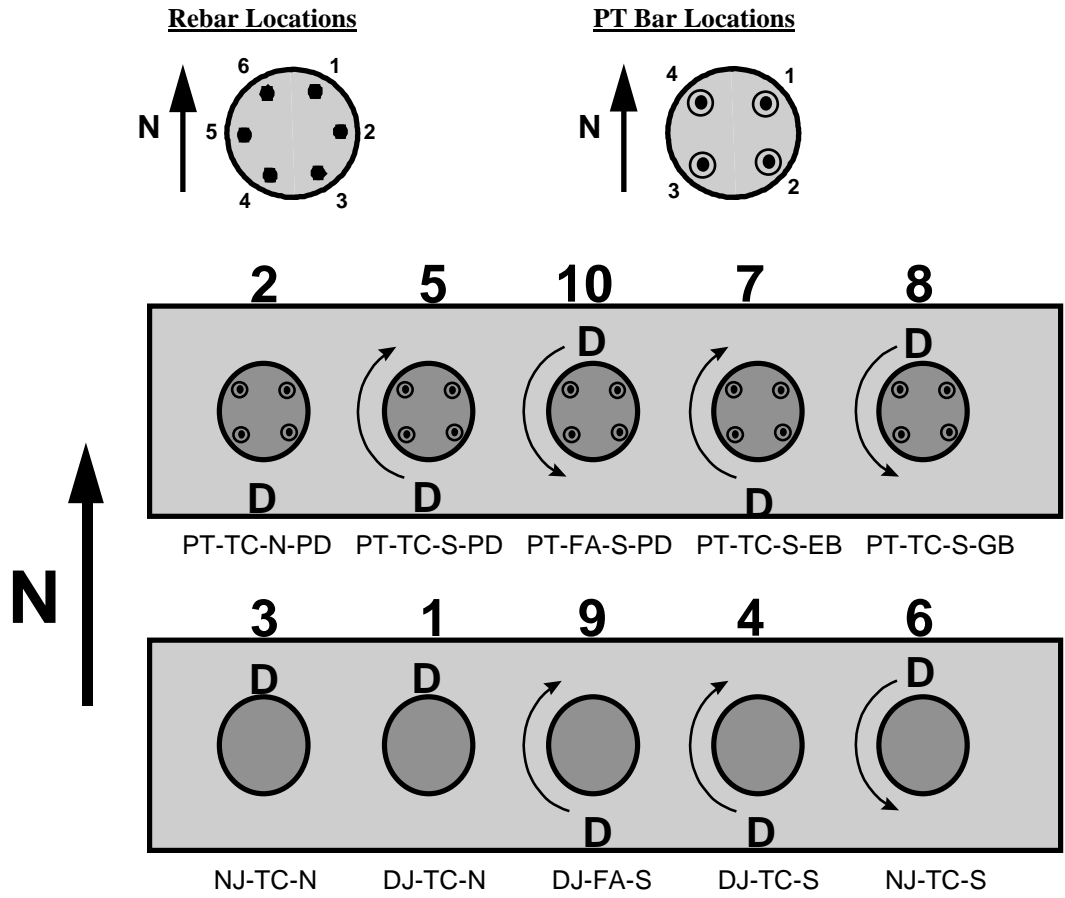
Figure 3.12 - Column Specimen Locations and Related Test Details

3.6   MATERIALS

Similar to the beam corrosion tests, materials and proportions were selected to match Texas Department of Transportation Standard Specifications where possible. Concrete was supplied by a local ready-mix concrete producer. Grouts for post-tensioning were batched in 18.9 liter (5 gal.) buckets using a paddle mixer mounted to a large hand-held drill. Mild steel reinforcement was supplied and fabricated by a local steel fabricator. Post-tensioning hardware was fabricated by the supplier. The materials used in the column corrosion tests are summarized in Table 3.4. Complete details of specimen construction are provided in Section 3.7.

Table 3.4 - Construction Material Details: Column Specimens

Item	Description			
Column Concrete: Texas DOT Class C Concrete for Bridge Substructures	• w/c = 0.45 (based on slump, max. allowable w/c = 0.53) • f'c = 25 MPa (3600 psi) minimum allowable • batch proportions: (per 0.764 m^3 (1 yd^3))			
	Coarse Aggregate (19 mm)		851 kg	1877 lbs
	Fine Aggregate		538 kg	1186 lbs
	Type I/II Cement		256 kg	564 lbs
	Water		115 kg	254 lbs
	Set retarder		710 ml	24 oz
	Entrained Air Admixture		118 ml	4 oz
	• cylinder strengths:	7-day	30.0 MPa	4358 psi
	(average)	14-day	36.2 MPa	5250 psi
		28-day	36.4 MPa	5284 psi
Column Concrete: Texas DOT Class C Concrete with 31% Fly Ash by Weight	• w/(c +p) = 0.42 • f'c = 25 MPa (3600 psi) minimum allowable • batch proportions: (per 0.764 m^3 (1 yd^3))			
	Coarse Aggregate (19 mm)		834 kg	1855 lbs
	Fine Aggregate		586 kg	1245 lbs
	Type I/II Cement		164 kg	362 lbs
	Class C Fly Ash		73 kg	162 lbs
	Water		100 kg	220 lbs
	Set retarder		591 ml	20.0 oz
	Entrained Air Admixture		104 ml	3.5 oz
	• cylinder strengths:	7-day	30.7 MPa	4447 psi
	(average)	28-day	44.6 MPa	6473 psi
Foundation Concrete Mix 1 (for RC Columns, Capitol Aggregates Mix 241)	• w/(c + p) = 0.39 • f'c = 55 MPa (8000 psi) design strength • batch proportions: (per 0.764 m^3 (1 yd^3))			
	Coarse Aggregate (19 mm)		812 kg	1790 lbs
	Fine Aggregate		513 kg	1131 lbs
	Type I/II Cement		238 kg	525 lbs
	Class C Fly Ash		102 kg	225 lbs
	Water		134 kg	295 lbs
	Set Retarder		665 ml	22.5 oz
	• avg. cylinder strengths:	28-day	42.9 MPa	6220 psi
Foundation Concrete Mix 2 (for PT Columns, Capitol Aggregates Mix 246)	• w/(c + p) = 0.25 • f'c = 96 MPa (14,000 psi) design strength • batch proportions: (per 0.764 m^3 (1 yd^3))			
	Coarse Aggregate (12.7 mm)		812 kg	1665 lbs
	Fine Aggregate		513 kg	1371 lbs
	Type I/II Cement		238 kg	714 lbs
	Class C Fly Ash		102 kg	254 lbs
	Water		134 kg	240 lbs
	Superplasticizer		4730 ml	160 oz
	• cylinder strengths:	7-day	35.2 MPa	5102 psi
	(average)	14-day	52.0 MPa	7536 psi
		28-day	58.5 MPa	8478 psi

Table 3.4 (Continued) - Construction Material Details: Column Specimens

Item	Description
TxDOT Grout for Post-Tensioning (see note at end of Section 3.7.4)	• w/c = 0.44 • batch proportions: (per 0.028 m^3 (1 ft^3)) Type I Cement 37.4 kg 82.4 lbs Water 16.4 kg 36.2 lbs
Threaded Prestressing Bars	• 16 mm (5/8 in.) diameter high strength threaded prestressing bar • Grade 157 (1080 MPa, 157 ksi) • Supplier: Dywidag Systems, Inc.
Mild Steel Reinforcement	• ASTM A615, Grade 60 (400 MPa, 60 ksi)
Steel Duct	• Corrugated, semi-rigid, galvanized steel duct • 40 mm (1.575 in.) outside diameter • Supplier: Dywidag Systems, Inc.
Plastic Duct	• Corrugated, flexible plastic duct • 51 mm (2 in.) outside diameter • Supplier: Dywidag Systems, Inc.
Epoxy Bonding Agent	• Sikadur 32 High-Mod - Epoxy Bonding Adhesive • Supplier: Sika

Column specimen concrete and foundation concrete were sampled for strength testing using typical practices. Concrete cylinder strength data for the column specimens is listed in Table 3.5 and Table 3.6. All cylinder strengths exceeded the minimum requirements for TxDOT Class C Concrete for Bridge Substructures (Table 3.5). Foundation concrete strengths did not reach their design values, but were deemed sufficient. The foundation concrete mix designs were selected from a catalog of concrete mixes available from the ready-mix concrete supplier. Grout for post-tensioning was not sampled for strength testing, as such testing is not required by TxDOT specifications.

Table 3.5 - TxDOT Class C Concrete Cylinder Strengths

Column Numbers	Average Cylinder Strength		
	7 Day	**14 Day**	**28 Day**
1, 3, 4, 6	33.0 MPa (4791 psi)	42.6 MPa (6177 psi)	42.0 MPa (6091 psi)
2, 5, 9, 10	27.0 MPa (3924 psi)	29.8 MPa (4324 psi)	30.9 MPa (4478 psi)
Averages	30.0 MPa (4358 psi)	36.2 MPa (5250 psi)	36.4 MPa (5284 psi)

Table 3.6 - 35% Fly Ash Concrete Cylinder Strengths

Column Numbers	Average Cylinder Strength		
	7 Day	**14 Day**	**28 Day**
7	35.2 MPa (5107 psi)	41.6 MPa (6028 psi)	46.2 MPa (6706 psi)
8	26.1 MPa (3788 psi)	n/a	43.0 MPa (6240 psi)
Averages	30.7 MPa (4447 psi)	n/a	44.6 MPa (6473 psi)

3.7 CONSTRUCTION

The column foundations were constructed inside the Ferguson Laboratory. Column reinforcement was prepared and placed on the foundations inside the lab. The foundations were then moved outside and into their final position prior to casting of the columns. Post-tensioning and loading of the columns took place in their final position. All construction, post-tensioning and loading was performed by the graduate and undergraduate research assistants working on the project.

3.7.1 Foundations

All foundation reinforcement was epoxy-coated. Reinforcement assemblies were prepared following typical construction practices for epoxy-coated reinforcement. Epoxy-coated tie wire was used, and all cut ends and damaged areas were repaired using appropriate patching materials. Reusable wooden forms were constructed for casting the foundations. Concrete was supplied by a local ready-mix producer, and poured using a concrete bucket on an overhead crane. Concrete was placed and vibrated with hand held concrete vibrators following typical practice. The concrete was wet cured for a minimum of three days. Several photos of the foundation reinforcement are shown in Figure 3.13.
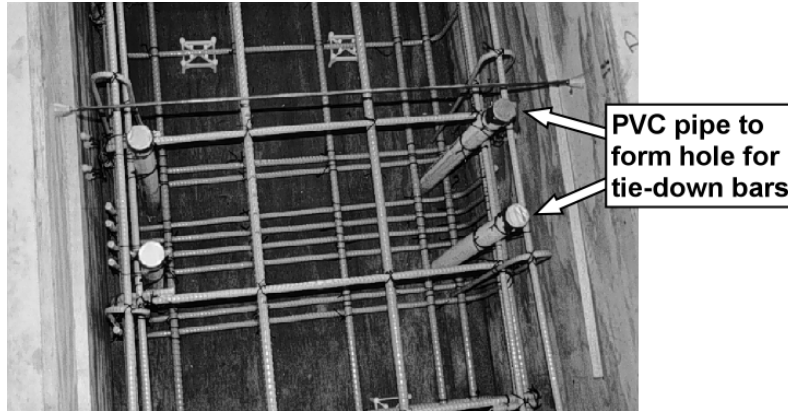
Top View
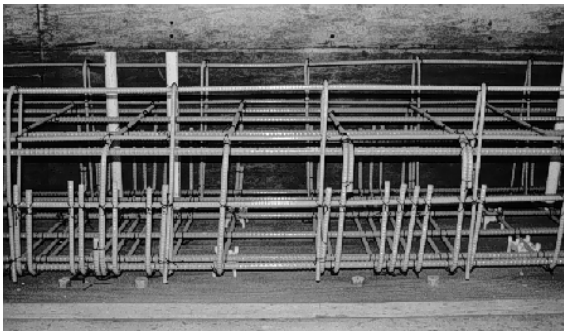
Side View
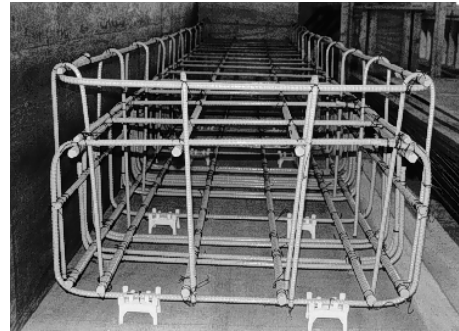
End View
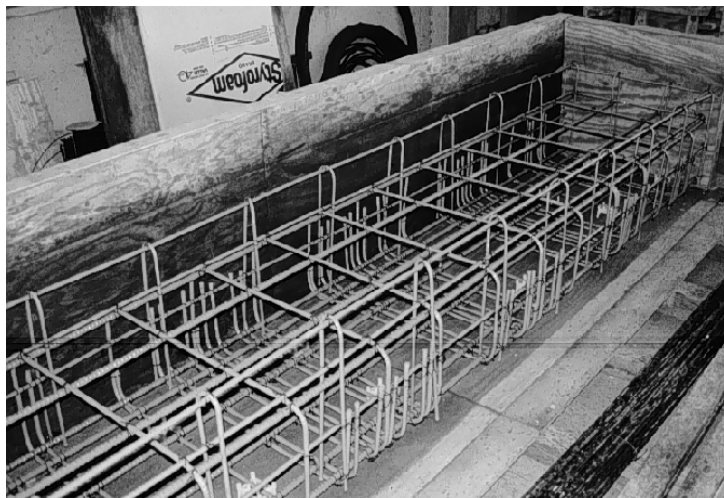
Overall View

Figure 3.13 - Foundation Reinforcement

3.7.2 Columns

Column reinforcement and post-tensioning hardware were assembled and placed on the foundation inside the lab. Ground clamps were used to attach a ground wire to the mild steel reinforcement for half-cell potential measurements during testing. Cardboard tube forms were used to form the columns. Tubes were fixed in position using a wooden frame to prevent movement during concrete casting. Concrete was tremied into the columns using a concrete bucket mounted on a forklift. Column construction is shown in Figure 3.14.
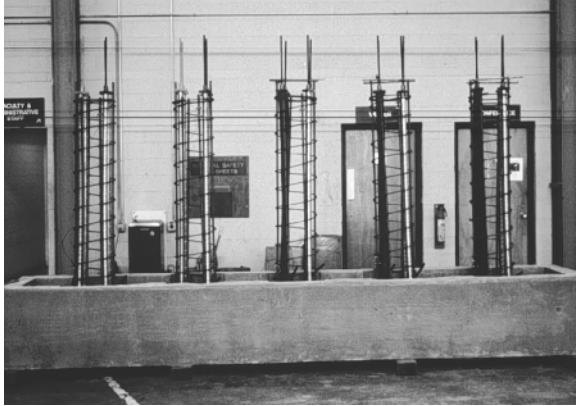
Column Reinforcement on Foundation

Ground Clamp to Attach Ground Wire

Pouring Column Concrete with Tremie Tube Attached to Concrete Bucket

Figure 3.14 - Column Construction

The post-tensioned columns required several additional details. As described in Section 3.3.2, short lengths of post-tensioning bar were cast into the foundation to provide anchorage for the column post-tensioning bars. Figure 3.15 shows the four post-tensioning bars protruding from the foundation. Shallow, square pockets were formed around each bar to accommodate rubber gaskets to seal the "dead end" of the post-tensioning ducts. The column post-tensioning bars were coupled to the protruding bars prior to placement of the ducts. The assembled reinforcement and post-tensioning hardware are shown in Figure 3.15. Plastic grout tubes were attached to the ducts near the base of the column, as visible in Figure 3.15. The post-tensioned columns were cast to a reduced height of 1.68 m (5.5 ft) to permit later capping of the columns to protect the post-tensioning

anchorages. Four of the six reinforcing bars and the spiral reinforcement were reduced in length to accommodate the reduced column height. The remaining two vertical bars were extended full height with the post-tensioning bars to provide continuity with the concrete cap. After post-tensioning and grouting was completed, one full turn of the spiral reinforcement was placed around the protruding bars, and the column was capped with concrete to its full height. The configuration of the column immediately prior to capping is shown in Figure 3.15. Ground clamps were used to attach ground wires to the post-tensioning bar ends prior to capping.
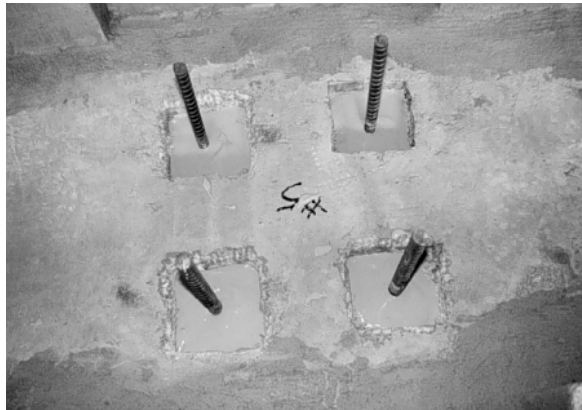
PT Bars Protruding from Foundation

Gasket Around Post-Tensioning Bar
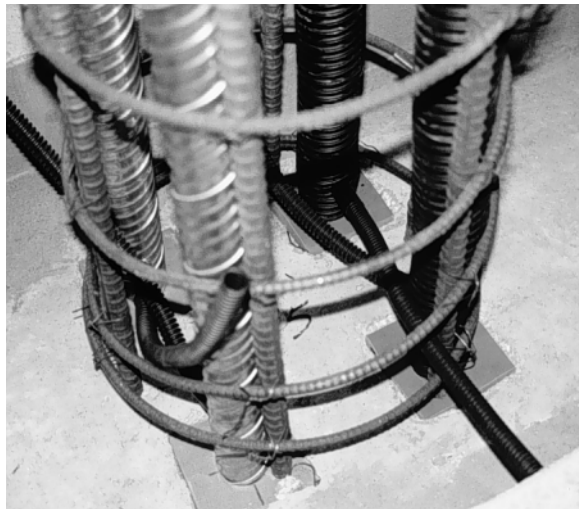
Reinforcement, Ducts and Grout Tubes

Top of Column Prior to Capping

Figure 3.15 - Post-Tensioned Column Construction Details

3.7.3   Column Post-Tensioning

The column post-tensioning process was simpler than that for the beam specimens. Due to the specimen size, straight tendon path and use of post-tensioning bars rather than strands, prestress losses during stressing were negligible. The post-tensioning jacking force, F_{pj}, was taken equal to the initial prestress force, F_{pi} ($0.68f_{pu}A_{pbar}$ = 133 kN (30 kips)).

Each bar was post-tensioned individually. The post-tensioning hardware consisted of a steel post-tensioning chair and 534 kN (120 kips) hollow stressing ram, as shown in Figure 3.16. A short extension bar was temporarily coupled to the bar to be stressed to provide the necessary length to pass through the stressing ram. The post-tensioning force during stressing was monitored using a load cell and by a pressure gauge on the hydraulic pump. Once the desire force was achieved, the nut on the post-tensioning bar was tightened to refusal using a large wrench to minimize seating losses.
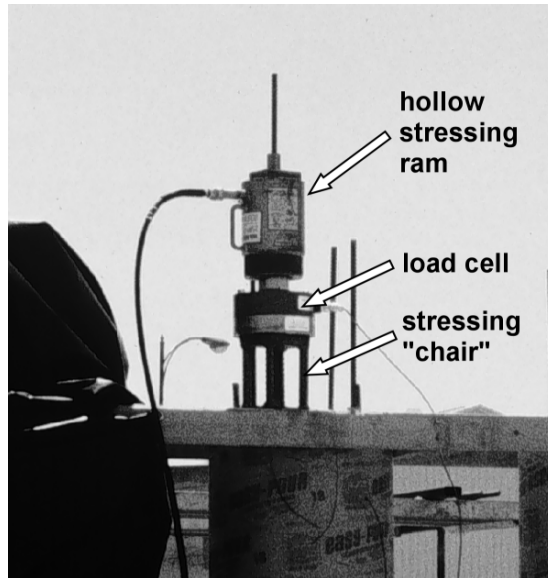
Figure 3.16 - Column Post-Tensioning

3.7.4   Grouting

The post-tensioned columns were grouted immediately following post-tensioning.   All grouting procedures were performed according to TxDOT Specifications. The grouting setup is shown in Figure 3.17. A 19 mm (0.75 in.) grout tube with shut off valve was used for the inlet. The vent at the top of the column was provided by drilling a 6 mm (0.25 in.) hole through the bearing plate adjacent to the nut.   Grouts were mixed in large buckets using a paddle mixer on a large hand held drill, and pumped immediately using an electric grout pump.   Grout was poured into the pump reservoir through a screen to remove lumps, if any.   The grout was continuously stirred in the reservoir to prevent segregation.   Grout was pumped into each duct without stoppage.   Once a continuous flow of grout was exiting the vent with no slugs of air or water, the vent was closed by hammering a wooden dowel into the hole. The pump was then restarted for a period of 2 to 3 seconds before closing the valve on the inlet tube.

3.7.4.1   Important Note

After the column grouting had been completed, the possibility of an error in the post-tensioning grout came to light. It is possible that incorrectly labeled cement barrels may have resulted in partial or complete cement replacement with Class F fly ash. The amount of fly ash, if any, is not certain. If the fly ash content is high, very little hydration will have occurred. The effect of this uncertainty on the experimental results is not certain.   Persons performing invasive inspections or autopsies on the columns should be aware of the possibility of fly ash in the grout. The most likely columns to contain fly ash grout are PT-TC-S-EB and PT-TC-S-GB.
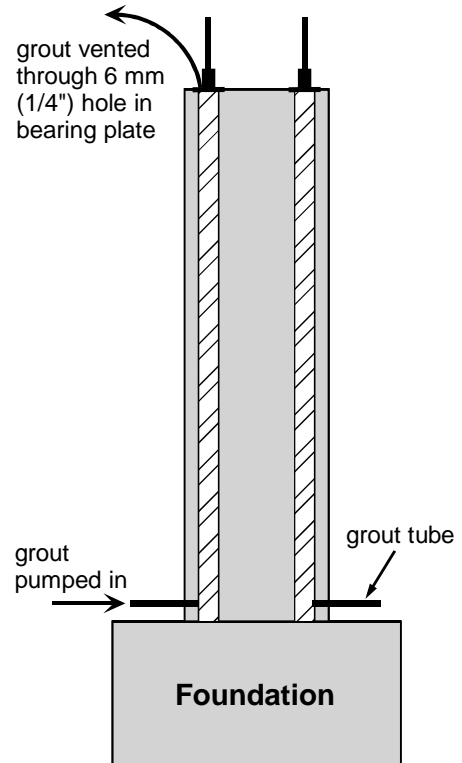
Figure 3.17 - Inlet and Vent for Grouting

3.7.5   Column Loading

The column specimens were loaded (where applicable) after all construction was completed. The top surface of the columns was prepared using Plaster-of-Paris to level the surface and provide even bearing for the stiffened loading plates (details of the loading plates are shown in Appendix B). Column loading was performed using

the apparatus shown in Figure 3.18. The necessary applied forces are shown in Figure 3.19. A separate hydraulic pump was used for each ram, and the forces T_1 and T_2 were applied simultaneously in four increments of 22% and a final increment of 11%. The applied forces were monitored during each increment using load cells and pressure gauges on each pump. Tie-down bar nuts were tightened to refusal using a large wrench once the desired forces had been attained. The identical apparatus and procedure is used for regular re-loading of the columns to restore any losses resulting from creep and shrinkage of the concrete.
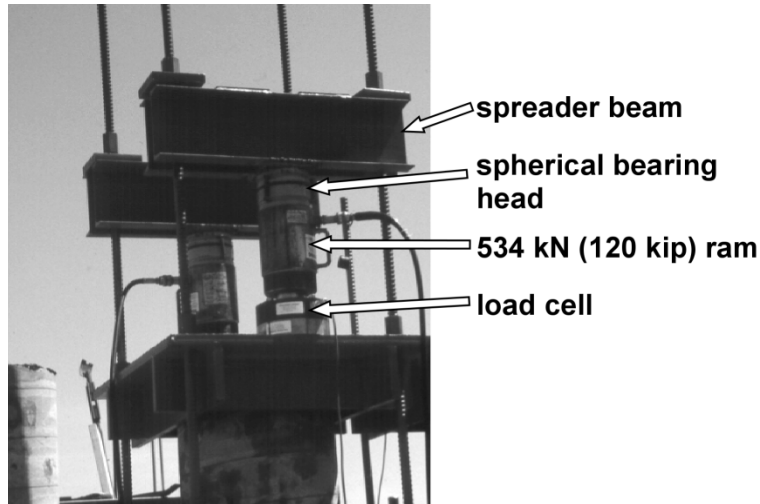
Figure 3.18 - Column Loading Apparatus
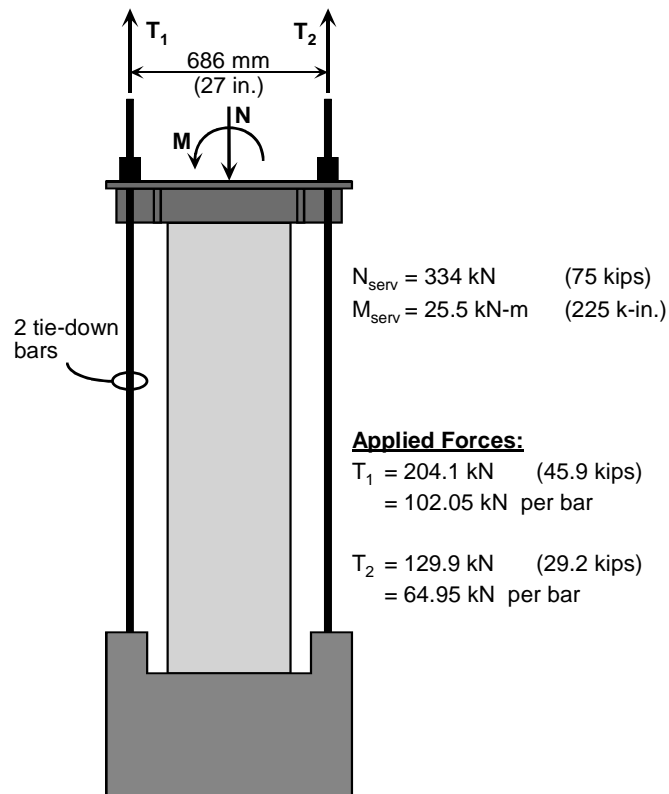
Figure 3.19 - Column Loading Forces

138

3.8 LONG-TERM MONITORING DATA & RESULTS

The column monitoring involves periodic half-cell potential measurements as well as visual monitoring for corrosion products. Chloride samples are taken occasionally from columns to monitor the ingress of chlorides through the depth of the concrete.

3.8.1 Half-Cell Potential Measurements

A wire was attached to the steel cage prior to concrete casting. Half-cell potential readings measured against a saturated calomel electrode are taken once a month. Figure 3.20 shows the bar placement and level numbering for readings. The readings are taken on 3 of the 6 reinforcing bars (labeled 1, 3, 6) and on all 4 post-tensioning bars at 3 different heights (labeled levels 1, 3, 5) in the column.
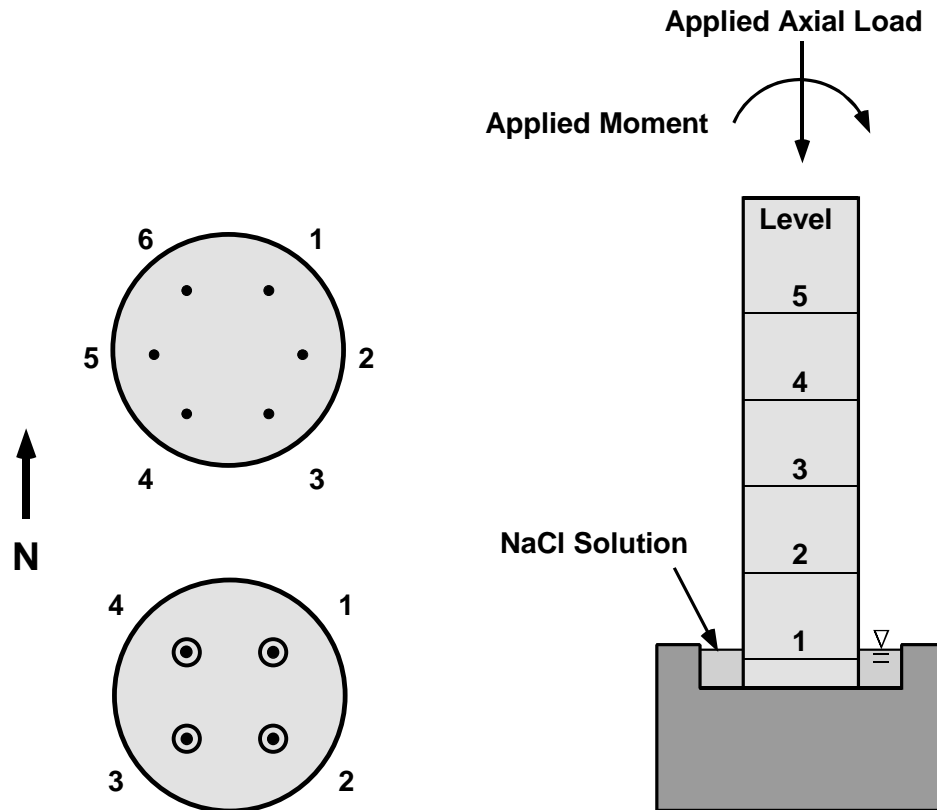
Figure 3.20 - Numbering for Half-Cell Potential Measurements

The column specimens began exposure testing in July of 1996. Plots of average half-cell potential readings through the end of April of 1999 (998 days) are given in Figure 3.21-Figure 3.29. The ASTM corrosion thresholds are given on the plots for reference. Readings taken at level 1 may be higher than expected since the concrete is continuously submerged at this level. The trend of the values is more important than the actual number, and values can be compared among different columns since exposure testing is consistent for all of the columns.

Figure 3.21-Figure 3.23 give the half-cell potentials for the non post-tensioned columns at levels 1, 3, and 5 (bottom, mid-height, and top level), respectively. The readings at the mid-height and top levels are generally in the range indicating less than 10% probability of corrosion. The values for the bottom level are higher, as expected since at this level the concrete is submerged. There are no distinct trends in the half-cell potential readings for the column specimens, although Specimen NJ-TC-S (no joint, TxDOT Class C concrete, service load) has slightly higher half-cell potentials at all levels.

Figure 3.24-Figure 3.29 show the half-cell potentials for the post-tensioned columns. Readings for reinforcing bars and post-tensioning bars are separated into separate plots. The post-tensioned specimens each have two plain post-tensioning bars/ducts and two bars or ducts that investigate a protection variable. The different

variables are separated for each specimen in the plots. In general, the values are below the 10% probability of corrosion line, although the submerged concrete gives somewhat higher readings. The only specimen showing consistently higher readings than the other specimens is the specimen with epoxy-coated post-tensioning bars. These higher readings do not necessarily indicate that the epoxy bars are corroding more rapidly than the other bars. Other researchers have found that half-cell readings on epoxy-coated steel with imperfections in the coating tend to be higher than expected.

Table 3.7 and Table 3.8 provide a summary of the average half-cell potential readings for the non post-tensioned and post-tensioned columns. Additional plots of half-cell potentials of each reading location for each column are included in Appendix B. As expected, readings are generally higher for readings taken on the dripper side of the column.
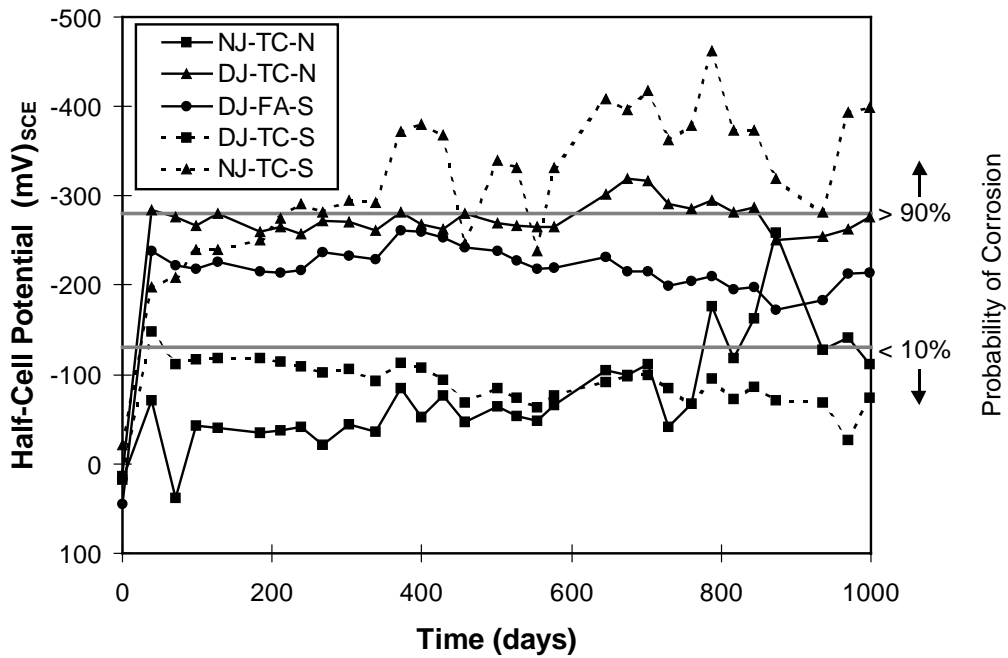
Figure 3.21 - Half-Cell Potential Readings at Level 1
(Non Post-Tensioned Columns)
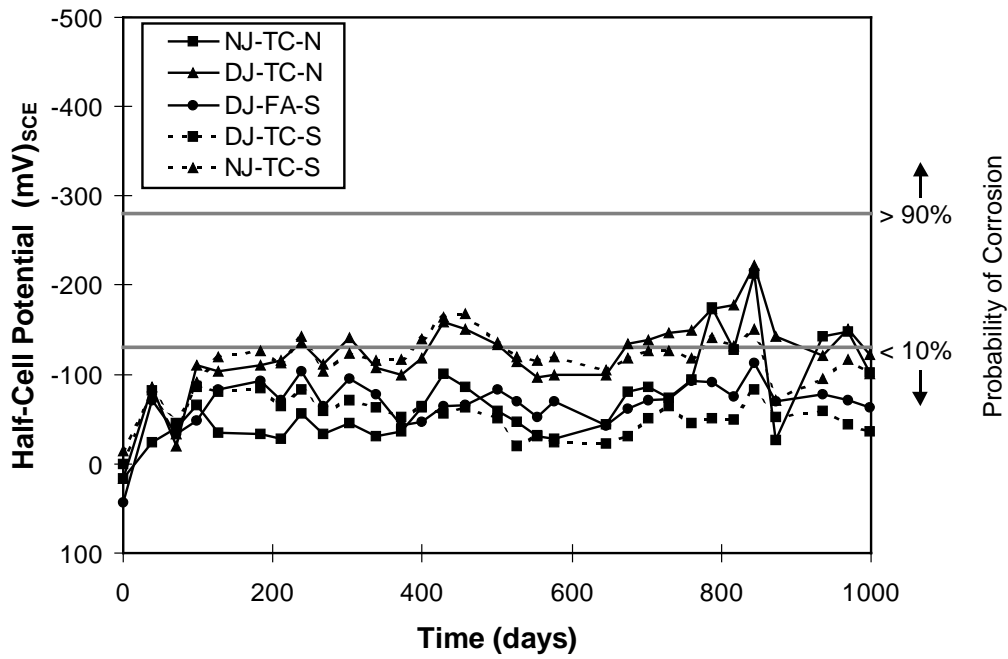
Figure 3.22 - Half-Cell Potential Readings at Level 3
(Non Post-Tensioned Columns)
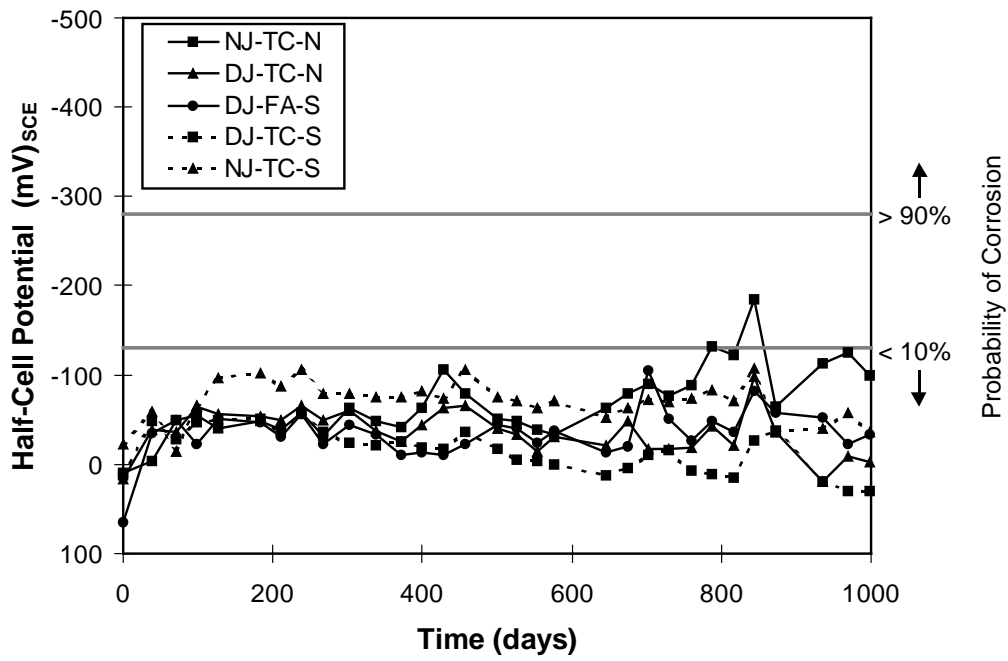
Figure 3.23 - Half-Cell Potential Readings at Level 5
(Non Post-Tensioned Columns)

141
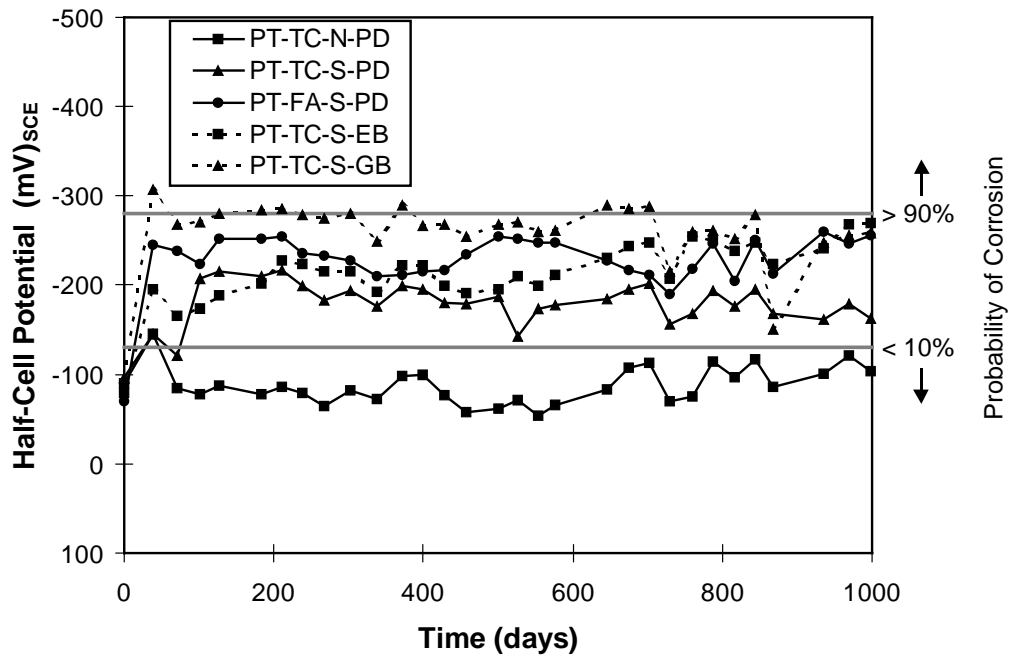
Figure 3.24 - Half-Cell Potential Readings for Reinforcing Bars at Level 1
(Post-Tensioned Columns)
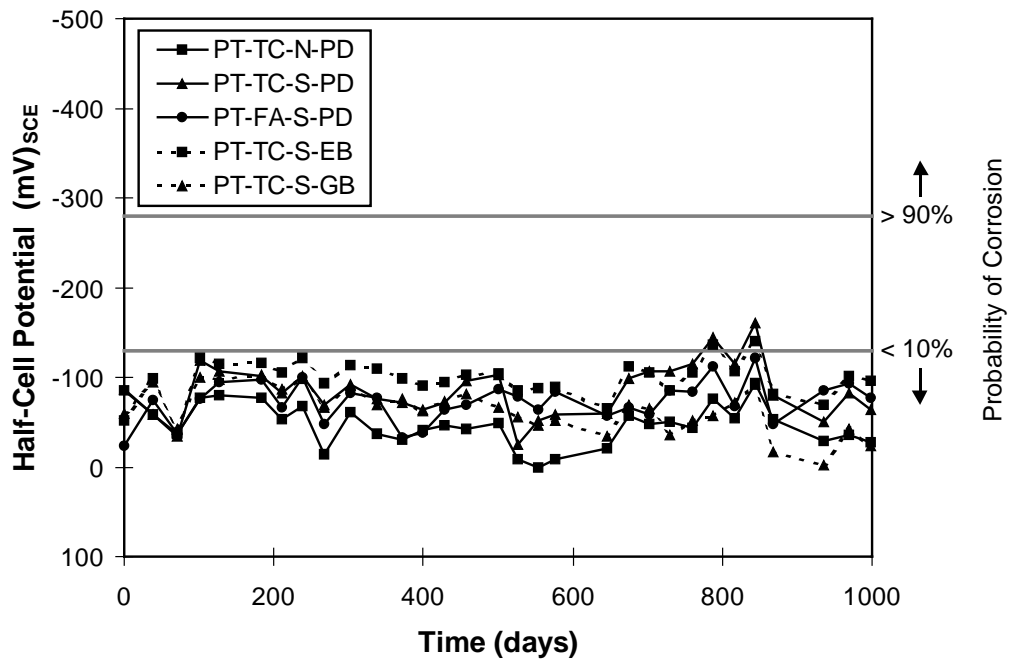
Figure 3.25 - Half-Cell Potential Readings for Reinforcing Bars at Level 3
(Post-Tensioned Columns)
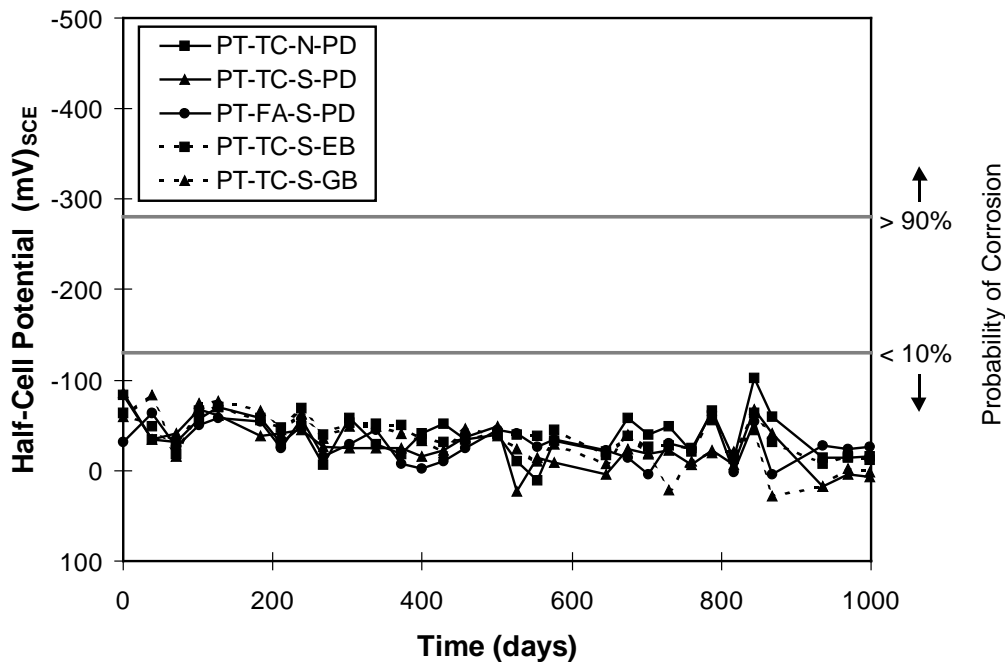
Figure 3.26 - Half-Cell Potential Readings for Reinforcing Bars at Level 5
(Post-Tensioned Columns)
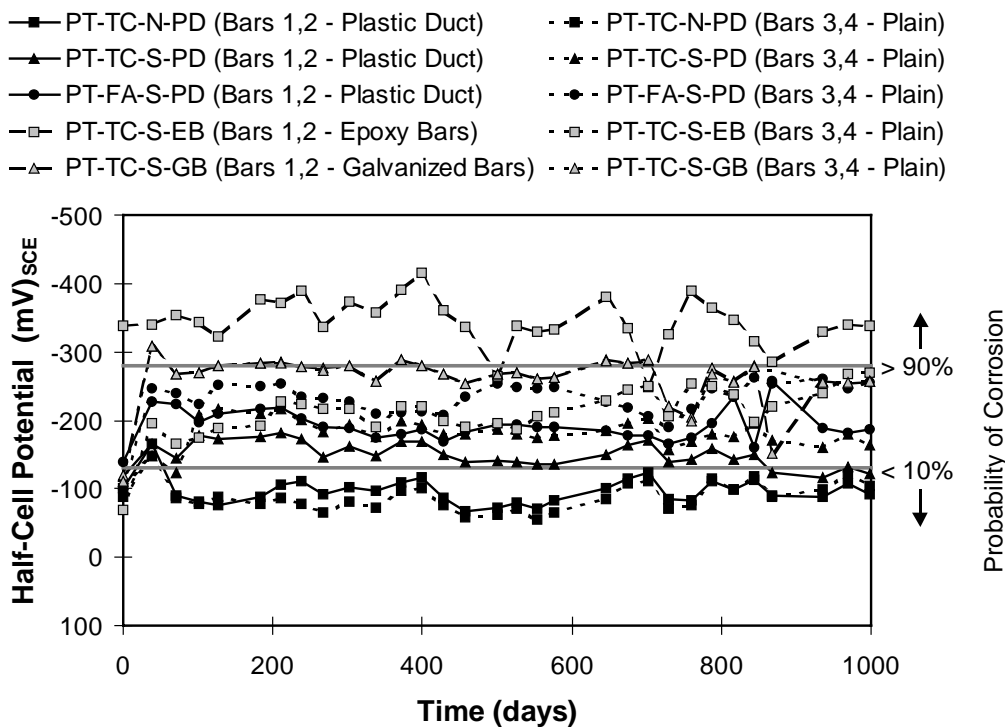
Figure 3.27 - Half-Cell Potential Readings for Post-Tensioning Bars at Level 1
(Post-Tensioned Columns)
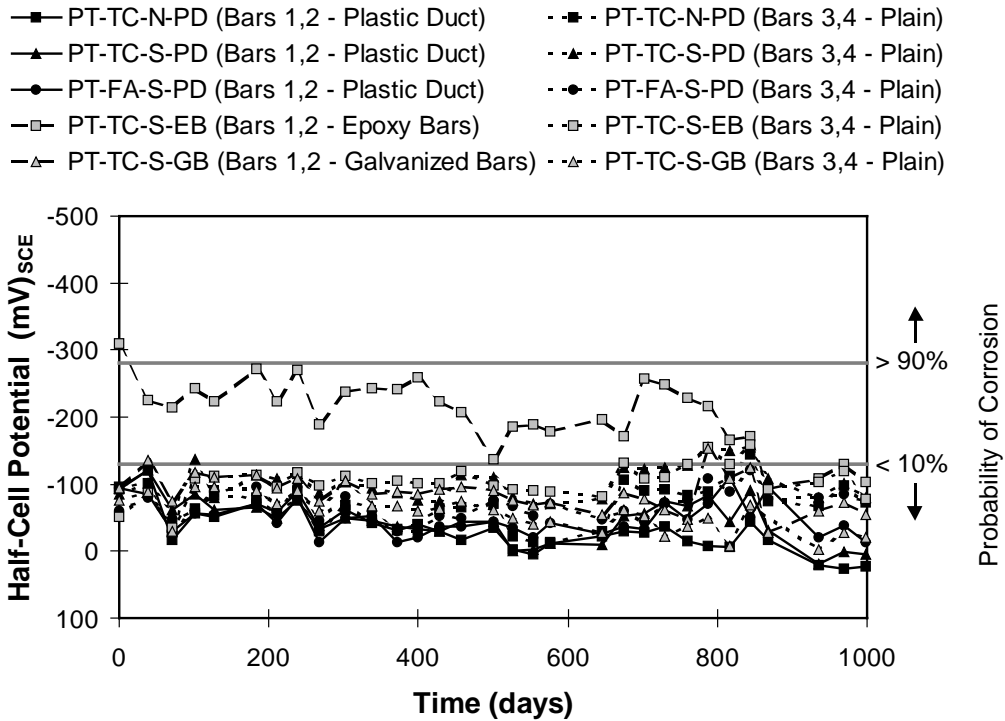
Figure 3.28 - Half-Cell Potential Readings for Post-Tensioning Bars at Level 3 (Post-Tensioned Columns)
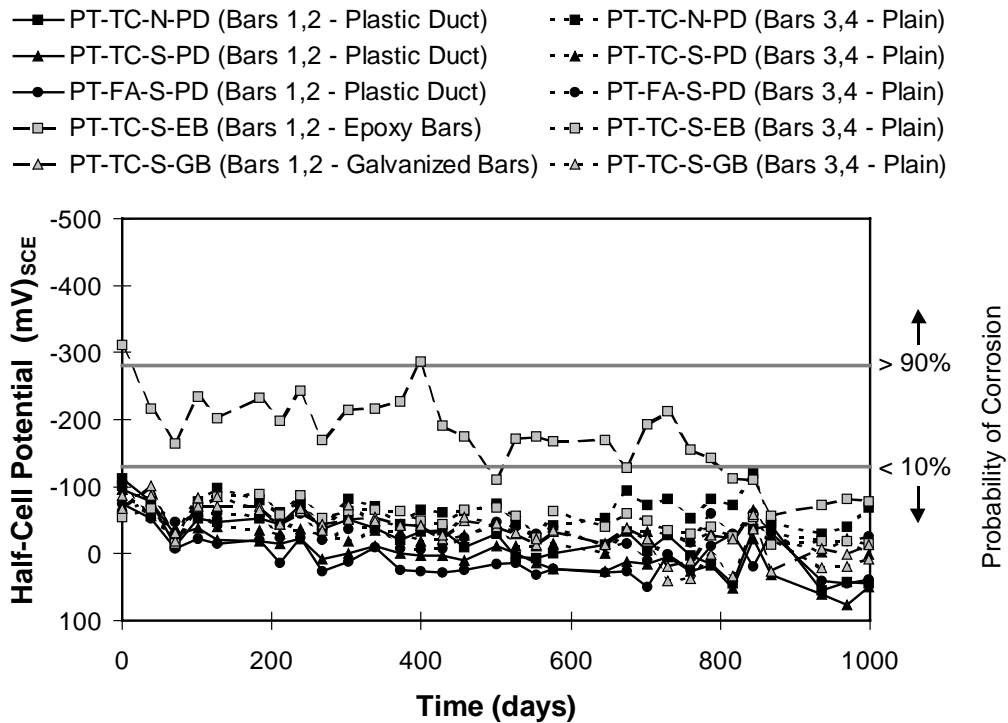
Figure 3.29 - Half-Cell Potential Readings for Post-Tensioning Bars at Level 5 (Post-Tensioned Columns)

Table 3.7 - Nonprestressed Column Average Half-Cell Readings Summary

Specimen	Level	Probability of Corrosion
NJ-TC-N	5	uncertain
	3	uncertain
	1	uncertain
DJ-TC-N	5	low
	3	uncertain
	1	high
DJ-FA-S	5	low
	3	low
	1	uncertain
DJ-TC-S	5	low
	3	low
	1	low
NJ-TC-S	5	low
	3	uncertain
	1	high

Table 3.8 - Post-Tensioned Column Average Half-Cell Readings Summary

Specimen	Level	Probability of Corrosion		
		Rebar	PT Bars (Plain)	PT Bars (Protected)
PT-TC-N-PD	5	low	low	low
	3	low	low	low
	1	low	low	low
PT-TC-S-PD	5	low	low	low
	3	low	low	low
	1	uncertain	uncertain	uncertain
PT-FA-S-PD	5	low	low	low
	3	low	low	low
	1	uncertain	uncertain	uncertain
PT-TC-S-EB	5	low	low	uncertain
	3	low	low	uncertain
	1	uncertain	uncertain	high
PT-TC-S-GB	5	low	low	low
	3	low	low	low
	1	uncertain	uncertain	uncertain

3.8.1.1 Using Half-Cell Potential Data to Compare Specimen Performance

The half-cell potential measurements represent the largest volume of collected data to monitor specimen condition during testing. Evaluation of many of the variables at this stage of testing must rely largely on the half-cell potential data. Before entering into an in depth analysis of the half-cell potential data, it is important to

emphasize that half-cell potentials are only an indicator of corrosion incidence, and a correlation with corrosion rate can not be made. The ASTM C876 guidelines for interpreting potentials indicate the probability of corrosion. Very negative potentials can be used to suggest a higher probability of corrosion activity, but not necessarily a higher corrosion rate.

Many factors can influence measured half-cell potentials, including concrete cover thickness, concrete resistivity, concrete moisture content, different metals and availability of oxygen. Therefore, comparisons of half-cell potentials for different test specimens should only be made for measurements taken under similar conditions.

Finally, the most useful application of half-cell potential measurements is possible when regular measurements are made over an extended period, as in this testing program. A common trend observed in corrosion research is that a transition from fluctuating or steady more positive potentials to a stable condition of more negative potentials is normally associated with the onset of corrosion. Transition to stable potentials within the range of –400 mV to –650 mV is frequently associated with a loss of passivity and corrosion initiation.

3.8.1.2   Very Negative Half-Cell Potentials

The average potentials at the column base are at or near the ASTM guideline for high corrosion probability for several column specimens, as shown in Figure 3.30. However, this elevated potential does not necessarily mean that corrosion is occurring for two reasons.

First, the readings at the column base are taken below the water level where the concrete is continually submerged. When the oxygen supply is restricted, as in the case of submerged concrete, the rate of the cathodic reaction is reduced and the corroding system is said to be under diffusion control. A system under diffusion control is illustrated by mixed potential theory in Figure 3.31. Because the slope of the cathodic reaction becomes very steep, the corrosion potential at equilibrium is very negative and the corrosion rate is small. Thus, very negative half-cell potentials in submerged concrete should not necessarily be interpreted as an indication of significant corrosion activity.
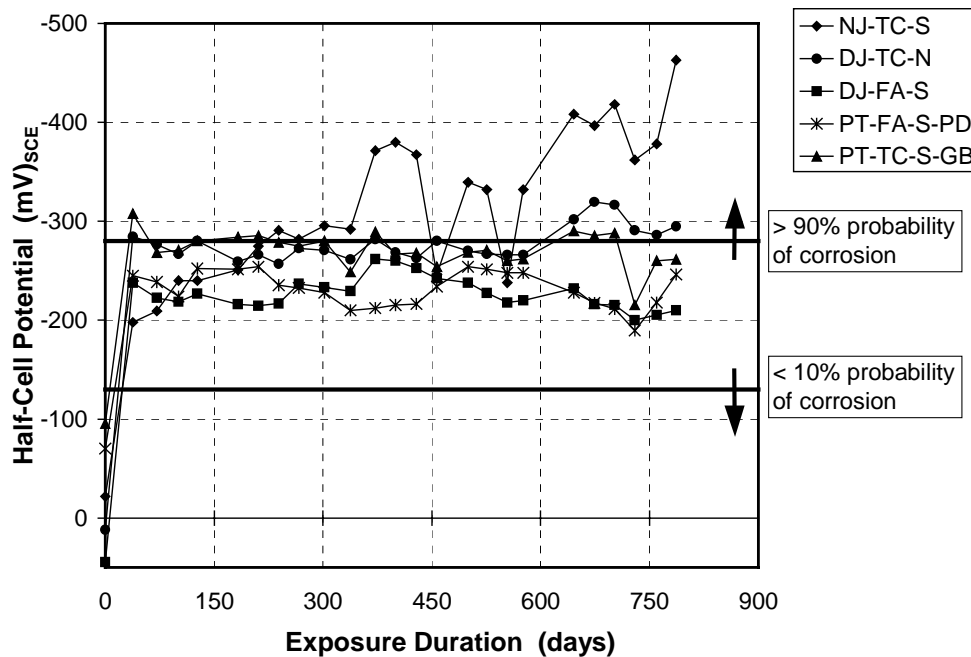
Figure 3.30 - Very Negative Half-Cell Potentials at Column Base in Selected Specimens
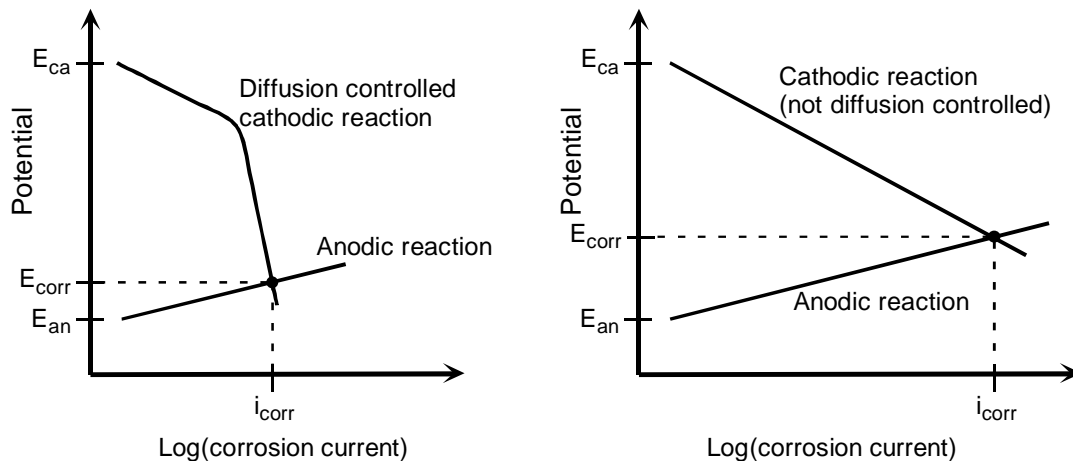
Figure 3.31 - Effect of Diffusion Controlled Cathodic Polarization (Lack of Oxygen) on Corrosion Potential and Current

The second factor to consider is the changes in potential measurements over time. When the readings over the duration of testing are considered, most specimens show consistent half-cell potentials since the start of exposure with no significant deviations, with the exception of NJ-TC-S. Normally, the onset of corrosion would be indicated by a well defined transition to stable, more negative potentials. Since this transition has not occurred in most columns, it is likely that the steel is not corroding. For column NJ-TC-S, a continuing trend of more negative potentials could suggest an initiation of corrosion activity.

3.8.2   Chloride Penetration

Chloride samples were taken from selected column specimens at 20 months and 32 months. Additional samples will be taken at one-year intervals. Samples were taken from specimens representing each concrete type, joint type, and load level. Powder samples were taken for three depths: 13 mm (7-19 mm), 25 mm (19-32 mm), and 50 mm (45-57 mm). The 50 mm depth data represent the chloride concentration at the bar level. The chloride samples were also taken at three heights to investigate possible "wicking" effects: 75 mm, 230 mm, and 380 mm up from the base of the column. The 75 mm height represents the constantly submerged concrete. The majority of samples were taken from the side of the column not exposed to the saltwater dripper runoff, but one column was also sampled from the saltwater dripper side for comparison. Each sample is taken from two locations and the powder is combined to give a representative sample. From a representative sample, several acid-soluble chloride tests are run and the results are averaged.

Figure 3.32-Figure 3.37 show the chloride penetration data at 20 months and at 32 months. Samples investigating load level were taken only at 32 months. The figures show the chloride content for each specimen at a given depth. Corrosion thresholds depend on many variables besides chloride content. The chloride threshold values shown are calculated for TxDOT Class C concrete and values differ slightly for concrete containing fly ash, but an approximate threshold value is given for illustrative purposes. Additional figures showing the chloride penetration data for each specimen are given in Appendix B.

Chloride contents for a sample depth of 13 mm (0.5") are shown in Figure 3.32 and Figure 3.33. At 20 months, all specimens had chloride levels above the threshold value at the two heights closest to the base, while the majority of the values were below the threshold at the top height. At 32 months, the majority of the chloride levels had increased beyond the threshold value at all heights. At this sample depth, the fly ash concrete showed the best performance, and the post-tensioned joint showed the highest chloride contents.

Figure 3.34 and Figure 3.35 show the chloride contents at a sample depth of 25 mm (1"). At 20 months the doweled joint specimen and no joint specimen had chloride levels above the threshold value at the submerged level. The majority of the specimens had chloride contents near the threshold level at the middle sample height. At the top sample height, all specimens had chloride contents below the threshold level. At 32 months, the majority of specimens showed significantly increased chloride levels, especially at the middle sample height. Chloride contents at the top sample height remained below the threshold value. Again, the fly ash specimen showed the best performance.

Chloride contents at a sample depth of 50 mm are shown in Figure 3.36 and Figure 3.37. The samples taken at this depth represent the chloride penetration at bar level and provide insight into the potential corrosion in the specimens. The majority of the specimens showed chloride levels below the threshold value at both 20 months and 32 months. In some cases, chloride levels at 32 months were slightly lower than at 20 months, which is likely due to the variance in collection locations. Samples must be drilled from new locations for each test. Although powder from two locations is mixed for each set of samples, and drilling for later samples is near the original locations, some variation is expected.

Figure 3.38 and Figure 3.39 show comparisons between samples taken from the dripper side and from the nondripper side of a column. The dripper side samples were taken only at 32 months and were taken only in the nonsubmerged concrete. The major difference in chloride contents is seen in the samples taken at the middle sample height. Chloride levels in the dripper side sample are very high. At the 13 mm depth, chloride levels for this specimen are almost 25 times the threshold value.

The upward migration of chlorides in the columns is evident from the chloride samples. Significant levels of chlorides were found in samples taken 130 mm and 280 mm above the water line. Several specimens showed higher levels of chlorides at the middle sample level than at the submerged sample level. It is likely that the effect of wicking combined with an environment that allows drying of the concrete is resulting in more severe exposure conditions for these samples.
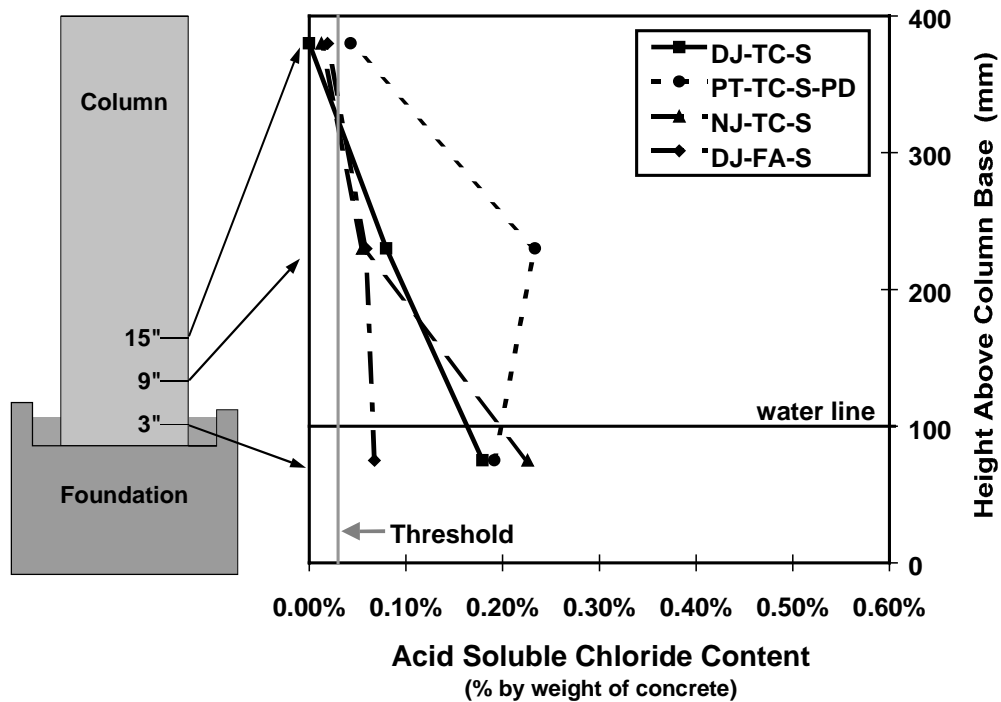
Figure 3.32 - Column Chloride Penetration at 13 mm for 20-Month Exposure

148
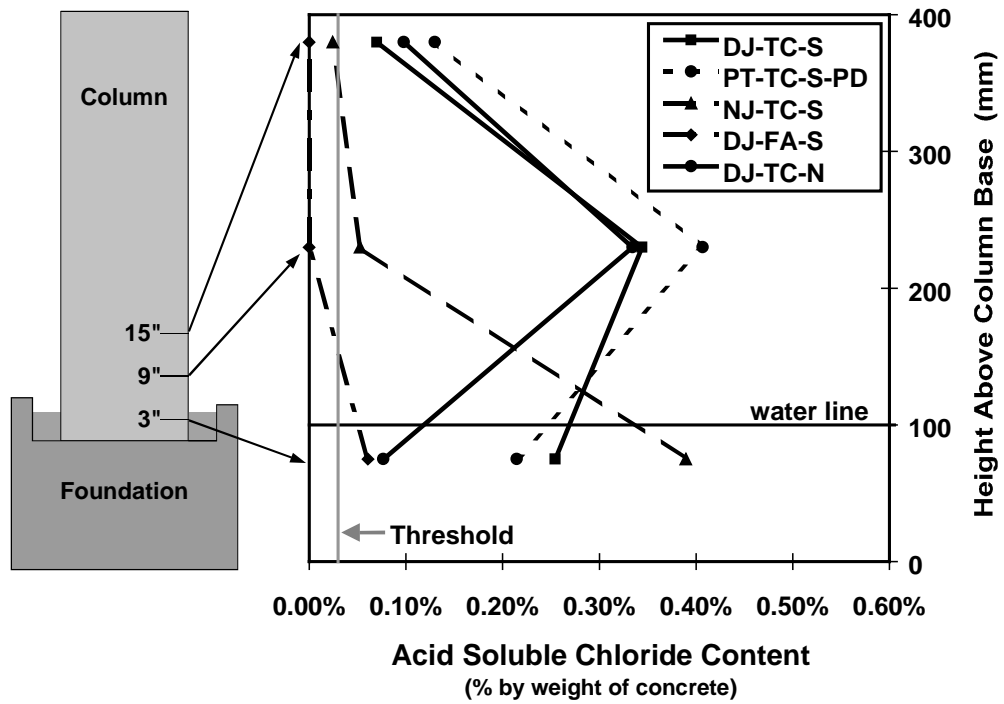
Figure 3.33 - Column Chloride Penetration at 13 mm for 32-Month Exposure
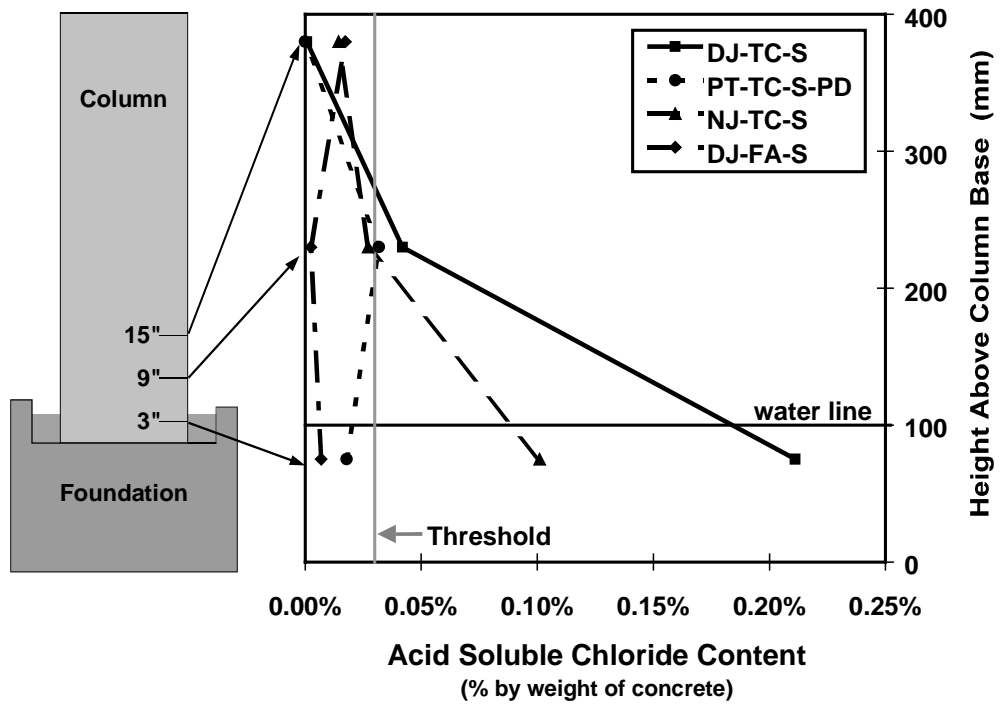
Figure 3.34 - Column Chloride Penetration at 25 mm for 20-Month Exposure

149
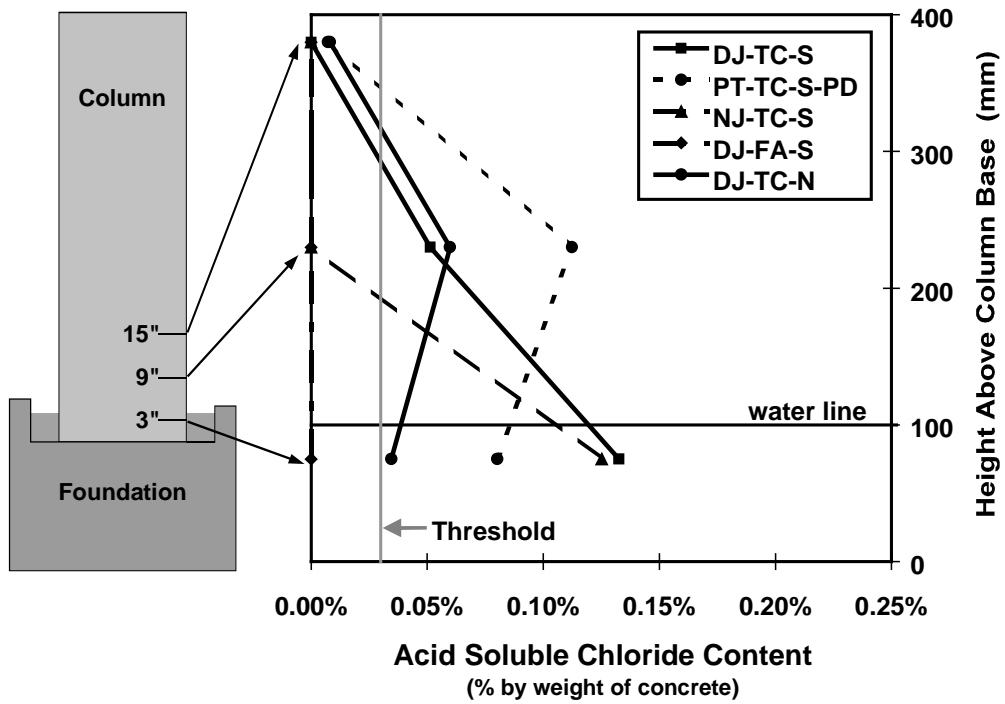
Figure 3.35 - Column Chloride Penetration at 25 mm for 32-Month Exposure
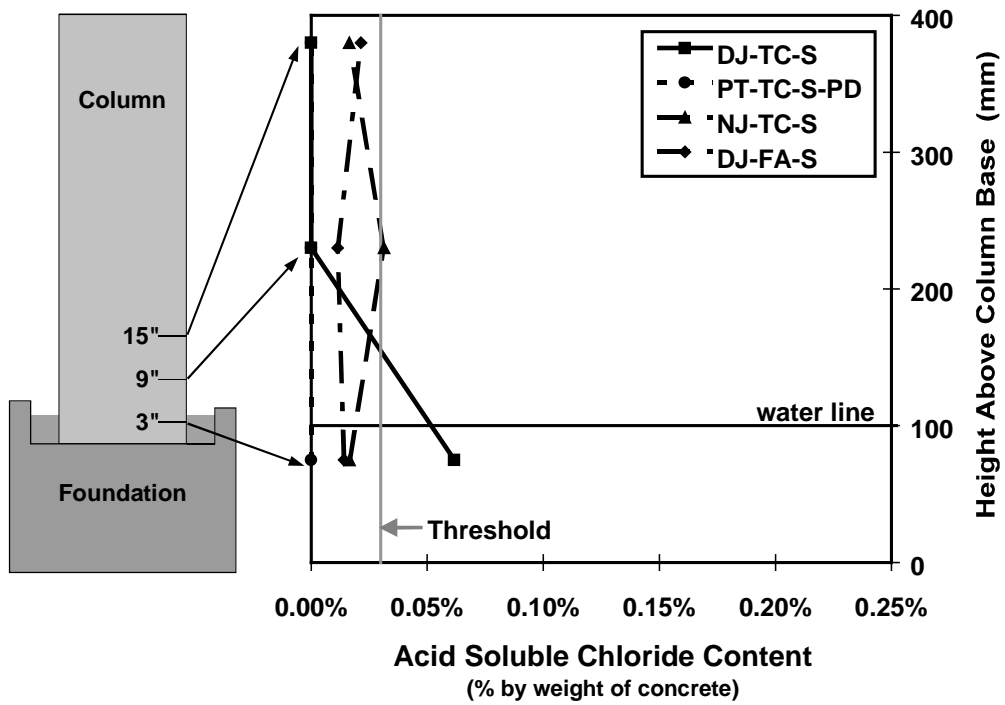
Figure 3.36 - Column Chloride Penetration at 50 mm for 20-Month Exposure

150
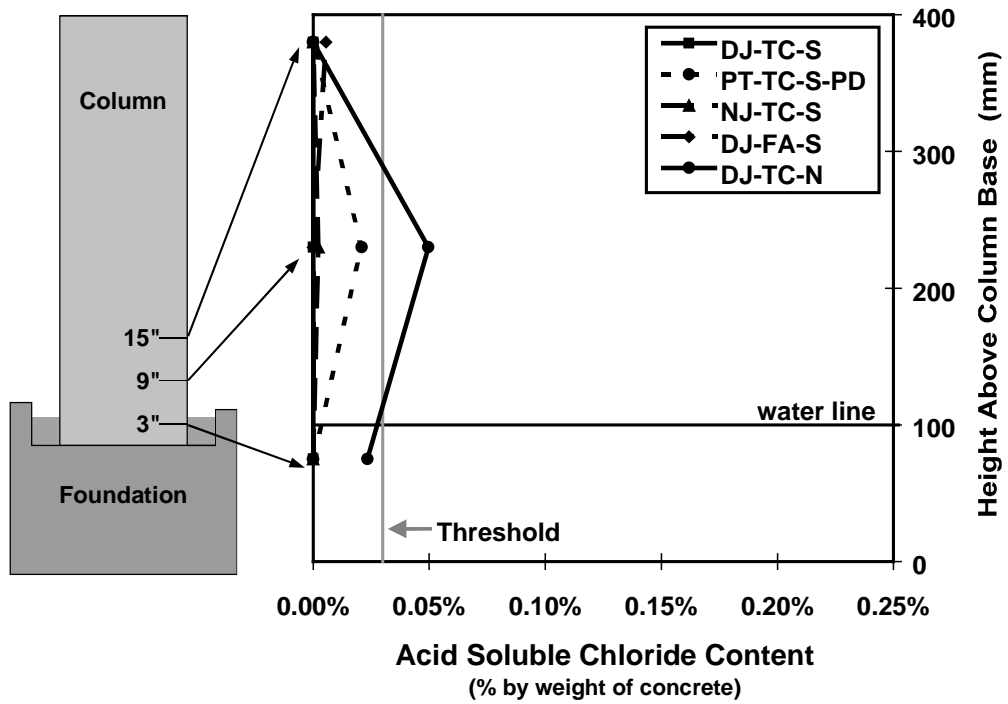
Figure 3.37 - Column Chloride Penetration at 50 mm for 32-Month Exposure
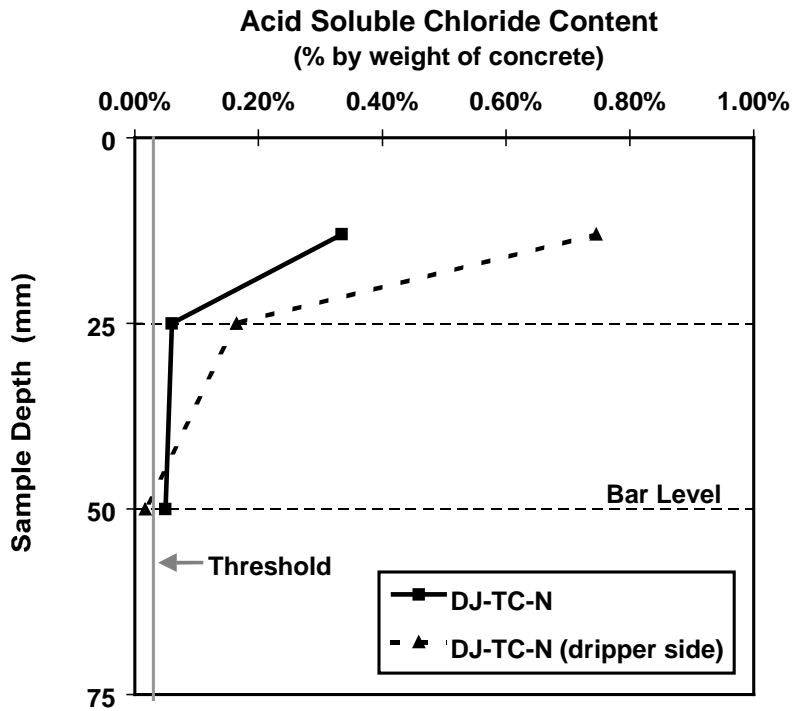
Figure 3.38 - Effect of Dripper on Chloride Penetration, 230 mm Above Base

151

Acid Soluble Chloride Content
(% by weight of concrete)
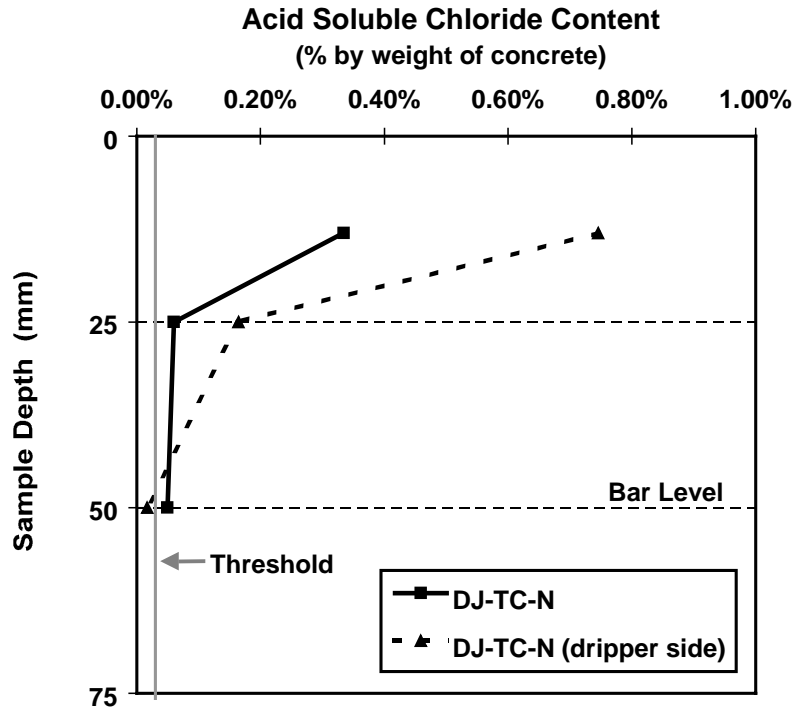
Figure 3.39 - Effect of Dripper on Chloride Penetration, 230 mm Above Base

Acid Soluble Chloride Content
(% by weight of concrete)
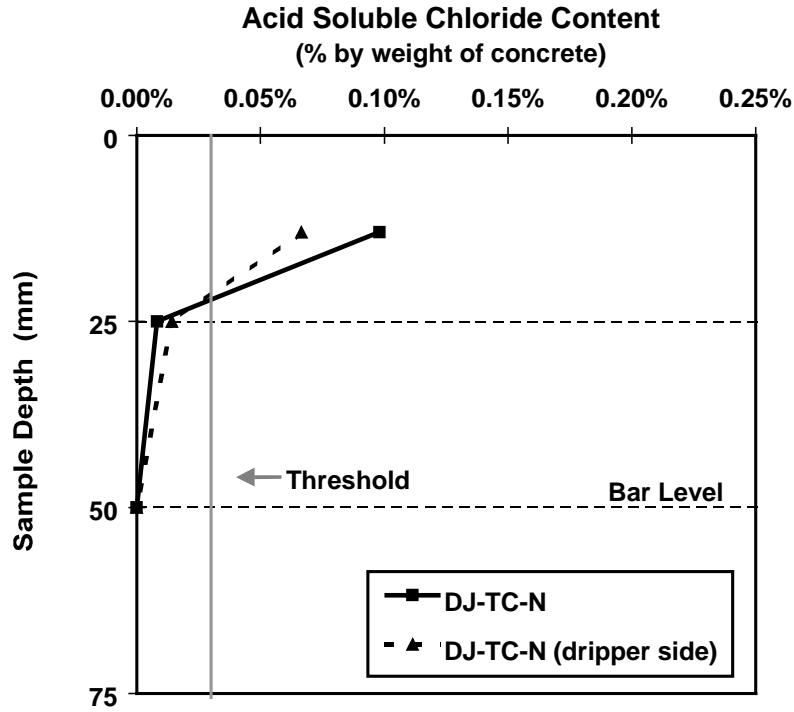
Figure 3.40 - Effect of Dripper on Chloride Penetration, 380 mm Above Base

3.9   AUTOPSY

3.9.1   Limited Autopsy

Two columns were chosen for invasive inspection: one non post-tensioned column and one post-tensioned column. Half-cell readings showed little indication that certain columns were likely to be more corroded than others. Specimen DJ-TC-N (doweled joint, Texas Class C concrete, and no loading) was chosen from the non post-tensioned specimens since it had somewhat higher half-cell readings than the other specimens. Specimen PT-TC-S-PD (Texas Class C concrete, service load, and plastic duct) was chosen from the non post-tensioned specimens.

3.9.1.1   Chloride Samples

The invasive inspections were performed on the saltwater dripper side of the columns since the corrosion in this area is likely to be the most severe. The chloride profiles for the columns chosen for limited autopsy were already known for the nondripper side, since these columns were chosen for the chloride samples as discussed in Section 3.8.2. Additional samples were taken for each specimen on the dripper side near the autopsy area. Results are shown in Figure 3.41. Both columns show chloride levels significantly higher than the threshold level at depths of 13 mm (0.5") and 25 mm (1"). Chloride has penetrated to the bar level, although the levels are not yet over the threshold value.
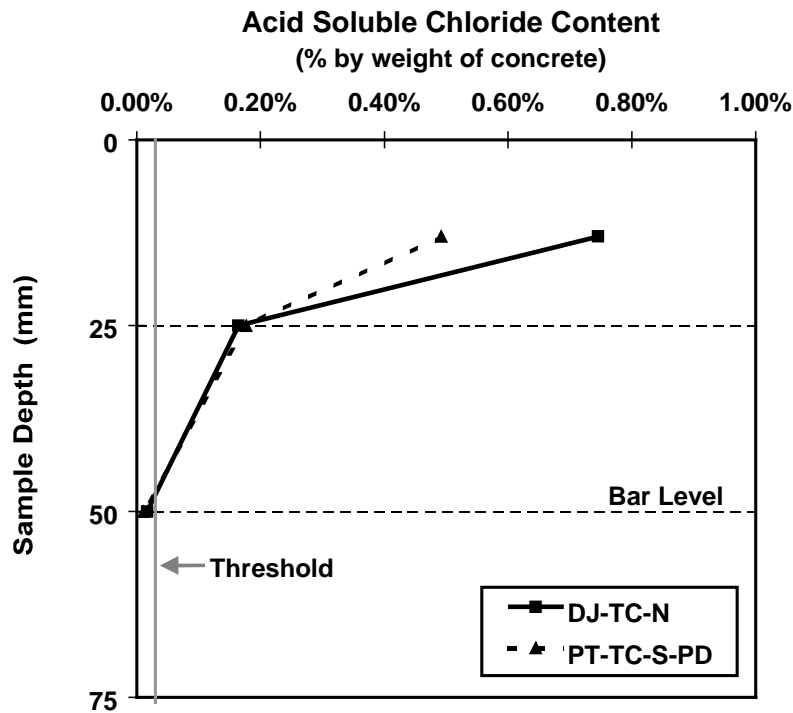
Figure 3.41 - Chloride Penetration at Column Limited Autopsy Sites

3.9.1.2   Inspection of Reinforcement

In the post-tensioned specimen, two of the ducts are plastic and two are standard galvanized duct. The galvanized duct on the dripper side was chosen for inspection since there was more likelihood of corrosion on this duct. A diagram showing the reinforcement chosen for invasive inspection is shown in Figure 3.42.

Specimen DJ-TC-N   *Specimen PT-TC-S-PD*
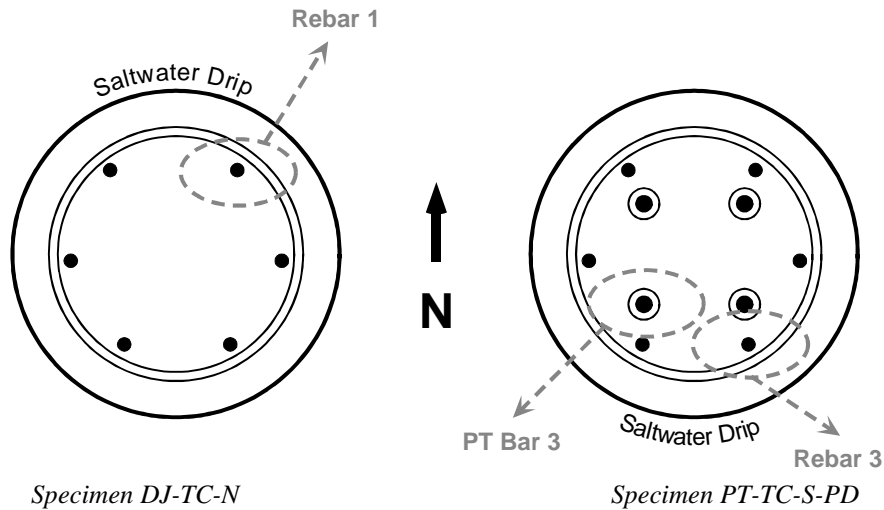
Figure 3.42 - Reinforcement Chosen for Inspection

3.9.2   Specimen DJ-TC-N

A 30 mm (1 ¼") starter hole was drilled 230 mm (9") from the column base to evaluate the condition of the reinforcing bars and spiral reinforcement. The hole was drilled up to just short of the level of the reinforcing steel and the remaining concrete above the steel was chipped away carefully by hand.   Once the steel was exposed, additional concrete was removed from the area with careful drilling and hand chipping to further expose the steel. Figure 3.43 shows the reinforcing bar after removal of the cover. The sketch shows locations of corrosion noted during the invasive inspection. The bar was in very good condition, but showed some light pitting corrosion. These findings are consistent with the half-cell potential readings, which have moved below the line of low probability of corrosion and are now in the uncertain range. The light corrosion found also indicates that the column specimens will need to continue exposure testing before final autopsy.
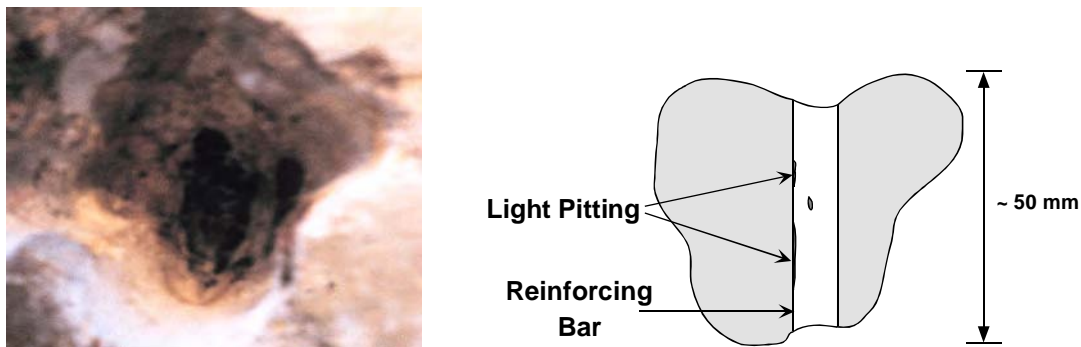
Figure 3.43 - Reinforcing Bar Condition, Specimen DJ-TC-N

3.9.3   Specimen PT-TC-S-PD

The condition of both the standard reinforcement and the post-tensioning duct was evaluated in this specimen. One hole was drilled at 230 mm (9") from the column base to evaluate the standard reinforcement, and an additional hole was drilled at the same height to expose the post-tensioning duct. The procedure for concrete removal was similar to that described in the preceding section. Extreme care was taken to expose the duct without damaging it, because even hand chipping can leave indentations in the galvanized steel duct. At both drill locations, interference from bolster strips made exposing the reinforcement difficult.   The exposed reinforcing bar and bolster strips showed no sign of corrosion.   The exposed duct also showed no signs of corrosion. The findings indicate that there is likely little or no corrosion on the reinforcing bars in the post-tensioned specimens and that it may be a number of years before significant corrosion begins on the post-tensioning ducts.

Staining

The majority of the column specimens show slight staining on the dripper side as shown in Figure 3.44. The results of the invasive inspection indicate that the staining is likely due to bar chairs / bolster strips. A close up of the spalling near the plastic tipped chairs is shown in the figure. Although the staining is not indicating significant corrosion, it is unsightly and can be easily remedied by the use of fully plastic bar chairs.

Repair

The holes were patched by coating with a layer of epoxy followed by fill with nonshrink grout. A patching material made with SikaLatex R was used to fill any remaining small holes and to even out the finish. The specimens were then returned to exposure testing with the remaining columns.

Figure 3.44 - Column Staining

3.9.4 *Full Autopsy*

When half-cell potential readings and limited autopsy findings indicate much more severe corrosion, all column specimens will be fully autopsied. The reinforcement cage, post-tensioning bars, and duct will be thoroughly inspected. Chloride samples will be taken from both the concrete and grout for each specimen. Samples should be taken at several heights to investigate the effects of wicking. Before beginning the full autopsies, the loading plates and bars should be removed. It will also be necessary to remove the lip of the base ponding area so that the column base may be easily accessed.

3.10 CONCLUSIONS

Findings for the column specimens will be more conclusive after the final autopsy of all specimens, but preliminary conclusions can be drawn from the half-cell potential readings, chloride samples, and limited autopsies.

Half-cell potential measurements indicate higher corrosion activity on the dripper side on the columns and at points nearer the base. Readings are also higher for the submerged concrete and for the epoxy-coated bars, although this increase is not necessarily an indication of corrosion. Readings are typically high in these circumstances due to a restriction of oxygen in the corrosion cell caused by being submerged or the epoxy coating. In general, half-cell readings are indicating little corrosion activity.

Chloride penetration tests showed evidence of vertical migration of chlorides in the columns.   Higher levels of chlorides were found at the middle sample level than at the bottom (submerged) sample level for several columns. The effect of wicking combined with an environment that allows drying of the concrete is likely resulting in more severe exposure conditions for these samples. Chloride concentrations on the dripper side of the columns were considerably higher than on the non-dripper side.

The limited autopsies revealed light pitting corrosion on a reinforcing bar for the non post-tensioned specimen inspected. The post-tensioned specimen examined showed no evidence of corrosion on the reinforcing bar or on the galvanized steel duct. These findings are consistent with the half-cell potential data for the column specimens. The invasive inspections indicate that exposure testing should continue for at least several more years to give beneficial results.

CHAPTER 4
SUMMARY AND CONCLUSIONS

4.1   LARGE-SCALE BEAM SPECIMENS

Twenty-seven large-scale beam specimens were used to evaluate the effect of post-tensioning on durability and to evaluate the relative performance of a large number of corrosion protection variables. Beams were fabricated in two phases in order to begin exposure testing on a portion of the specimens while the remaining specimens were being fabricated. In Phase I (16 beams), researchers investigated the effect of prestress level and crack width and also included one of the high performance grout specimens. In Phase II (11 beams), researchers investigated duct splices, grout type, concrete type, strand type, duct type, and end anchorage protection. The Phase I beams began exposure testing in December of 1997 and the Phase II beams began exposure testing in December of 1998. Findings for the beam specimens will be more conclusive after the final autopsy of all specimens, but preliminary conclusions can be drawn from the half-cell potential readings, chloride samples, and limited autopsies.

4.1.1   Half-Cell Potential Measurements

Half-cell potential measurements are taken at one-month intervals over a grid extending beyond the exposure testing area on the top surface of the beam. Data are analyzed as a contour plot of measurements over the beam surface to compare specimens at any given instance, and average values are used to compare specimens over time. Conclusions to date are as follows:

- As the level of post-tensioning increases, durability is increased.

- Cracking is the major source of chloride ingress observed to date.

- At this time there is no significant difference in corrosion protection between the 100% U PS and 100% S PS sections. This trend indicates that the 100% U PS section may have a better benefit to cost ratio. The advantage of the uncracked specimen (100% S PS) may become more apparent as the exposure testing continues.

- Corrosion activity extends outside of the ponded region.

- Fly ash addition to the concrete improves durability due to lowered permeability.

- The high performance concrete tested improves durability by both crack control and lowered permeability.

- Benefits from the plastic duct, strand coatings, and encapsulated system are not likely to be fully known until final autopsy due to the difficulty in monitoring these types of materials with half-cell potentials.

4.1.2   Chloride Samples

Chloride samples on the ponding blocks for the Phase I beam specimens were taken after 7 months and 14 months of exposure testing. Samples were also taken from selected specimens during limited autopsy. Conclusions to date are as follows:

- Uncracked and unponded control blocks have negligible chlorides at all depths.

- Uncracked ponded blocks show penetration of chlorides, but chlorides are negligible at bar level for uncracked concrete.

- Samples taken from limited autopsy specimens indicate significantly higher chlorides at locations with cracks.

- Chloride penetration is reduced in the post-tensioned specimens.

4.1.3 Corrosion Rate Measurements Using Polarization Resistance

Corrosion rate measurements were obtained using the three electrode procedure to measure polarization resistance. Two different devices were used: 3LP and PR Monitor. The PR Monitor uses a guard electrode for signal confinement and compensates for concrete resistance. Corrosion rate measurements were taken after seven, twelve and fifteen months of exposure. Conclusions to date are as follows:

- Corrosion rates obtained using the 3LP device were extremely high and did not correlate with specimen condition and half-cell potentials. The PR Monitor indicated lower corrosion activity than the 3LP, although moderate to high corrosion rates were indicated for most beams.

- The corrosion activity indicated by both devices, and in particular the 3LP, contradicted the half-cell potential measurements for some specimens. In general, the highest corrosion rates were obtained for the 100%U PS beams, while the most negative half-cell potentials were measured for the Non-PS beams. Numerous possible factors were investigated, but no firm conclusions could be made other than several limitations exist for the 3LP device and the polarization resistance technique in general.

- The corrosion rate measurements indicated localized areas of high corrosion activity may be present in some beams. This occurrence was confirmed in the 100%U PS beams during the limited autopsy by invasive inspection, where severe corrosion was found on stirrups coinciding with flexural cracks.

- The PR Monitor appears to provide a better assessment of corrosion rate than the 3LP device. Because of differences between the devices, it is not recommended to directly compare corrosion rates obtained using the 3LP and PR Monitor.

- The 3LP device suffers from an unconfined polarizing signal. As a result, the polarized area of steel will unknowingly be larger than expected in most cases, resulting in an overestimation of corrosion rate.

- The three-electrode technique for measuring polarization resistance appears to be most useful for relative comparisons of corrosion activity rather than a quantitative assessment of corrosion rate. Relative comparisons should only be made for similar beams and similar conditions, and therefore the comparison of corrosion rates for the different levels of prestress investigated is questionable.

- Corrosion rate measurements in post-tensioned concrete structures should be approached with caution and should not be relied on as a sole method to evaluate corrosion activity.

- Regular corrosion rate measurements over time are needed to assess the amount of corrosion related distress in structural concrete. Discrete measurements may occur at instances where corrosion rates are higher or lower than normal and give a false indication of the specimen or structural element condition.

- The PR Monitor is recommended for future corrosion rate measurements in this testing program. The 3LP device could be used as a second choice.

4.1.4 Crack Width Prediction for Structural Concrete with Mixed Reinforcement

- Comparison of measured crack data with several crack prediction models produced widely varying results. This finding suggests that not all crack prediction methods are appropriate for structural concrete members with a combination of mild steel and prestressed reinforcement.

- The Gergely-Lutz crack width model provided an excellent prediction of maximum crack widths for the Non-PS and 2/3 PS beams and a conservative estimate for the 100%U PS beams. The Gergely-Lutz model was applied using the recommendations of Armstrong et al. This model is relatively easy to apply and is recommended for sections with mixed reinforcement.

- The Batchelor and El Shahawi crack width expression provided a very good prediction of maximum crack widths for the 2/3 PS and 100%U PS beams. This very simple model is also recommended for sections with mixed reinforcement.

4.1.5 Limited Autopsy by Invasive Inspection

Three specimens were chosen for limited autopsy. Two of the 100% U PS specimens and one Non-PS specimen were inspected. Conclusions from the limited autopsies are as follows:

- The Non-PS specimen showed signs of corrosion at both inspected locations. The stirrup under the crack had extensive light pitting with two concentrated areas of pitting. The reinforcement away from the crack had only one area of noticeable pitting.

- The stirrup in the cracked region for the post-tensioned specimen with little staining showed no signs of corrosion. The stirrup uncovered under a crack with staining showed similar corrosion to the stirrup in the Non-PS section.

- The post-tensioning duct showed no signs of corrosion and was fully grouted at the inspection location.

- The heavily cracked Phase I specimens are showing a large amount of staining at the cracks. In addition, many of the Phase I specimens are showing staining from the corrosion of the plastic-tipped steel bolster strips. In some cases, the concrete has spalled revealing the plastic tips. This unsightly staining and spalling may be remedied by the use of fully plastic chairs. Plastic chairs were used in the Phase II specimens so that their use could be evaluated. At this point, the staining and spalling away from cracked areas observed in the Phase I specimens is not evident in the Phase II specimens.

- Visible signs of corrosion of the reinforcement were limited to the cracked locations at this stage of exposure testing. The large number of cracks and greater crack widths associated with the specimens containing lower levels of prestressing will likely cause deterioration of the these specimens first. A greater depth of concrete with a reduced number of cracks protects the post-tensioning ducts.

4.2 LARGE-SCALE COLUMN SPECIMENS

Ten large-scale column specimens were used to examine corrosion protection mechanisms and chloride ion transport ("wicking" effect) in various column connection configurations and to evaluate column corrosion protection measures. Variables included foundation connection, post-tensioning system protection, concrete type, and loading. Column exposure testing began in July of 1996. Findings for the column specimens will be more conclusive after the final autopsy of all specimens, but preliminary conclusions drawn from the half-cell potential readings, chloride samples, and limited autopsies are given below.

4.2.1 Half-Cell Potential Measurements

Half-cell potential measurements were taken at one-month intervals. Readings are taken at several heights for the reinforcing bars and the post-tensioning bars. The conclusions from the readings to date are as follows:

- Corrosion activity is higher on the dripper side of the column.

- Corrosion activity is higher at levels closer to the base.

- Readings are higher for the submerged concrete and for the epoxy-coated bars, although this increase is not necessarily an indication of corrosion. Readings are typically high in these circumstances due to a restriction of oxygen in the corrosion cell below the water level.

4.2.2 Chloride Samples

Chloride samples were taken directly from the column specimens after 20 months and 32 months of exposure testing. Samples were taken at several heights from the base and on both the dripper and non-dripper sides of the columns. The conclusions from the samples taken to date are as follows:

- Data from chloride samples taken on the non-dripper side of the columns indicate that chlorides have traveled significantly above the water line ("wicking" effect).

- Chloride levels on the dripper side were significantly higher than levels on the non-dripper side.

- Columns with fly ash concrete showed the lowest levels of chloride penetration.

- Several specimens showed higher levels of chlorides at the middle sample level than at the submerged sample level. It is likely that the effect of wicking combined with an environment that allows drying of the concrete is resulting in more severe exposure conditions for these samples.

4.2.3   Limited Autopsy by Invasive Inspection

Two columns were chosen for invasive inspection: one post-tensioned column and one non post-tensioned column. No visible signs of corrosion were found on the reinforcing bar or post-tensioning duct for the post-tensioned specimen. The reinforcing bar uncovered in the non post-tensioned specimen had some light pitting corrosion. These findings were consistent with findings from the half-cell potential readings.

CHAPTER 5
IMPLEMENTATION RECOMMENDATIONS

After final autopsy of all of the long-term beam and column exposure specimens, findings will be more conclusive. Based on the chloride samples, half-cell monitoring, and limited autopsies performed through April of 1999, several items are recommended for immediate implementation to improve durability in post-tensioned substructures.

ITEM 1: POST-TENSIONING

The specimens are showing increased durability with post-tensioning. The increase in durability should be considered along with the other benefits of post-tensioning when choosing a type of construction.

ITEM 2: PLASTIC DUCT

Plastic duct is recommended for use throughout the substructure to eliminate the potential for spalling and staining that is possible with galvanized duct. The plastic duct also can provide an impermeable membrane to protect the strand from chloride ingress.

ITEM 3: PLASTIC CHAIRS

Fully plastic chairs are recommended for use throughout the substructure to eliminate unsightly staining and spalling. Chairs or bolster strips that contain any steel (included plastic tipped steel chairs) should be avoided.

ITEM 4: FLY ASH CONCRETE

Fly ash concrete is recommended for all substructure elements. The significantly reduced permeability slows chloride ingress. This substitution can be accomplished with little or no additional cost.

ITEM 5: HIGH PERFORMANCE CONCRETE

The high performance concrete specimens are showing improved corrosion resistance due to both the lowered concrete permeability and crack control.

APPENDIX A

LONG-TERM BEAM CORROSION TESTS: SUPPLEMENTARY MATERIAL

Analysis of Section 100%S for Maximum Allowable Loading

Gross Section Properties:

$A_g = 457.2 \times 609.6 = 278{,}709 \text{ mm}^2$

$S_b = S_t = \dfrac{(457.2)(609.6)^2}{6} = 28{,}316{,}847 \text{ mm}^3$

At Transfer:

extreme fiber stress compression, $f_c \leq 0.60 \, f'_{ci} = 21 \text{ MPa (3 ksi)}$

extreme fiber stress tension, $f_t \leq 0.25\sqrt{f'_{ci}} = 1.48 \text{ MPa (0.214 ksi)}$

prestress force at transfer, $T_i = 8 \times 0.65(1860 \text{ MPa}) \times 99 \text{ mm}^2$

$= 958 \text{ kN (215 kips)}$

tendon eccentricity at midspan, $e = 200 \text{ mm (8 in.)}$

$$f_c = \frac{958{,}000}{278{,}709} + \frac{(958{,}000)(200)}{28{,}316{,}847} = 10.2 \text{ MPa (1.48 ksi)}$$

$$f_t = \frac{958{,}000}{278{,}709} - \frac{(958{,}000)(200)}{28{,}316{,}847} = -3.33 \text{ MPa} (-.483 \text{ ksi})$$

- At transfer, the extreme fiber stress in tension exceeds the allowable value, and a portion of the superimposed loading will have to be applied to satisfy stress limits.
- The tendon profile will be draped to reduce the tendon eccentricity near the member ends to satisfy stress limits.

Compute Maximum Permissible Service Loading:

extreme fiber stress compression, $f_c \leq 0.45 \, f'_c = 15.75 \text{ MPa (2.28 ksi)}$

extreme fiber stress tension, $f_t \leq 0.5\sqrt{f'_c} = 2.96 \text{ MPa (0.429 ksi)}$

effective prestress force, $T_e = 8 \times 0.55(1860 \text{ MPa}) \times 99 \text{ mm}^2$

$= 814 \text{ kN (183 kips)}$

tendon eccentricity at midspan, $e = 200 \text{ mm (8 in.)}$

Case 1: $f_c = 0.75 f_{cmax}$

$$f_c = 0.75 \times 15.75 = \frac{814,000}{278,709} - \frac{(814,000)(200)}{28,316,847} + \frac{M_{serv}}{28,316,847}$$

$M_{serv} = 414.6\ kN - m\ \ (3670\ k - in.)$

$$f_t = \frac{814,000}{278,709} + \frac{(814,000)(200)}{28,316,847} - \frac{414.6 \times 10^6}{28,316,847} = -5.97\ MPa\ (-.866\ ksi)\ \ too\ high!$$

Case 2: $f_t = 0.75 f_{tmax}$

$$f_t = 0.75 \times (-2.96) = \frac{814,000}{278,709} + \frac{(814,000)(200)}{28,316,847} - \frac{M_{serv}}{28,316,847}$$

$M_{serv} = 308.4\ kN - m\ \ (2730\ k - in.)$

$$f_c = \frac{814,000}{278,709} - \frac{(814,000)(200)}{28,316,847} + \frac{308.4 \times 10^6}{28,316,847} = 8.06\ MPa\ (1.17\ ksi)\ \ \ O.K.$$

- Base total permissible service load on Case 2.
- Use $M_{serv} = 310.7$ kN-m (2750 k-in.)
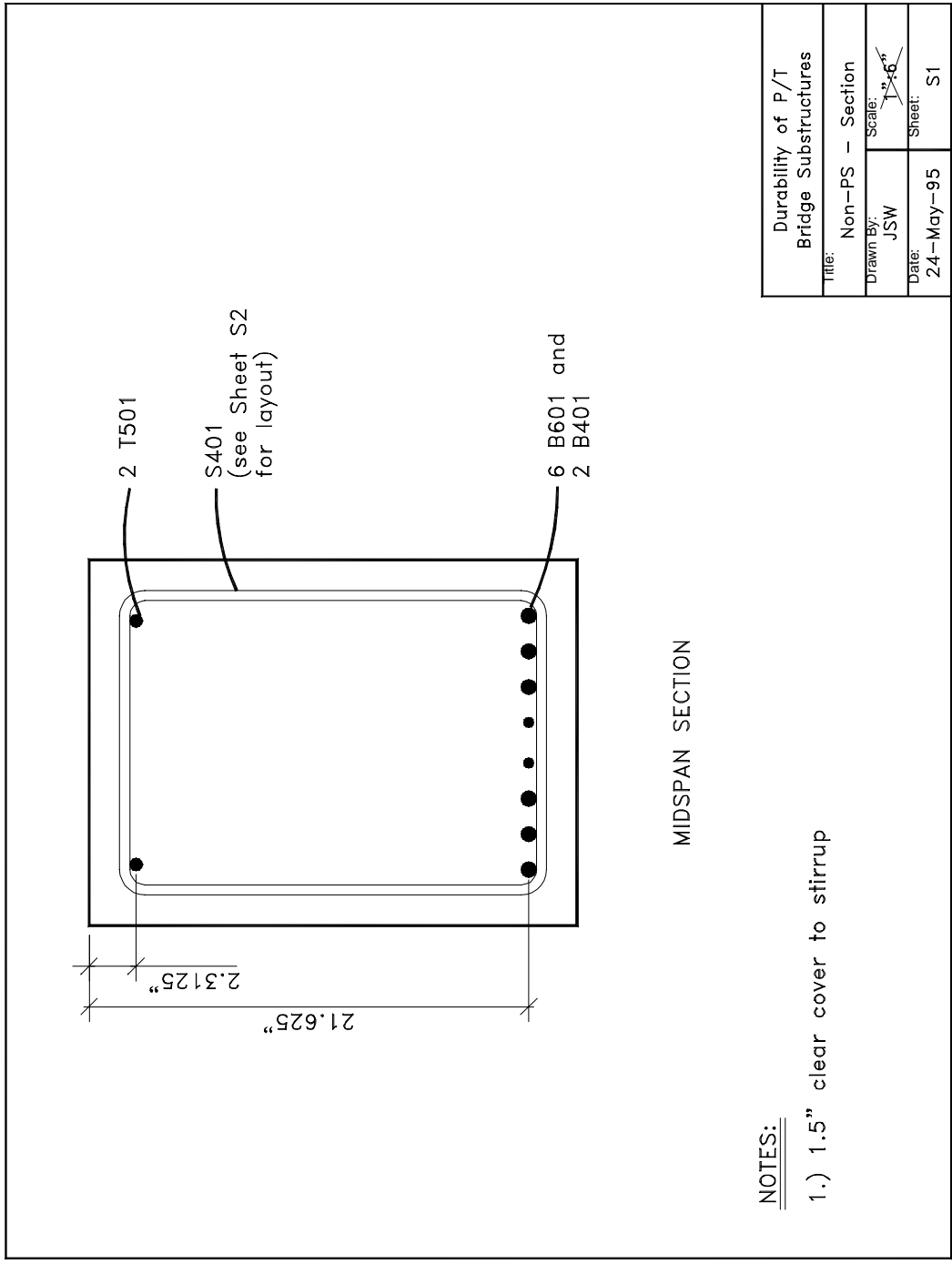
Figure A.1 - Sheet S1: Non-PS Section
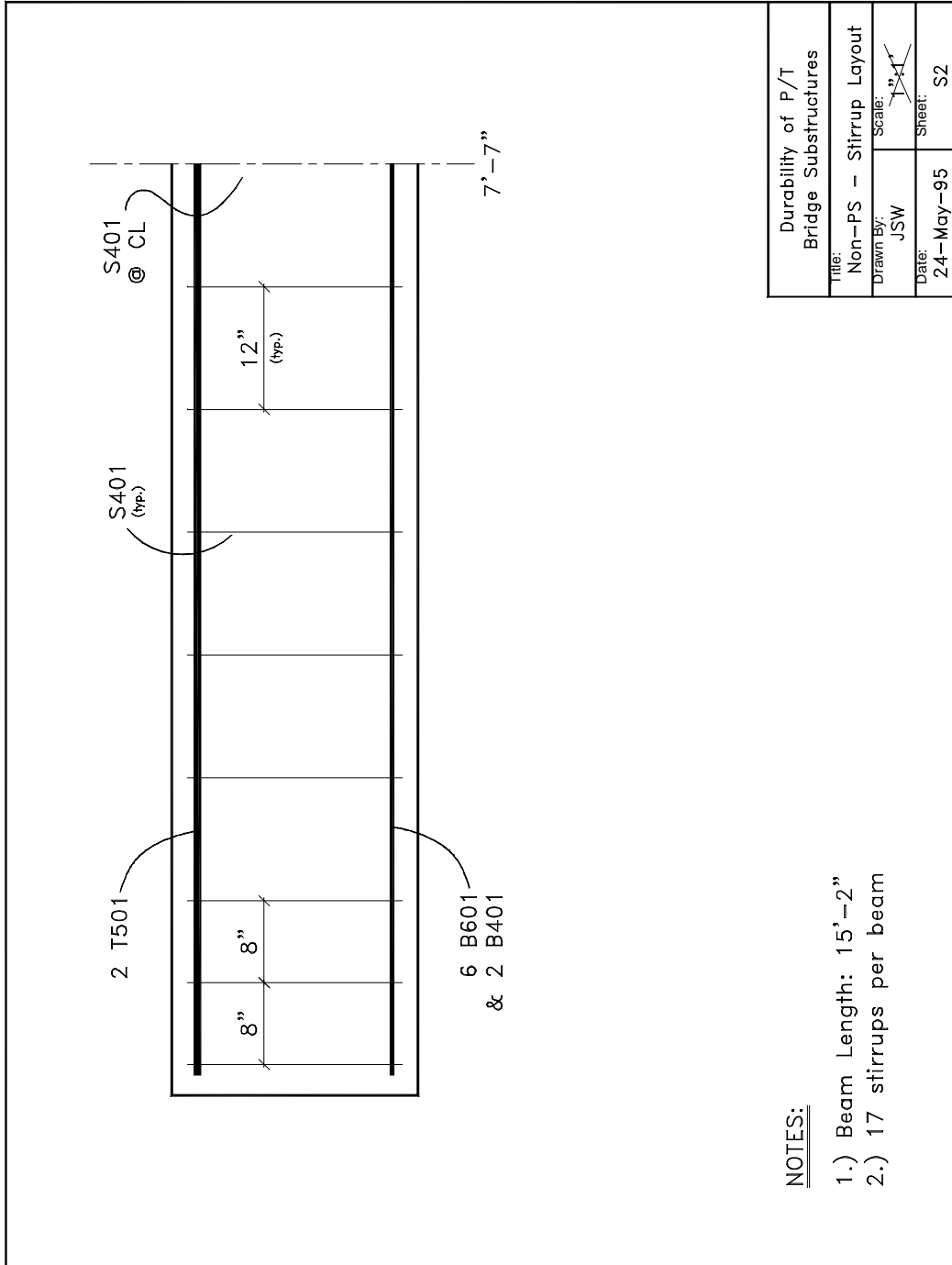
Figure A.2 - Sheet S2: Non-PS Stirrup Layout
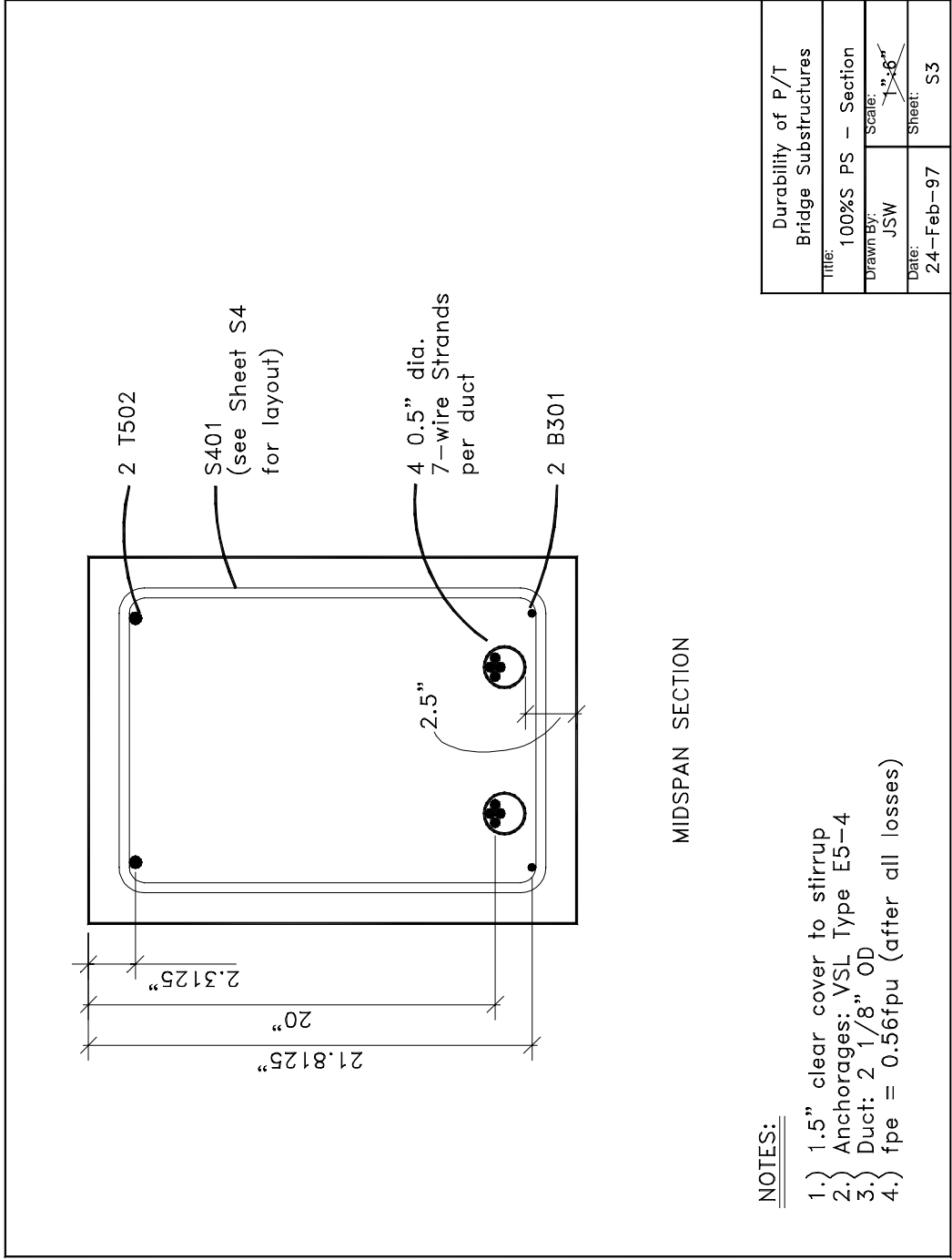
Figure A.3 - Sheet S3: 100%S PS Section

The drawing contains the following labels and annotations:

Title block:
Durability of P/T
Bridge Substructures
Title: 100%S PS - Section
Drawn By: JSW
Scale: 1":6"
Date: 24-Feb-97
Sheet: S3

Drawing labels:
- 2 T502
- S401 (see Sheet S4 for layout)
- 4 0.5" dia. 7-wire Strands per duct
- 2 B301
- 2.5"
- 2.3125"
- 20"
- 21.8125"

MIDSPAN SECTION

NOTES:
1.) 1.5" clear cover to stirrup
2.) Anchorages: VSL Type E5-4
3.) Duct: 2 1/8" OD
4.) fpe = 0.56fpu (after all losses)

168

Figure A.4 - Sheet S4: 100%S Stirrup Layout
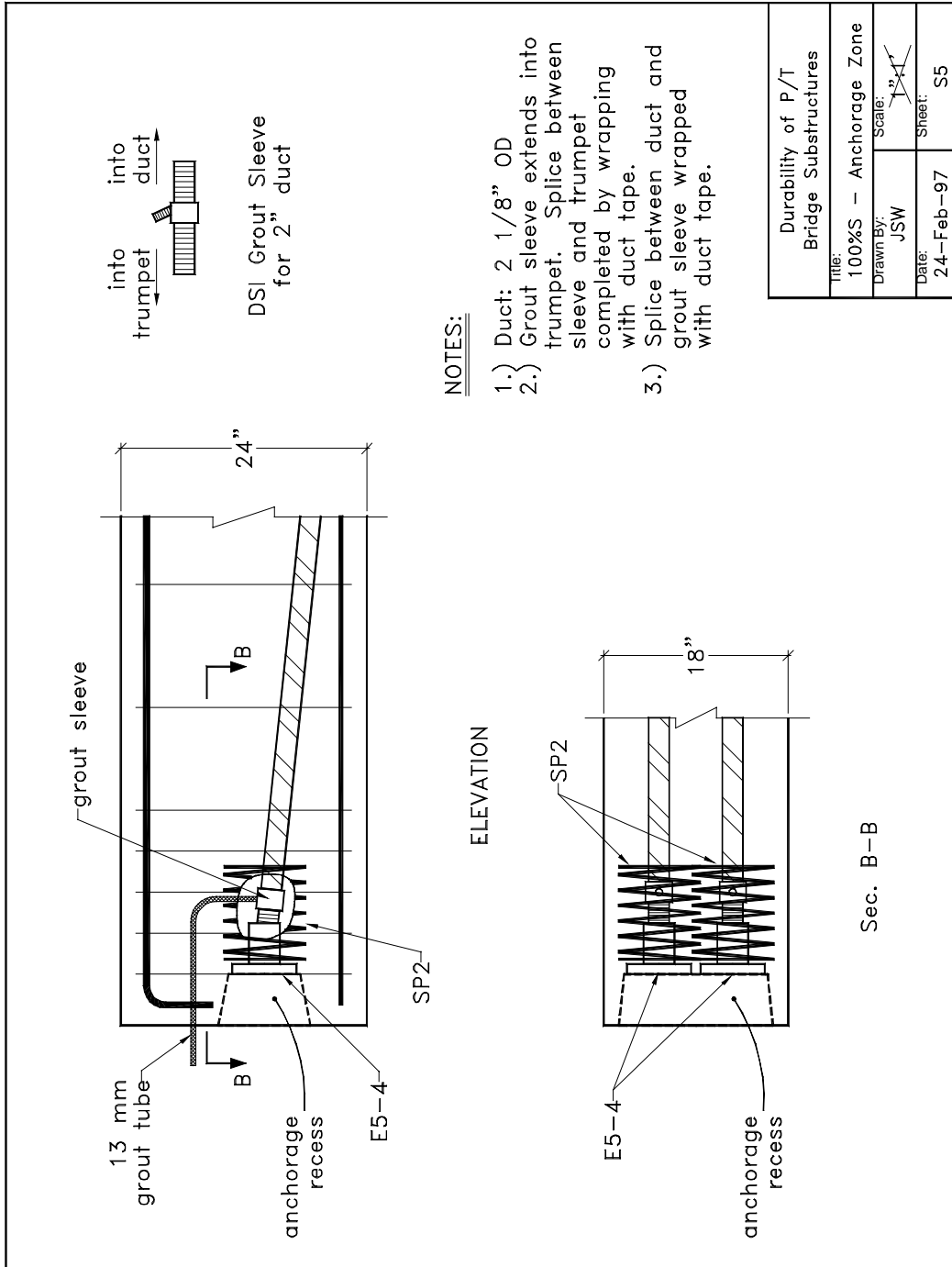
into trumpet → ← into duct

DSI Grout Sleeve for 2" duct

NOTES:

1.) Duct: 2 1/8" OD
2.) Grout sleeve extends into trumpet. Splice between sleeve and trumpet completed by wrapping with duct tape.
3.) Splice between duct and grout sleeve wrapped with duct tape.

24"

grout sleeve

B

13 mm grout tube

B

anchorage recess

E5-4

SP2

ELEVATION

18"

SP2

E5-4

anchorage recess

Sec. B-B

Durability of P/T Bridge Substructures		
Title: 100%S – Anchorage Zone		
Drawn By: JSW	Scale: 1"=1"	
Date: 24-Feb-97		Sheet: S5

Figure A.5 - Sheet S5: 100%S Anchorage Zone

170

Figure A.6 - Sheet S6: 100%S End Detail

171
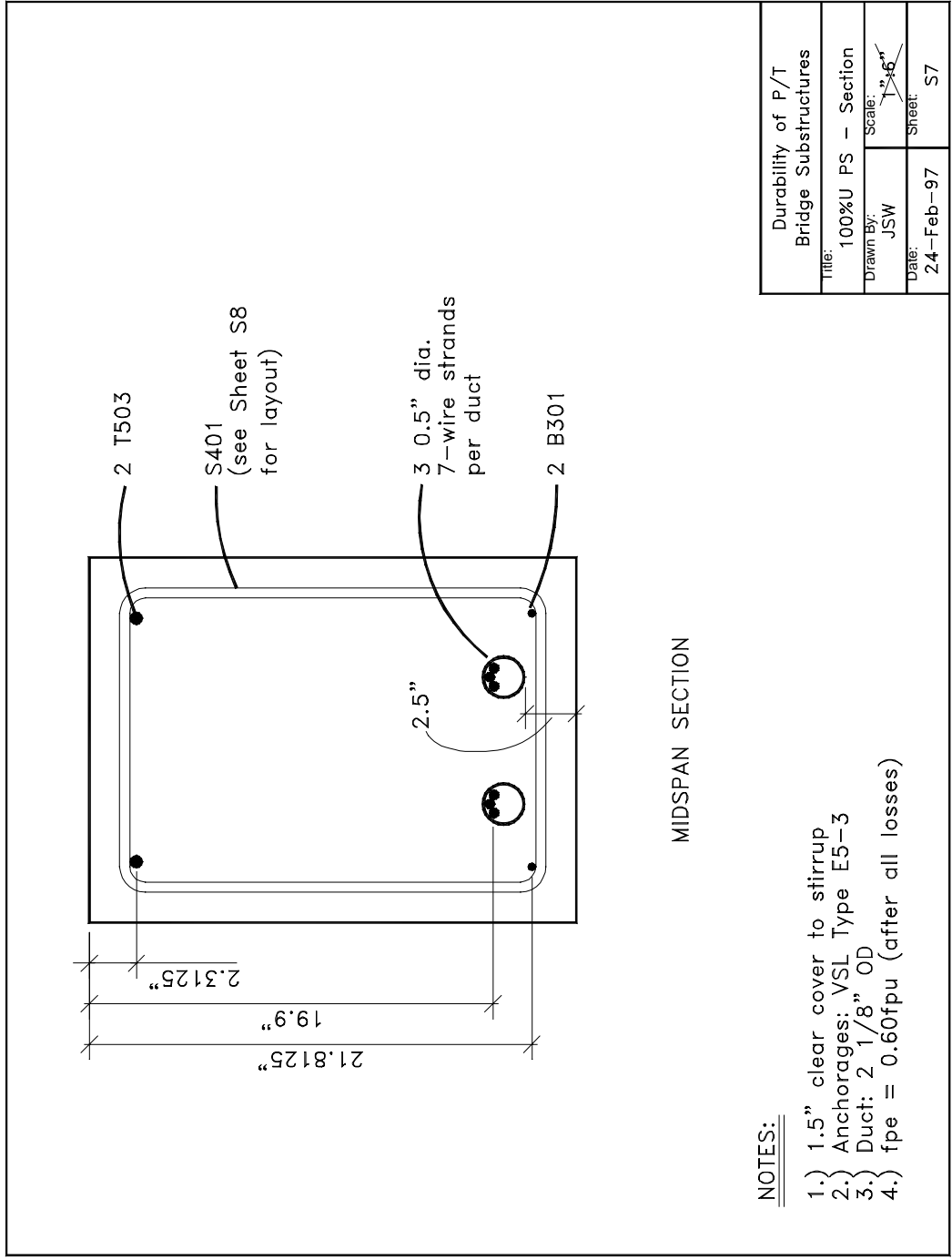
Figure A.7 - Sheet S7: 100%U PS Section
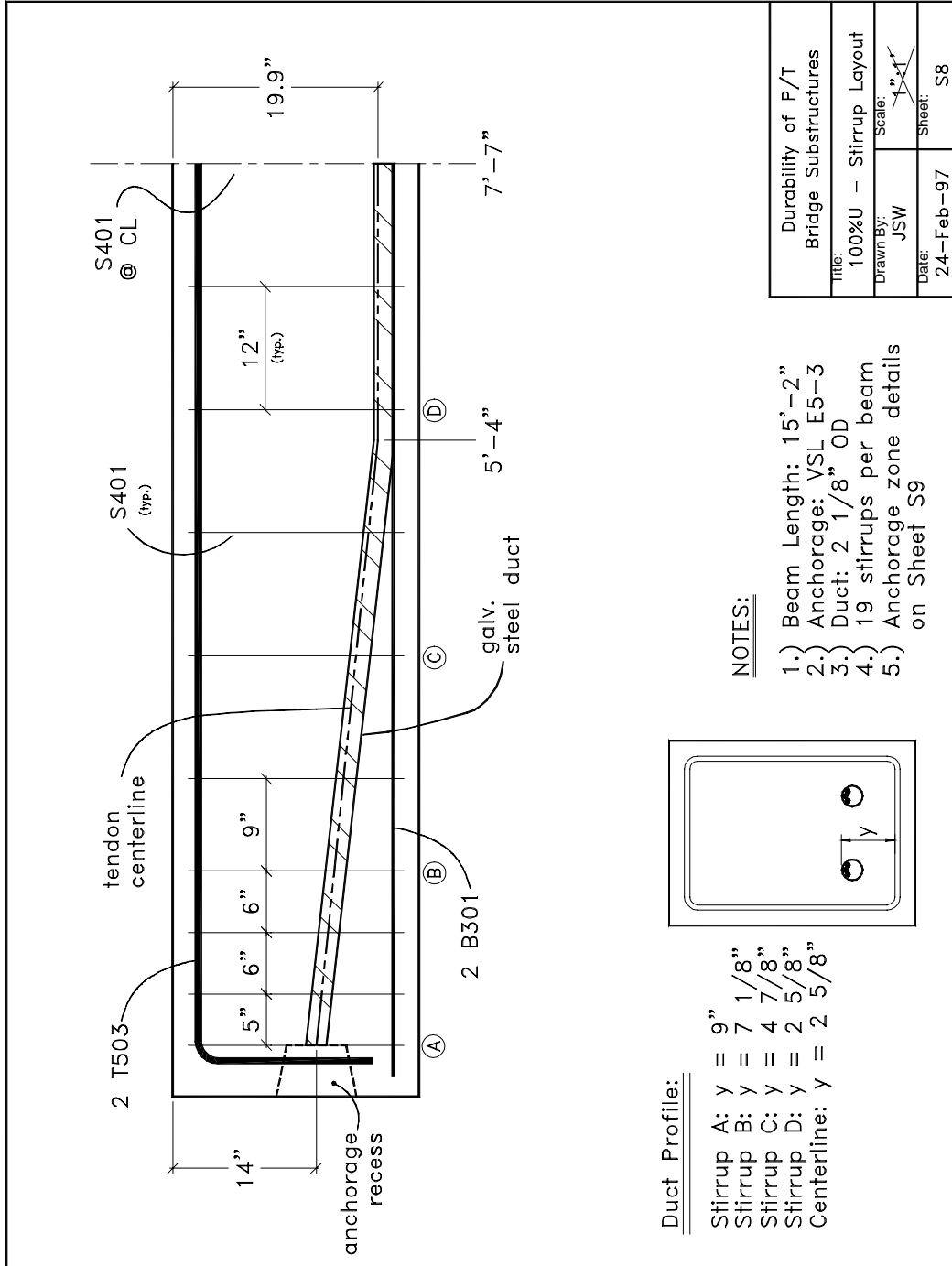
Figure A.8 - Sheet S8: 100%U Stirrup Layout

173

into trumpet ← → into duct

DSI Grout Sleeve for 2" duct

NOTES:

1.) Duct: 2 1/8" OD
2.) Grout sleeve extends into trumpet. Splice between sleeve and trumpet completed by wrapping with duct tape.
3.) Splice between duct and grout sleeve wrapped with duct tape.

24"

grout sleeve

B →

13 mm grout tube

← B

anchorage recess

SP1

E5-3

ELEVATION

18"

SP1

E5-3

anchorage recess

Sec. B-B

Durability of P/T Bridge Substructures	
Title: 100%U – Anchorage Zone	
Drawn By: JSW	Scale: 1"=1'
Date: 24-Feb-97	Sheet: S9

Figure A.9 - Sheet S9: 100%U Anchorage Zone

174

Sec. A-A

2"
14"
12"
5.875"
6.25"
5.875"
5.875"
5"

A

8"

18"
5.5"
10"
6"
24"

anchorage recess

END VIEW

NOTES:

1.) Anchorage: VSL Type E5-3
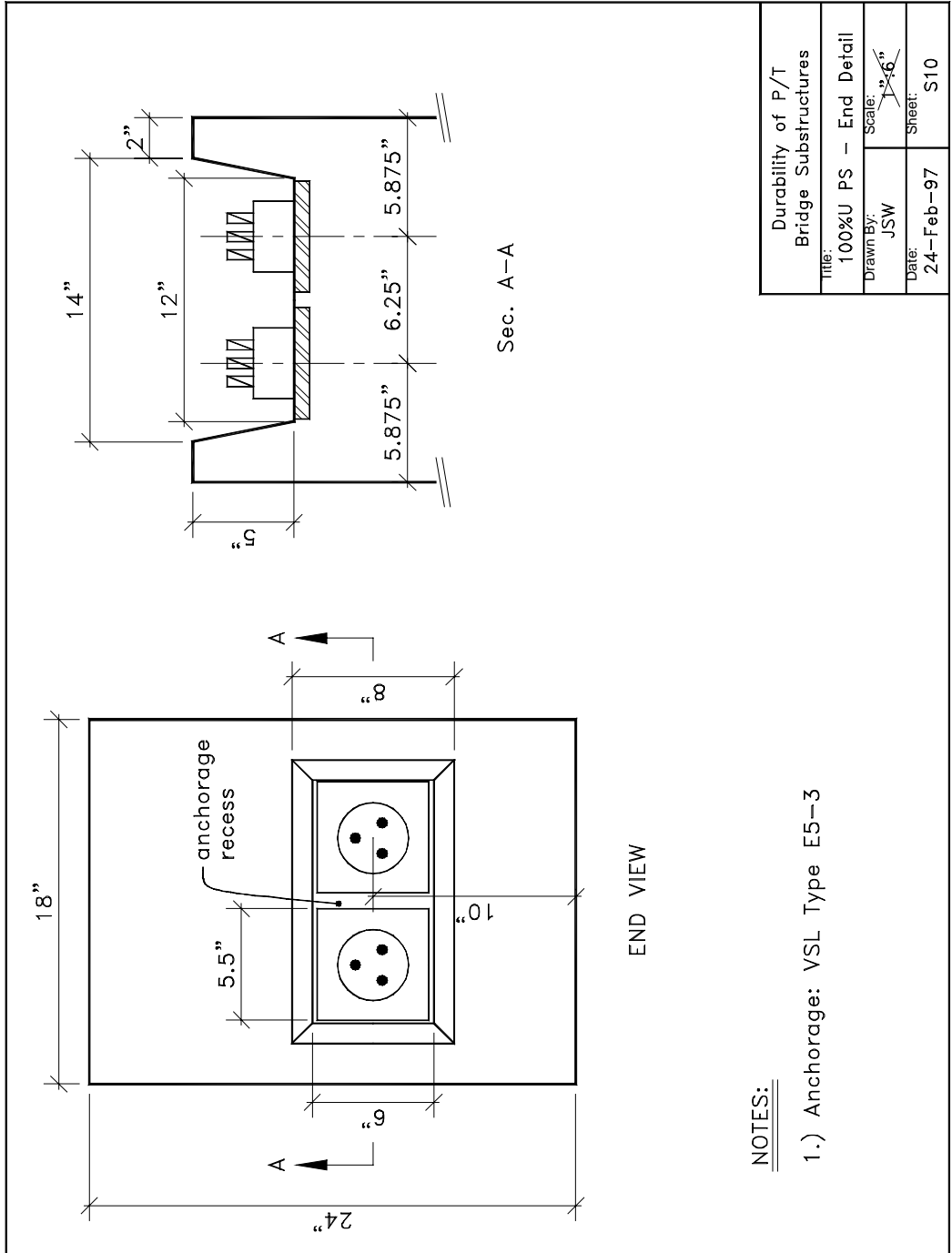
Figure A.10 - Sheet S10: 100%U End Detail

175
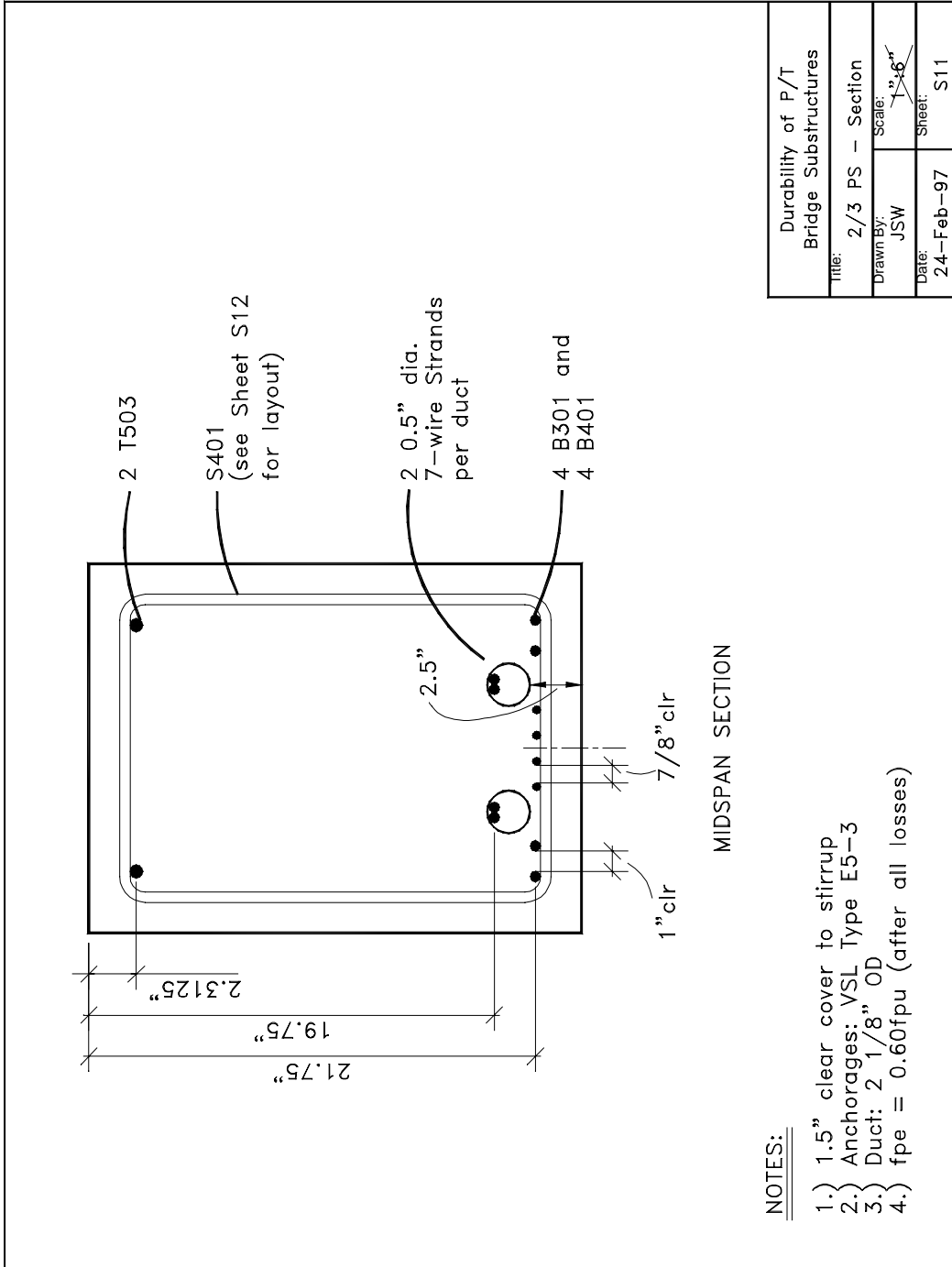
Figure A.11 - Sheet S11: 2/3 PS Section

176
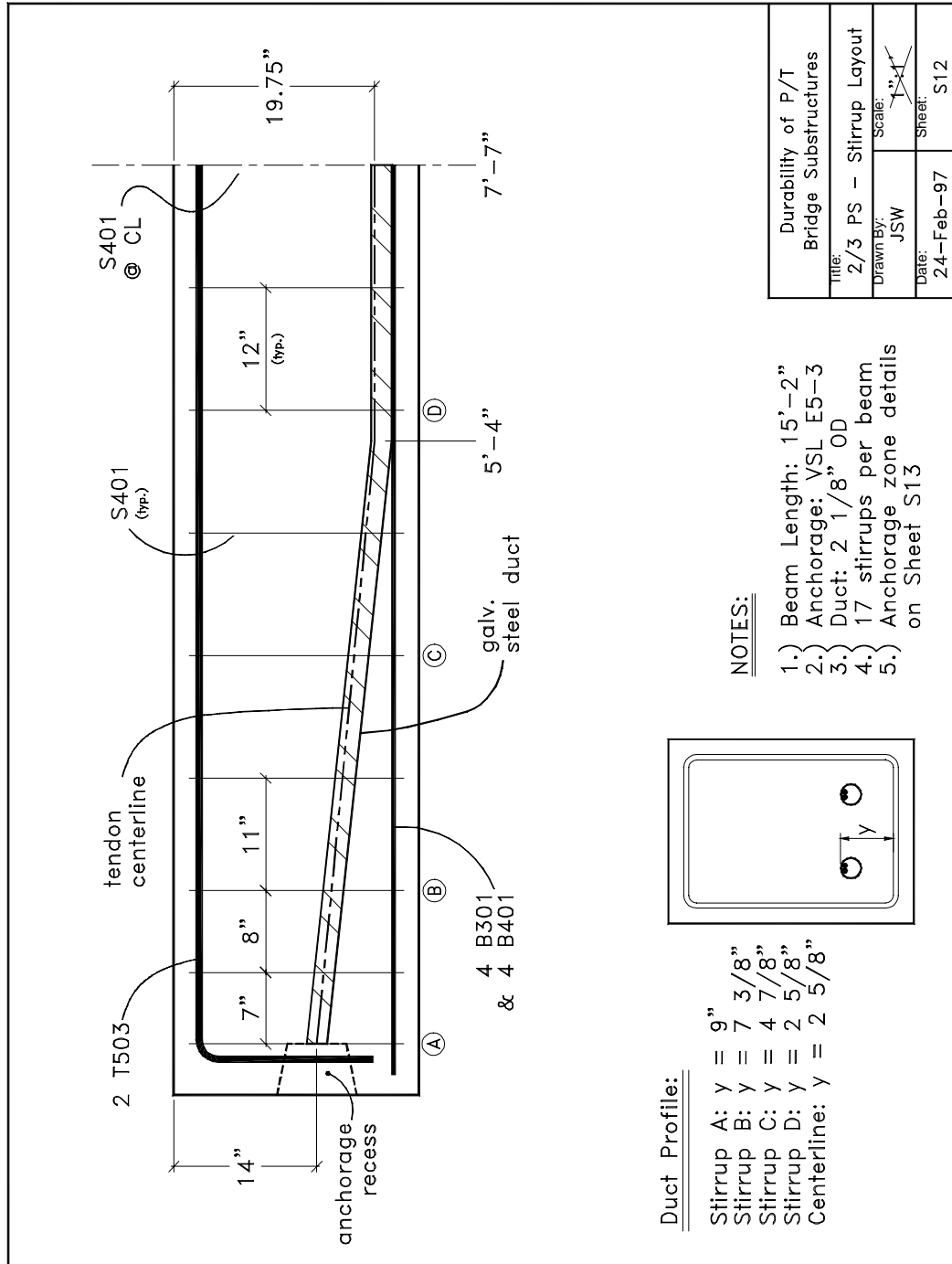
Figure A.12 - Sheet S12: 2/3 PS Stirrup Layout

The figure contains the following labels and annotations:

19.75"

S401 @ CL

7'—7"

12" (typ.)

S401 (typ.)

5'—4"

tendon centerline

11"

galv. steel duct

8"

7"

2 T503

14"

anchorage recess

4 B301 & 4 B401

Ⓐ Ⓑ Ⓒ Ⓓ

NOTES:
1.) Beam Length: 15'—2"
2.) Anchorage: VSL E5—3
3.) Duct: 2 1/8" OD
4.) 17 stirrups per beam
5.) Anchorage zone details on Sheet S13

Duct Profile:
Stirrup A: y = 9"
Stirrup B: y = 7 3/8"
Stirrup C: y = 4 7/8"
Stirrup D: y = 2 5/8"
Centerline: y = 2 5/8"

Title: Durability of P/T Bridge Substructures
2/3 PS — Stirrup Layout
Scale: 1"
Drawn By: JSW
Sheet: S12
Date: 24—Feb—97

177

Figure A.13 - Sheet S13: 2/3 PS Anchorage Zone
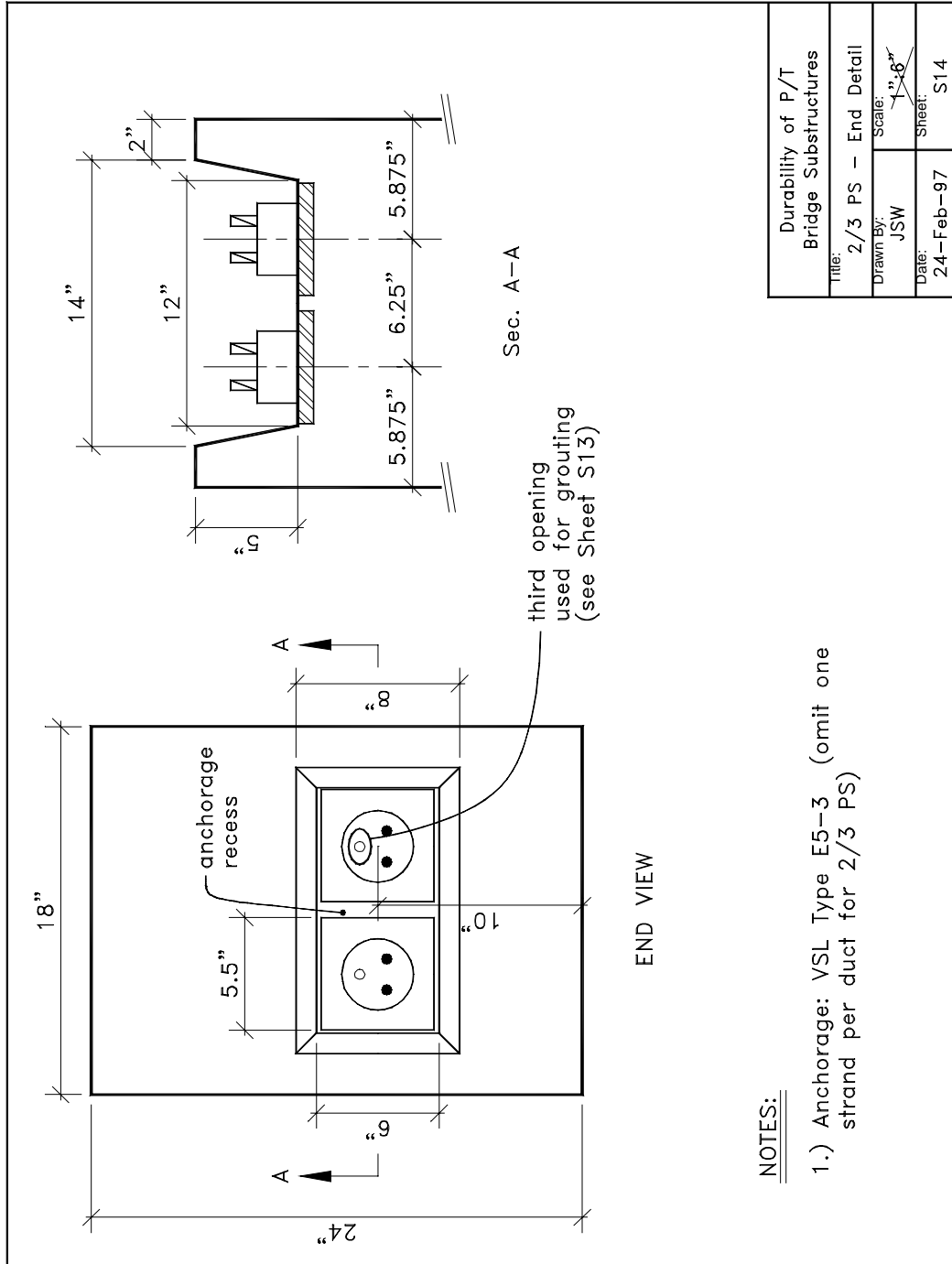
Figure A.14 - Sheet S14: 2/3 PS End Detail

179

2 T501

S401
(see Sheet S16
for layout)

16 B501

MIDSPAN SECTION

2.5"

19.875"

21.5"

NOTES:
1.) 1.5" clear cover to stirrup
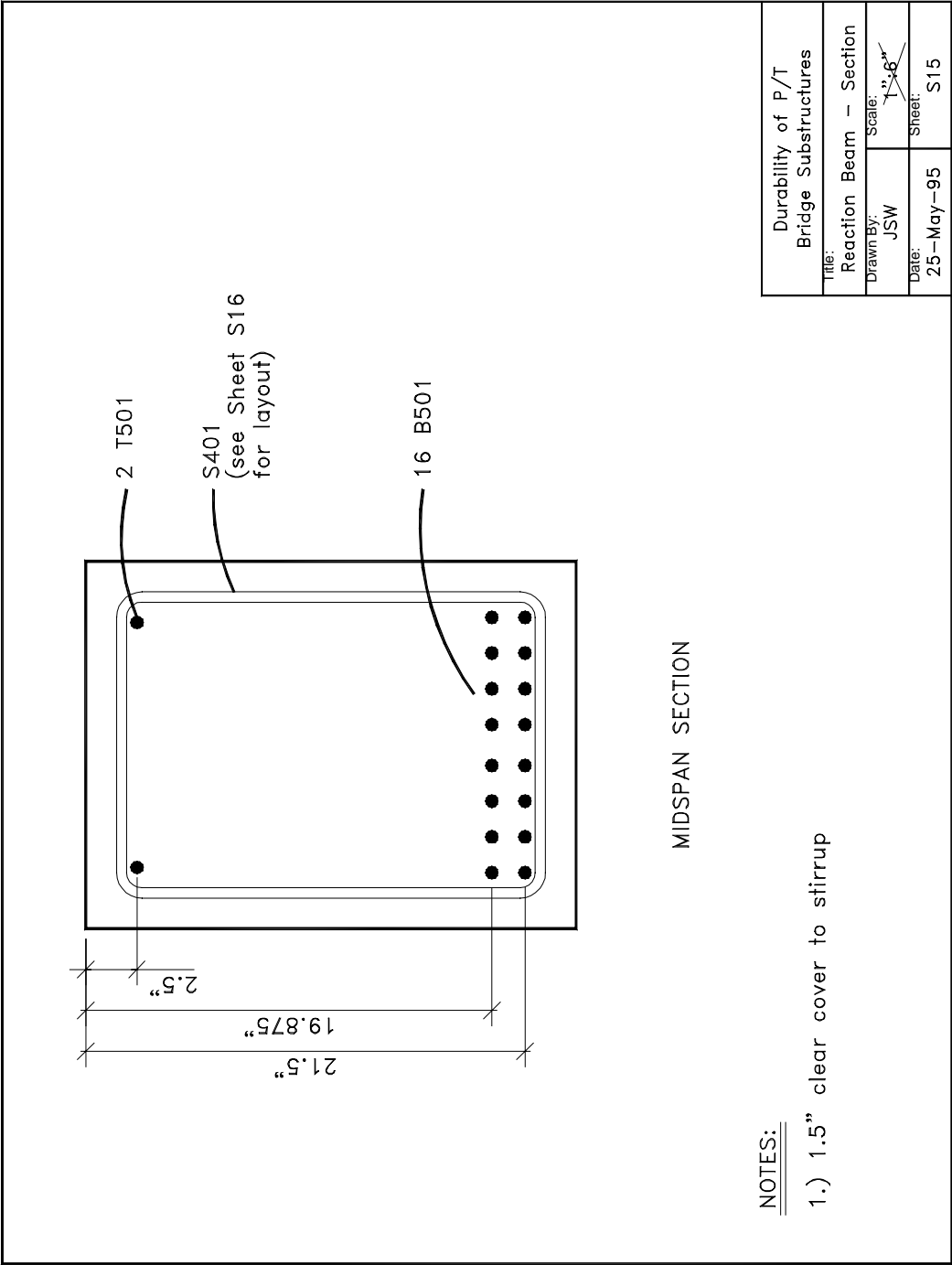
Figure A.15 - Sheet S15: Reaction Beam Section
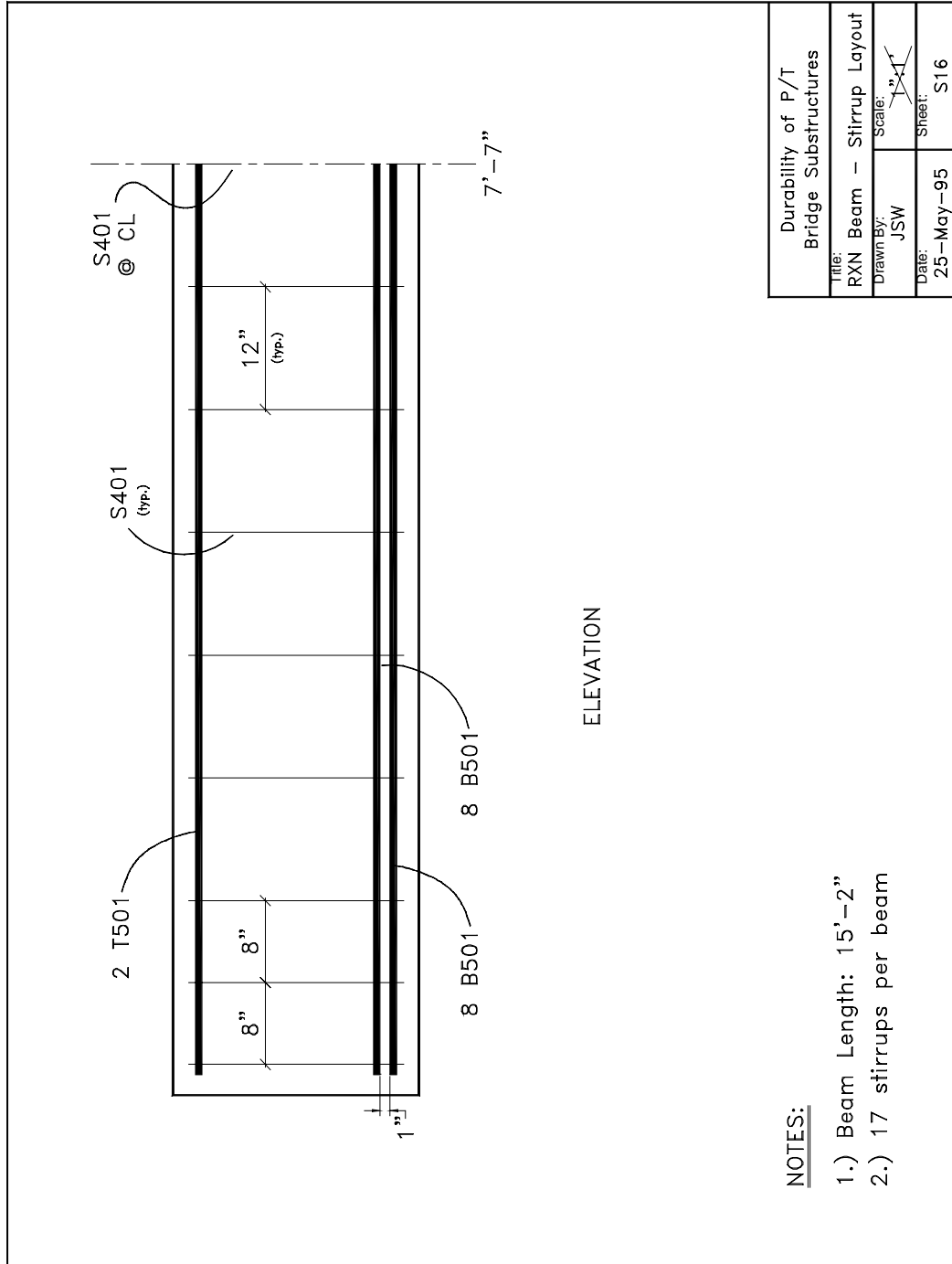
Figure A.16 - Sheet S16: Reaction Beam Stirrup Layout

181
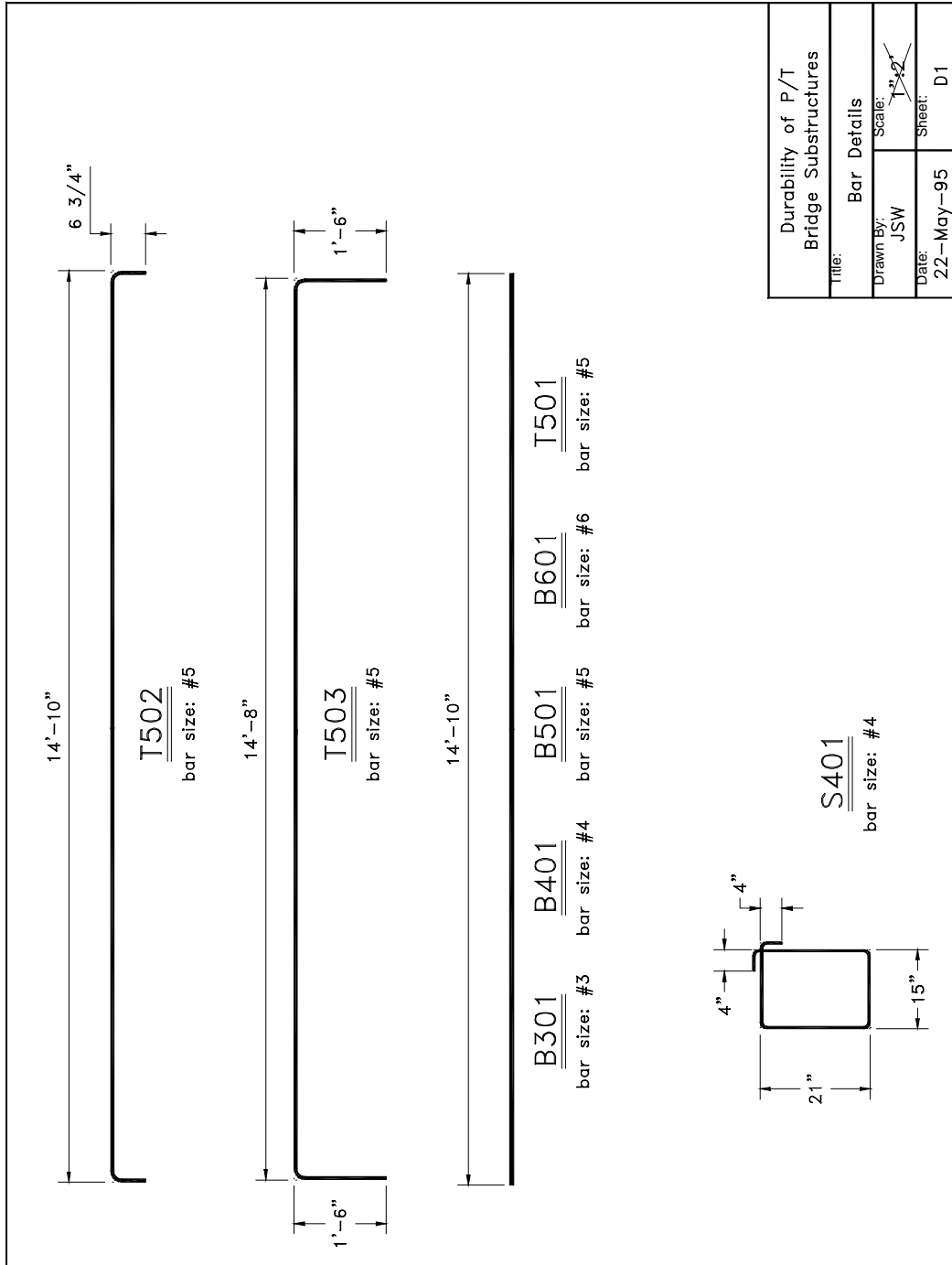
Figure A.17 - Sheet D1: Bar Details

E5-4
VSL Anchorage Type E
(Dimensions as supplied)

E5-3
VSL Anchorage Type E
(Dimensions as supplied)

trumpet

bearing plate

anchor head

2 3/8"

Sec. B-B

ø3 3/4"

2 3/8"

Sec. D-D

ø3 3/8"

3"

4"

Sec. A-A

1"

ø2 3/8"

TOP VIEW

6 1/4"

6 1/4"

3"

4"

Sec. C-C

3/4"

ø1 7/8"

TOP VIEW

5 1/2"

5 1/2"

8"

9"

SP2
#4 x 8 turns
pitch = 1.5"
(for E5-4)

one flat turn at each end

6"

SP1
#4 x 6 turns
pitch = 1.5"
(for E5-3)

8"

Durability of P/T Bridge Substructures

Title: Anchorage Hardware

Drawn By: JSW

Scale: 1":6"

Date: 26-Feb-97

Sheet: D2

Figure A.18 - Sheet D2: Anchorage Hardware

183

Splice Locations:

Midspan Splice

Use with IS or HS splices

4'-10" 2'-3"

"No Splice"

Splices moved from critical region

Use with IS splice only

2'-7" 2'-3" 4'-6"

Damaged Splice

Compare pristine and damaged splices in the same duct

Use with IS and ISD or HS and HSD splices

IS or HS ISD or HSD

4'-10" 9" 3'

Splice Details:

Industry Standard (IS) Splice

Damaged case (ISD) has poor or incomplete tape wrapping

12" oversized duct wrap with duct tape

Heat Shrink (HS) Splice

Damaged case (HSD) has 1" cut in heat shrink at splice

heat shrink tubing (4" initial dia.) 8"

NOTE:
Details shown are for 2 1/8" OD galvanized steel duct.

Durability of P/T Bridge Substructures

Title: PT Duct and Splice Details

Drawn By: JSW

Date: 9-Jun-97

Scale: 1"-2'

Sheet: D3

Figure A.19 - Sheet D3: Post-Tensioning Duct and Splice Details
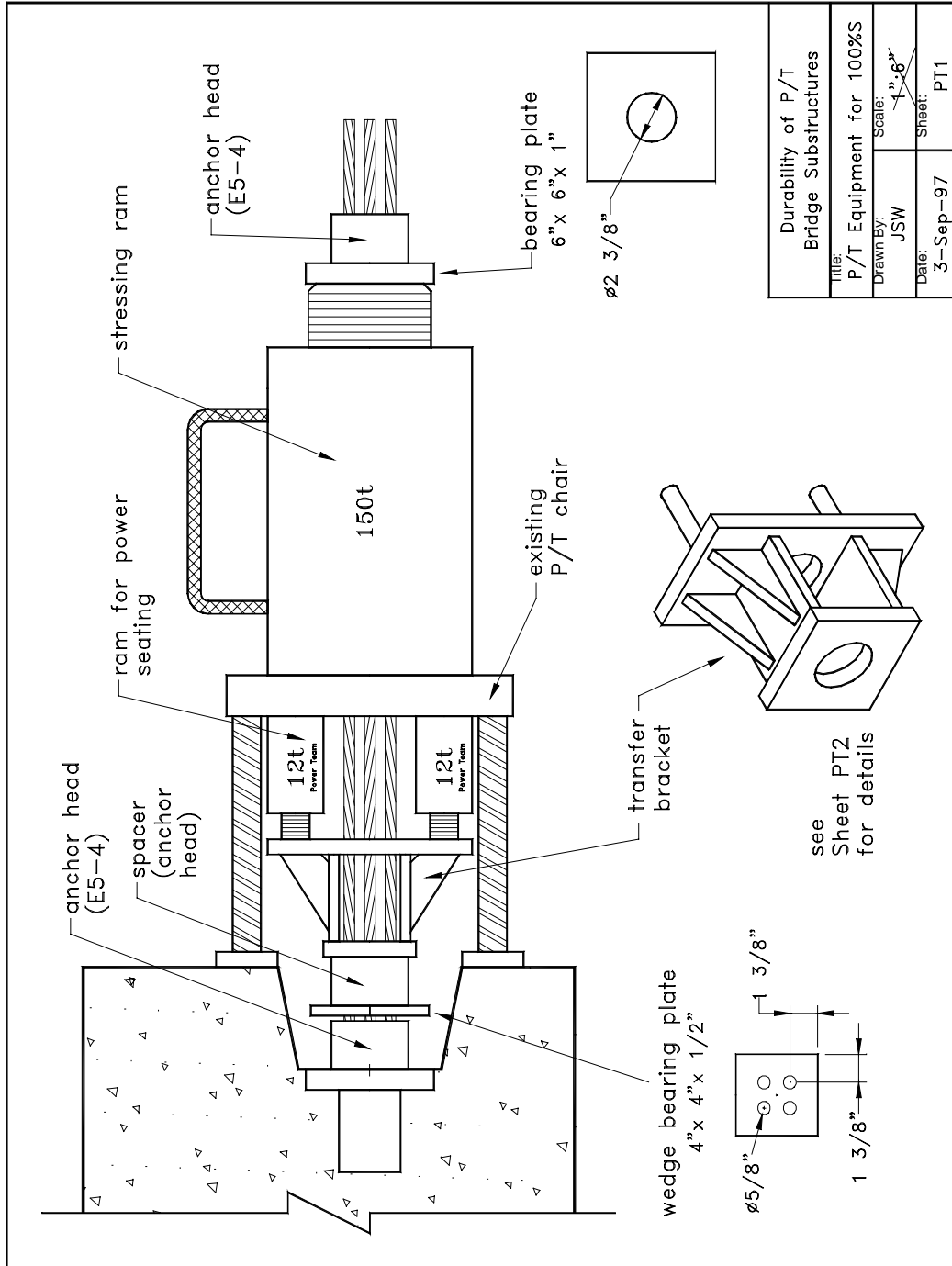
184

Figure A.20 - Sheet PT1: Post-Tensioning Equipment for 100%S Beams
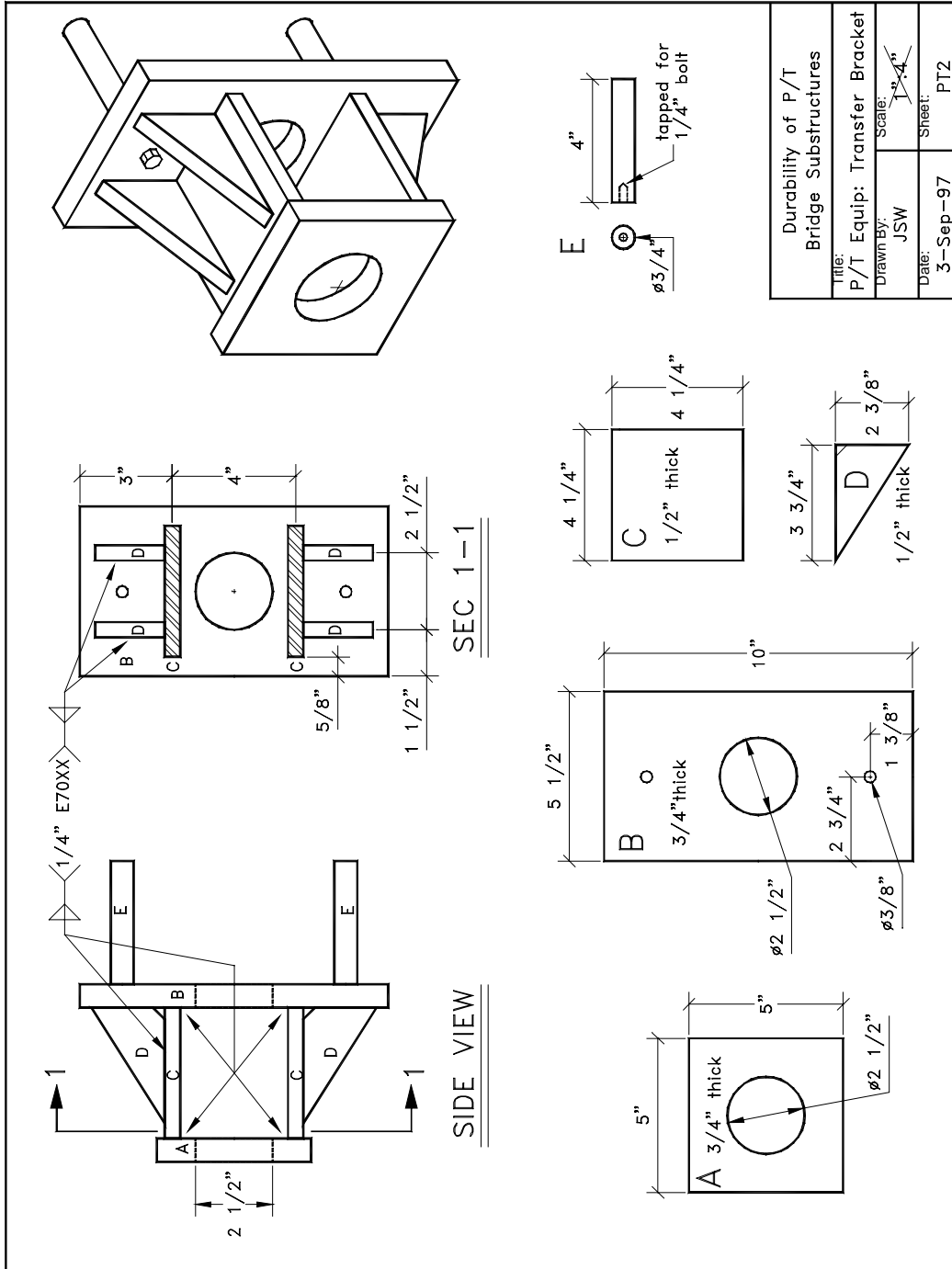
Figure A.21 - Sheet PT2: Post-Tensioning Equipment Transfer Bracket for Power Seating of Wedges

A.1   CONCRETE MIX DESIGN DETAILS

Three types of concrete were used for the large-scale beam specimens. The actual mix designs list a maximum aggregate size of 40 mm (1 ½"), but this sizewas changed to a maximum aggregate size of 20 mm (¾") to accommodate the test specimen dimensions. Table A.1 shows the batch quantities for the Texas Class C concrete for bridge substructure used for the laboratory specimens, and Table A.2 shows the quantities for the Texas Class C with fly ash. The high performance mix design is shown in Table B3. This mix was patterned after a mix used for a cast-in-place bridge deck in San Angelo, Texas. The original San Angelo mix design strength was 41.3 MPa (6 ksi), but cylinder break strengths were around 68.8 MPa (10 ksi) due to the low water-cement ratio. The mix was batched to a slump of 25-50 mm (1-2") with additional superplasticizer added on site to reach a slump of around 200 mm (8").

Typically, the fly ash used in Texas is a Class C fly ash. However, during the year that the beams were cast, only Class F fly ash was available due to a shortage of Class C fly ash. Therefore, all fly ash used in concrete for the beams was Class F fly ash.

Table A.1 - Mix Design for Texas Class C Concrete
(with max. aggregate = 20 mm)

	Quantity per m^3	Quantity per yd^3
Type I cement	335 kg	564 lbs.
Sand	703 kg	1186 lbs.
20 mm (¾") aggregate	1113 kg	1877 lbs.
Water	151 kg	254 lbs.
300R (retarder)	930 ml	24.0 oz
AE-90 (air entrainer)	155 ml	4.0 oz

Table A.2 - Mix Design for Texas Class C Concrete with Fly Ash
(with max. aggregate = 20 mm)

	Quantity per m^3	Quantity per yd^3
Type I cement	242 kg	409 lbs.
Class F Fly Ash	79 kg	133 lbs.
Sand	738 kg	1245 lbs.
20 mm (¾") aggregate	1118 kg	1885 lbs.
Water	142 kg	240 lbs.
300R (retarder)	775 ml	20.0 oz
AE-90 (air entrainer)	155 ml	4.0 oz

Table A.3 - High Performance Concrete Mix Design
(with max. aggregate = 20 mm)

	Quantity per m^3	Quantity per yd^3
Type I cement	311 kg	525 lbs.
Class F Fly Ash	104 kg	175 lbs.
Sand	729 kg	1229 lbs.
20 mm (¾") aggregate	1118 kg	1885 lbs.
Water	120 kg	202 lbs.
300R (retarder)	1089 ml	28.1 oz
AE-90 (air entrainer)	120 ml	3.1 oz
Batched for 25-50 mm (1-2") slump 110 oz./yd^3 high range water reducer (Rheobuild 1000) added on site		

A.2   COATED STRAND PROPERTIES

The elongation curves and material certification from Florida Wire and Cable for the epoxy-coated strand (Flo-Bond™) and galvanized strand are shown in Figures A.22-A.25.

Florida Wire and Cable, Inc.

825 NORTH LANE AVENUE / 32254 • P. O. BOX 6835 / 32236 • JACKSONVILLE, FLORIDA

TELEPHONE (904) 781-9224

TELEX NO 517964

FAX (904) 693-7377

Setting Standards Worldwide.

S.A.#   QA052   REPORT NUMBER: 20913

REPRESENTATIVE LOAD ELONGATION CURVE

1/2" 270 KSI LOW RELAXATION - FLO-BOND STRAND
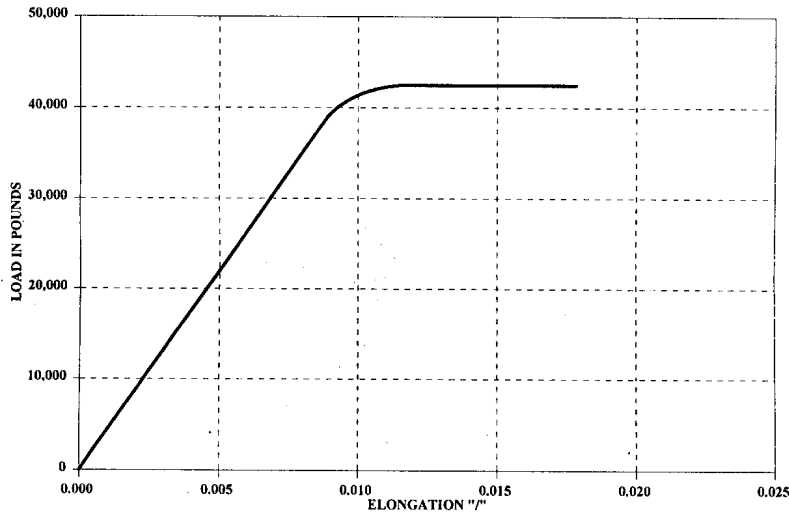
Production Lot / Heat Number: 38385

Heat Number/Production Lot Number may be comprised of several "heats" of steel per ASTM A-416

	STANDARD	METRIC (SI)	COIL NUMBER(S):
BREAKING LOAD	43,562 lbf.	193.8 kN	13012800143
LOAD @ 1% EXT.	41,123 lbf	182.9 kN	
ULT. ELONGATION	5 %	5 %	
NOMINAL AREA	0.153 in^2	98.70 mm^2	
M.O.E.	28,600,000 P.S.I.	197190 MPa	
ASTM BREAK/LOAD	41300 lbf	183.7 kN	

ELONG. @ 30,975   lbf =   0.00708 in/in

ELONG. @ 137.8   kN =   0.00708 mm/mm

Figure A.22 - Epoxy-Coated Strand Elongation Curve

FLORIDA WIRE AND CABLE, INC.

825 NORTH LANE AVE. - JACKSONVILLE, FL 32254

MATERIAL CERTIFICATION

Certification #:	00020913

Customer:
UNIVERSITY OF TEXAS
U.T. CENTRAL RECEIVING
ATTN: ACCOUNTS PAYABLE
2200 COMAL STREET
AUSTIN, TX 78722

Date: 07/02/98

CURVE(S)

Florida Wire and Cable Incorporated hereby certifies that test of specimens:

1/2"DIA. GRADE 270 LOW-RELAXATION FLO-BOND STRAND

52

Taken at random from a lot consisting of Coil/Reel Numbers:

13012800143

HEAT #/PRODUCTION LOT:

38385

HEAT NUMBER/PRODUCTION LOT NUMBER(S) MAY BE COMPRISED OF SEVERAL 'HEATS' OF STEEL PER ASTM A-416-93
Florida Wire and Cable, Inc. hereby certifies that all manufacturing
processes used in the production of the rod and strand described above
occured in the United States of America in compliance with the "BUY
AMERICA" provision of the Surface Transportation Assistance Act of 1982.

F.W.C. Order No.: 45981

Customer Order No.: 1998A53010

were made in accordance with the particulars relating to such tests set forth in
the above specifications and meets all requirements of these specifications.
Representative test results are attached.

Certification prepared by: _Wanda Roue_

Figure A.23 - Epoxy-Coated Strand Material Certification

190

Florida Wire and Cable, Inc.

S.A.#   QA046   REPORT NUMBER: 00023209

REPRESENTATIVE LOAD ELONGATION CURVE
1/2 270 KSI GALVANIZED STRESS RELIEVED

Heat # 38904

THIS PRODUCT WAS MANUFACTURED TO MEET THE REQUIREMENTS OF FLORIDA
WIRE AND CABLE, INC. SPECIFICATIONS FOR GALVANIZED PC STRAND

	STANDARD		METRIC (SI)		COIL NUMBER(S):
BREAKING LOAD	41,830	lbf	186.1	kN	
LOAD @ 1% EXT.	37,748	lbf	167.9	kN	2703182167
ULT. ELONGATION	5.99	%	5.99	%	
NOMINAL AREA	0.153	in^2	98.70	mm^2	
M.O.E.	28,800,000	P.S.I.	198569	MPa	
SPEC. BREAK/LOAD	41300	lbf	183.7	kN	
ELONG. @ 30,975	lbf =	0.00703 in/in			
ELONG. @ 137.8	kN =	0.00703 mm/mm			

Figure A.24 - Galvanized Strand Elongation Curve

FLORIDA WIRE AND CABLE, INC.
825 NORTH LANE AVE. - JACKSONVILLE, FL 32254

MATERIAL CERTIFICATION

Certification #:   00023209

UNIVERSITY OF TEXAS

Customer: U.T. CENTRAL RECEIVING   **Date:**   09/30/98
ATTN: ACCOUNTS PAYABLE
2200 COMAL STREET
AUSTIN, TX 78722   **CURVE(S)**

Florida Wire and Cable Incorporated hereby certifies that test of specimens:

1/2" DIA. 7 WIRE GRADE 270 CLASS A GALVANIZED PC STRAND ON REEL

Taken at random from a lot consisting of Coil/Reel Numbers: **HEAT #/PRODUCTION LOT:**

27031821697   38974

HEAT NUMBER/PRODUCTION LOT NUMBER(S) MAY BE COMPRISED OF SEVERAL 'HEATS' OF STEEL PER ASTM A-416-93
Manufactured under Florida Wire & Cable, Inc. specifications for the product
listed above.

F.W.C. Order No.:   45981

Customer Order No.:   1998A53010

were made in accordance with the particulars relating to such tests set forth in
the above specifications and meets all requirements of these specifications.
Representative test results are attached.

Certification prepared by: _Kerry Hill 9/30/98_

Figure A.25 - Galvanized Strand Material Certification

192

A.3   CONCRETE STRENGTH DATA

The cylinder break strengths for all concrete batches used in the large-scale beam specimens are shown in Tables A.4-A.7.

Table A.4 - Phase I Beam Concrete Strengths (part 1)

Date Cast	Test Day	Size	Mix	Force (k)	Strength			
					psi	Average (psi)	MPa	Average (MPa)
10/16/95	1	6"	TxDOT	42.7	1510	1400	10.4	9.7
	1		Class C	36.5	1290		8.9	
	3		Beams:	104.0	3680	3610	25.4	24.9
	3		1.1	99.8	3530		24.3	
	7		1.2	130.8	4630	4590	31.9	31.6
	7		1.3	128.6	4550		31.4	
	14			127.4	4510	4690	31.1	32.3
	14			137.9	4880		33.6	
	28			152.6	5400	5200	37.2	35.9
	28			141.3	5000		34.5	
8/8/96	4	6"	TxDOT	94.2	3330	3540	23.0	24.4
	4		Class C	105.6	3740		25.8	
	7		Beams:	116.5	4120	4120	28.4	28.4
	7		1.4	116.2	4110		28.3	
	14		2.1	124.5	4410	4460	30.4	30.7
	14		2.2	127.5	4510		31.1	
	28			137.9	4880	4820	33.6	33.2
	28			134.3	4750		32.7	
	56			153.0	5410		37.3	
	56			147.4	5220	5230	36.0	36.1
	56			143.3	5070		34.9	

Table A.5 - Phase I Beam Concrete Strengths (part 2)

Date Cast	Test Day	Size	Mix	Force (k)	psi	Average (psi)	MPa	Average (MPa)
8/22/96	4	6"	TxDOT	122.3	4330	4280	29.8	29.5
	4		Class C	119.8	4240		29.2	
	7		Beams:	139.4	4930	4980	34.0	34.3
	7		2.3	141.8	5020		34.6	
	14		2.4	157.0	5560	5530	38.3	38.2
	14		2.11	155.7	5510		38.0	
	28			174.0	6160	6010	42.5	41.4
	28			165.4	5850		40.3	
	56			179.1	6340	6280	43.7	43.3
	56			176.0	6230		42.9	
2/5/97	5	6"	TxDOT	112.0	3960	3970	27.3	27.3
	5		Class C	112.1	3970		27.4	
	16		Beams:	140.6	4980	4950	34.3	34.2
	16		3.1	139.4	4930		34.0	
	28		3.2	152.6	5400	5370	37.2	37.0
	28		3.3	150.7	5330		36.7	
	56			154.2	5460	5460	37.6	37.6
2/19/97	5	6"	TxDOT	122.4	4330	4140	29.8	28.5
	5		Class C	111.4	3940		27.2	
	8		Beams:	126.0	4460	4510	30.7	31.1
	8		3.4	128.8	4560		31.4	
	15		3.5	138.0	4880	4940	33.6	34.1
	15			141.3	5000		34.5	
	28			161.3	5710	5760	39.4	39.7
	28			164.2	5810		40.0	
	56			163.7	5790	5780	39.9	39.8
	56			162.9	5760		39.7	
3/14/97	4	6"	TxDOT	84.1	2980	3060	20.5	21.1
	4		Class C	88.9	3150		21.7	
	7		Beams:	101.1	3580	3560	24.7	24.5
	7		4.1	99.8	3530		24.3	
	14		4.2	117.8	4170	4210	28.7	29.0
	14			120.2	4250		29.3	
	28			131.7	4660	4800	32.1	33.1
	28			139.4	4930		34.0	
	56			136.3	4820	4850	33.2	33.4
	56			137.9	4880		33.6	

Table A.6 - Phase II Beam Concrete Strengths (part 1)

Date Cast	Test Day	Size	Mix	Force (k)	Strength			
					psi	Average (psi)	MPa	Average (MPa)
3/3/98	3	6"	TxDOT	121.68	4300	4300	29.6	29.6
	7		Class C	142.56	5040	5040	34.7	34.7
	14		Beams:	152.17	5380	5380	37.1	37.1
	23		2.7	163.83	5800	5800	40.0	40.0
	28		2.8	161.38	5700		39.3	
	28		2.10	163.45	5780	5800	39.9	39.9
	28			166.52	5900		40.7	
	56			167.08	5910	5910	40.7	40.7
3/18/98	2	4"	TxDOT	29.07	2310	2310	15.9	15.9
	8		Class C	51.81	4120	4120	28.4	28.4
	14		Fly Ash	67.06	5330	5330	36.7	36.7
	28		Beams:	77.93	6200		42.7	
	28		1.5	75.77	6030	6200	41.6	42.7
	28		2.5	79.94	6360		43.9	
	56		3.6	78.46	6240	6240	43.0	43.0
4/13/98	3	4"	HPC	54.89	4370	4370	30.1	30.1
	3	(6")	Test	132.05	4670	4670	32.2	32.2
	7		Truck	77.93	6200	6200	42.7	42.7
	14			82.69	6580	6580	45.4	45.4
	23			79.94	6360	6360	43.9	43.9
	30			76.95	6120		42.2	
	30			96.16	7650	6750	52.7	46.5
	30			81.50	6480		44.7	
	56			91.59	7290		50.3	
	56			98.34	7820	7500	53.9	51.7
	56			92.86	7390		51.0	

Table A.7 - Phase II Beam Concrete Strengths (part 2)

Date Cast	Test Day	Size	Mix	Force (k)	Strength			
					psi	Average (psi)	MPa	Average (MPa)
4/21/98	3	4"	HPC	66.97	5330	5330	36.7	36.7
	7		Beams:	87.80	7000	7000	48.3	48.3
	15		1.6	106.8	8500	8500	58.6	58.6
	22		2.6	115.65	9200	9200	63.4	63.4
	28		3.7	115.15	9160		63.2	
	28			114.91	9140	9330	63.0	64.3
	28			121.59	9670		66.7	
	56			120.56	9590		66.1	
	56			123.22	9860	9770	68.0	67.4
	56			123.95	9860		68.0	
6/22	4	6"	TxDOT	113.59	4020	4020	27.7	27.7
	7		Class C	118.5	4190	4190	28.9	28.9
	14		Beams:	131.8	4660	4660	32.1	32.1
	21		2.9	137.13	4850	4850	33.4	33.4
	28		2.12	139.39	4930		34.0	
	28			138.82	4910	4940	33.9	34.0
	28			141.19	4990		34.4	
	56			138.13	4890		33.7	
	56			144.37	5110	5010	35.2	34.5
	56			142.00	5020		34.6	

196

A.4 CRACK PATTERNS

A.4.1 Phase I Specimens

Figures A.26-A.36 show the crack patterns for each of the Phase I large-scale beam specimens. Uncracked specimens are not shown.
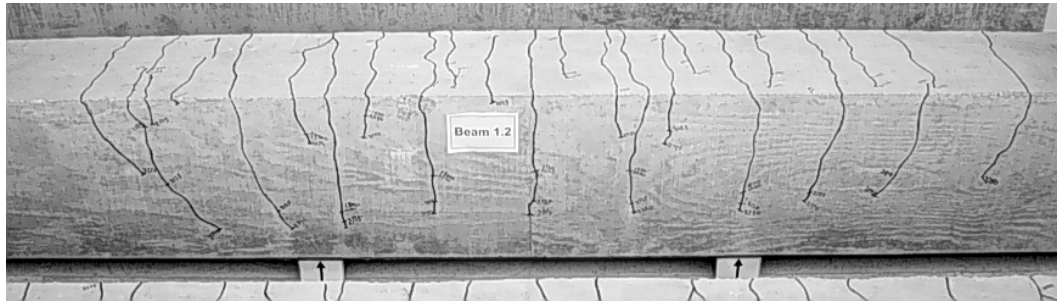
Figure A.26 - Crack Pattern for Specimen 1.2
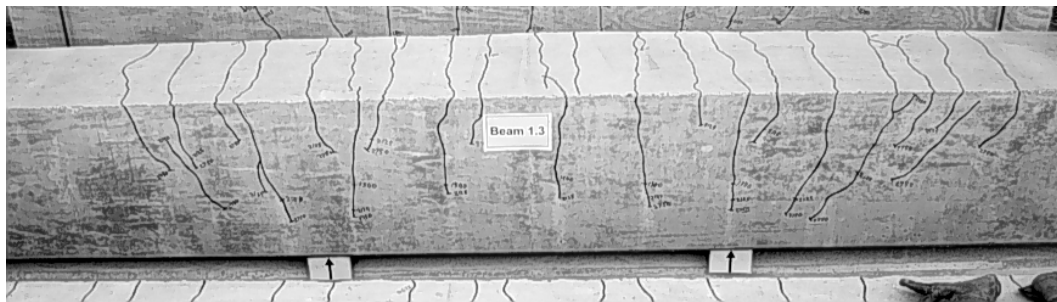
Figure A.27 - Crack Pattern for Specimen 1.3
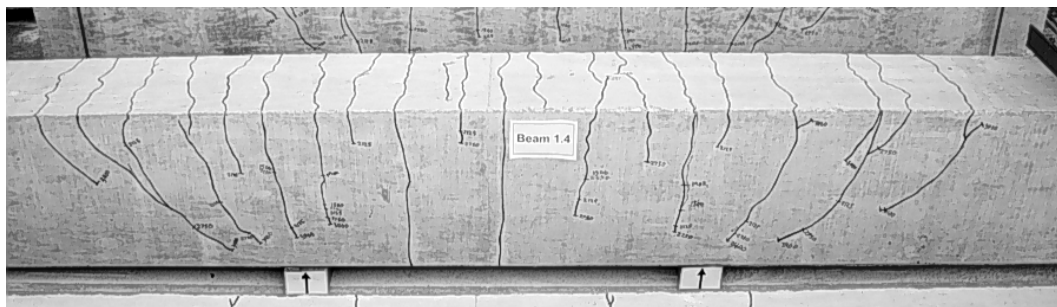
Figure A.28 - Crack Pattern for Specimen 1.4
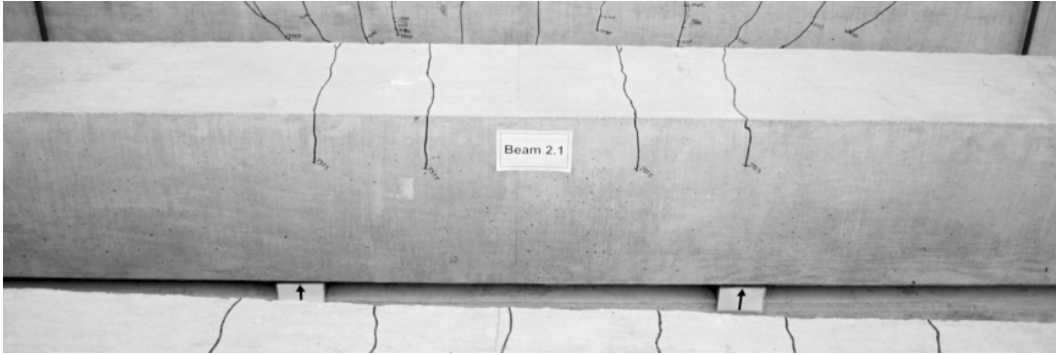
Figure A.29 - Crack Pattern for Specimen 2.1
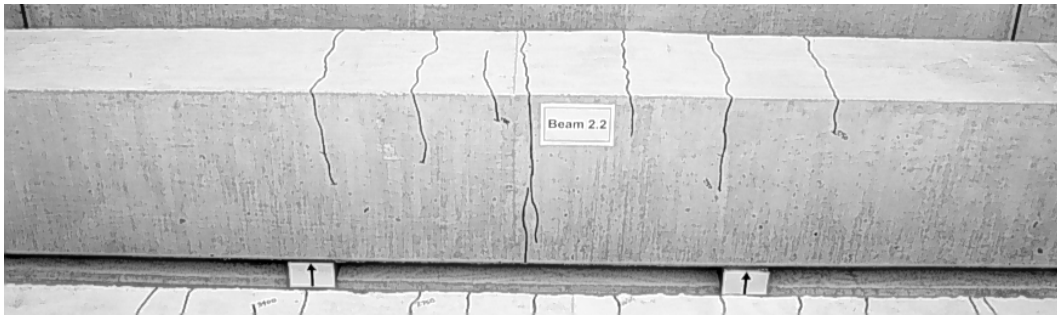
Figure A.30 - Crack Pattern for Specimen 2.2
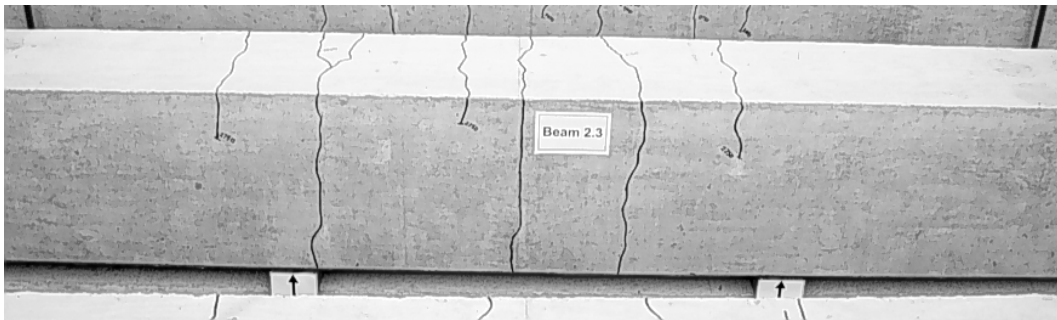
Figure A.31 - Crack Pattern for Specimen 2.3
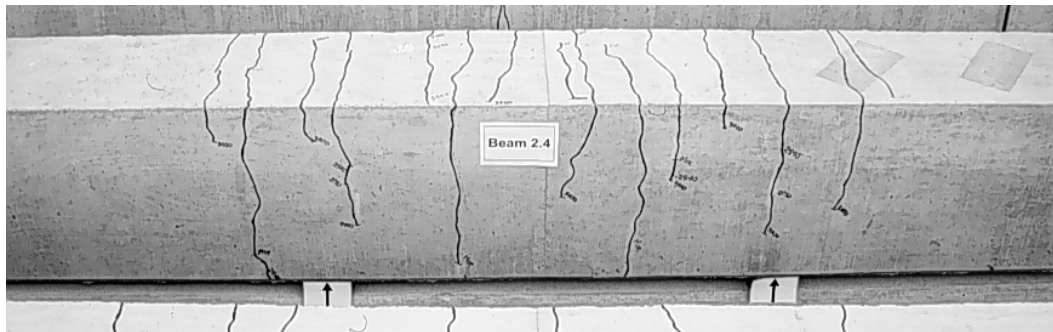
Figure A.32 - Crack Pattern for Specimen 2.4
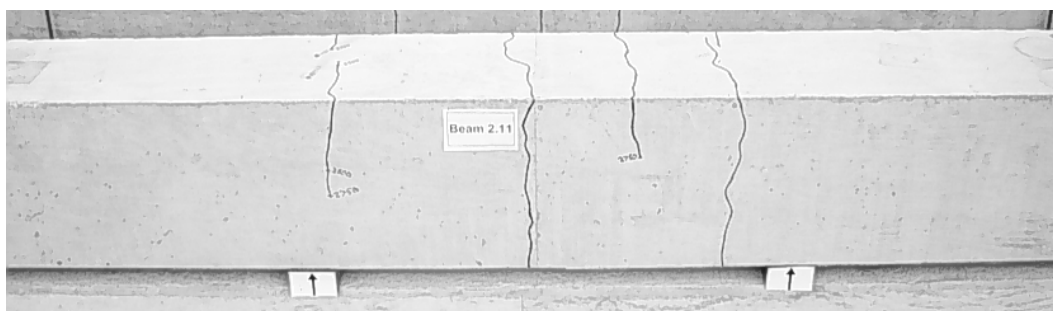
Figure A.33 - Crack Pattern for Specimen 2.11
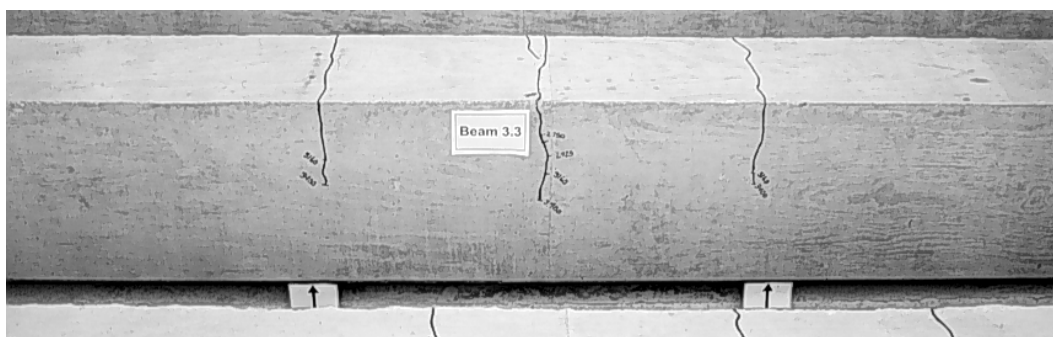
Figure A.34 - Crack Pattern for Specimen 3.3
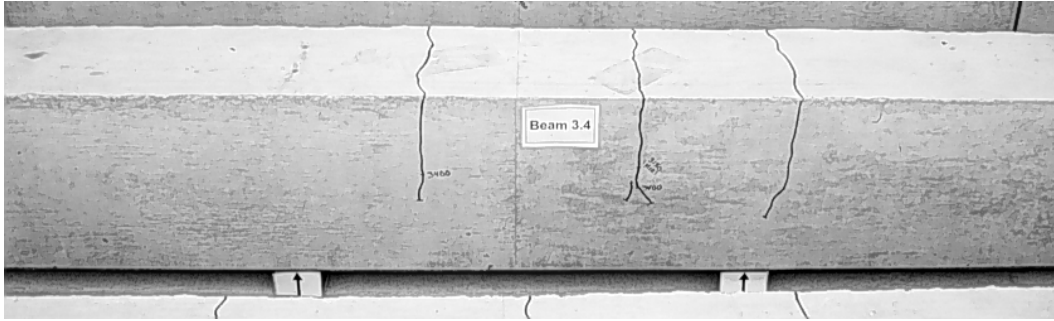
Figure A.35 - Crack Pattern for Specimen 3.4
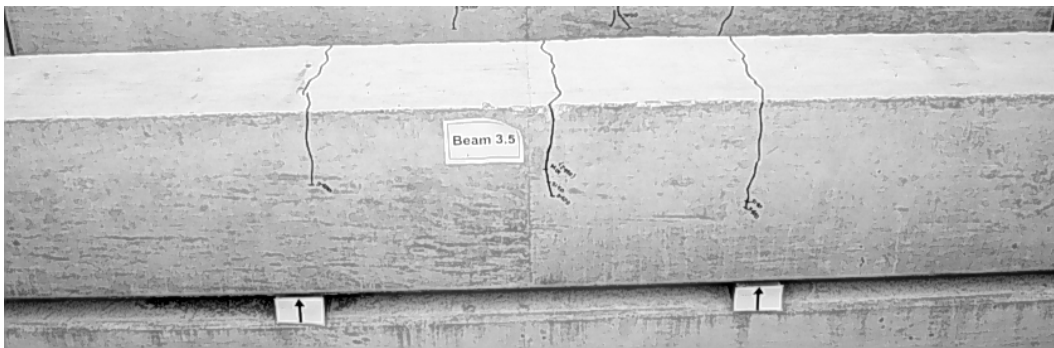
Figure A.36 - Crack Pattern for Specimen 3.5

A.4.2 Phase II Specimens

Figures A.37-A.47 show the crack patterns for each of the Phase II large-scale beam specimens.
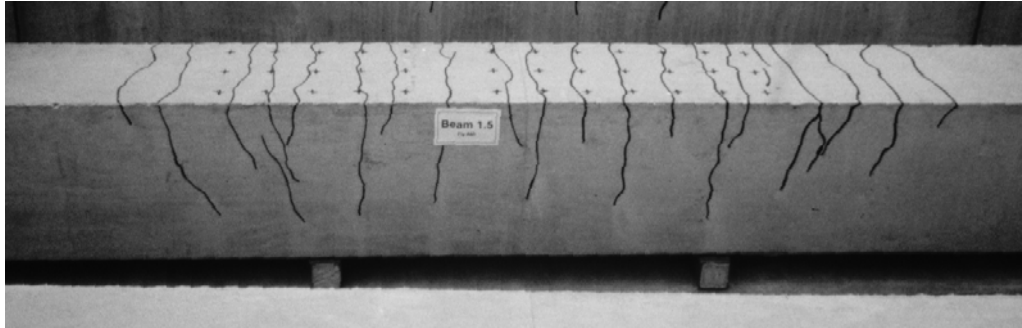
Figure A.37 - Crack Pattern for Specimen 1.5
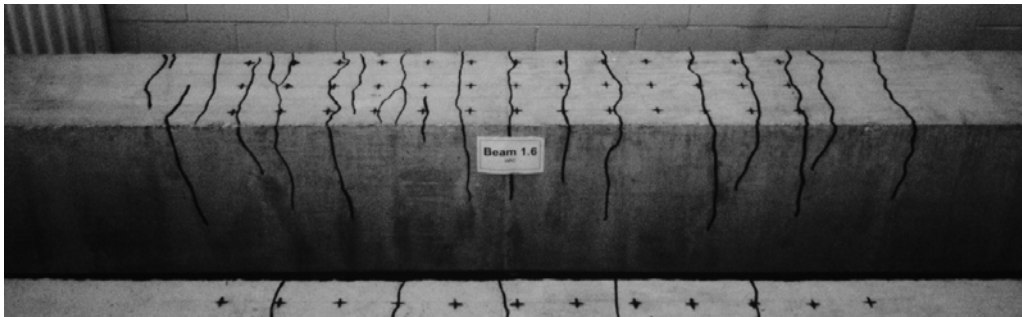
Figure A.38 - Crack Pattern for Specimen 1.6
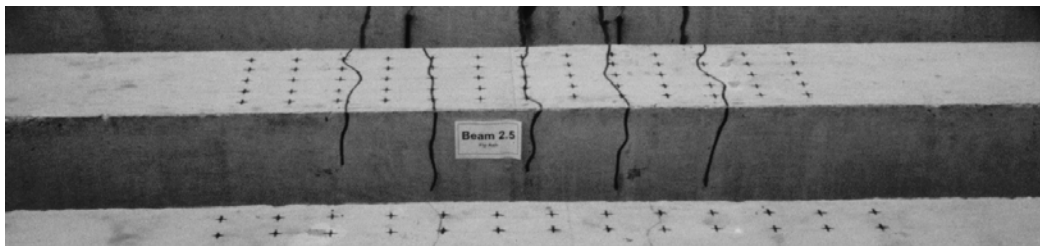
Figure A.39 - Crack Pattern for Specimen 2.5
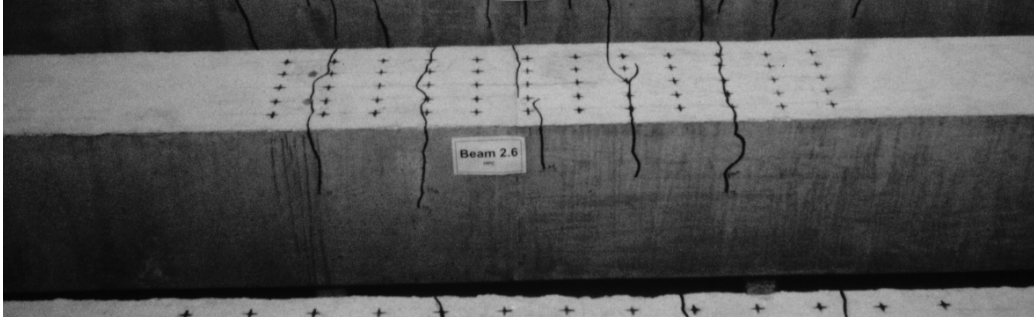
Figure A.40 - Crack Pattern for Specimen 2.6
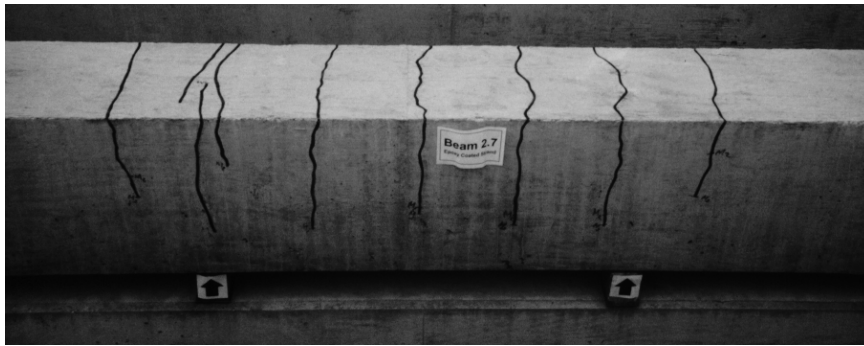
Figure A.41 - Crack Pattern for Specimen 2.7

Figure A.42 - Crack Pattern for Specimen 2.8

Figure A.43 - Crack Pattern for Specimen 2.9

Figure A.44 - Crack Pattern for Specimen 2.10
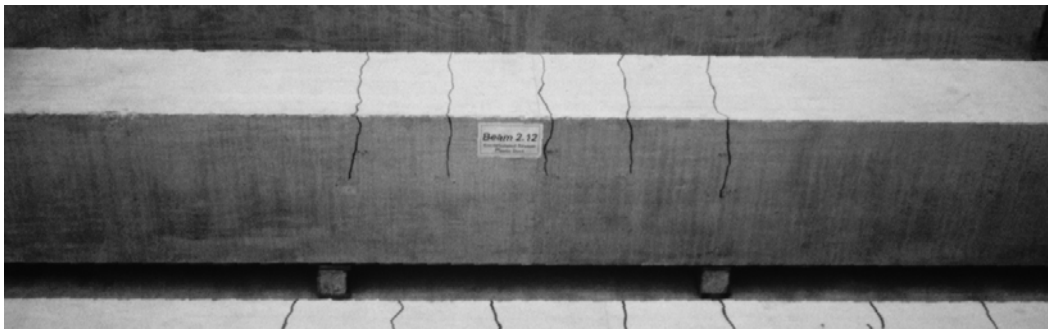
Figure A.45 - Crack Pattern for Specimen 2.12
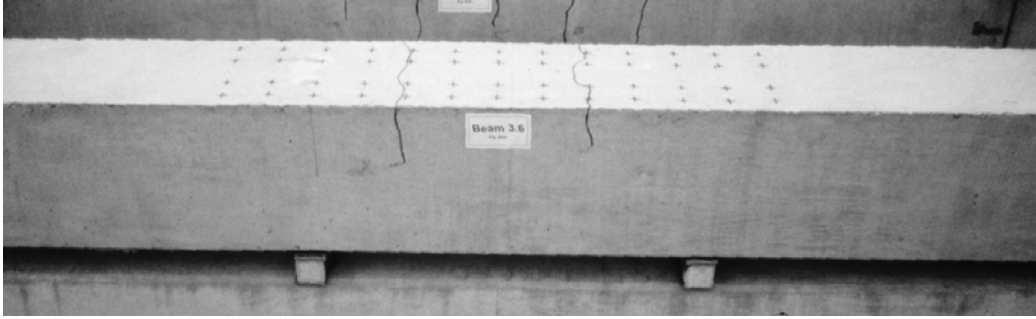
Figure A.46 - Crack Pattern for Specimen 3.6
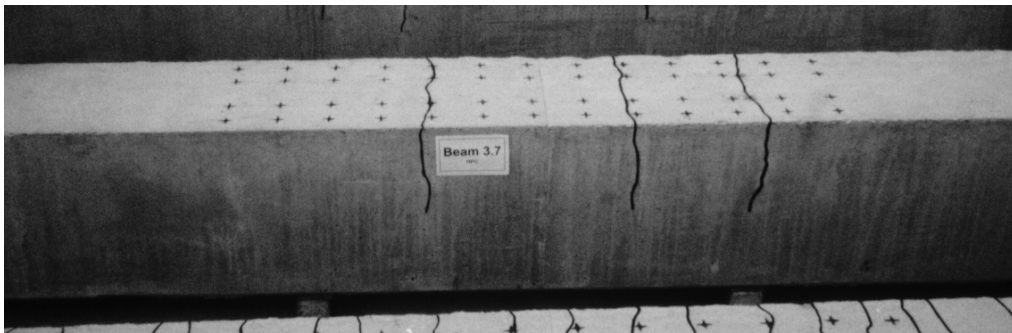
Figure A.47 - Crack Pattern for Specimen 3.7

A.5   CRACK WIDTHS AT START OF EXPOSURE TESTING

A.5.1   Phase I Specimens

Figures A.48-A.58 show maximum and minimum crack width measurements for each crack along the length of the specimen. The crack width values are given for the load value at the start of exposure testing. The points indicating crack width measurements are connected for clarity.
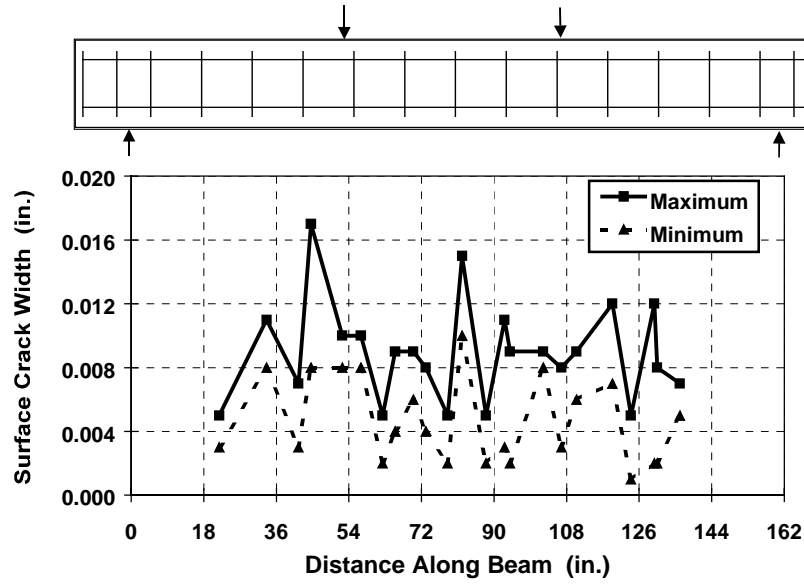
Figure A.48 - Crack Widths at Service Load for Specimen 1.2
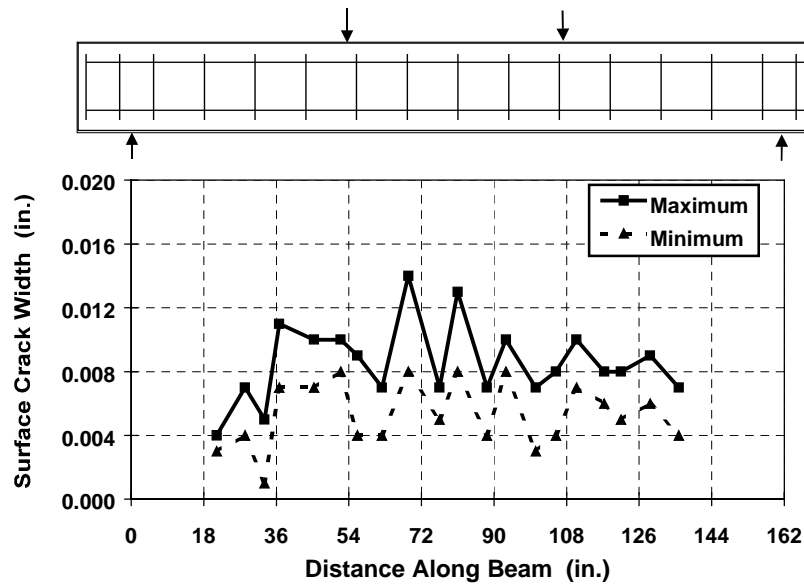
Figure A.49 - Crack Widths at Service Load for Specimen 1.3
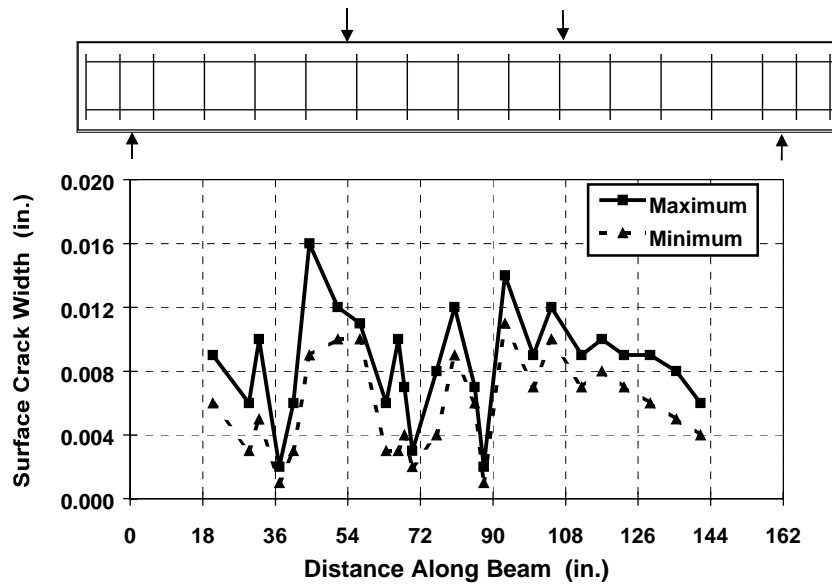
Figure A.50 - Crack Widths at Service Load (after Overload) for Specimen 1.4
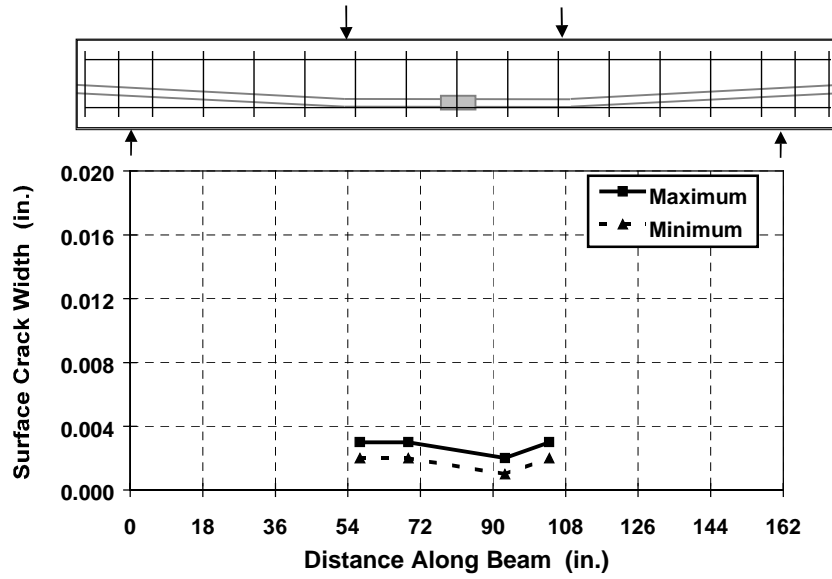
Figure A.51 - Crack Widths at 85% of Service Load for Specimen 2.1

206
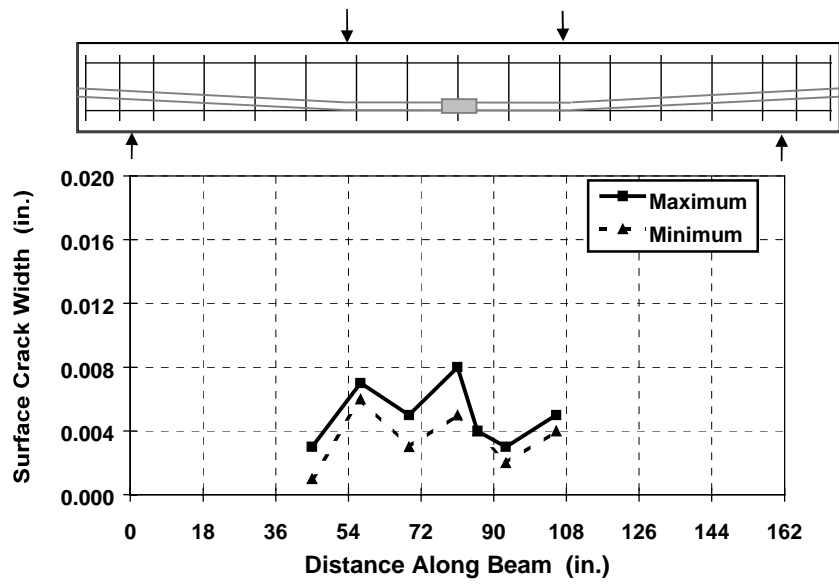
Figure A.52 - Crack Widths at Service Load for Specimen 2.2
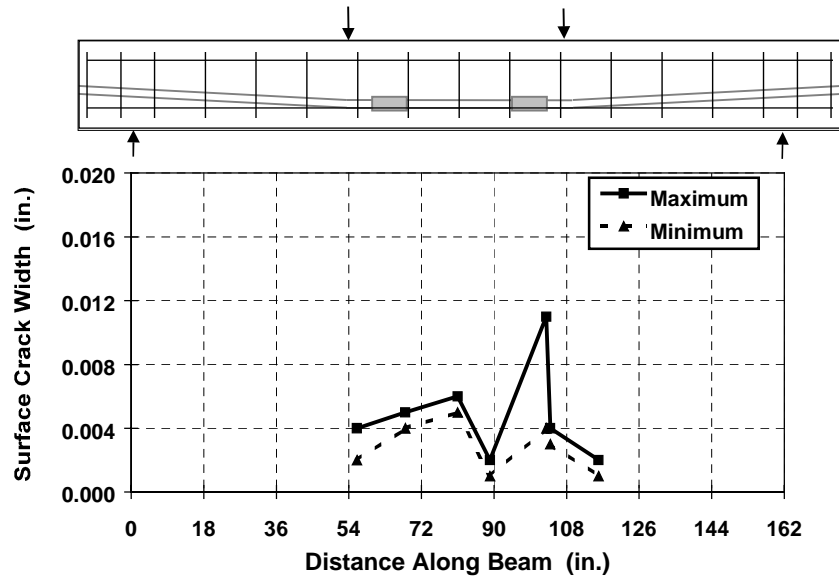
Figure A.53 - Crack Widths at Service Load for Specimen 2.3

207
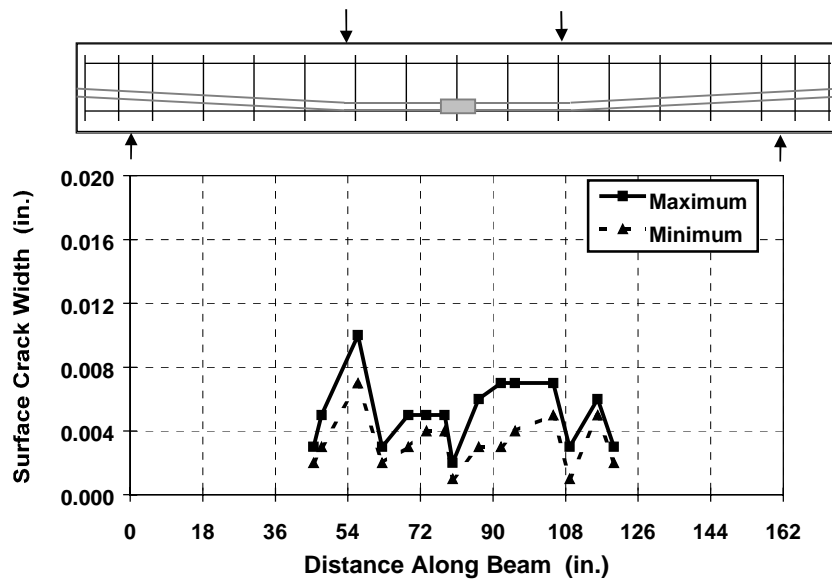
Figure A.54 - Crack Widths at Service Load (after Overload) for Specimen 2.4
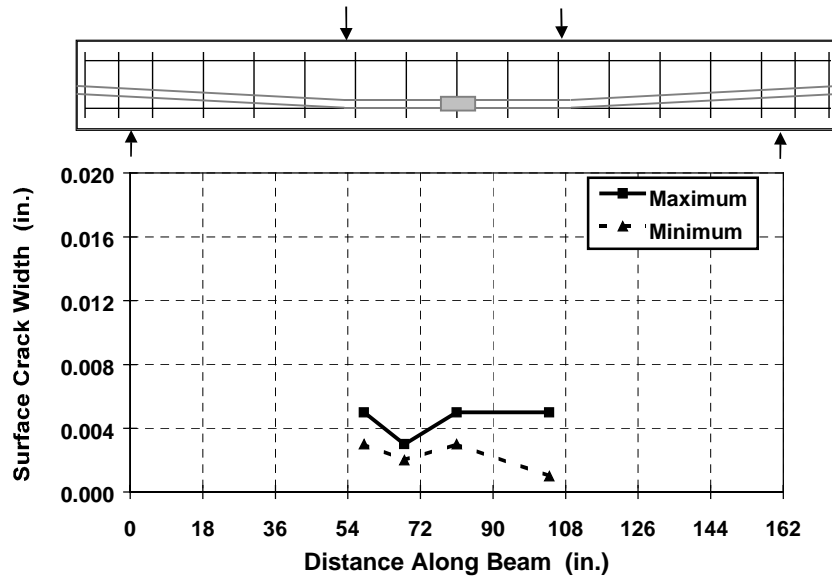
Figure A.55 - Crack Widths at Service Load for Specimen 2.11
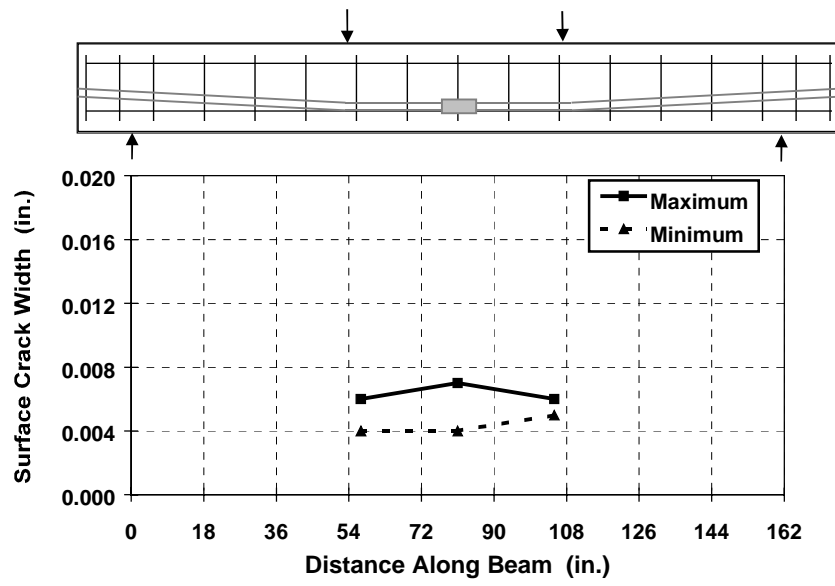
Figure A.56 - Crack Widths at Service Load (after Overload) for Specimen 3.3
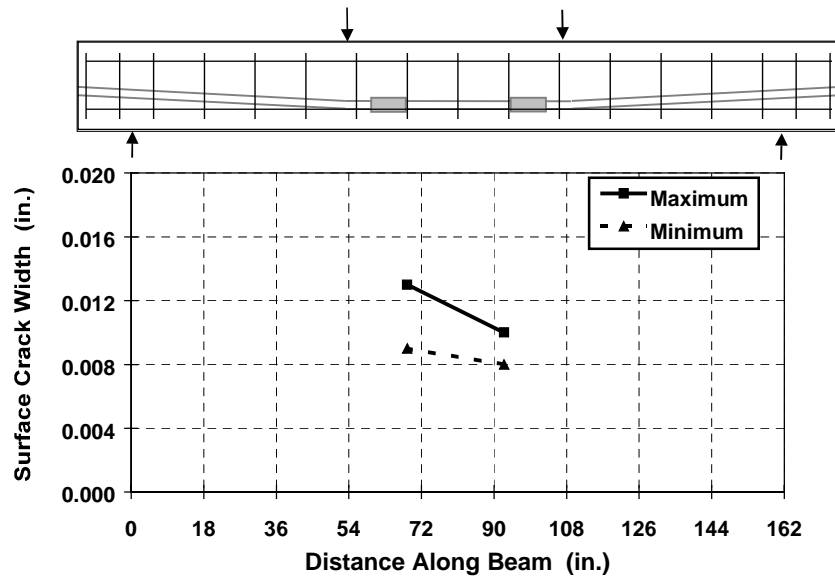
Figure A.57 - Crack Widths at Service Load (after Overload) for Specimen 3.4
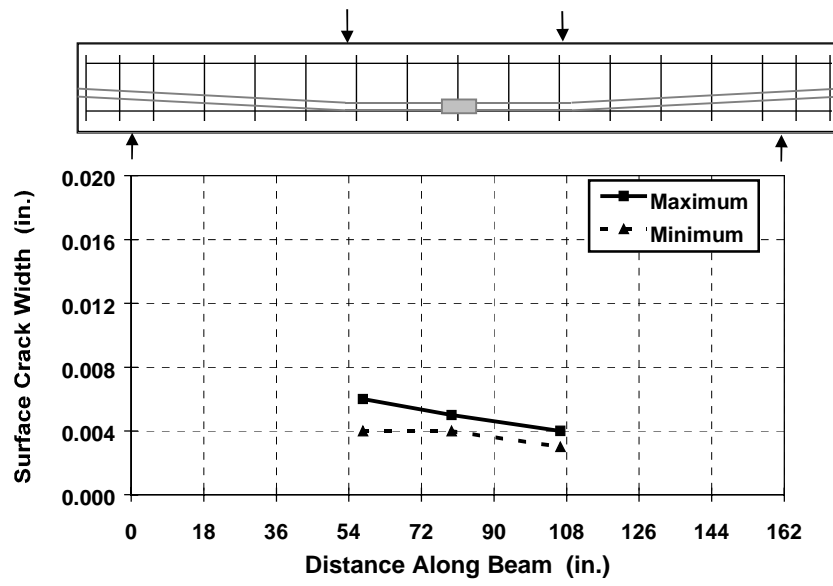
Figure A.58 - Crack Widths at Service Load (after Overload) for Specimen 3.5

A.5.2 Phase II Specimens

Figures A.59-A.69 show maximum and minimum crack width measurements for each crack along the length of the specimen. The crack width values are given for the load value at the start of exposure testing. The points indicating crack width measurements are connected for clarity.
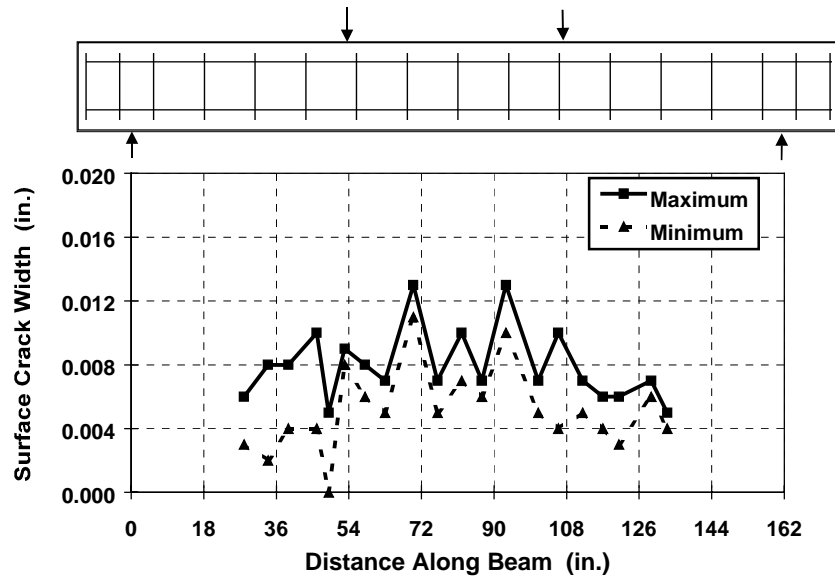
Figure A.59 - Crack Widths at Service Load for Specimen 1.5
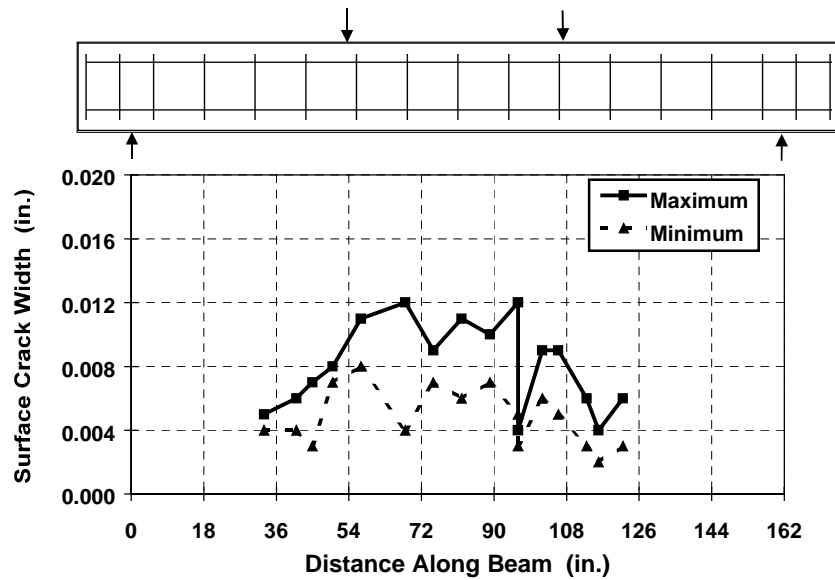
Figure A.60 - Crack Widths at Service Load for Specimen 1.6
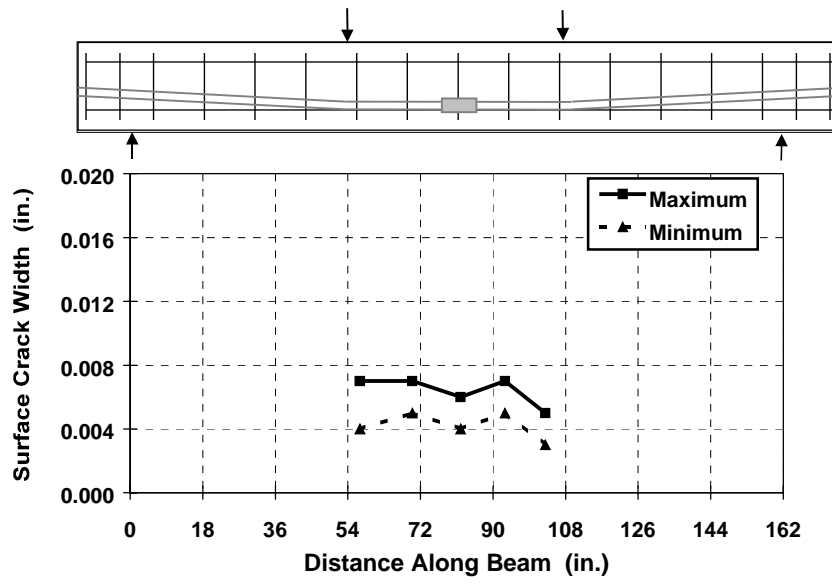
Figure A.61 - Crack Widths at Service Load for Specimen 2.5
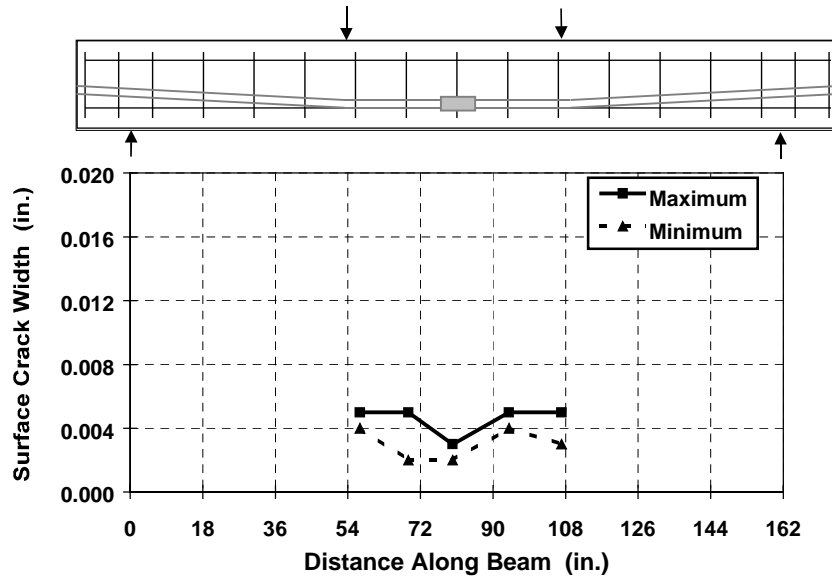
Figure A.62 - Crack Widths at Service Load for Specimen 2.6

212
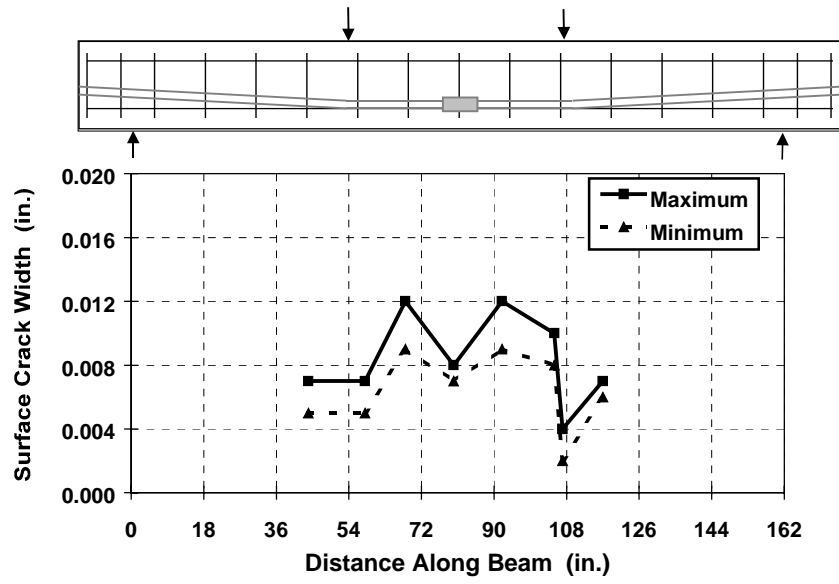
Figure A.63 - Crack Widths at Service Load for Specimen 2.7
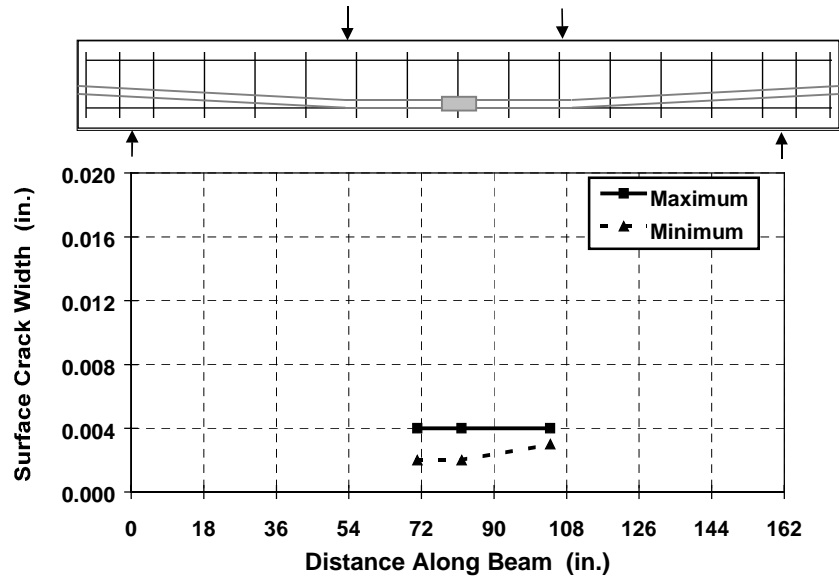
Figure A.64 - Crack Widths at Service Load for Specimen 2.8

213
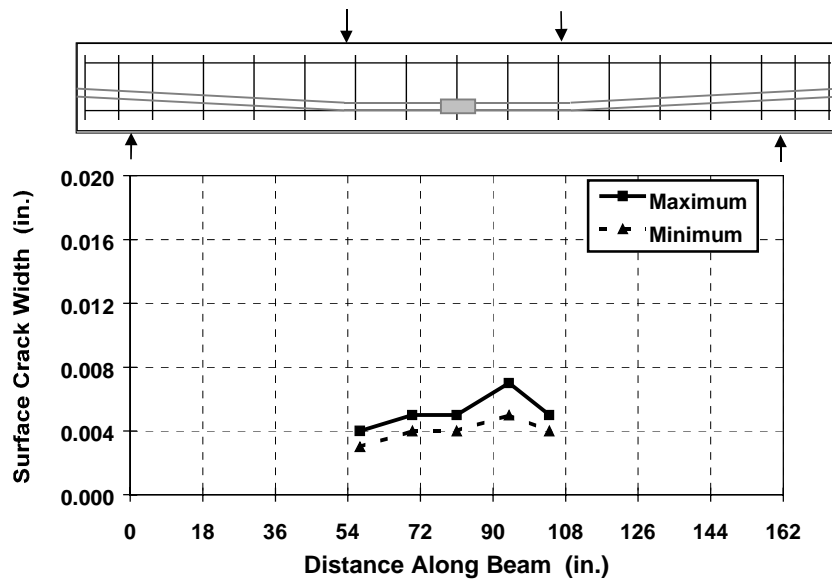
Figure A.65 - Crack Widths at Service Load for Specimen 2.9
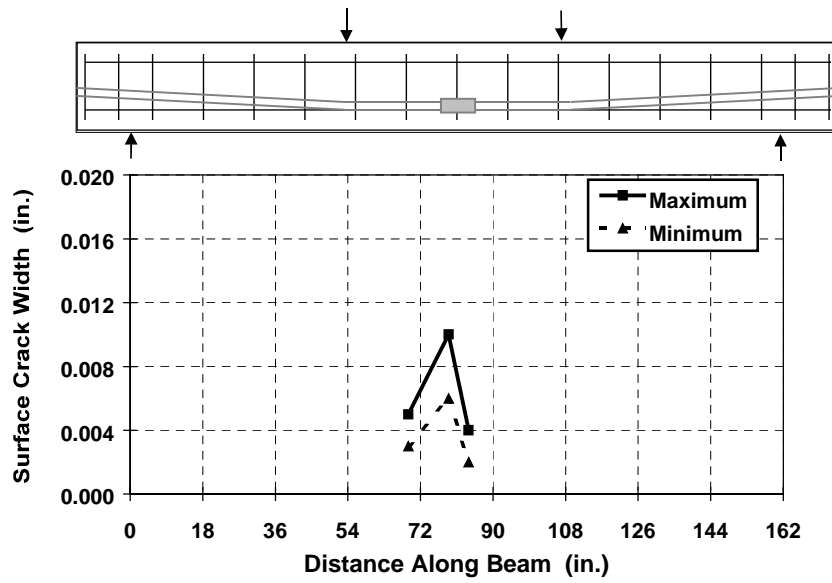
Figure A.66 - Crack Widths at Service Load for Specimen 2.10

214
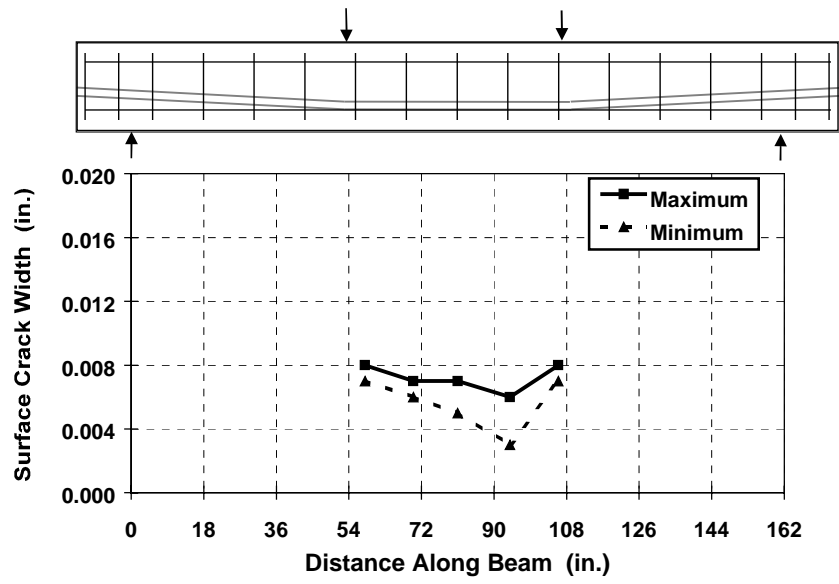
Figure A.67 - Crack Widths at Service Load for Specimen 2.12
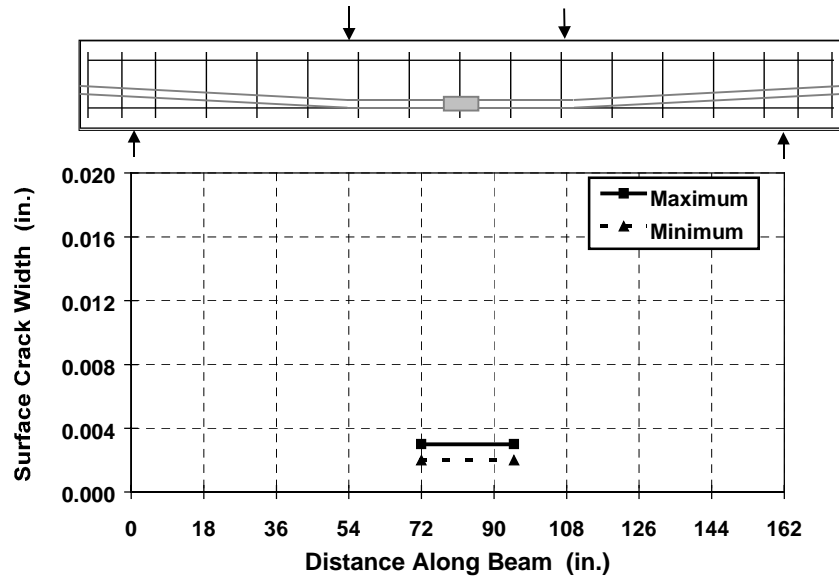
Figure A.68 - Crack Widths at Service Load for Specimen 3.6
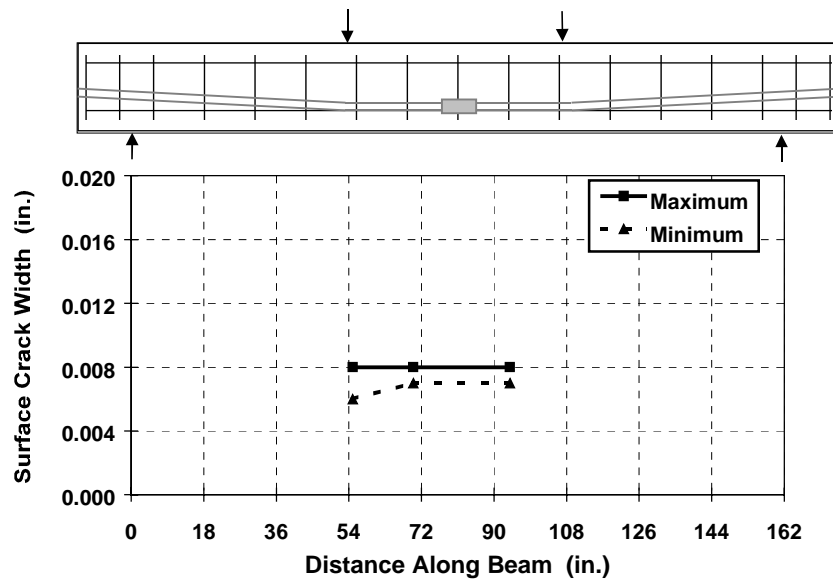
Figure A.69 - Crack Widths at Service Load (after Overload) for Specimen 3.7

A.6 HALF-CELL POTENTIAL READINGS

A.6.1 Phase I Specimens

Figures A.70-A.85 show half-cell potential readings for each of the large-scale beam specimens in Phase I through the end of April of 1999 (498 days). The highest reading from a given day is plotted along with an average of the values in the ponded region for that day.
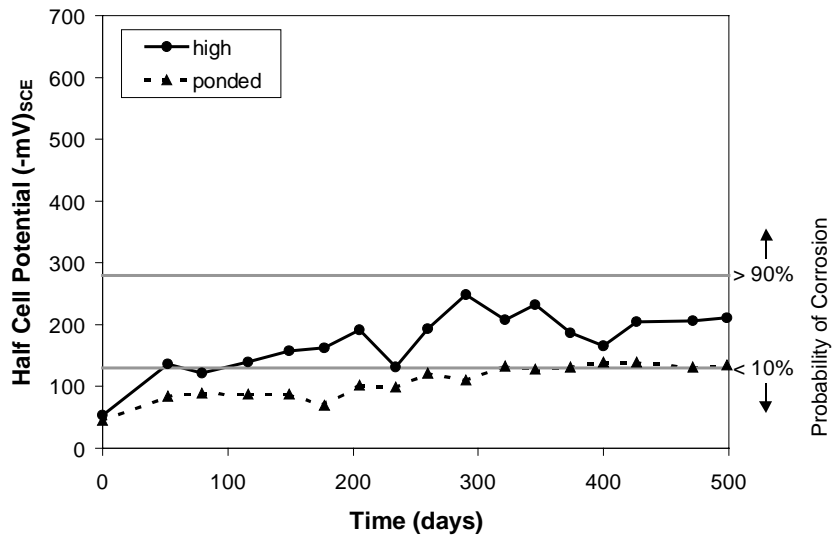
Figure A.70 - Half-Cell Potential Readings for Specimen 1.1
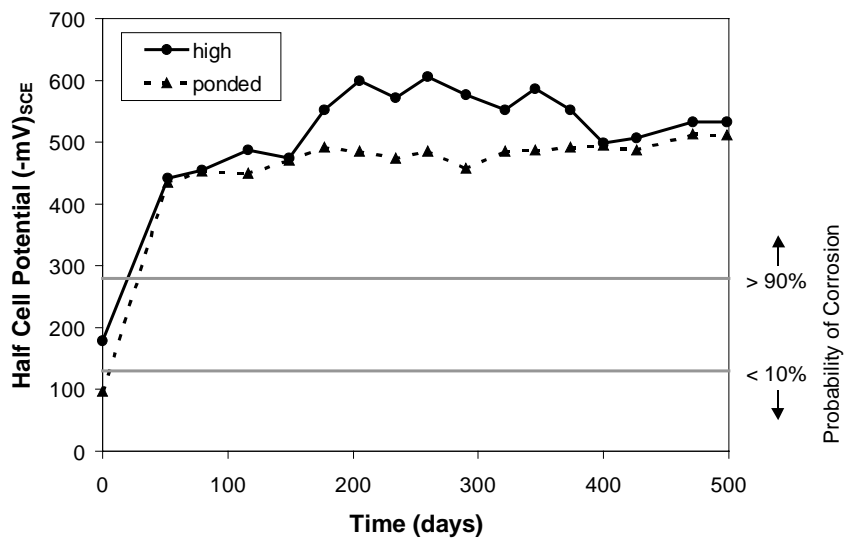
Figure A.71 - Half-Cell Potential Readings for Specimen 1.2
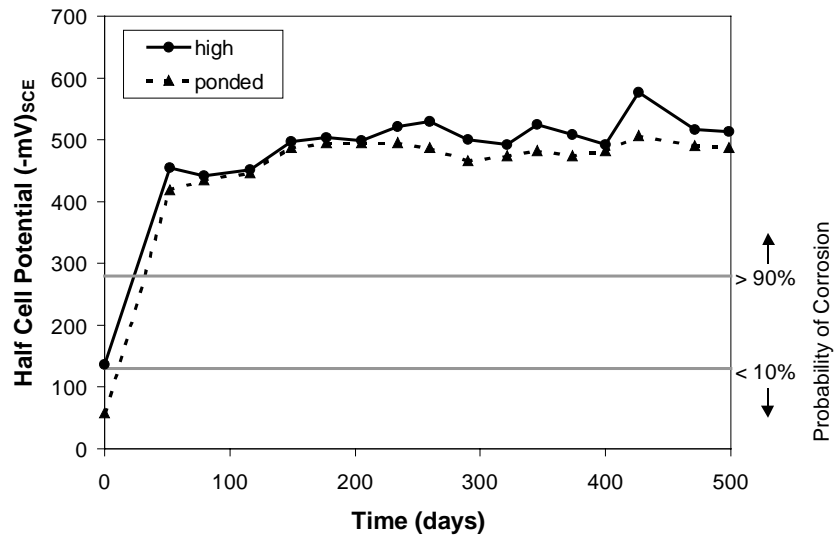
Figure A.72 - Half-Cell Potential Readings for Specimen 1.3
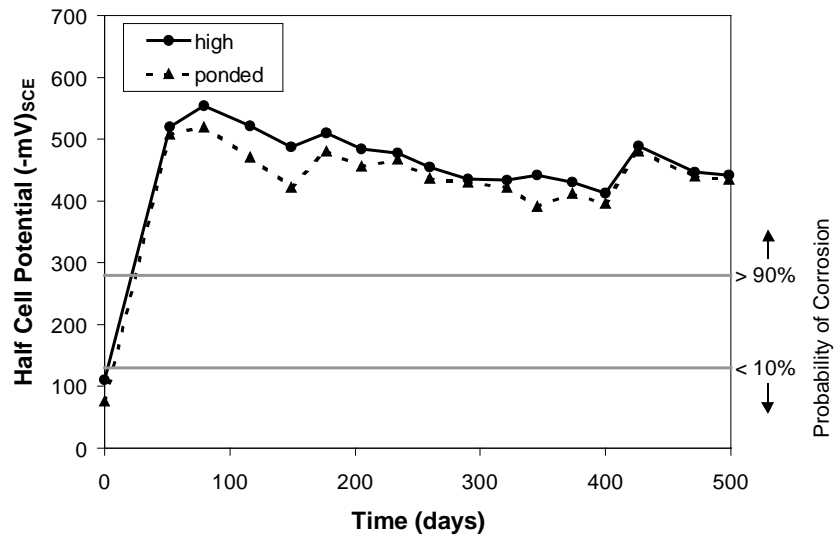
Figure A.73 - Half-Cell Potential Readings for Specimen 1.4
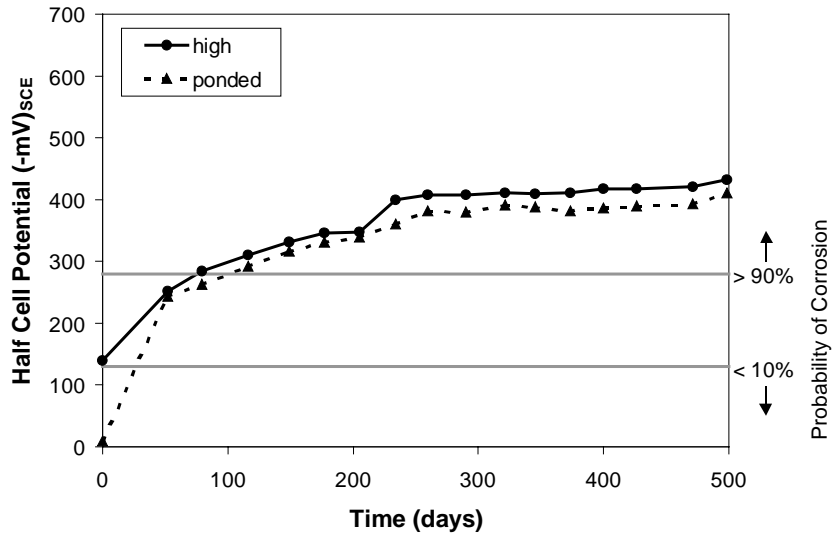
Figure A.74 - Half-Cell Potential Readings for Specimen 2.1
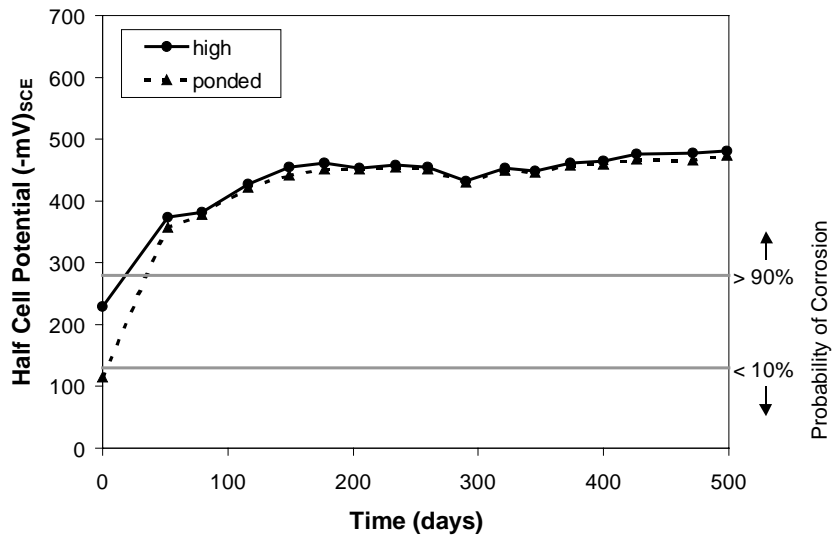
Figure A.75 - Half-Cell Potential Readings for Specimen 2.2
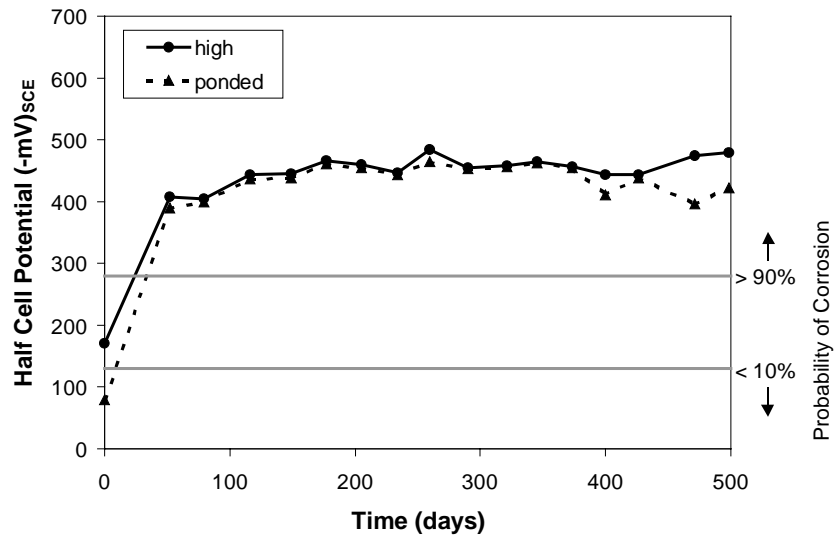
Figure A.76 - Half-Cell Potential Readings for Specimen 2.3
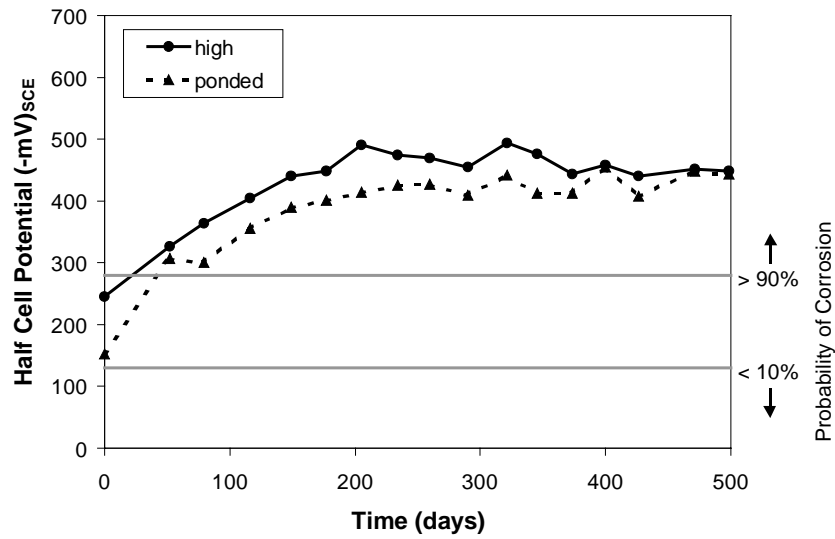
Figure A.77 - Half-Cell Potential Readings for Specimen 2.4
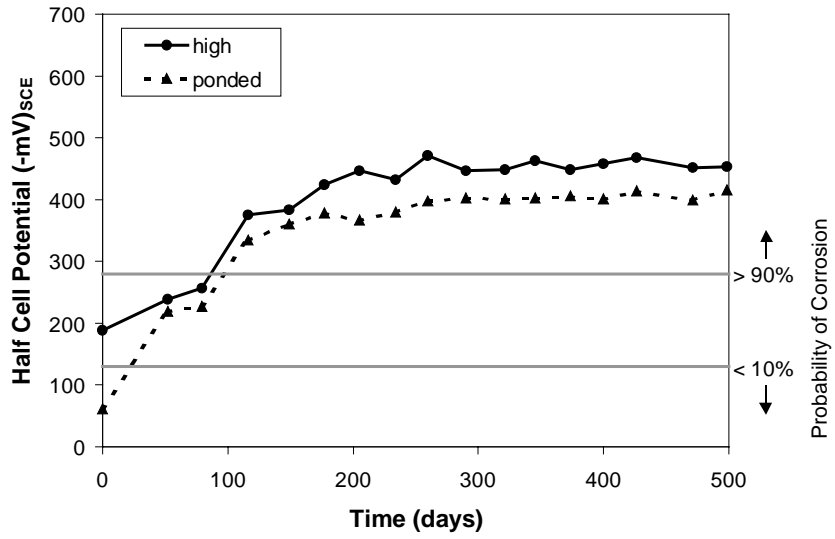
Figure A.78 - Half-Cell Potential Readings for Specimen 2.11
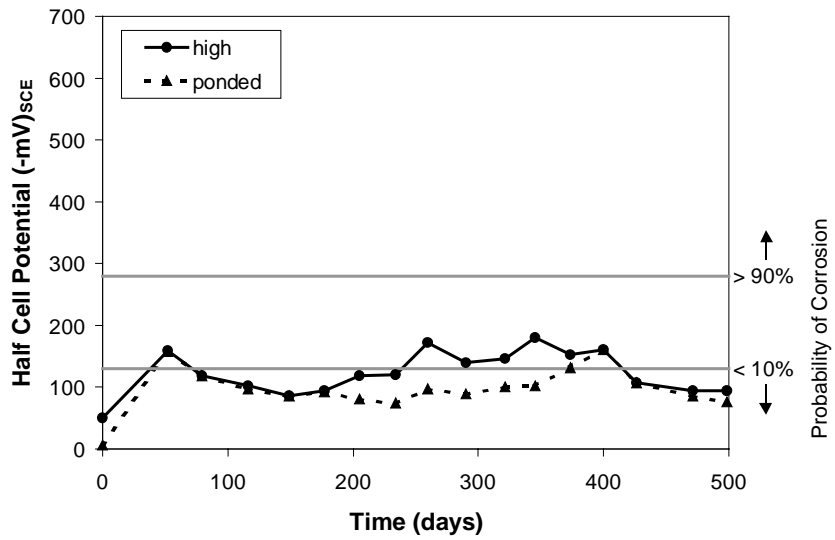
Figure A.79 - Half-Cell Potential Readings for Specimen 3.1
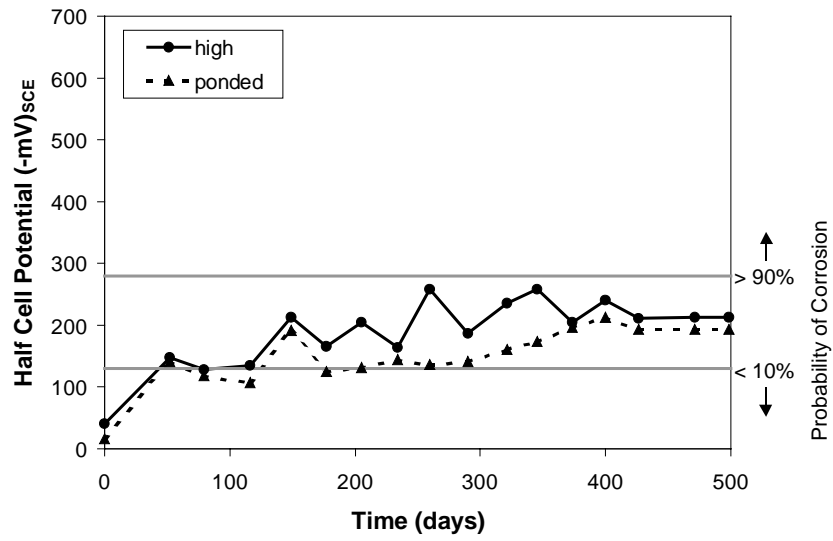
Figure A.80 - Half-Cell Potential Readings for Specimen 3.2
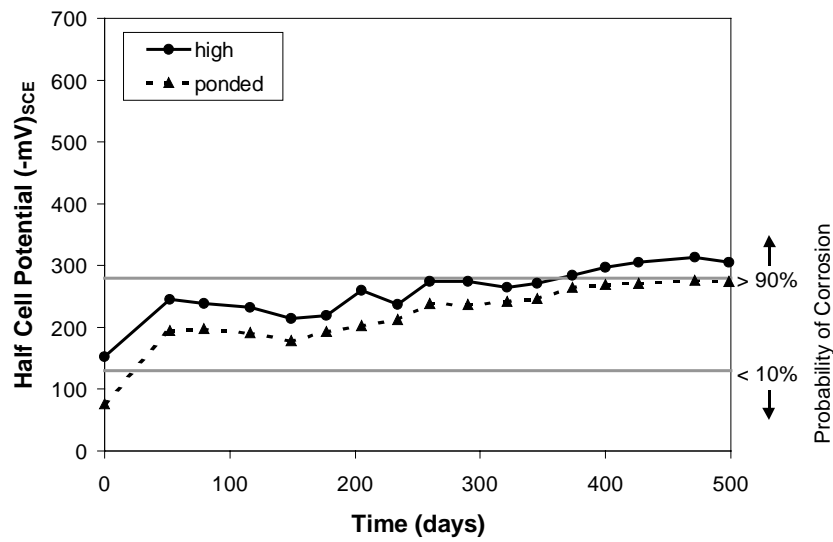
Figure A.81 - Half-Cell Potential Readings for Specimen 3.3
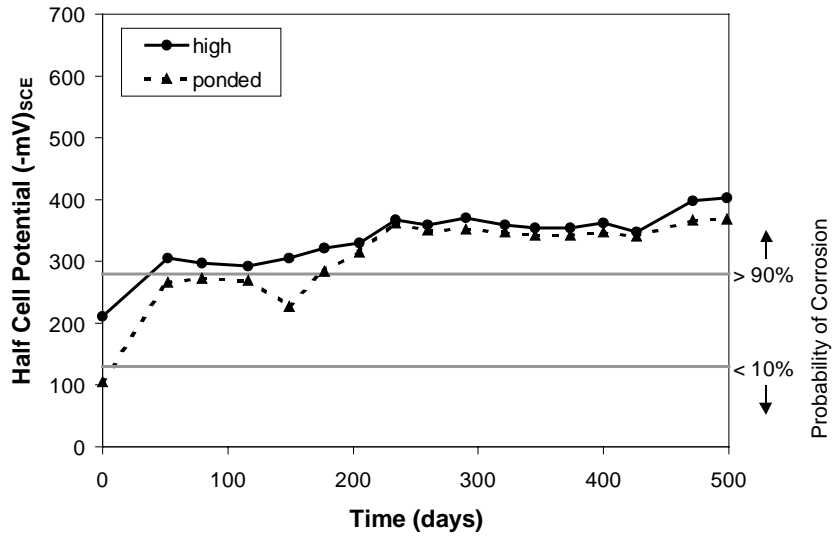
Figure A.82 - Half-Cell Potential Readings for Specimen 3.4
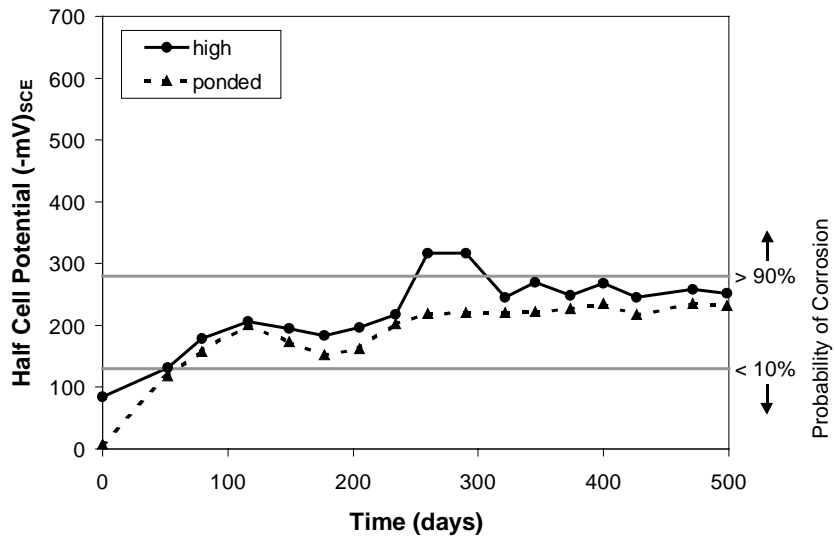
Figure A.83 - Half-Cell Potential Readings for Specimen 3.5
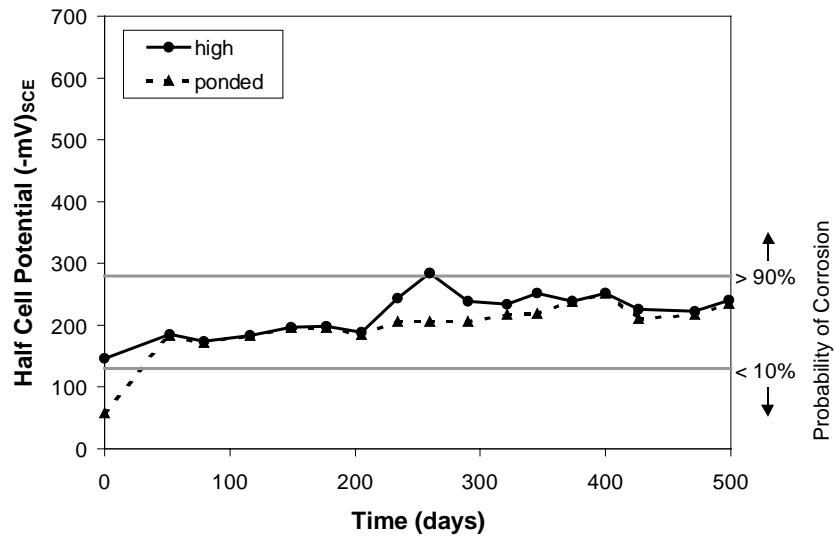
Figure A.84 - Half-Cell Potential Readings for Specimen 4.1
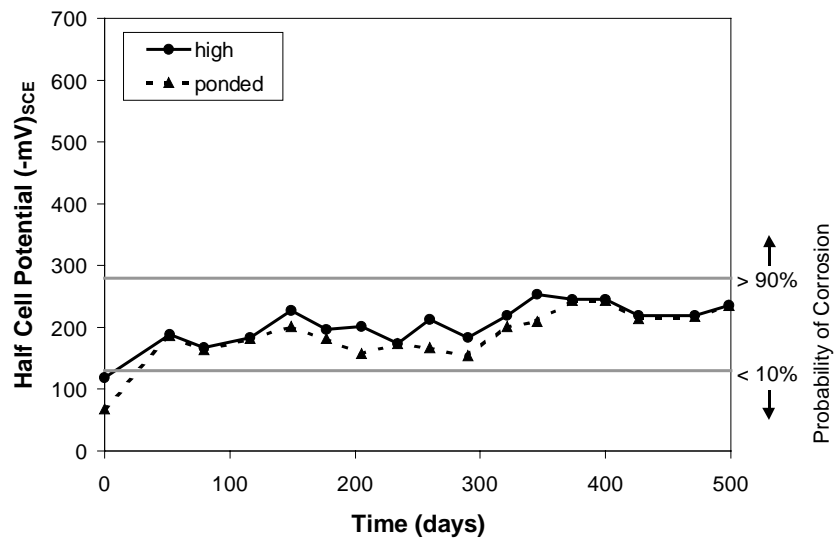
Figure A.85 - Half-Cell Potential Readings for Specimen 4.2

224

A.6.2 Phase II Specimens

Figures A.86-A.96 show half-cell potential readings for each of the large-scale beam specimens in Phase II through the end of April of 1999 (139 days). The highest reading from a given day is plotted along with an average of the values in the ponded region for that day.
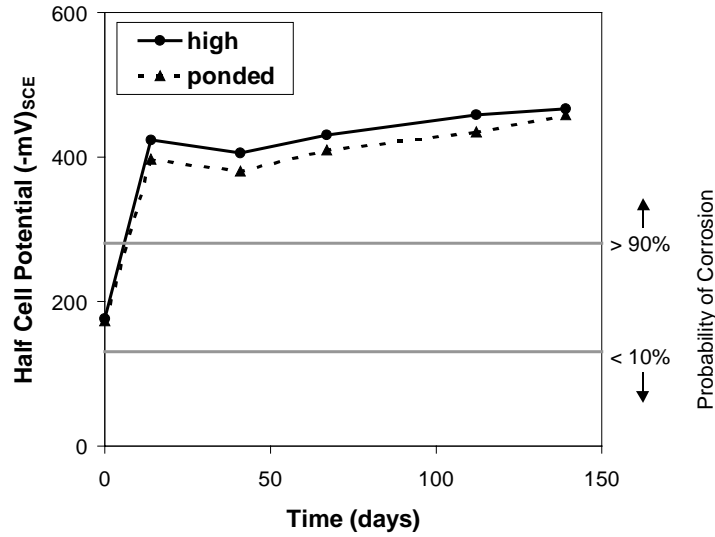
Figure A.86 - Half-Cell Potential Readings for Specimen 1.5
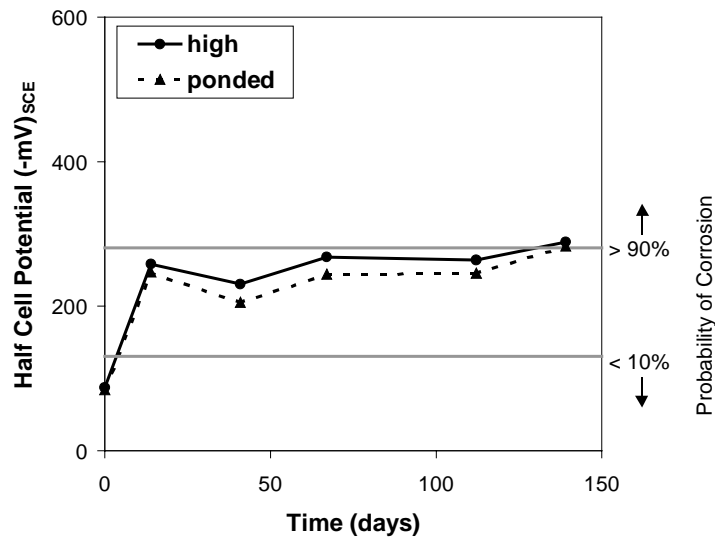
Figure A.87 - Half-Cell Potential Readings for Specimen 1.6
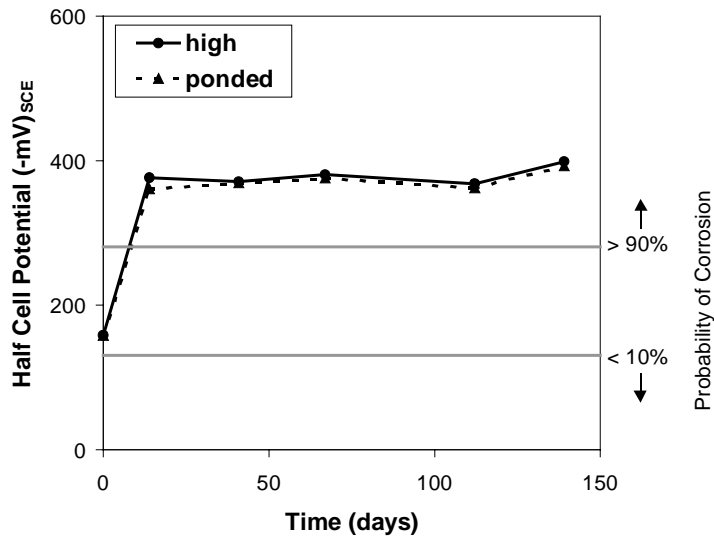
Figure A.88 - Half-Cell Potential Readings for Specimen 2.5
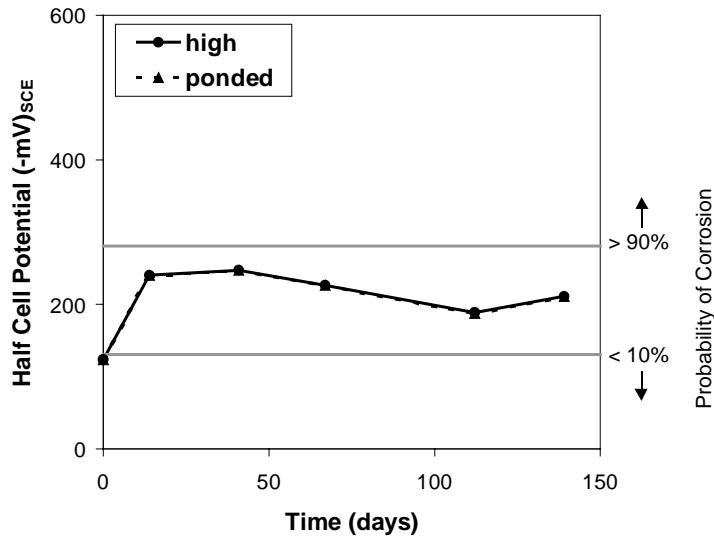
Figure A.89 - Half-Cell Potential Readings for Specimen 2.6
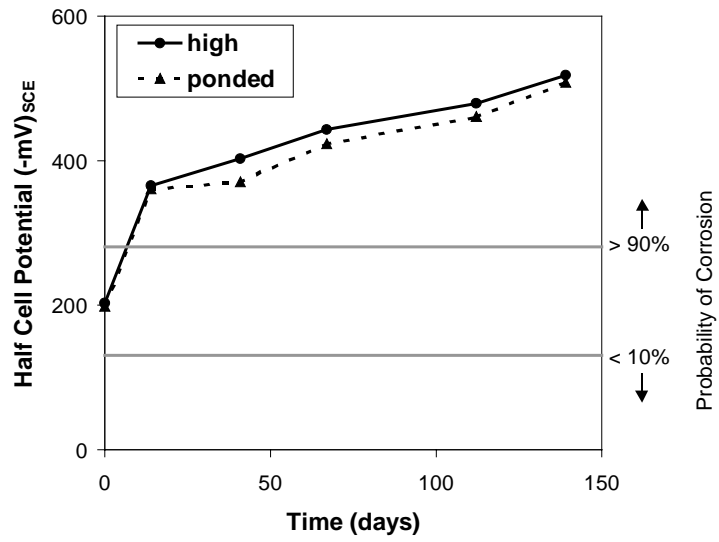
Figure A.90 - Half-Cell Potential Readings for Specimen 2.7
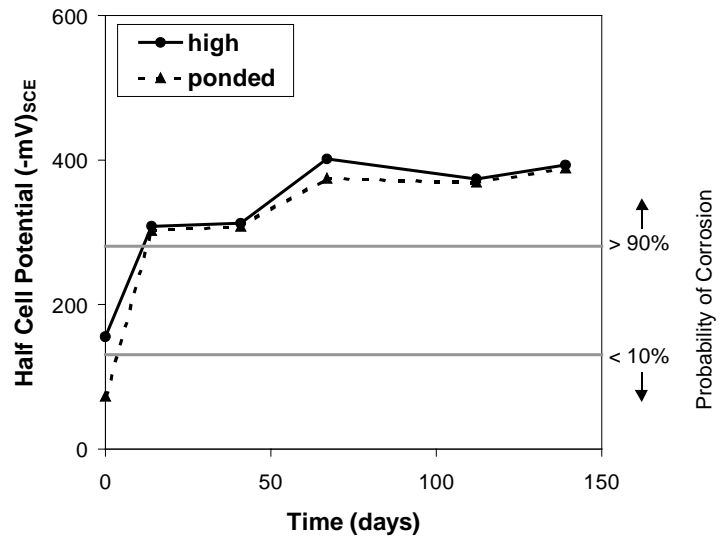
Figure A.91 - Half-Cell Potential Readings for Specimen 2.8
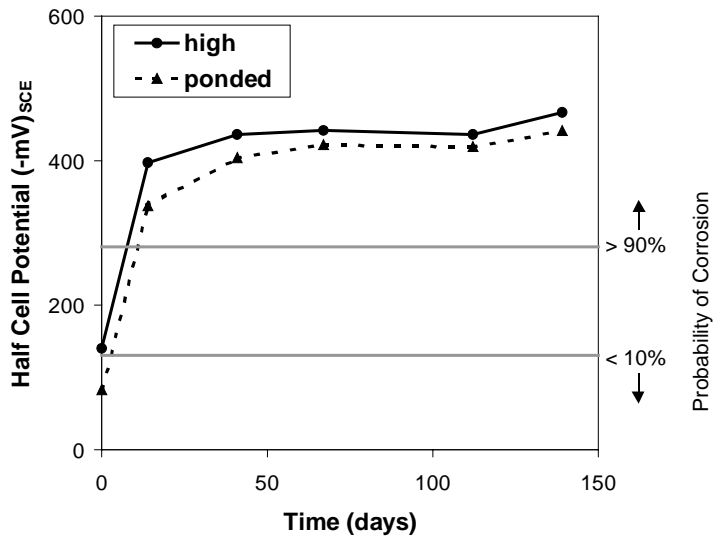
Figure A.92 - Half-Cell Potential Readings for Specimen 2.9
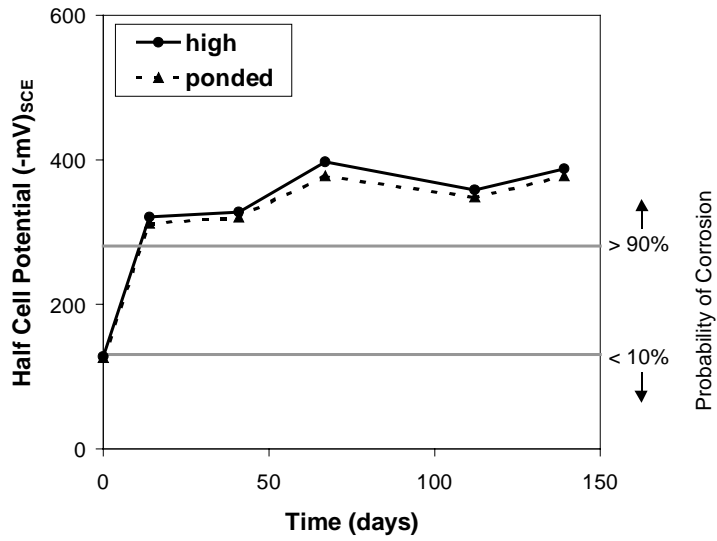
Figure A.93 - Half-Cell Potential Readings for Specimen 2.10

228
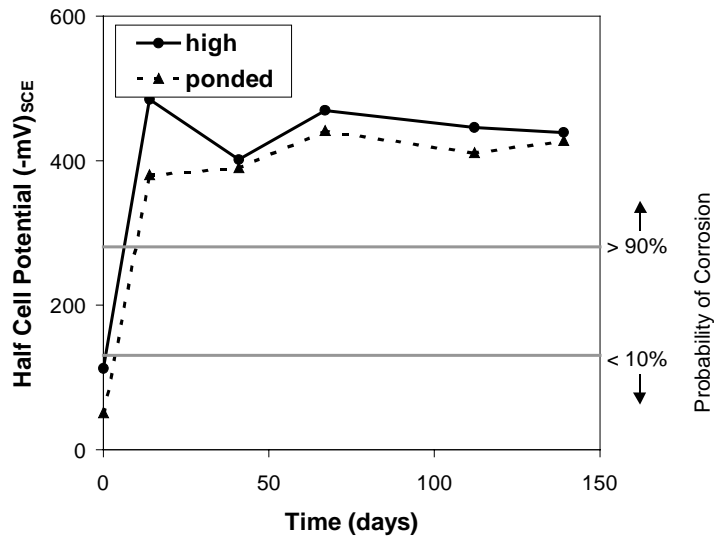
Figure A.94 - Half-Cell Potential Readings for Specimen 2.12
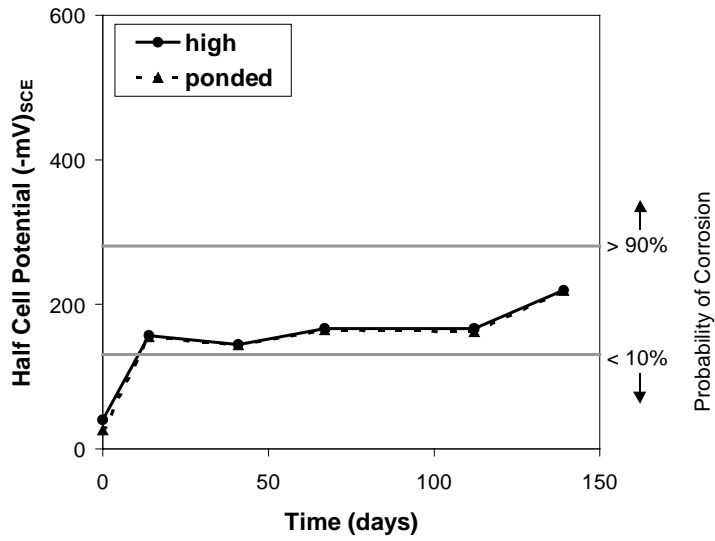
Figure A.95 - Half-Cell Potential Readings for Specimen 3.6

229
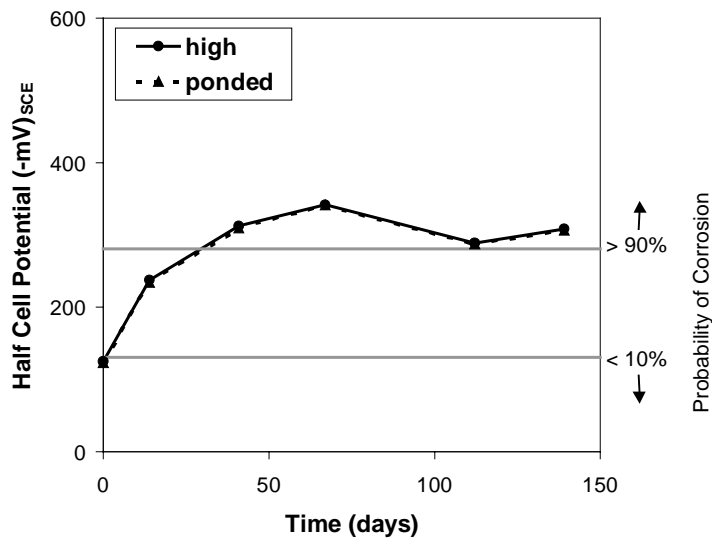
Figure A.96 - Half-Cell Potential Readings for Specimen 3.7

APPENDIX B

LONG-TERM COLUMN CORROSION TESTS: SUPPLEMENTARY MATERIAL
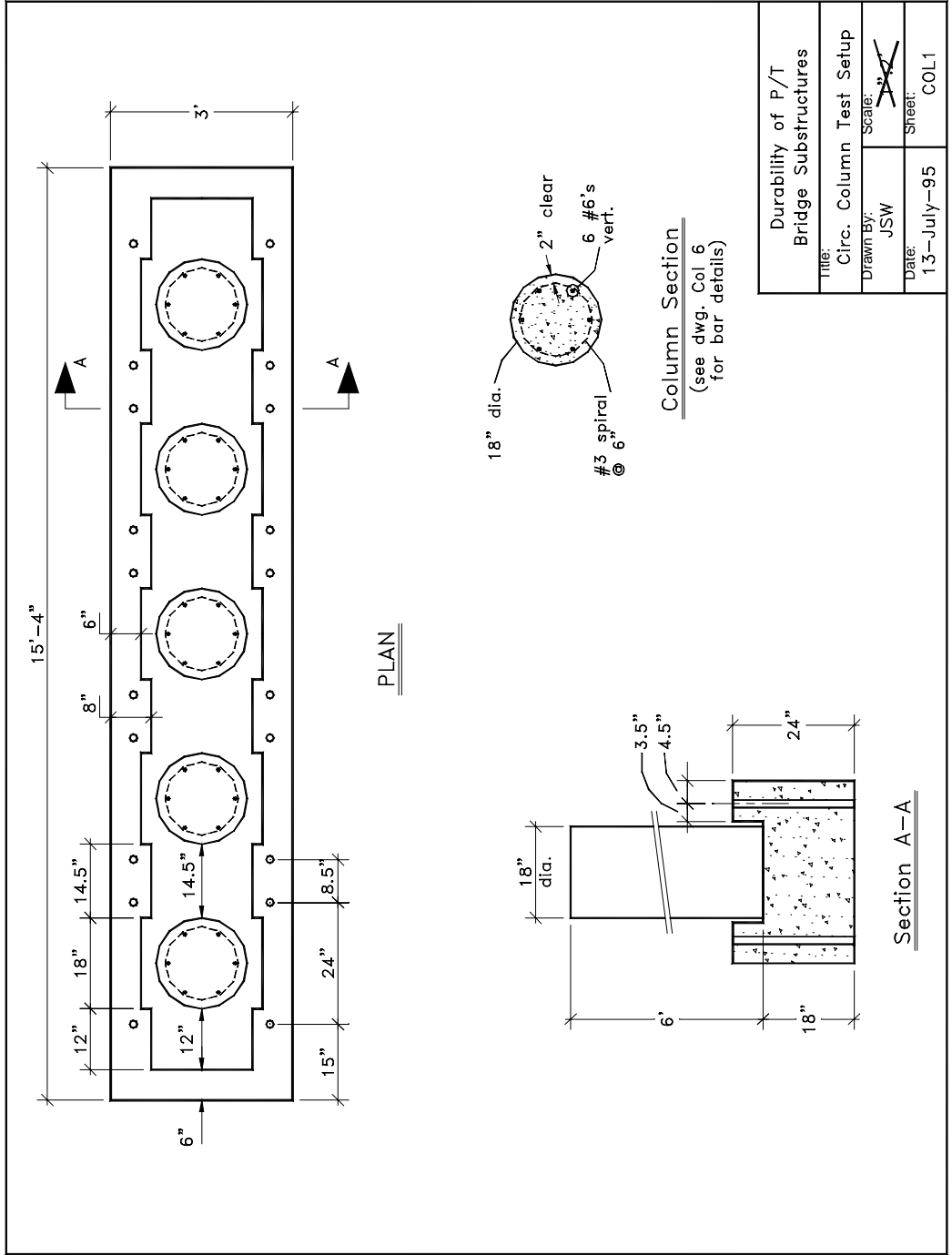
Figure B.1 – Sheet COL1: Column Foundation
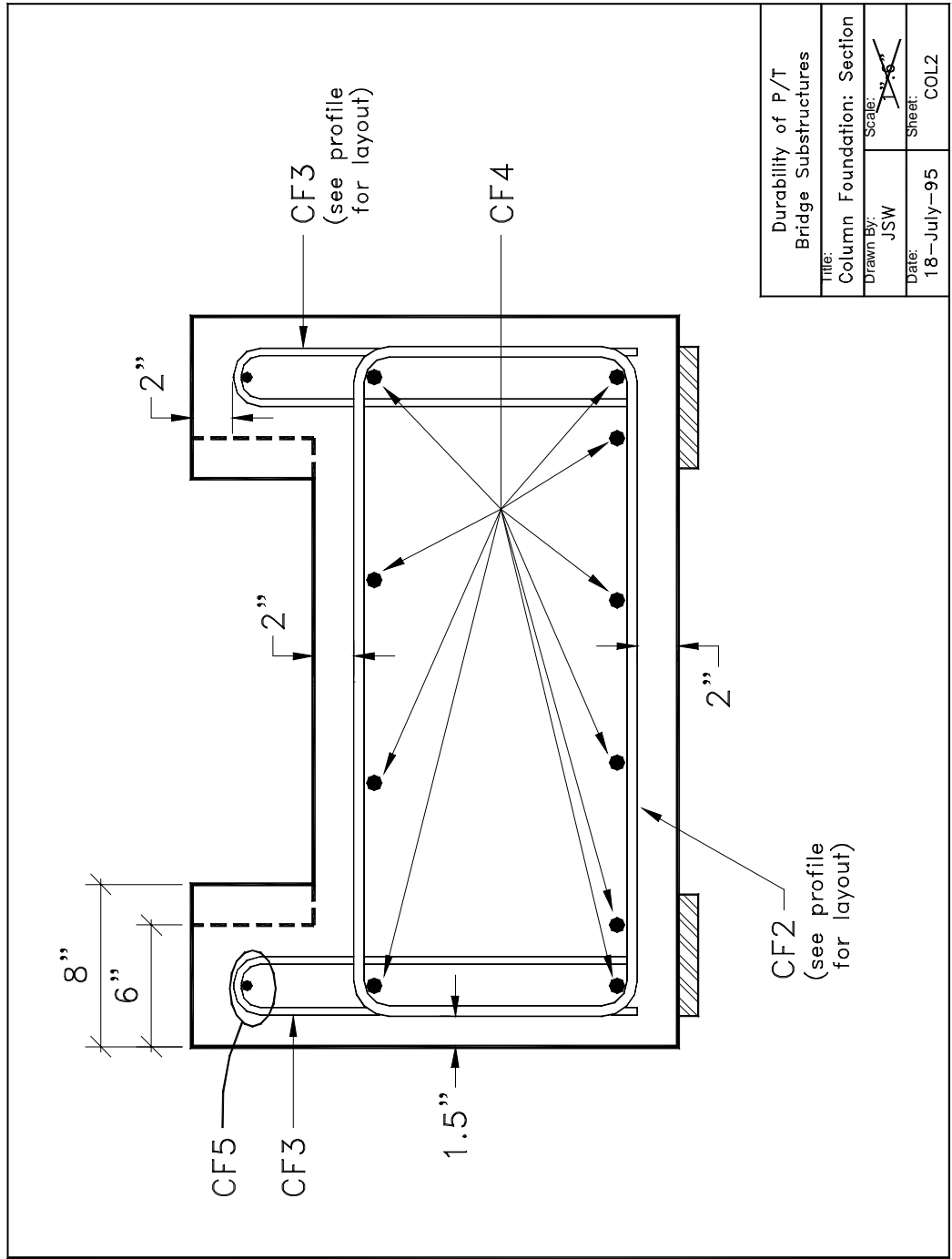
Figure B.2 - Sheet COL2: Column Foundation Section
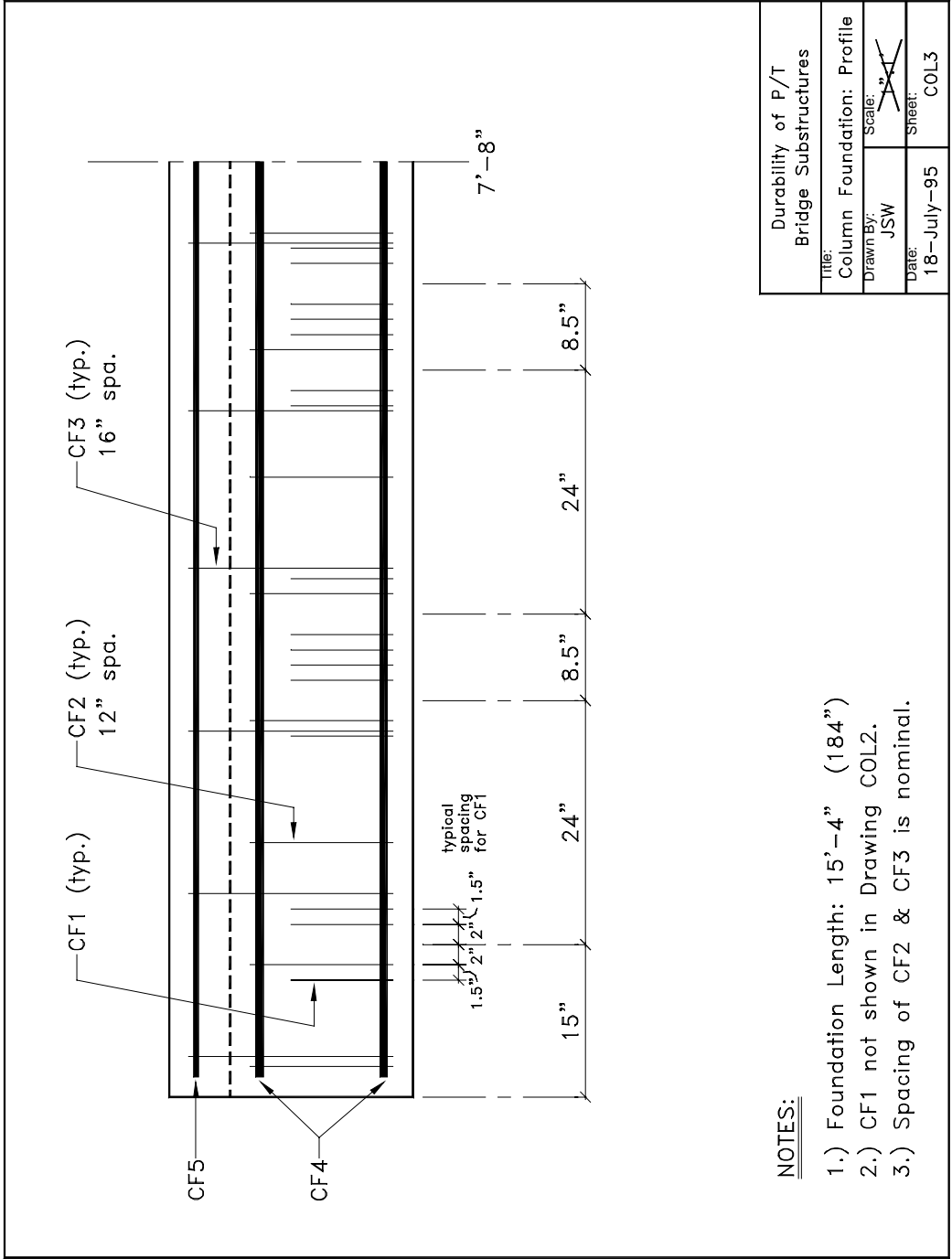
Figure B.3 - Sheet COL3: Column Foundation Profile
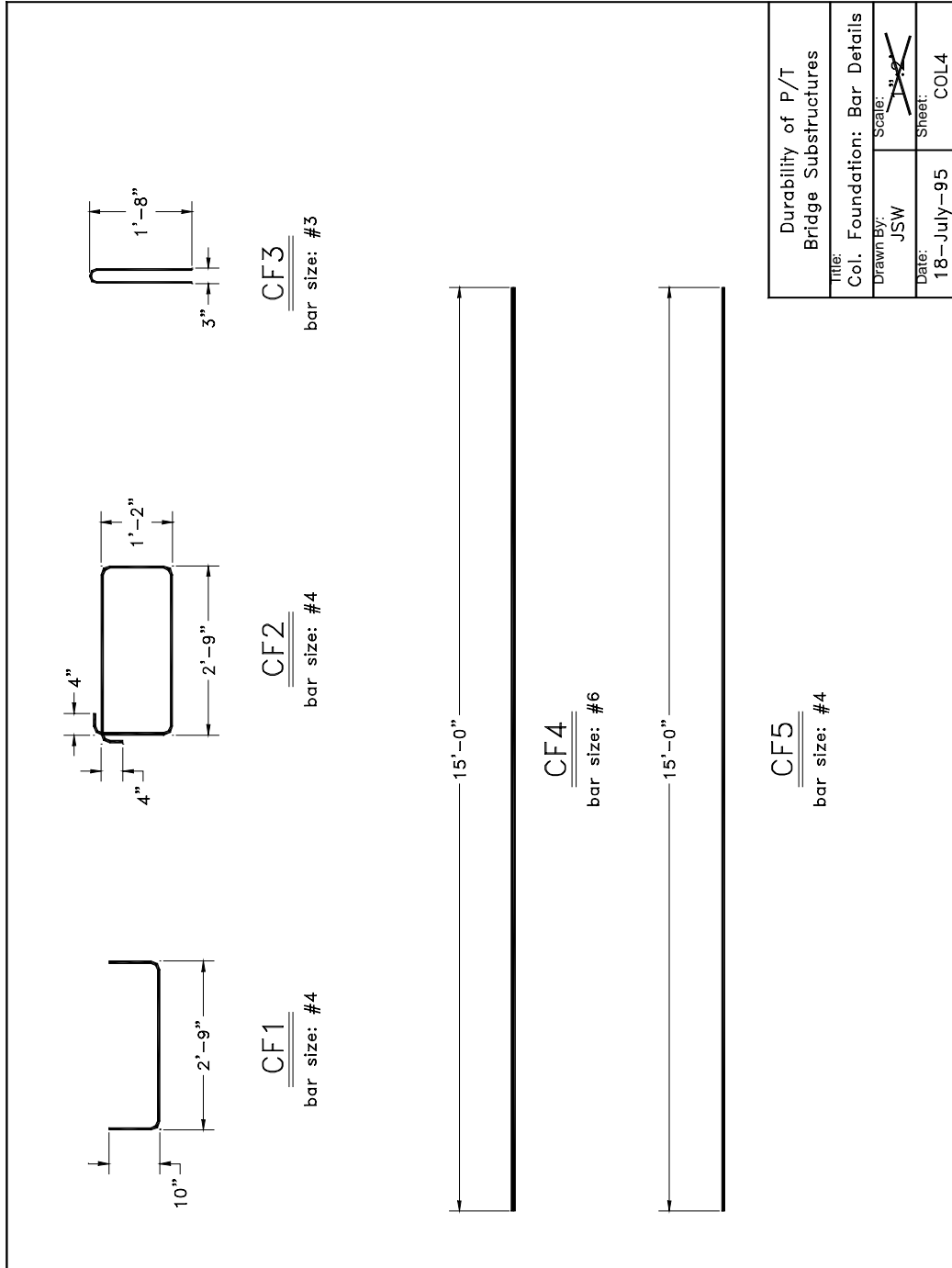
234

Figure B.4 - Sheet COL4: Column Foundation Bar Details
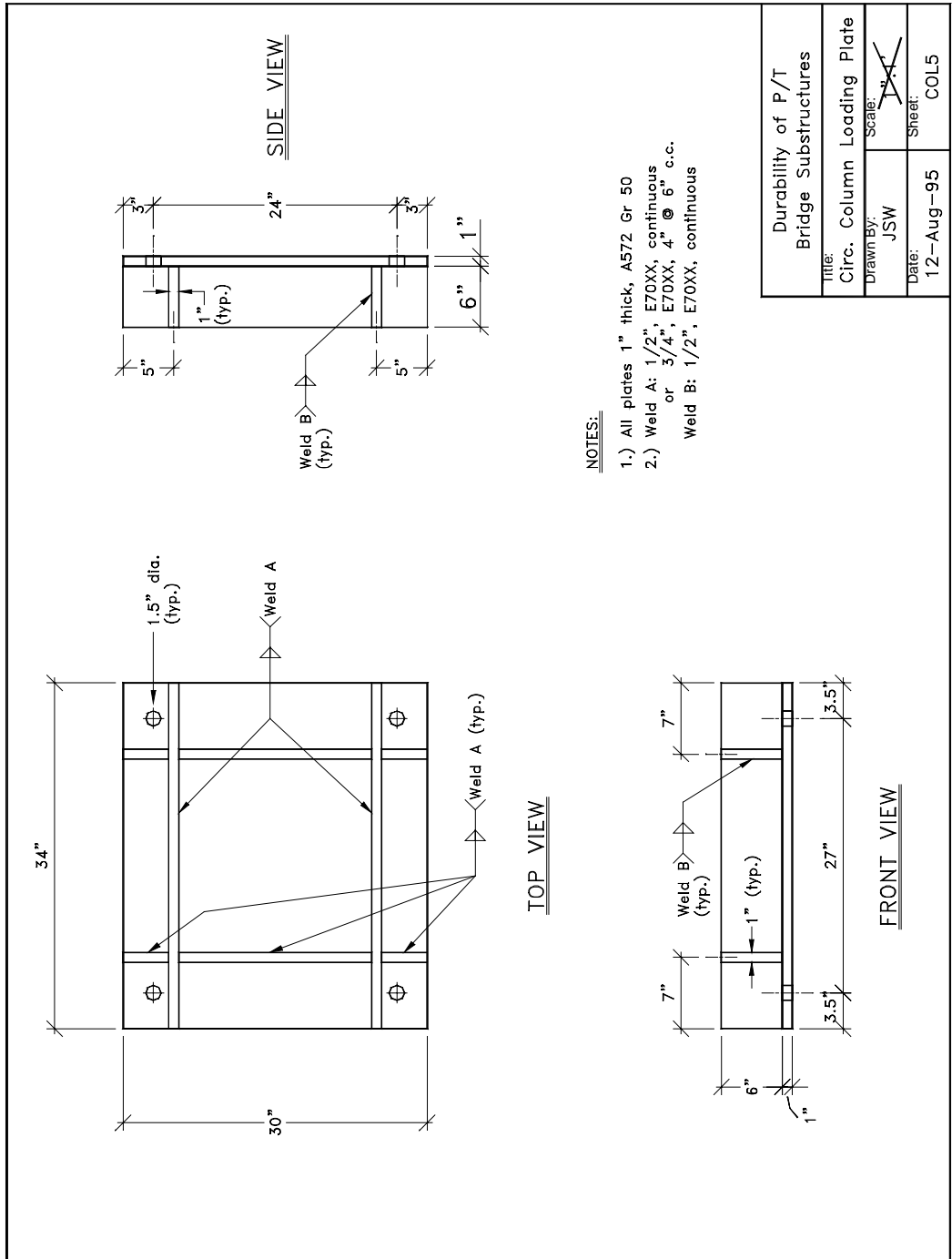
Figure B.5 - Sheet COL5: Column Loading Plate

SIDE VIEW

3" 24" 3"

1" (typ.)

Weld B
(typ.)

5" 5"

6" 1"

TOP VIEW

1.5" dia.
(typ.)

Weld A

Weld A (typ.)

34"

30"

FRONT VIEW

7" 3.5"

Weld B
(typ.)

1" (typ.)

27"

7" 3.5"

6" 1"

NOTES:

1.) All plates 1" thick, A572 Gr 50
2.) Weld A: 1/2", E70XX, continuous
    or 3/4", E70XX, 4" @ 6" c.c.
    Weld B: 1/2", E70XX, continuous

Durability of P/T
Bridge Substructures

Title:
Circ. Column Loading Plate

Drawn By: Scale:
JSW

Date: Sheet:
12-Aug-95   COL5

236

CF6
bar size: #6

3'-10 5/8"

1'-0"

CF7
bar size: #6

5'-10"

CZ
spiral size: #3

one flat turn
top & bottom

5'-9"

6" pitch

13 1/2"

Durability of P/T
Bridge Substructures

Title:
Circ. Column: Bar Details

Drawn By:
CJL (JSW)

Scale:

Date:
04-Aug-95

Sheet:
COL6

Figure B.6 - Sheet COL6: Column Reinforcing Bar Details

B.1   HALF-CELL POTENTIALS

Figures B.7-B.36 show half-cell potential readings for each of the column specimens through April of 1999 (998 days). Plots are given for each specimen for readings of individual bars at each level and also for average readings of bars at each level.
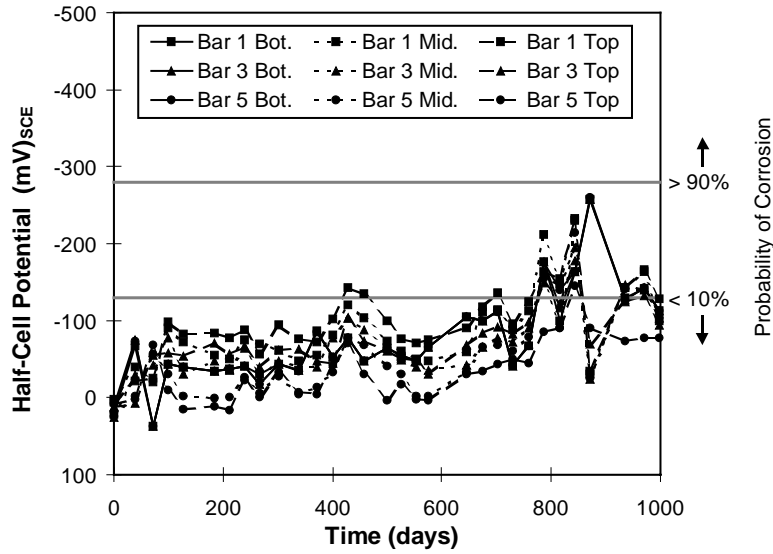
Figure B.7 - Half-Cell Potentials for Specimen NJ-TC-N
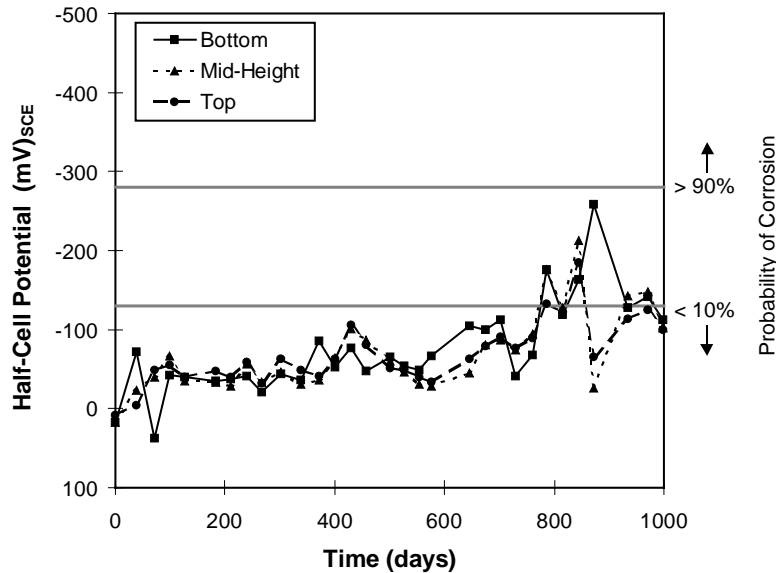
Figure B.8 - Half-Cell Potential Averages for Specimen NJ-TC-N
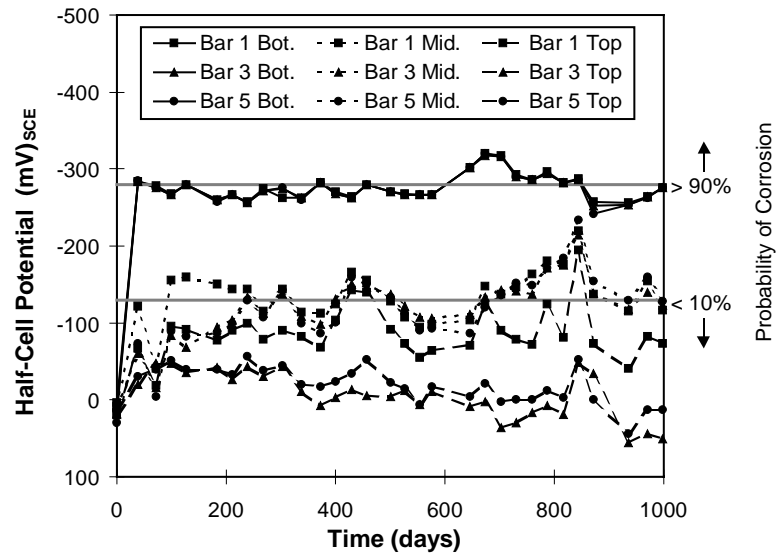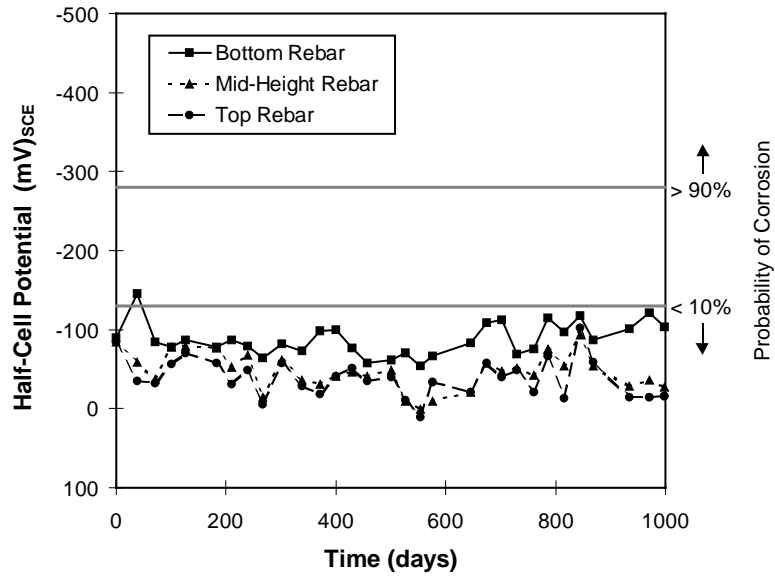
Figure B.9 - Half-Cell Potentials for Specimen DJ-TC-N
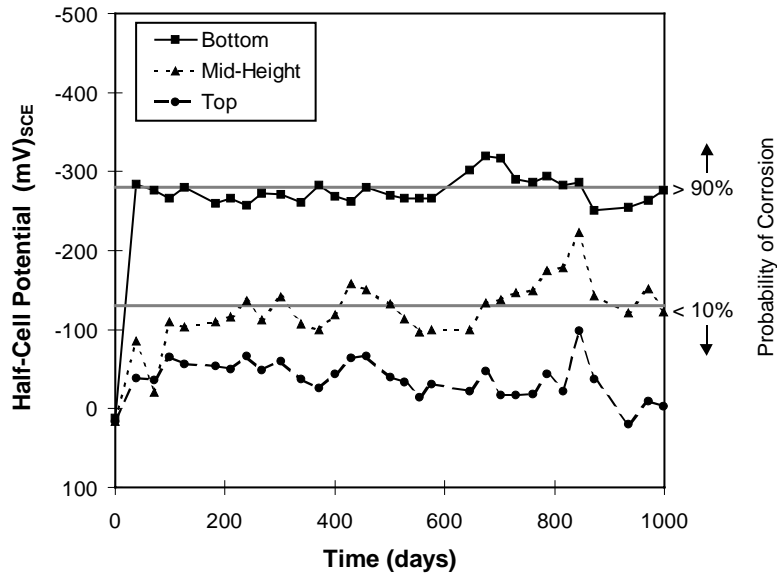
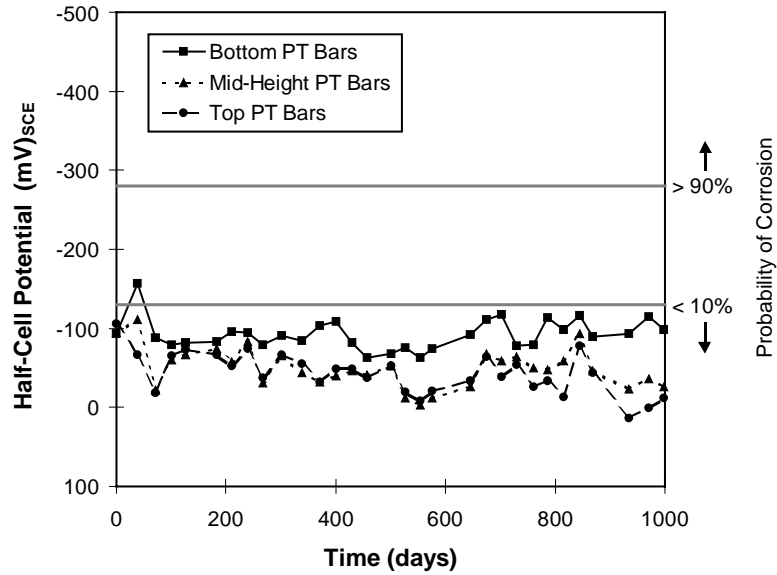*Figure B.10 - Half-Cell Potential Averages for Specimen DJ-TC-N*
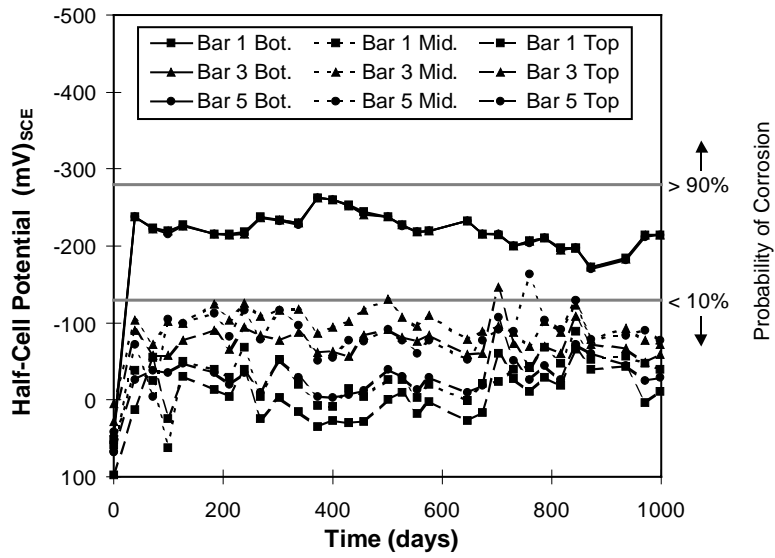
Figure B.11 - Half-Cell Potentials for Specimen DJ-FA-S
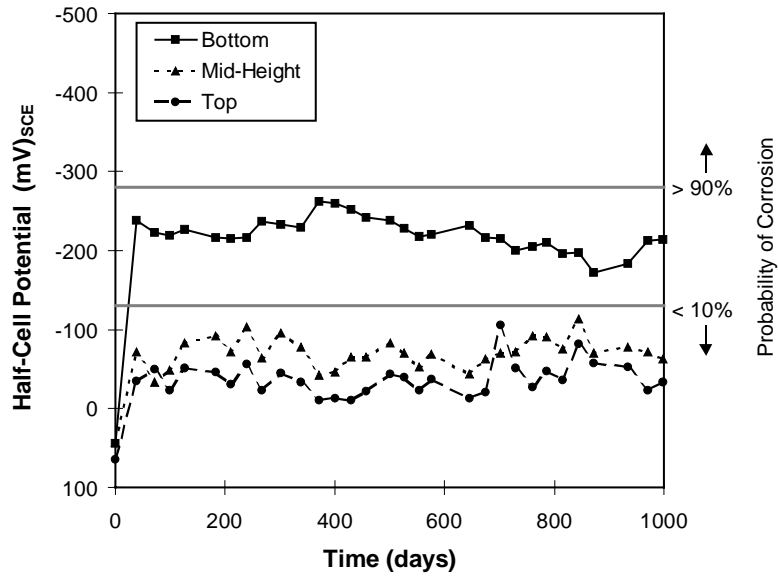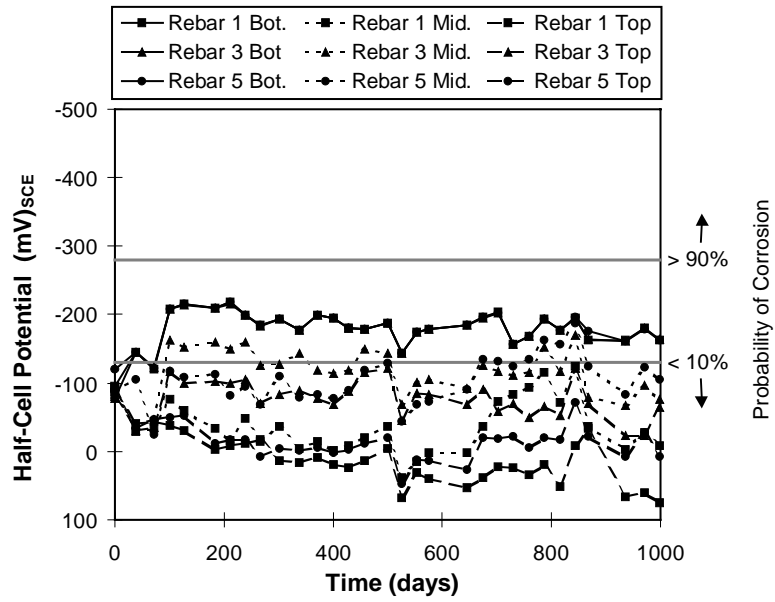

Figure B.12 - Half-Cell Potential Averages for Specimen DJ-FA-S
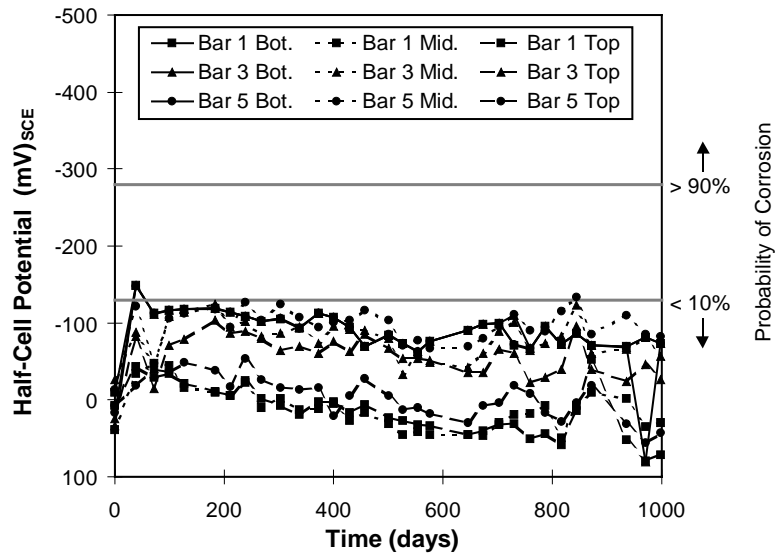
Figure B.13 - Half-Cell Potentials for Specimen DJ-TC-S
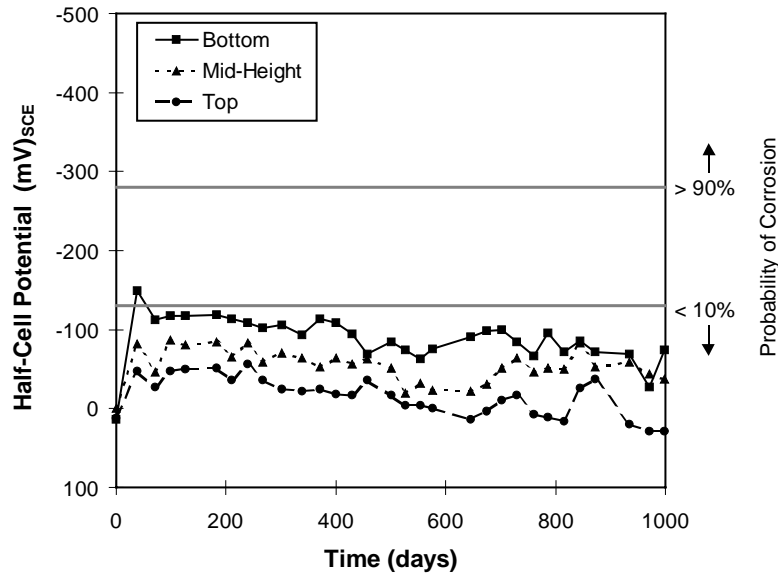
Figure B.14 - Half-Cell Potential Averages for Specimen DJ-TC-S
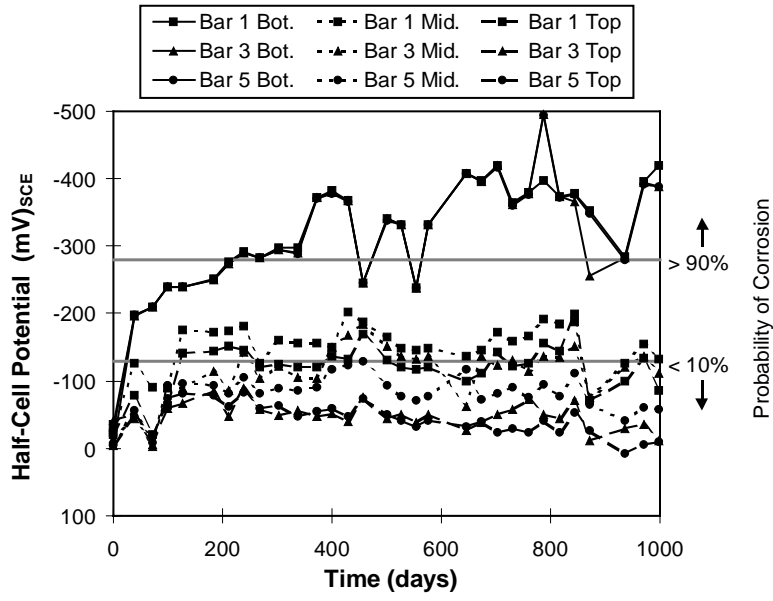
Figure B.15 - Half-Cell Potentials for Specimen NJ-TC-S
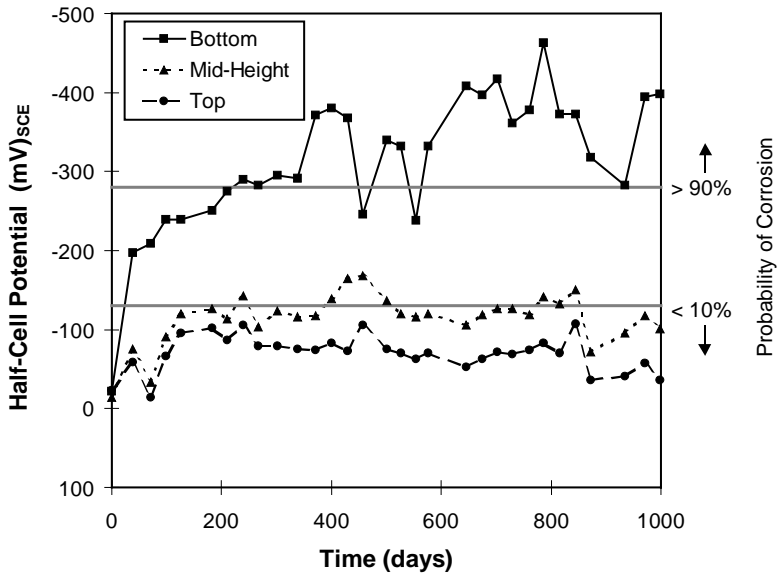
Figure B.16 - Half-Cell Potential Averages for Specimen NJ-TC-S
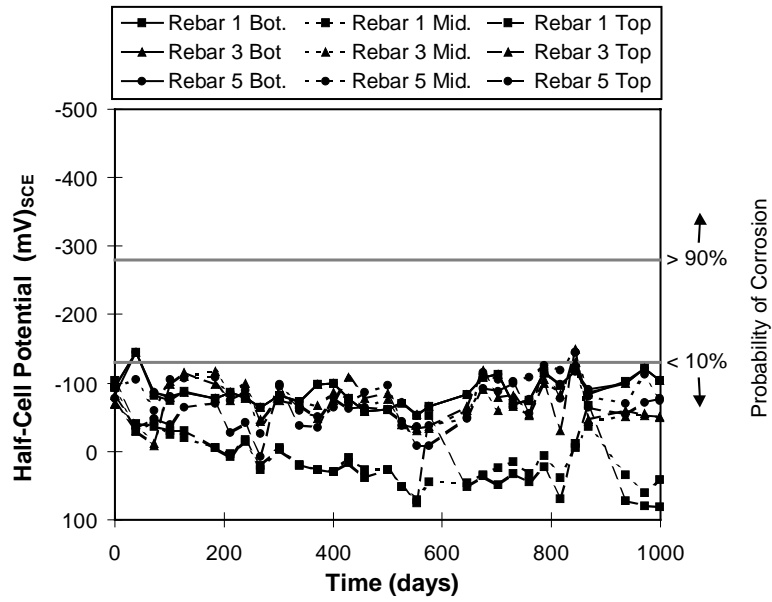
Figure B.17 - Half-Cell Potentials for Specimen PT-TC-N-PD, Rebar

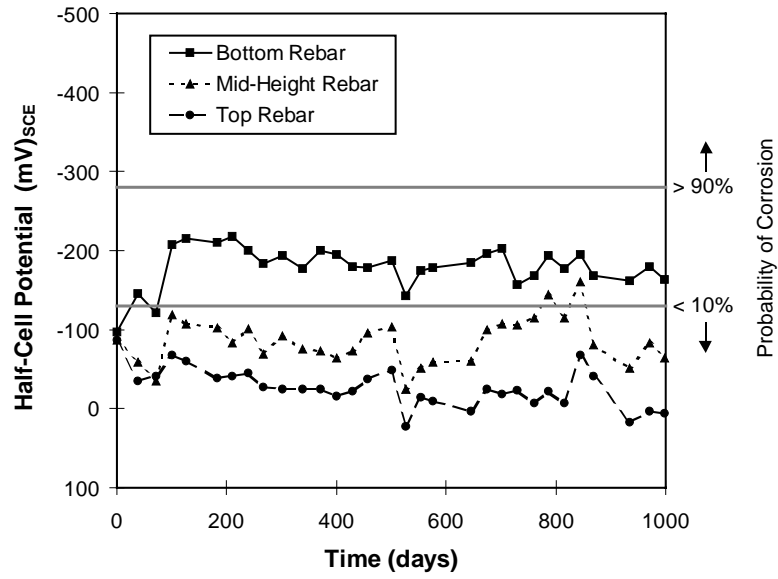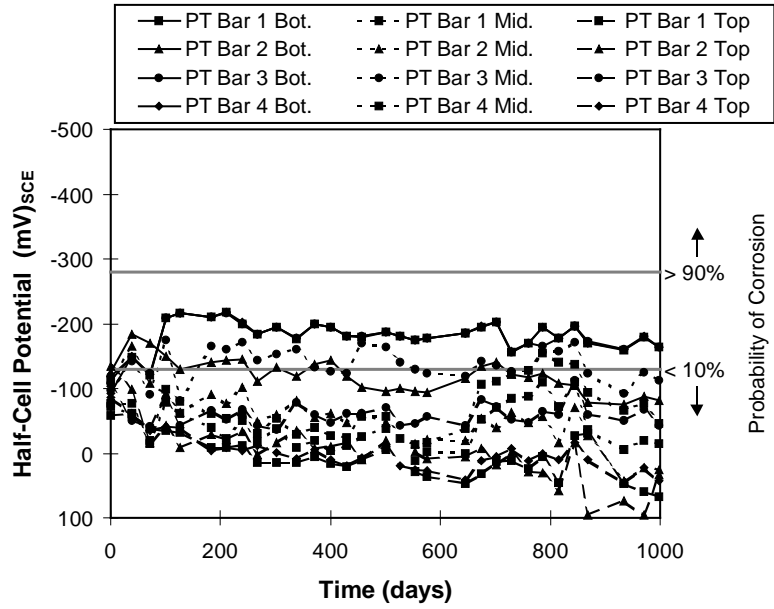*Figure B.18 - Half-Cell Potential Averages for Specimen PT-TC-N-PD, Rebar*
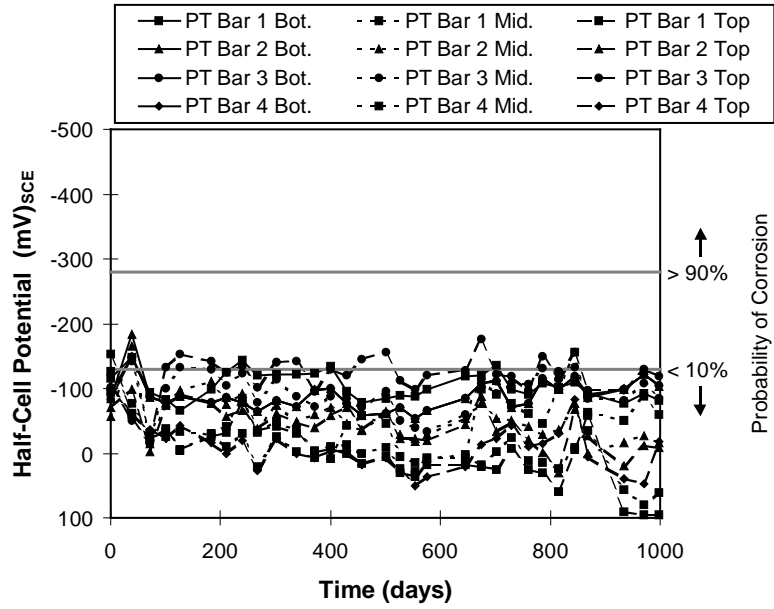
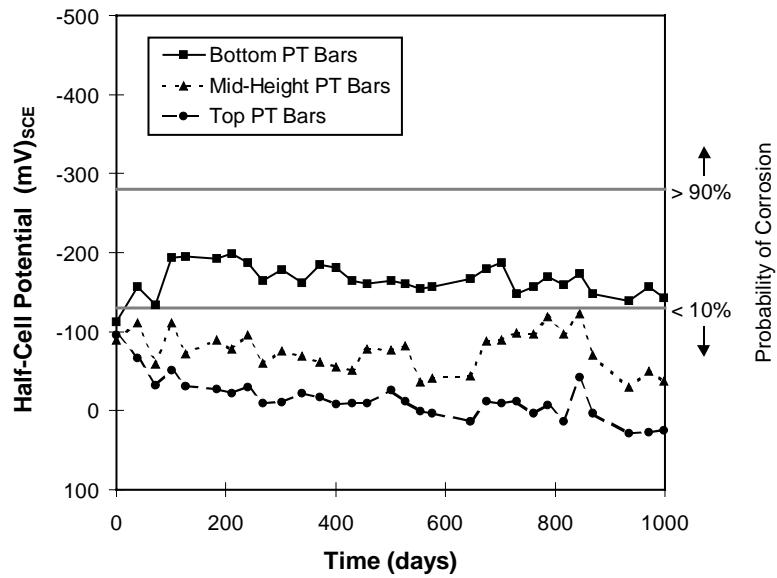*Figure B.19 - Half-Cell Potentials for Specimen PT-TC-N-PD, PT Bars*

Figure B.20 - Half-Cell Potential Averages for Specimen PT-TC-N-PD, PT Bars

Figure B.21 - Half-Cell Potentials for Specimen PT-TC-S-PD, Rebar

Figure B.22 - Half-Cell Potential Averages for Specimen PT-TC-S-PD, Rebar

245

Figure B.23 - Half-Cell Potentials for Specimen PT-TC-S-PD, PT Bars

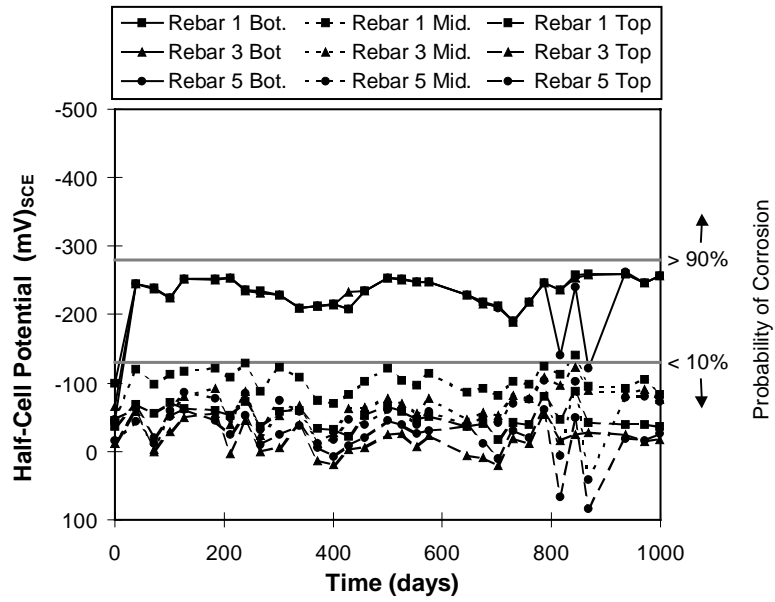*Figure B.24 - Half-Cell Potential Averages for Specimen PT-TC-S-PD, PT Bars*

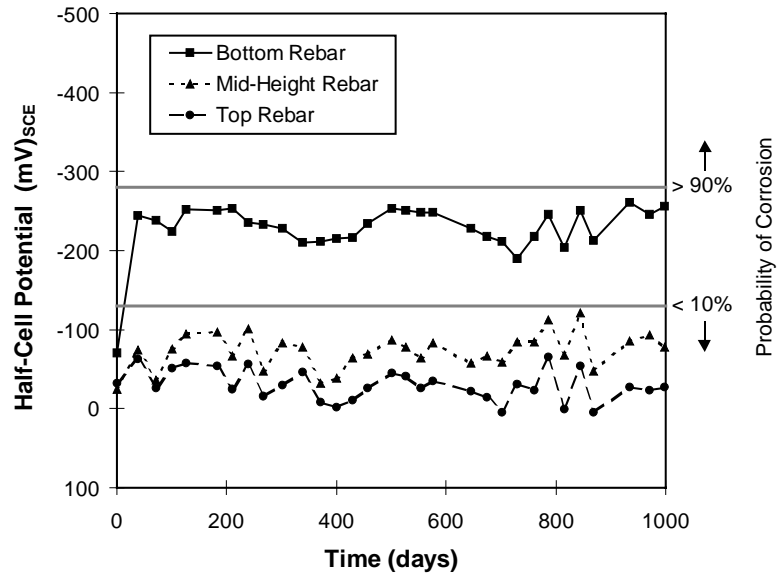*Figure B.25 - Half-Cell Potentials for Specimen PT-FA-S-PD, Rebar*

Figure B.26 - Half-Cell Potential Averages for Specimen PT-FA-S-PD, Rebar
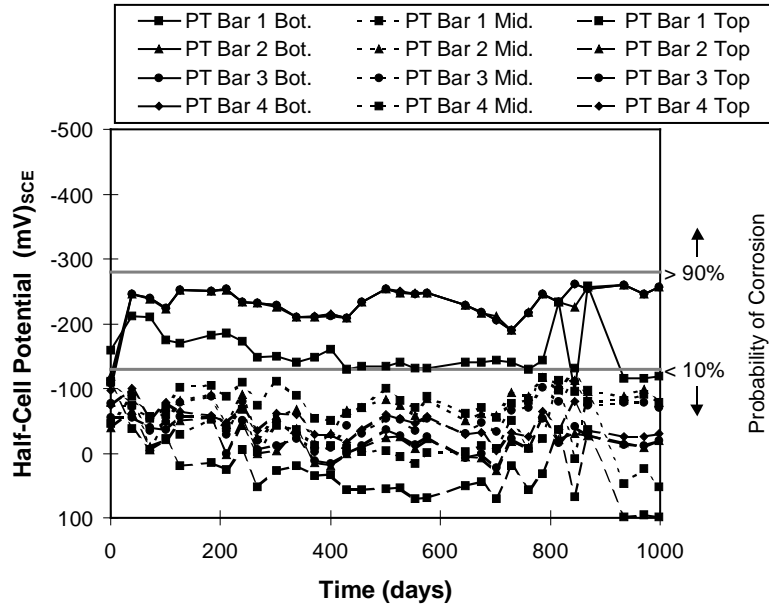
247

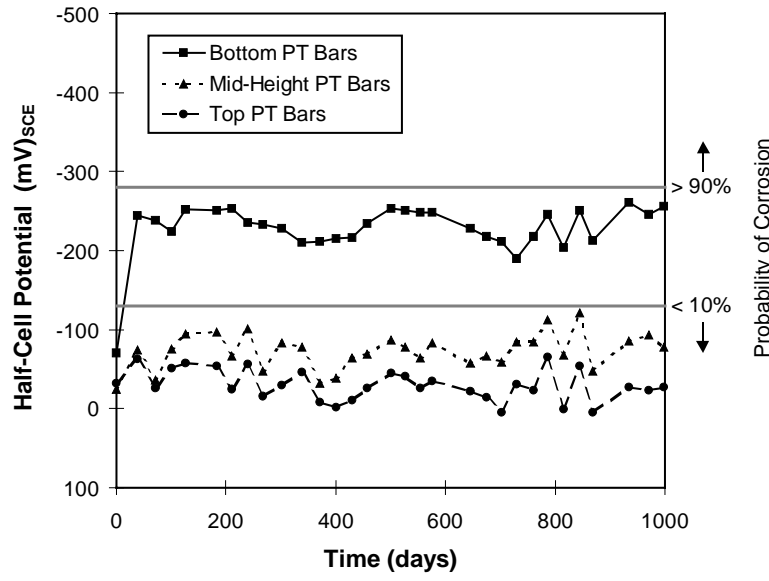*Figure B.27 - Half-Cell Potentials for Specimen PT-FA-S-PD, PT Bars*

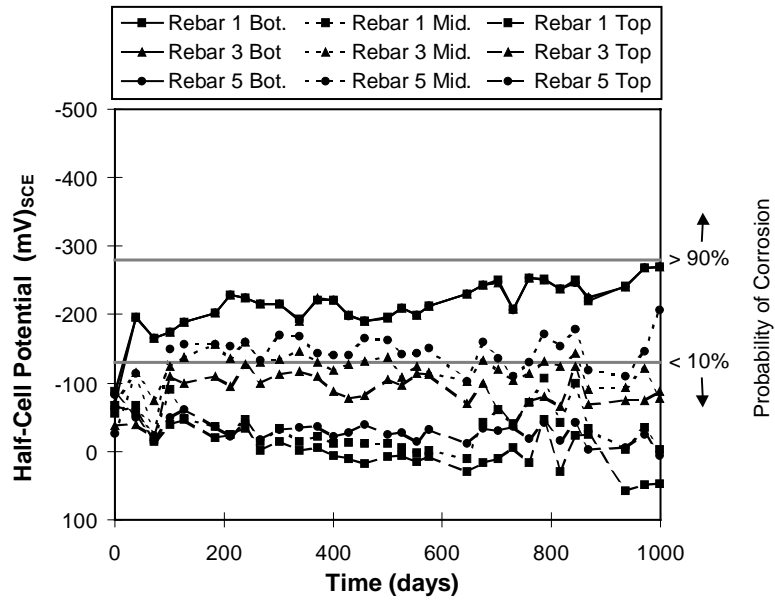*Figure B.28 - Half-Cell Potential Averages for Specimen PT-FA-S-PD, PT Bars*

248

Figure B.29 - Half-Cell Potentials for Specimen PT-TC-S-EB, Rebar

Figure B.30 - Half-Cell Potential Averages for Specimen PT-TC-S-EB, Rebar

Figure B.31 - Half-Cell Potentials for Specimen PT-TC-S-EB, PT Bars

Figure B.32 - Half-Cell Potential Averages for Specimen PT-TC-S-EB, PT Bars

250
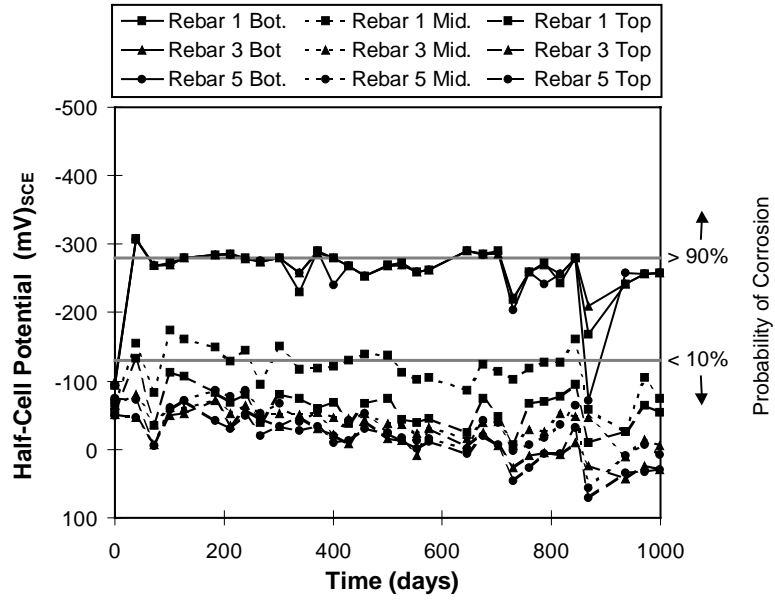
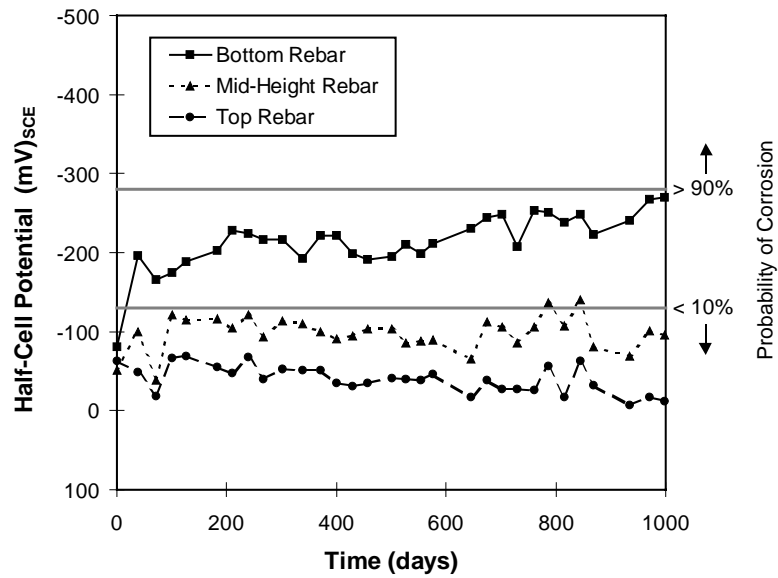*Figure B.33 - Half-Cell Potentials for Specimen PT-TC-S-GB, Rebar*

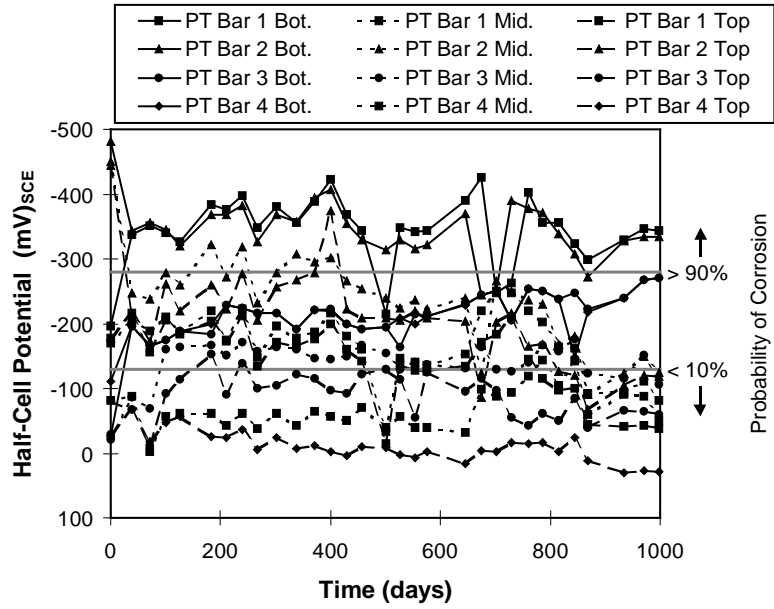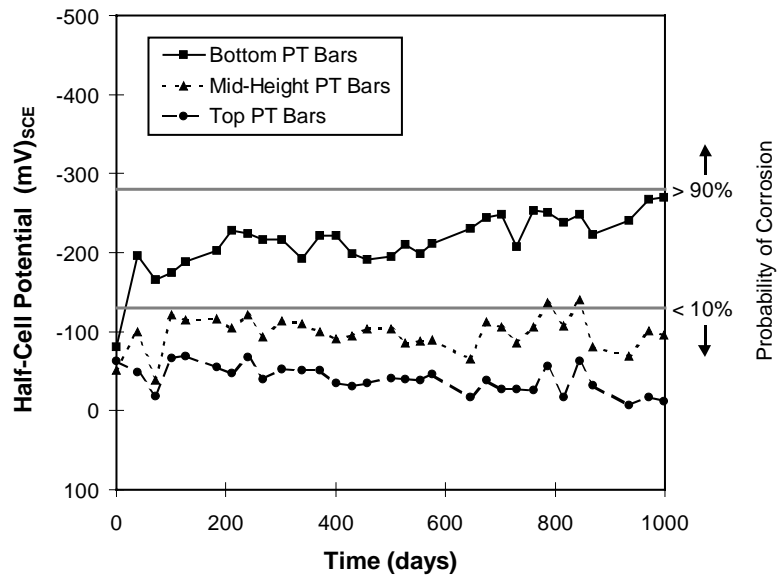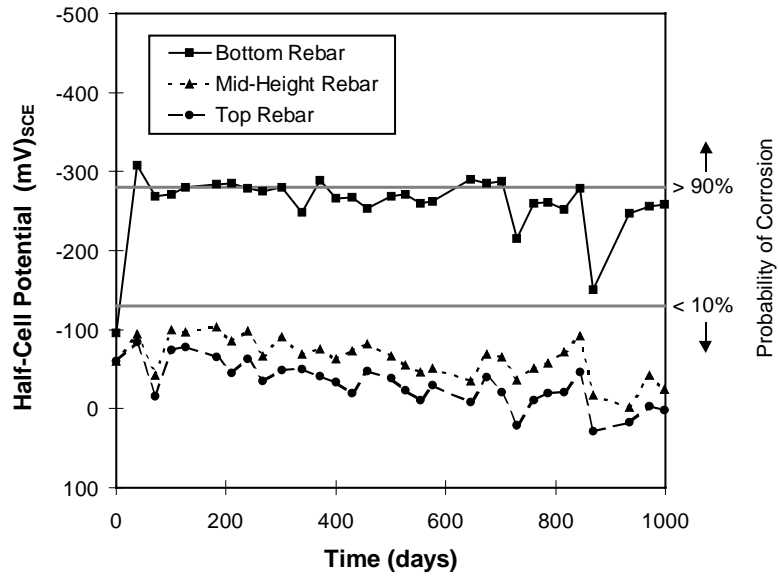*Figure B.34 - Half-Cell Potential Averages for Specimen PT-TC-S-GB, Rebar*
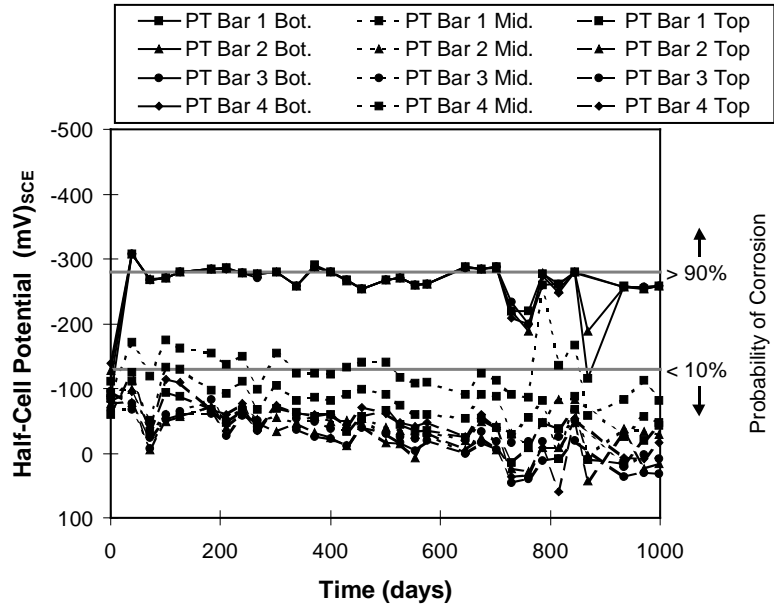
Figure B.35 - Half-Cell Potentials for Specimen PT-TC-S-GB, PT Bars
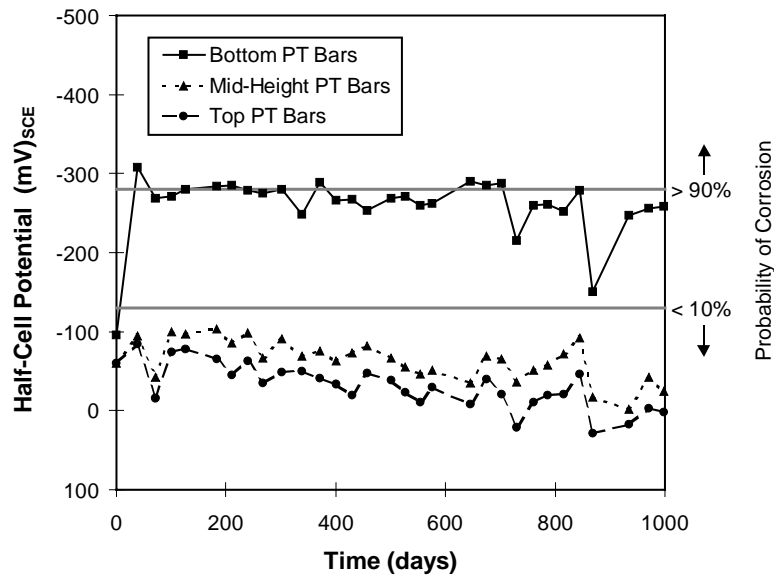
Figure B.36 - Half-Cell Potential Averages for Specimen PT-TC-S-GB, PT Bars

B.2 CHLORIDE PENETRATION PROFILES

Figures B.37-B.46 show the chloride penetration profiles for each of the columns sampled. Columns chosen represent concrete type, joint type, load level, and effect of dripper location.
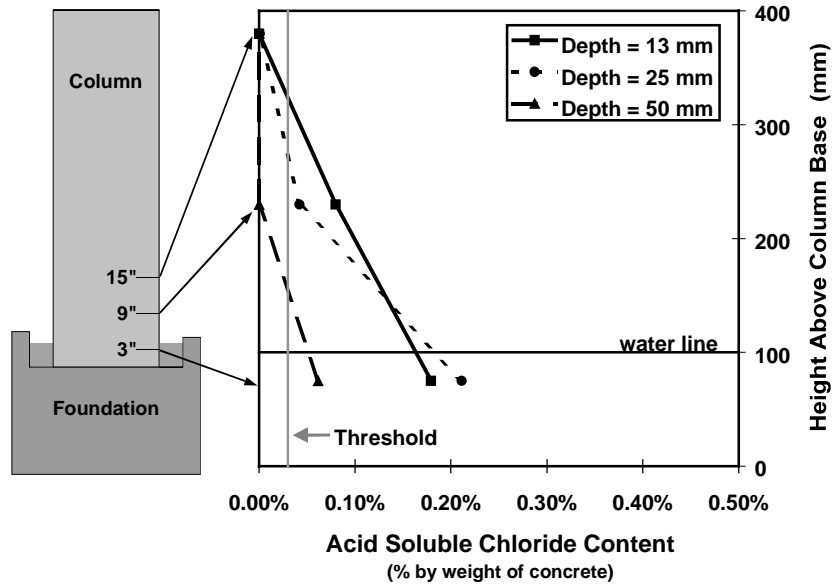
Figure B.37- Chloride Penetration at 20 Months, Specimen DJ-TC-S
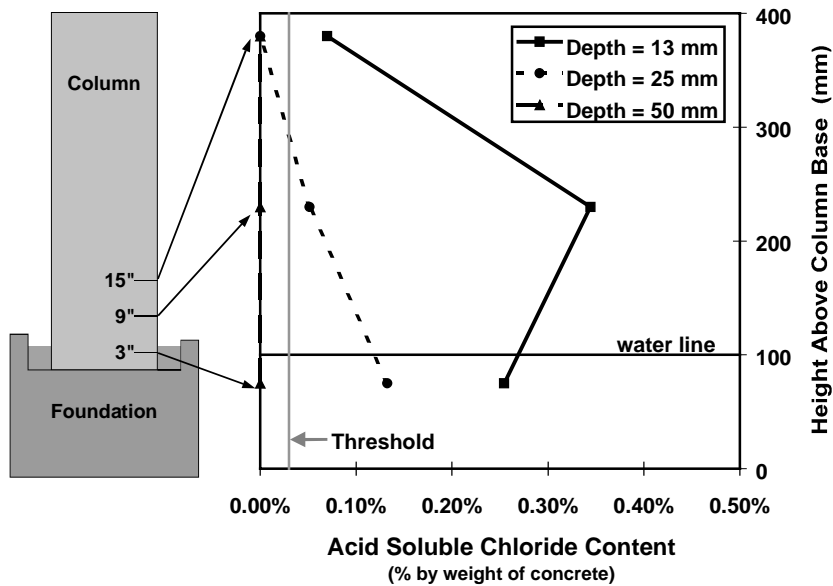
Figure B.38 - Chloride Penetration at 32 Months, Specimen DJ-TC-S
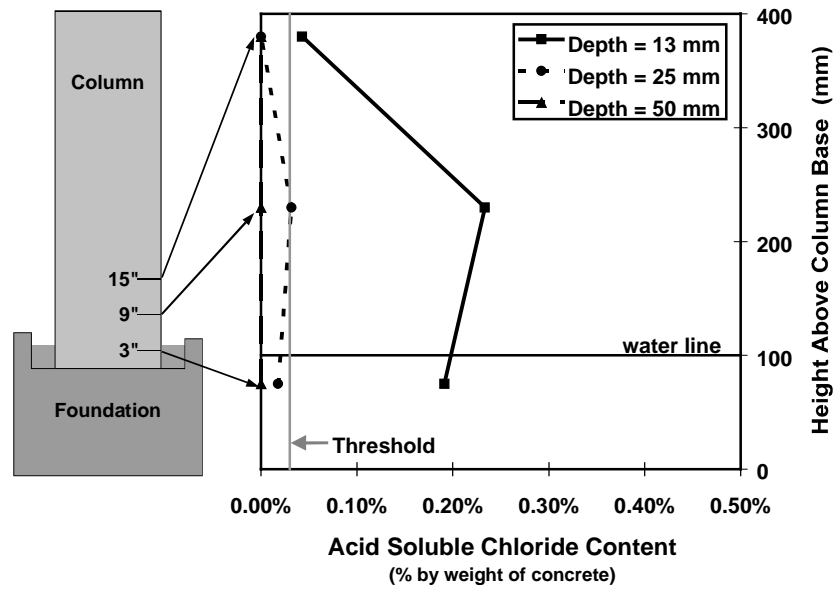
Figure B.39 - Chloride Penetration at 20 Months, Specimen PT-TC-S-PD

Figure B.40 - Chloride Penetration at 32 Months, Specimen PT-TC-S-PD

Figure B.41 - Chloride Penetration at 20 Months, Specimen NJ-TC-S

Figure B.42 - Chloride Penetration at 32 Months, Specimen NJ-TC-S

255

Figure B.43 - Chloride Penetration at 20 Months, Specimen DJ-FA-S

Figure B.44 - Chloride Penetration at 32 Months, Specimen DJ-FA-S

Figure B.45 - Chloride Penetration at 32 Months, Specimen DJ-TC-N

Figure B.46 - Chloride Penetration at 32 Months, Specimen DJ-TC-N Dripper Side

REFERENCES

1. **AASHTO**, *LRFD Bridge Construction Specifications*, 1st Edition, American Association of State Highway and Transportation Officials, Washington, D.C., 1998.

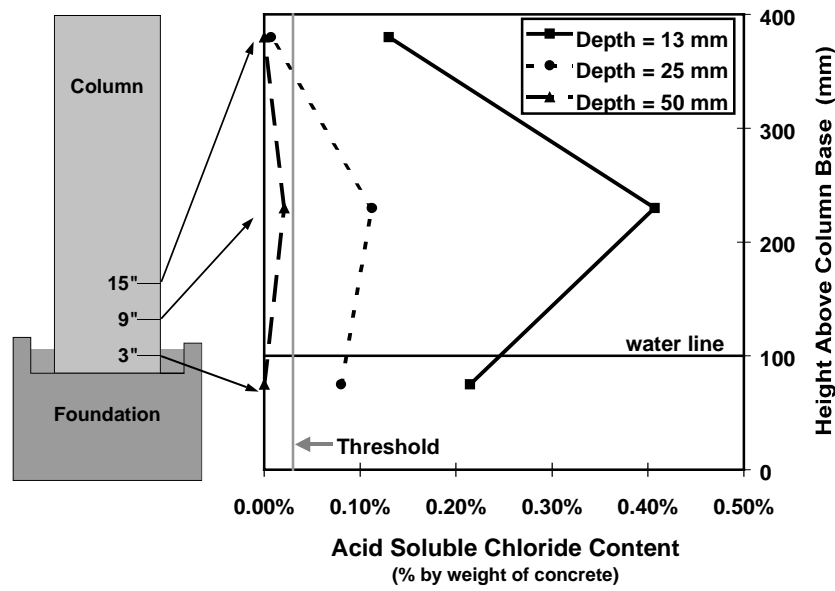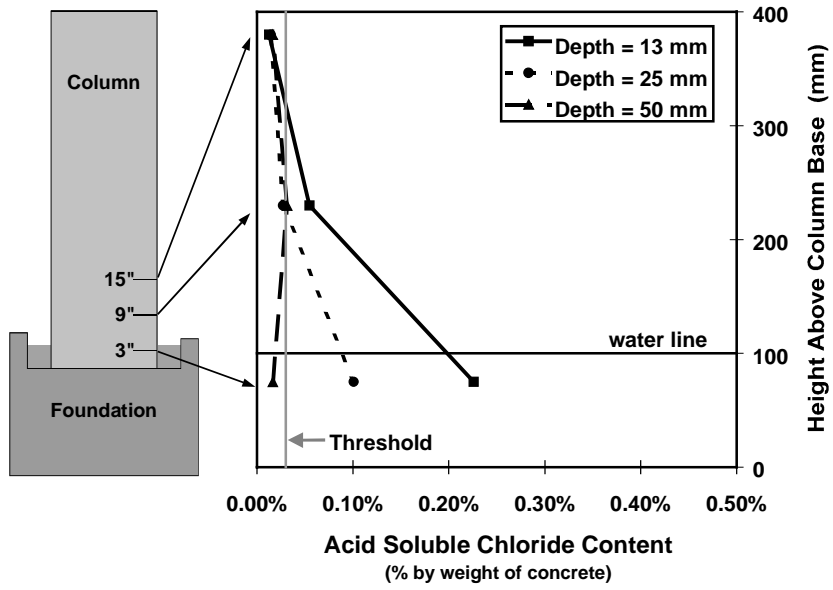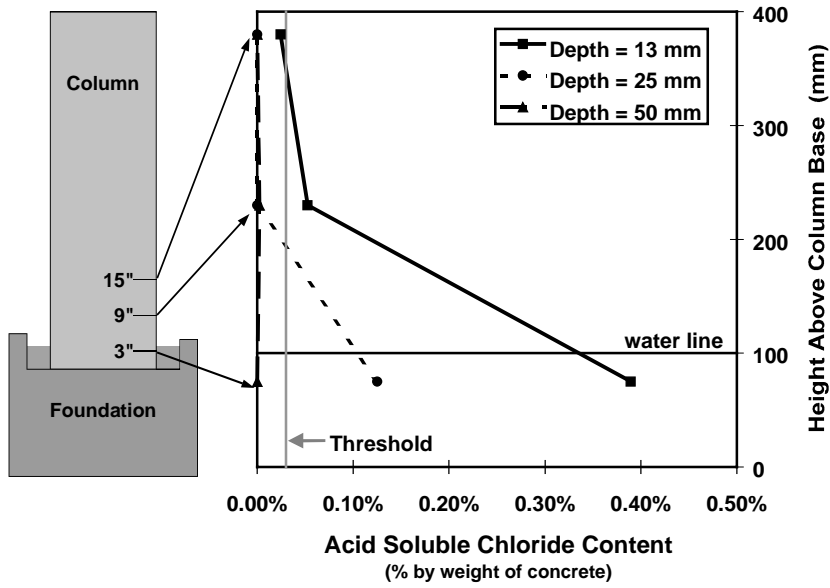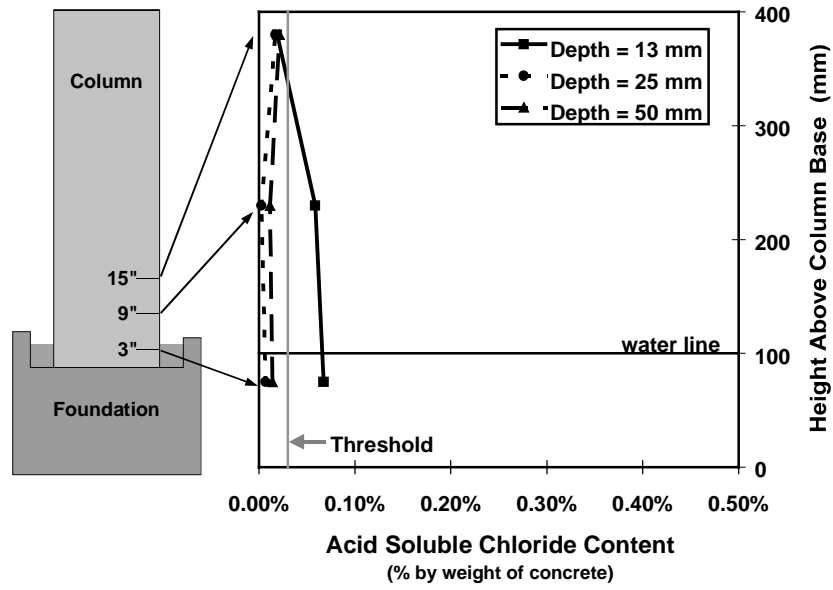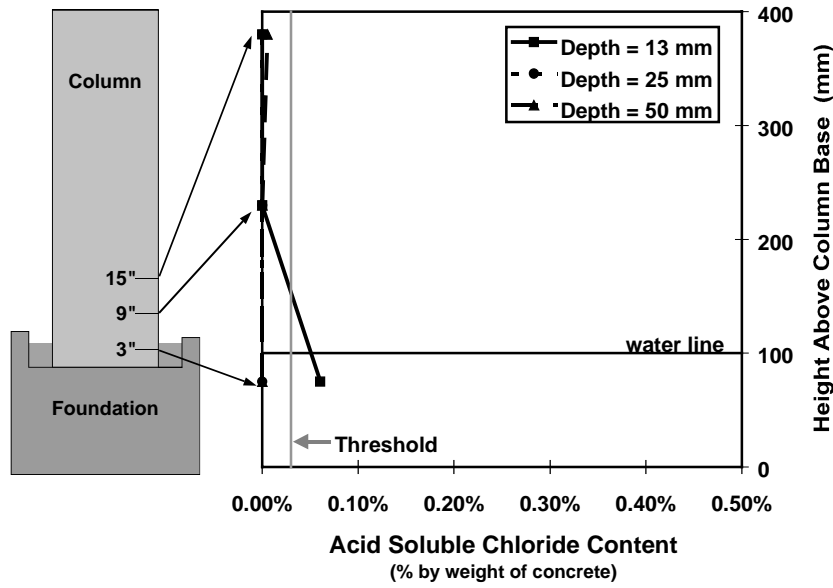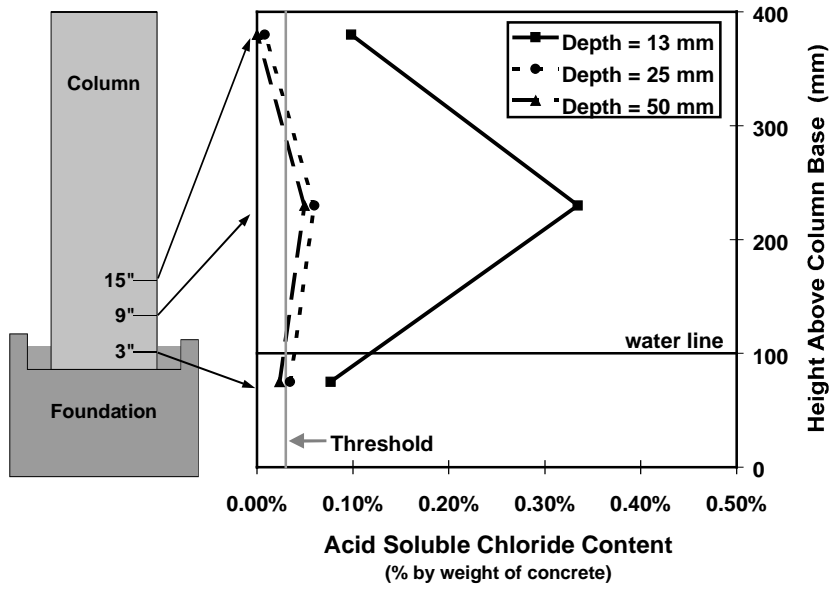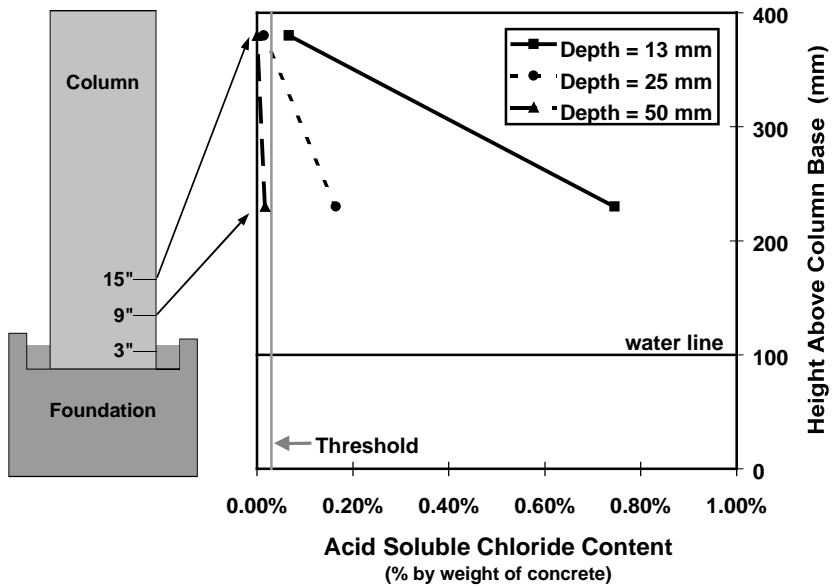2. **AASHTO**, *LRFD Bridge Design Specifications*, 2nd Edition, American Association of State Highway and Transportation Officials, Washington, D.C., 1998.

3. **AASHTO**, Standard Method of Test for Resistance of Concrete to Chloride Ion Penetration," AASHTO Designation T 259-80, American Association of State Highway and Transportation Officials, Washington, D.C., 1980.

4. **AASHTO**, Standard Method of Test for Sampling and Testing for Chloride Ion in Concrete and Concrete Raw Materials," AASHTO Designation T 260-94, American Association of State Highway and Transportation Officials, Washington, D.C., 1994.

5. **ACI Committee 209,** "Prediction of Creep, Shrinkage and Temperature Effects in Concrete Structures" (ACI 209R-92), American Concrete Institute, Detroit, Michigan, 1992.

6. **ACI Committee 222,** "Corrosion of Metals in Concrete," ACI 222R-96, American Concrete Institute, Detroit, Michigan, 1996.

7. **ACI Committee 222,** "Corrosion of Metals in Concrete," *American Concrete Institute Manual of Concrete Practice*, Part 1, Committee Report ACI 222R-96, American Concrete Institute, Detroit, MI 1997.

8. **ACI Committee 318,** "Building Code Requirements for Structural Concrete" (ACI 318-95), American Concrete Institute, Detroit, MI, 1995, 369 pp.

9. **ACI Committee 318**, *Building Code Requirements for Reinforced Concrete and Commentary (ACI 318-89)*, American Concrete Institute, Detroit, November 1989.

10. **Aitcin, P., Ballivy, G. and Parizeau, R.,** "The Use of Condensed Silica Fume in Grouts," *Innovative Cement Grouting,* SP-83, American Concrete Institute, 1984, pp. 1-18.

11. **American Society for Testing and Materials,** *Standard Test Method for Compressive Strength of Grouts for Preplaced-Aggregate Concrete in the Laboratory*, ASTM C942-86, Philadelphia, PA, 1986.

12. **American Society for Testing and Materials,** *Standard Test Method for Expansion and Bleeding of Freshly Mixed Grouts for Preplaced-Aggregate Concrete in the Laboratory*, ASTM C940-87, Philadelphia, PA, 1987.

13. **American Society for Testing and Materials,** *Standard Test Method for Flow of Grout for Preplaced-Aggregate Concrete (Flow Cone Method),* ASTM C939-94a, Philadelphia, PA, 1994.

14. **American Society for Testing and Materials,** *Standard Test Method for Half-Cell Potentials of Uncoated Reinforcing Steel in Concrete*, ASTM A876-87, Philadelphia, PA, 1987.

15. **Andrade, C., Castelo, V., Alonso, C. and Gonzalez, J.A.,** "The Determination of Corrosion Rate of Steel Embedded in Concrete by the Polarization Resistance and AC Impedance Methods," Corrosion Effect of Stray Currents and the Techniques for Evaluating Corrosion of Rebars in Concrete, ASTM STP 906, V. Chaker, Editor, American Society for Testing and Materials, Philadelphia, PA, 1986, pp. 43-63.

16. **Armstrong, S.D.,** "Design and Behavior of Large concrete Cantilever Overhangs with Combinations of Prestressed and Non-Prestressed Reinforcement," *Masters Thesis,* The University of Texas at Austin, August 1994.

17. **Armstrong, S.D., Salas, R.M., Wood, B.A., Breen, J.E. and Kreger, M.E.,** "Behavior and Design of Large Structural Bridge Pier Overhangs," Research Report 1364-1, Center for Transportation Research, The University of Texas at Austin, 1997, 272 pp.

18. **ASTM,** "Standard Specification for Coal Fly Ash and Raw or Calcined Natural Pozzolan for Use as a Mineral Admixture in Concrete," ASTM C618-98, American Society for Testing and Materials, Philadelphia, PA, 1998.

19. **ASTM**, "Standard Test Method for Half-Cell Potentials of Uncoated Reinforcing Steel in Concrete," ASTM C876-91, American Society for Testing and Materials, Philadelphia, Pa., 1991.

20. **ASTM**, "Standard Specification for Epoxy-Coated Reinforcing Steel Bars," ASTM A775-97, Philadelphia, PA, 1997.

21. **ASTM**, "Standard Test Method for Determining the Effects of Chemical Admixtures on the Corrosion of Embedded Steel Reinforcement in Concrete Exposed to Chloride Environments," ASTM G109-92, American Society for Testing and Materials, Philadelphia, PA, 1992.

22. **Batchelor, B.DEV., and El Shahawi, M.,** "A Review of Cracking of Partially Prestressed Concrete Members," *Canadian Journal of Civil Engineering*, Vol. 12, 1985, pp. 645-652.

23. **Berke, N.S. et al.,** "Protection Against Chloride-Induced Corrosion," *Concrete International: Design and Construction*, Vol. 10, No. 12, December 1998, pp. 45-55.

24. **Berke, N.S.,** "Corrosion Inhibitors in Concrete," *Concrete International,* July 1991, pp. 24-27.

25. **Berke, N.S.,** "Resistance of Microsilica Concrete to Steel Corrosion, Erosion and Chemical Attack," *Fly Ash, Silica Fume, Slag, and Natural Pozzolans in Concrete: Proceedings of the Third International Conference,* Trondheim, Norway, SP-114, V.M. Malhotra, Ed., 1989, pp. 861-886.

26. **Berke, N.S.,** "The Use of Anodic Polarization to Determine the Effectiveness of Calcium Nitrite as an Anodic Inhibitor," *STP 906,* American Society for Testing and Materials, Philadelphia, PA, 1988.

27. **Berke, N.S., Shen, D.F. and Sundberg, K.M.,** "Comparison of Current Interruption and Electrochemical Impedance Techniques in the Determination of Corrosion Rates of Steel in Concrete," *The Measurement and Correction of Electrolyte Resistance in Electrochemical Tests, STP 1056,* L.L. Scribner and S.R. Taylor, Eds, American Society for Testing and Materials, Philadelphia, PA, 1990, pp. 191-201.

28. **Bonomo, R.J.,** "Permanent Ground Anchors Using Epoxy Coated Strand," *ADSC,* March-April 1984, pp. 15-21.

29. **Breen, J.E., Burdet, O., Roberts, C., Sanders, D. and Wollman, G.,** "Anchorage Zone Reinforcement for Post-Tensioned Concrete Girders," NCHRP Report 356, Transportation Research Board, Washington, D.C., 1994, 204pp.

30. **Cady, P., and Gannon, E.,** "Condition Evaluation of Concrete Bridges Relative to Reinforcement Corrosion, Volume 8: Procedure Manual," SHRP-S/FR-92-330, Strategic Highway Research Program, Washington, D.C., 1992, 124 pp.

31. **CEB-FIP,** *CEB-FIP Model Code for Concrete Structures 1990*, Bulletin D'Information No. 213/214, Comité Euro-International du Béton, Lausanne, May 1993, 437 pp.

32. **CEB-FIP,** *Model Code for Concrete Structures: CEB-FIP International Recommendations*, 3rd Edition, Comité Euro-International du Béton, Paris, 1978, 348 pp.

33. **Clear, K.,** "Measuring the Rate of Corrosion of Steel in Field Concrete Structures," Transportation Research Record 1211, pp. 28-37, 1989.

34. **Collins M.P., and Mitchell, D.,** *Prestressed Concrete Structures,* Prentice Hall, NJ, 1991.

35. **CONCORR, Inc.,** "FHWA – SHRP Showcase: Assessment of Physical Condition of Concrete Bridge Components," Federal Highway Administration, Washington, D.C., July 1996.

36. **Diederichs, U. and Schutt, K.,** "Silica Fume Modified Grouts for Corrosion Protection of Post-Tensioning Tendons," *Fly Ash, Silica Fume, Slag, and Natural Pozzolans in Concrete: Proceedings of the Third International Conference,* Trondheim, Norway, SP-114, V.M. Malhotra, Ed., 1996, pp. 1173-1195.

37. **Domone, P.L. and Jefferis, S.A.,** *Structural Grouts,* Blackie Academic & Professional, London, 1994.

38. **Domone, P.L. and Tank, S.B.,** "Use of Condensed Silica Fume in Portland Cement Grouts," *Fly Ash, silica Fume, Slag, and Natural Pozzolans in Concrete: Proceedings, Second International Conference,* Madrid, Spain, SP 91-61, V.M. Malhotra, Ed., 1986, pp. 1232-1260.

39. **Ehrhardt, W.C.,** "IR Drop in Electrochemical Corrosion Studies – Part I: Basic Concepts and Estimates of Possible Measurement Errors," *The Measurement and Correction of Electrolyte Resistance in Electrochemical Tests, STP 1056,* L.L. Scribner and S.R. Taylor, Eds., American Society for Testing and Materials, Philadelphia, PA, 1990, pp. 27-58.

40. **Elsener, B., and Böhni, H.,** "Potential Mapping and Corrosion of Steel in Concrete," Corrosion Rates of Steel in Concrete, ASTM STP 1065, Berke, N.S., Chaker, V., and Whiting, D., Editors, American Society for Testing and Materials, Philadelphia, PA, 1990, pp. 143-156.

41. **Fidjestol, P.,** "Reinforcement Corrosion and the Use of CSF-Based Additives," *Concrete Durability: Katherine and Bryant Mather International Conference,* SP-100, J.M. Scanlon, Ed., 1987, pp. 1445-1458.

42. **Flis, J., Sehgal, A., Li, D., Kho, Y, Sabol, S., Pickering, H., Osseo-Asare, K, and Cady, P.D.,** "Condition Evaluation of Concrete Bridges Relative to Reinforcement Corrosion, Volume 2: Method for Measuring the Corrosion Rate of Reinforcing Steel," SHRP-S/FR-92-104, Strategic Highway Research Program, Washington, D.C., 1992, 105 pp.

43. **Fontana, M.G.,** *Corrosion Engineering*, McGraw-Hill Book Company, New York, 1986.

44. **Freeman, R.B. and Carrasquillo, R.L.,** "Production of Sulfate-Resistant Concrete Containing High-Calcium Fly Ash and Sodium Sulfate Admixture," *Fly Ash, Silica Fume, Slag, and Natural Pozzolans in Concrete: Proceedings, Fifth International Conference*, Milwaukee, Wisconsin, SP 153-9, V.M. Malhotra, Ed., 1995, pp. 153-175.

45. **Gautefall, O. and Havdahl, J.,** "Effect of Condensed Silica Fume on the Mechanism of Chloride Diffusion into Hardened Cement Paste," *Fly Ash, Silica Fume, Slag, and Natural Pozzolans in Concrete: Proceedings, Third International Conference,* Trodheim, Norway, SP-114, V.M. Malhotra, Ed., 1989, pp. 849-860.

46. **Gergely, P. and Lutz, L.A.,** "Maximum Crack Width in Reinforced Concrete Flexural Members," *Causes, Mechanism, and Control of Cracking in Concrete,* SP 20, American Concrete Institute, Detroit, MI, 1968, pp. 87-117.

47. **Ghali, A., and Favre, R.**, *Concrete Structures: Stresses and Deformations,* 2nd. Edition, E & FN Spon, London, 1994. (see also Ghali, A., "Stress and Strain Analysis in Prestressed Concrete: A Critical Review," *PCI Journal*, Vol. 34, No. 6, November-December 1989, pp. 80-97.)

48. **Gross, S.P., "**Field Performance of Prestressed High Performance Concrete Highway Bridges in Texas," *Ph.D. Dissertation*, The University of Texas at Austin, December 1998.

49. **Hamilton, H.R., III,** "Investigation of Corrosion Protection Systems for Bridge Stay Cables," *Ph.D. Dissertation,* The University of Texas at Austin, September 1995.

50. **Henriksen, C.F., Knudsen, A. and Braestrup, M.W.,** "Cable Corrosion: Undetected?" *Concrete International,* October 1998, pp. 69-72.

51. **Hope, B.B. and Ip, A.K.,** "Corrosion Inhibitors for Use in Concrete," *ACI Materials Journal,* November-December 1989, pp. 602-608.

52. **Hope, B.B. and Ip, A.K.,** "Grout for Post-Tensioning Ducts," *ACI Materials Journal,* July-August 1988, pp. 234-240.

53. **Ikawa, K., Ishii, K., Fukute, T. and Seki, H.,** "Behavior and Protection of Hydrogen Embrittlement on Tendons of PC Members," *Concrete in Marine Environment: Proceedings of the Third CANMET/ACI International Conference,* St. Andrews by-the-Sea, Canada, SP-163, V.M. Malhotra, Ed., 1996, pp. 253-273.

54. **Isecke, B.,** "Collapse of the Berlin Congress Hall Prestressed Concrete Roof," *Materials Performance*, December 1982, pp. 36-39.

55. **Jones, D.A.,** *Principles and Prevention of Corrosion,* 2nd Edition, Prentice Hall, Inc., Upper Saddle River, NJ, 1996.

56. **Jones, D.A.,** *Principles and Prevention of Corrosion,* Mac Millan Publishing Company, New York, 1992.

57. **Kahhaleh, K.Z.,** "Corrosion Performance of Epoxy-Coated Reinforcement," Doctor of Philosophy Dissertation, The University of Texas at Austin, May 1994.

58. **Klingner, R.,** "Advanced Reinforced Concrete Structures," Course Notes CE383N, The University of Texas at Austin, 1994.

59. **Koester, B.D.,** "Evaluation of Cement Grouts for Strand Protection Using Accelerated Corrosion Tests," *Masters Thesis*, The University of Texas at Austin, December 1995.

60. **Kosmatka, S.H. and Panarese, W.C.,** *Design and Control of Concrete Admixtures, Thirteenth Edition,* Portland Cement Association, Skokie, IL, 1988.

61. **Lankard, D.R., Thompson, N., Sprinkel, M.M. and Virmani, Y.P.,** "Grouts for Bonded Post-Tensioned Concrete Construction: Protecting Prestressing Steel from Corrosion," *ACI Materials Journal,* September-October 1993, pp. 406-414.

62. **Larosche, C.J.,** "Test Method for Evaluating Corrosion Mechanisms in Standard Bridge Columns," Master's Thesis, The University of Texas at Austin, August 1999.

63. **Lin, T.Y. and Burns, N.H.,** *Design of Prestressed Concrete Structures, Third Edition,* John Wiley and Sons, New York, 1981.

64. **Mindness, S. and Young, J.F.,** *Concrete,* Prentice-Hall, Englewood Cliffs, NJ, 1981.

65. **Montani, R.,** "Concrete Repair and Protection with Corrosion Inhibitor*," Proceedings of the Seventh International Conference on Structural Faults and Repair,* Volume 2, Edinburgh, Scotland, 1997, pp. 253-264.

66. **Mott MacDonald,** *Sika Ferrogard® 901 & 903 Corrosion Inhibitors: Evaluation of Test Programme,* August 1996.

67. **Nmai, C.K.,** "Corrosion-Inhibiting Admixtures: Passive, Passive-Active versus Active Systems," *Advances in Concrete Technology: Proceedings of the Second CANMET/ACI International Symposium,* Las Vegas, Nevada, SP-154, V.M. Malhotra, Ed., 1995, pp. 565-585.

68. **Park R., and Paulay, T.,** *Reinforced Concrete Structures,* John Wiley and Sons, Inc., New York, 1975.

69. **Perenchio, W.F., Fraczek, J. and Pfeifer, D.W.,** "Corrosion Protection of Prestressing Systems in Concrete Bridges," NCHRP Report 313, Transportation Research Board, Washington, D.C., February 1989.

70. **Post-Tensioning Institute,** "Guide Specification for Grouting of Post-Tensioned Structures," *PTI Committee on Grouting Specifications, 5th Draft,* November 1997.

71. **Prestressed Concrete Institute Ad Hoc Committee on Epoxy-Coated Strand,** "Guidelines for the Use of Epoxy-Coated," *Journal of the Prestressed Concrete Institute,* July-August 1993, pp. 26-32.

72. **PTI Committee on Grouting Specifications,** "Guide Specification for Grouting of Post-Tensioned Structures," 5th Draft, Post-Tensioning Institute, Phoenix, AZ, November 1997, 37 pp.

73. **Ranish, E.H., Rostasy, F.S. and Herschelmann, F.,** "Properties of Cement Grouts with Silica Fume Addition for the Injection of Post-Tensioning Ducts," *Fly Ash, Silica Fume, Slag, and Natural Pozzolans in Concrete: Proceedings of the Third International Conference,* Trondheim, Norway, SP-114, V.M. Malhotra, Ed., 1996, pp. 1159-1171.

74. **Roe, A.,** "From Buildings to Bridges," *Engineering News Record*, Vol. 240, No. 3, January 19, 1998, pp. 40-44.

75. **Rosenberg, A., Hansson, C.M. and Andrade, C.,** "Mechanisms of Corrosion of Steel in Concrete," *Materials Science of Concrete I,* The American Ceramic Society, 1989, pp. 285-313.

76. **Schokker, Andrea J.,** "Improving Corrosion Resistance of Post-Tensioned Substructures Emphasizing High Performance Grouts," Doctor of Philosophy Dissertation, The University of Texas at Austin, May 1999.

77. **Schupack, M. and O'Neil, F.,** "Observations on the Results of a 33 Year Test of the Durability of 20 Post-Tensioned Beams Exposed at the Corps of Engineers Severe Weather Exposure Station at Treat Island, Maine," *U.S. Army Engineer Waterway Experiment Station Report,* Vols I & II, 1997.

78. **Schupack, M. and Suarez, M.G.,** "Some Recent Corrosion Embrittlement Failures of Prestressing Systems in the United States," *Journal of the Prestesssed Concrete Institute,* March-April 1982.

79. **Schupack, M.,** "Admixture for Controlling Bleed in Cement Grout Used in Post-Tensioning," *Journal of the Prestressed Concrete Institute,* November-December 1974.

80. **Schupack, M.,** "Durability Study of a 35-year-old Post-Tensioned Bridge," *Concrete International,* February 1994.

81. **Schupack, M.,** "Grouting Tests on Large Post-Tensioning Tendons for Secondary Nuclear Containment Structures," *Journal of the Prestressed Concrete Institute,* March-April 1971, pp. 85-97.

82. **Schupack, M.,** "Post-Tensioning Tendons after 35 Years," *Concrete International,* March 1994, pp. 50-54.

83. **Shaw, M.,** "Migrating Corrosion Inhibitors for Reinforced Concrete Protection*," Proceedings of the Seventh International Conference on Structural Faults and Repair,* Volume 2, Edinburgh, Scotland, 1997, pp. 317-324.

84. **Silvestri, Giovanni**, Personal Communication, VSL Corporation, Grand Prairie, TX, March 1997.

85. **Sprinkel, M.,** "High Performance Silica Fume Grout for Post-Tensioning Ducts," *Proceedings of the PCI/FHWA International Symposium on High Performance Concrete,* L.S. Johal, ed., New Orleans, LA, 1997, pp. 343-354.

86. Standard Specifications for Construction of Highways, Streets and Bridges, Texas Department of Transportation, March 1995.

87. *Standard Specifications for Construction of Highways, Streets and Bridges,* Special Provision to Item 426 (Prestressing), Sub-Section: Construction Methods, Texas Department of Transportation, 1995. (also, personal communication with Dean Van Landuyt, Texas Department of Transportation, April 1997.)

88. **Suri, K.M., and Dilger, W.H.,** "Crack Width of Partially Prestressed Concrete Members," *ACI Journal,* Vol. 83, No. 5, September-October 1986, pp. 784-797.

89. **Swamy, R.N.,** "Design for Durability and Strength Through the Use of Fly Ash and Slag in Concrete," *Advances in Concrete Technology: Proceedings of the Third CANMET/ACI International Conference,* Auckland, New Zealand, SP-171, V.M. Malhotra, Ed., 1997, pp. 1-71.

90. **Texas State Department of Highways and Public Transportation,** Bridge Design Guide, First Edition, Austin, Texas, 1990.

91. **Thompson, N.G., Lankard, D. and Sprinkel, M.,** "Improved Grouts for Bonded Tendons in Post-Tensioned Bridge Structures," *Report No. FHWA-RD-91-092, Federal Highway Administration,* Cortest Columbus Technologies, January 1992.

92. **Tikalsky, P.J., Carrasquillo, R.L. and Snow, P.J.,** "Sulfate Resistance of Concrete Containing Fly Ash," Durability of Concrete, G.M. Idorn International Symposium, SP 131-13, J. Holm and M. Geiker, Eds, 1990, pp. 255-264.

93. **Vaca-Cortes, Enrique**, "Corrosion Performance of Epoxy-Coated Reinforcement in Aggressive Environments," Doctor of Philosophy Dissertation, The University of Texas at Austin, May 1998.

94. **Verhulst, S.M.,** "Evaluation and Performance Monitoring of Corrosion Protection Provided by Fiber-Reinforced Composite Wrapping," Master of Science Thesis, The University of Texas at Austin, May 1999.

95. **Vignos, R.P.,** "Test Method for Evaluating the Corrosion Protection of Internal Tendons Across Segmental Bridge Joints," *Masters Thesis*, The University of Texas at Austin, May 1994.

96. **VSL Corporation,** *VSLAB+ ™,* brochure.

97. "VSL Post-Tensioning Systems," Product Information Pamphlet, VSL Corporation, (undated).

98. **West, J.S.,** "Durability Design of Post-Tensioned Bridge Substructures," Doctor of Philosophy Dissertation*,* The University of Texas at Austin, May 1999.

99. **Wheat, H.G., and Eliezer, Z.,** "Some Electrochemical Aspects of Corrosion of Steel in Concrete," *Corrosion*, Vol. 41, No. 11, November 1985, pp. 640-645.

100. **Whiting, D. and Detwiler, R.,** "Silica Fume Concrete for Bridge Decks," *NCHRP Report 410, National Cooperative Highway Research Program,* National Academy Press, Washington, D.C., 1998.

101. **Working Party of the Concrete Society, "**Durable Bonded Post-Tensioned Concrete Bridges," Technical Report No. 47, August 1996.

102. **Yamaoka, Y., Hideyoshi, T. and Kurauchi, M.,** "Effect of Galvanizing on Hydrogen Embrittlement of Prestressing Wire," *Journal of the Prestressed Concrete Institute,* July-August 1988.